AD
AO35994

NAVAL POSTGRADUATE SCHOOL
Monterey, California

THESIS

AEOLIAN TONES FROM CIRCULAR CYLINDERS
OF NON-UNIFORM CROSS SECTION

by

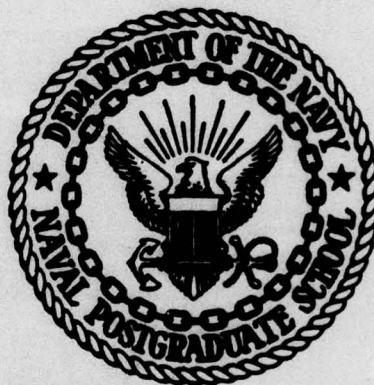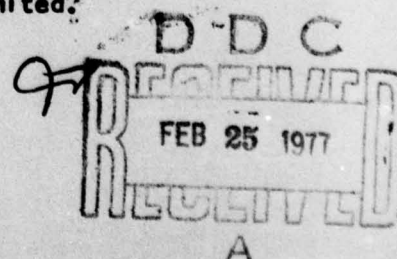Steven Robert Cohen

June 1976

Thesis Advisor: J.V. Sanders

Approved for public release; distribution unlimited.

REPORT DOCUMENTATION PAGE		READ INSTRUCTIONS BEFORE COMPLETING FORM
1. REPORT NUMBER	2. GOVT ACCESSION NO.	3. RECIPIENT'S CATALOG NUMBER
4. TITLE (and Subtitle) Aeolian Tones from Circular Cylinders of Non-Uniform Cross Section.		5. TYPE OF REPORT & PERIOD COVERED Ph.D. Thesis; June 1976
		6. PERFORMING ORG. REPORT NUMBER
7. AUTHOR(s) Steven Robert/Cohen		8. CONTRACT OR GRANT NUMBER(s)
9. PERFORMING ORGANIZATION NAME AND ADDRESS Naval Postgraduate School Monterey, California 93940		10. PROGRAM ELEMENT, PROJECT, TASK AREA & WORK UNIT NUMBERS
11. CONTROLLING OFFICE NAME AND ADDRESS Naval Postgraduate School Monterey, California 93940		12. REPORT DATE June 1976
		13. NUMBER OF PAGES 280
14. MONITORING AGENCY NAME & ADDRESS(If different from Controlling Office)		15. SECURITY CLASS. (of this report) Unclassified
		15a. DECLASSIFICATION/DOWNGRADING SCHEDULE

Doctoral thesis,   280 p.

16. DISTRIBUTION STATEMENT (of this Report)

Approved for public release; distribution unlimited.

17. DISTRIBUTION STATEMENT (of the abstract entered in Block 20, if different from Report)

18. SUPPLEMENTARY NOTES

19. KEY WORDS (Continue on reverse side if necessary and identify by block number)

Aeolian Tones   Non-Uniform Cylinders
Circular Cylinders
Lighthill's theory of aerodynamic sound
Lift Force
Correlation Length

20. ABSTRACT (Continue on reverse side if necessary and identify by block number)

Lighthill's theory of aerodynamic sound is reviewed. Applications of this theory to different cylinder classes are synthesized and extended to cylinder types not addressed previously. An experiment wherein cylinders are placed in an open jet, permitting simultaneous measurement of total lift force, correlation parameters and radiated sound intensity, is conducted. Over the ⟶ next page

251450 LB

(20. ABSTRACT Continued)

Reynolds number range 10^3 to 5×10^4, the theory of aerodynamic
sound is validated for uniform, roughened, skewed, finned
and notched cylinders and for cylinders with splitter plates.
Reduction of lift force, by any means, is shown to reduce
radiated sound intensity, and local lift force is found to
vary monotonically with the two dimensionality of the vortex
wake.

DD Form 1473
1 Jan 73
S/N 0102-014-6601

2

Aeolian Tones from Circular Cylinders of Non-Uniform Cross Section

by

Steven Robert Cohen
Lieutenant Commander, United States Navy
B.A., University of Virginia, 1961
M.S., Naval Postgraduate School, 1968

Submitted in partial fulfillment of the
requirements for the degree of

DOCTOR OF PHILOSOPHY

from the

NAVAL POSTGRADUATE SCHOOL
June 1976

Author: _Steven Robert Cohen_

Approved by:

James V. Sanders
J. V. Sanders
Assoc. Professor of Physics
Thesis Advisor

O B Wilson, Jr.
O. B. Wilson, Jr.
Professor of Physics

Geo L Sackman
G. S. Sackman
Assoc. Professor of
Electrical Engineering

K. E. Woehler
K. E. Woehler
Professor of Physics

M. Houlihan
M. Houlihan
Assoc. Professor of
Mechanical Engineering

Jack J Hoyt
Dr. Jack Hoyt
Naval Undersea Center
San Diego

Approved by: _K. E. Woehler_
Chairman, Department of Physics and Chemistry

Approved by: _Jack R Borsting_
Academic Dean

ABSTRACT

Lighthill's theory of aerodynamic sound is reviewed. Applications of this theory to different cylinder classes are synthesized and extended to cylinder types not addressed previously. An experiment wherein cylinders are placed in an open jet, permitting simultaneous measurement of total lift force, correlation parameters and radiated sound intensity, was conducted. Over the Reynolds number range 10^3 to 5×10^4, the theory of aerodynamic sound is validated for uniform, roughened, skewed, finned and notched cylinders and for cylinders with splitter plates. Reduction of lift force, by any means, is shown to reduce radiated sound intensity, and local lift force is found to vary monotonically with the two dimensionality of the vortex wake.

4

ACKNOWLEDGMENTS

In the interest of brevity, it is impossible to mention all who provided support during this research. However, I find it impossible not to thank Professor J. V. Sanders, my principal advisor, who permitted my pursuit of unproductive paths just long enough to maximize my learning experience, but who also, with subtle suggestion, succeeded in appropriately redirecting my efforts. Similarly, I am in debt to the other members of my doctoral committee who always furnished friendly ears and provided expert guidance and appreciated advice. I must also thank Dr. O. M. Griffen of the Naval Research Laboratory who suggested this avenue of research and supplied initial direction.

Construction of the wind tunnel would have been seriously delayed without the assistance of OM-1 Ken Richardson. Kudos also are due Bob Moeller who possesses the unique ability to convert rough sketches, words, and arm motions into perfectly fabricated mechanisms.

Finally, I owe special thanks to my wife, Carolyn, and to my two sons, Michael and Jeffrey who always understood why I spent evenings and weekends in the laboratory.

TABLE OF CONTENTS

LIST OF TABLES

LIST OF FIGURES

10

11

LIST OF PLATES

14

INTRODUCTION

Although aeolian tones were known in antiquity, their scientific study did not begin until Strouhal's experiment in 1878.[1,2] Strouhal discovered that the frequency ($\omega/2\pi$) of the aeolian tone increased with wind velocity ($\bar{U}$) and decreased with diameter (d). This dependence is now expressed in the dimensionless Strouhal number, $S = \omega d/2\pi\bar{U}$.

Strouhal's effort became known to Lord Rayleigh who, over the next twenty years, established that aeolian tones were both directional in nature[2,3] and associated with vortex sheet instability in the cylinder's wake.[4] Other experiments continued, and by the second decade of this century, the first pictures of the alternating vortex wake behind a cylinder had been obtained:[5,6] the vortex frequency was found to be identical to that of the aeolian tone;[7,8] van Karman's vortex stability theory was published;[9] and the transverse force on the cylinder was associated with alternating circulatory flow about the cylinder.[10] Lord Rayleigh observed that aeolian tones occurred in the absence of cylinder vibration[11] and further noted that the Strouhal number was solely a function of Reynolds number (Re = $\bar{U}d/\nu$).[11]

Subsequent efforts, continuing into the 1950's, experimentally quantified this Strouhal-Reynolds number relationship and confirmed that the Strouhal frequency applied to both the wake and the aeolian tone over the range of Reynolds

15

numbers from 100 to 10^6.[2,12-17] Several of these contributors concluded that the aeolian tone originated in the total lift force exerted by the flow on the cylinder, and furthermore, they confirmed that the directionality of the produced sound was that of a dipole with axis perpendicular to the axis of the cylinder and to the direction of flow.

In spite of these extensive experimental efforts, however, it was not until publication of Lighthill's now classic paper on the theory of aerodynamic sound that a mathematical prediction of the generated sound field could be attempted.[18] Curle extended Lighthill's general theory to account for the presence of solid boundaries,[19] and shortly thereafter, Phillips derived an expression for the intensity of sound produced by flow over a fixed, rigid, uniform cylinder.[2] Phillips related sound intensity (I) to local lift force (f_L), $\overline{U}$, d and a quantity he termed correlation distance (ℓ_c). This last quantity, now usually called correlation length, was introduced to account for phase variation of f_L along the length of the cylinder. It was interpreted to be the effective length over which f_L is of relatively constant phase.

Within the next ten years, several not entirely successful experiments were conducted to validate equations identical or essentially equivalent to that derived by Phillips.[2,15,20,21] These experiments measured I and compared this intensity to that predicted from measured or reported values of f_L

16

and ℓ_c. In no case were all three quantities measured simultaneously, a task which Lighthill understood to be extremely difficult.[22] As late as 1961, Lighthill noted that "the equation (for predicted sound intensity) must be considered unproved while no simultaneous measurement of all its terms exists."[22]

More recently, because of increased interest in this area, more refined equations for I as a function of f_L, ℓ_c and other parameters have been derived.[6,21,23,25] In addition, limited verification of their validity, satisfying Lighthill's above quoted simultaneity criterion, has occurred.[6,25] However, before discussing these theoretical and experimental advances, it is appropriate to address the rationale for this increased concern with the generation of aeolian tones.

In both air and water, flow over blunt bodies is a common occurrence. For cylinders, flow frequently occurs in the range of Reynolds number between 300 and 3×10^5. Throughout this range, the flow is characterized by a laminar boundary layer which separates at about 80 degrees from the stagnation point[26] and by a wake composed of alternating vortices, laminar near the cylinder, but growing turbulent several diameters downstream. The shedding of these vortices results in an alternating lift force on the cylinder and in an accompanying aeolian tone.

If the natural frequency of the body's motion is near that of the lift force, and if damping is small, the vortex shedding frequency becomes locked-in to or synchronized with

the body's frequency.[8,27-30] Large amplitude oscillatory
motion in the lift direction occurs, and the lift force is
amplified. This phenomenon of synchronization, wherein the
vortex shedding mechanism interacts with resonant vibrations
of a rigid body in the manner of a non-linear feedback oscilla-
tor, has recently received considerable engineering attention
in that it is the cause of costly structural failures. More-
over, with synchronization, laboratory studies of cylinders
are facilitated as lock-in removes three dimensional effects
from the flow and thereby potentially simplifies experiments
on aeolian tones.

Even without synchronization the lift force and resulting
vibrations are of engineering interest. For example, this
lift force may cause tow cable vibrations, usually termed
cable strum, in water. These vibrations often are mechani-
cally coupled to the towed body, and if the latter is a
hydrophone, they may be coupled acoustically as well. As
such, aeolian tone generation has application to oceano-
graphic studies and to naval sonar technology.

These applications as well as general scientific interest
have motivated revisions and extensions of Phillips' original
formula for the sound generated by flow over a uniform smooth
cylinder. Frenkiel more completely accounted for the con-
cept of effective length.[24] Fitzpatrick and Strassberg re-
ported an equation applicable to a particular class of non-
rigid smooth cylinders,[23] and Koopmann derived an expression
for a cylinder oscillating under conditions of synchronization.[6]

More recently, Leehey and Hanson experimentally verified a modification of Phillips' formula using a uniform cylinder at Reynolds numbers of 4100 and 6150.[25] Similarly, Koopmann's experiment validated his equation for a synchronized cylinder at a Reynolds number of 21,500.[6]

On the other hand, no synthesis of the various formulas applicable to uniform cylinders exists, and no theory for non-uniform cylinders has been developed. Experimentally, equations appropriate to uniform cylinders have been validated at only three particular Reynolds numbers, and no simultaneous measurement of f_L, ℓ_c and I have been made for non-uniform, roughened, or skewed cylinders, nor for cylinders with splitter plates. Moreover, the lack of experimental investigation into these areas is important in view of the above noted applications and of the wide scatter exhibited by f_L and ℓ_c data reported in the literature.[6,21,25,30-42] This scatter, in turn, is now understood in terms of variation in cylinder end conditions and in the turbulence level of the undisturbed flow.[21,43-45]

The purpose of the study herein reported, then, is to extend previous knowledge in these areas. Specifically, this research addresses the validation of the theory of aerodynamic sound for uniform cylinders over a broader Reynolds number range. In addition, it examines the relation between radiated sound and total lift force for a roughened cylinder, for two cylinders with splitter plates, and for finned, notched and skewed cylinders.

The present study also departs from previous research in that it compares directly measured total lift force (F_L) with radiated sound intensity (I). As such, it achieves the major advantage of an experiment using synchronization without the necessity of obtaining synchronization in the laboratory. Nevertheless, the synchronization phenomena is studied herein, although somewhat abortively. Finally, this experimental effort also measures ℓ_c so that parallel to the calculations of F_L from f_L and ℓ_c reported in earlier work, f_L is herein calculated from F_L and ℓ_c.

In Section I, the theory of aerodynamic sound is developed and applied to a variety of uniform cylinders, thereby providing, in one place and with a correction, a complete summary of previously reported theory. This development then is extended to a specified class of non-uniform cylinders. Sections II and III describe the instrumentation of the experiment, discuss the measurement techniques employed and report raw data. Section IV presents the processed results obtained and compares these results to those reported in previous investigations. This section also reports an effect wherein the local lift force is amplified or attenuated as the two-dimensionality of the vortex wake is increased or decreased. Conclusions appear in Section V, and some suggestions for future studies are included in Section VI.

I. **THEORY**

BASIC THEORY

In 1952, Lighthill introduced the theory of aerodynamic sound.[18] His paper remains so eminently readable that even a condensation of its essential elements is best presented in the format of the original, namely a qualitative discussion followed by a mathematical treatment.

Sound generation is the conversion of kinetic to acoustic energy. A source represents first order conversion, the fluctuation of mass in a fixed region of space. A dipole is second order conversion, the fluctuation of the rate of mass flux or momentum. Fluctuation of the rate of momentum flux ($\rho v_i v_j$) is third order conversion, is termed a quadrupole, and is the mechanism whereby aerodynamic sound is produced.

In a medium at rest, the local stress is the acoustic pressure ($a_o^2 \rho \delta_{ij}$), while in a flow the stress is more complex. Regardless of the form the latter stress takes, however, one may define the instantaneous applied stress (T_{ij}) as the difference between the true stress and the local pressure that would be present in the absence of flow. Equating this applied stress to a forcing function relative to the acoustic medium at rest then permits calculation of the radiated sound field.

This approach is exact in that T_{ij} includes the generation of sound, its convection with the flow, dissipation,

and all other flow or medium connected phenomena. Moreover, this approach is independent of the flow model used; for example, the flow is not required to be that of a Stokesian fluid. Nevertheless, the flow must be known, and when the flow is not describable in closed form, neither in general is the sound field, although simplifying assumptions may permit a closed form expression.

The basic description of linear acoustics encompasses an exact continuity equation

$$(1) \qquad \frac{\partial \rho}{\partial t} + \frac{\partial (\rho v_i)}{\partial y_i} = 0$$

and an approximate momentum equation

$$(2) \qquad \frac{\partial}{\partial t}(\rho v_i) + a_o^2 \frac{\partial \rho}{\partial y_i} = 0 .$$

Differentiation of the first with respect to space and the second with time yields the homogeneous wave equation

$$(3) \qquad \frac{\partial^2 \rho}{\partial t^2} - a_o^2 \nabla^2 \rho = 0 .$$

In flow, the exact momentum equation

$$(4) \qquad \frac{\partial}{\partial t}(\rho v_i) + \frac{\partial}{\partial y_j}(\rho v_i v_j + P_{ij}) = 0$$

must be used. The fluctuating Reynolds stress $(\rho v_i v_j)$

represents momentum convection, and p_{ij} is the compressive stress tensor.

T_{ij}, by definition, is

$$(5) \qquad T_{ij} = \rho \, v_i v_j + p_{ij} - a_o^2 \, \rho \, \delta_{ij} \, .$$

Differentiating (5) with respect to y_j and combining with (4) gives

$$(6) \qquad \frac{\partial}{\partial t}(\rho \, v_i) + a_o^2 \, \frac{\partial \rho}{\partial y_i} = - \frac{\partial T_{ij}}{\partial y_j} \, .$$

Finally, the inhomomogeneous wave equation

$$(7) \qquad \frac{\partial^2 \rho}{\partial t^2} - a_o^2 \, \nabla^2 \, \rho = \frac{\partial^2 T_{ij}}{\partial y_i \partial y_j}$$

results from differentiating (1) and (6) just as (3) was obtained from (1) and (2). Equation (7), then, is the governing equation for aerodynamic sound.

The solution of (7) is the well known[46] Kirchhoff solution of the inhomogeneous wave equation:

$$(8) \qquad \rho(x,t) - \rho_o = \frac{1}{4\pi a_o^2} \int_V \frac{1}{r} \Big[\frac{\partial^2 T_{ij}}{\partial y_i \partial y_j} \Big] \, dV(y)$$

$$+ \frac{1}{4\pi} \int_S \Big[\frac{1}{r} \frac{\partial \rho}{\partial n} + \frac{1}{r^2} \frac{\partial r}{\partial n} \rho + \frac{1}{a_o r} \frac{\partial r}{\partial n} \frac{\partial \rho}{\partial t} \Big] \, dS(y) \, .$$

The brackets indicate that the quantity contained within is to be evaluated at the retarded time, $t' = t - (\frac{r}{a_o})$. $r = |x_i - y_i|$, and the second term accounts for solid boundaries with normal $\vec{n}$.

In the absence of boundaries, the second term is zero, leaving only the quadrupole field. However, in most applications, including the present one, boundaries are of primary interest, and therefore, this development now must address Curle's extension[19] of Lighthill's theory.

First, it is desirable to convert (8) to a more appropriate form. To this end, one may write, for any function $f(y,t)$,

$$\frac{\partial(\frac{[f]}{r})}{\partial y} = \frac{\partial(f(y,t-\frac{r}{a_o})/r)}{\partial y} = -\frac{1}{r^2}\frac{\partial r}{\partial y}[f(y,t)] + \frac{1}{r}\frac{\partial[f(y,t)]}{\partial y} \; .$$

But,

$$(9) \quad \frac{\partial f(y,t-\frac{r}{a_o})}{\partial y} = [\frac{\partial f}{\partial y}] + \frac{\partial f(y,t-\frac{r}{a_o})}{\partial(t-\frac{r}{a_o})}\frac{\partial(t-\frac{r}{a_o})}{\partial y} = [\frac{\partial f}{\partial y}] - \frac{1}{a_o}\frac{\partial r}{\partial y}[\frac{\partial f}{\partial t}] \; .$$

Therefore,

$$(10) \quad \frac{\partial(\frac{[f]}{r})}{\partial y} = \frac{1}{r}[\frac{\partial f}{\partial y}] - \frac{1}{a_o r}\frac{\partial r}{\partial y}[\frac{\partial f}{\partial t}] - \frac{1}{r^2}\frac{\partial r}{\partial y}[f] \; .$$

24

Also,

$$(11) \quad \frac{\partial (\frac{[f]}{r})}{\partial x} = - \frac{1}{a_0 r} \frac{\partial r}{\partial x} [\frac{\partial f}{\partial t}] - \frac{1}{r_2} \frac{\partial r}{\partial x} [f]$$

$$= \frac{1}{a_0 r} \frac{\partial r}{\partial y} [\frac{\partial f}{\partial t}] + \frac{1}{r^2} \frac{\partial r}{\partial y} [f].$$

Hence, from (10) and (11),

$$(12) \quad \frac{1}{r} [\frac{\partial f}{\partial y}] = \frac{\partial}{\partial y} (\frac{[f]}{r}) + \frac{\partial}{\partial x} (\frac{[f]}{r}).$$

Now applying (12) to the first term of (8) twice, letting the general function f first be $\frac{\partial T_{ij}}{\partial y_j}$ and then be T_{ij}, yields

$$(13) \quad \int_V \frac{1}{r} [\frac{\partial^2 T_{ij}}{\partial y_i \partial y_j}] dV(y) = \frac{\partial^2}{\partial x_j \partial x_i} \int_V \frac{[T_{ij}]}{r} dV(y)$$

$$+ \frac{\partial}{\partial x_i} \int_V \frac{\partial}{\partial y_j} (\frac{[T_{ij}]}{r}) dV(y)$$

$$+ \int_V \frac{\partial}{\partial y_i} (\frac{1}{r} [\frac{\partial T_{ij}}{\partial y_j}]) dV(y)$$

which, upon application of the divergence theorem, becomes

$$(14) \quad \int_V \frac{1}{r} [\frac{\partial^2 T_{ij}}{\partial y_i \partial y_j}] dV(y) = \frac{\partial^2}{\partial x_i \partial x_j} \int_V \frac{[T_{ij}]}{r} dV(y)$$

$$+ \frac{\partial}{\partial x_i} \int_S \ell_j \frac{[T_{ij}]}{r} dS(y)$$

$$+ \int_S \frac{\ell_i}{r} [\frac{\partial T_{ij}}{\partial y_j}] dS(y).$$

25

ℓ_j is the direction cosine of $\vec{n}$.

Holding (14) in abeyance and noting that for any function (f), $\frac{\partial f}{\partial n} = \frac{\partial f}{\partial y_i} \ell_i$, permits expression of the second term of (8) as

$$\frac{1}{4\pi} \int_S \left[\frac{1}{r} \frac{\partial \rho}{\partial n} + \frac{1}{r^2} \frac{\partial r}{\partial n} \rho + \frac{1}{a_o r} \frac{\partial r}{\partial n} \frac{\partial \rho}{\partial t} \right] dS(y)$$

$$= \frac{1}{4\pi} \int_S \frac{\ell_i}{r} \left[\frac{\partial \rho}{\partial y_i} \right] dS(y)$$

$$+ \frac{1}{4\pi} \int_S \ell_i \left(\frac{1}{r^2} \frac{\partial r}{\partial y_i} [\rho] + \frac{1}{a_o r} \frac{\partial r}{\partial y_i} \left[\frac{\partial \rho}{\partial t} \right] \right) dS(y).$$

Applying (11) to the second term of this expression yields

$$(15) \quad \frac{1}{4\pi} \int_S \left[\frac{1}{r} \frac{\partial \rho}{\partial n} + \frac{1}{r^2} \frac{\partial r}{\partial n} \rho + \frac{1}{a_o r} \frac{\partial r}{\partial n} \frac{\partial \rho}{\partial t} \right] dS(y)$$

$$= \frac{1}{4\pi} \int_S \frac{\ell_i}{r} \left[\frac{\partial (\rho \delta_{ij})}{\partial y_j} \right] dS(y)$$

$$+ \frac{1}{4\pi} \frac{\partial}{\partial x_i} \int_S \ell_i \frac{[\rho]}{r} dS(y).$$

Then, the appropriate form for interpreting (8) is obtained by combining (8), (14) and (15).

$$(16) \quad \rho(x,t) - \rho_o = \frac{1}{4\pi a_o^2} \frac{\partial^2}{\partial x_i \partial x_j} \int_V \frac{[T_{ij}]}{r} dV(y)$$

$$+ \frac{1}{4\pi a_o^2} \frac{\partial}{\partial x_i} \int_S \frac{\ell_j}{r} [a_o^2 \rho \delta_{ij} + T_{ij}] dS(y)$$

$$+ \frac{1}{4\pi a_o^2} \int_S \frac{\ell_i}{r} \left[\frac{\partial}{\partial y_j} (a_o^2 \rho \delta_{ij} + T_{ij}) \right] dS(y).$$

26

In (16), the monopole and dipole terms from the homogeneous solution appear as does an original quadrupole contribution arising from the flow. Additionally, the second part of the second and third terms shows that the interaction of the flow with the boundary produces monopole and dipole sound contributions as well. Finally, using (4) and (5) in the latter two terms of (6) results in

$$(17) \quad \rho(x,t) - \rho_o = \frac{1}{4\pi a_o^2} \frac{\partial^2}{\partial x_i \partial x_j} \int_V \frac{[T_{ij}]}{r} \, dV(y)$$

$$+ \frac{1}{4\pi a_o^2} \frac{\partial}{\partial x_i} \int_S \frac{\ell_j}{r} [\rho \, v_i \, v_j + P_{ij}] \, dS(y)$$

$$- \frac{1}{4\pi a_o^2} \int_S \frac{\ell_i}{r} [\frac{\partial(\rho v_i)}{\partial t}] \, dS(y),$$

the form most appropriate for the present application. An original quadrupole contribution of strength T_{ij} again appears in this equation. The second term is a summed distribution of dipoles, with axis in the i direction, of strength $(\rho \, v_i \, v_{normal} + P_{inormal})$ at the internal boundary, and the third term is a distribution of monopole sources of strength $\rho \, v_{normal}$ at this boundary.

APPLICATION TO UNIFORM CYLINDERS

Before applying (17) to the case of interest, namely cylinders, it is useful to examine the first term. Both Lighthill and Curle noted that this quadrupole field is of order $(M_a)^2$ below that of the dipole term, where M_a is the

27

ratio of flow speed to sound speed.[18,19] Since, in the
experiment under consideration, M_a is less than 0.15,
ignoring this term introduces an error of less than two
percent in sound pressure and less than 0.4 percent in
intensity. Equation (17) is thus simplified to

$$(18) \quad \rho(x,t) - \rho_0 = - \frac{1}{4\pi a_0^2} \int_S \frac{\ell_i}{r} \left[\frac{\partial(\rho v_i)}{\partial t} \right] dS(y)$$

$$+ \frac{1}{4\pi a_0^2} \frac{\partial}{\partial x_i} \int_S \frac{\ell_j}{r} \left[\rho v_i v_j + p_{ij} \right] dS(y).$$

To further reduce complexity, ρ may be equated to ρ_0
on the right side of (18), permitting it to be removed from
the integral in the first term.

Continued reduction then requires specification of the
characteristics of the uniform cylinder under consideration.
Here, three cases are of interest; stationary cylinders,
non-stationary but rigid so that all motion is that of a
rigid body, and both non-rigid and non-stationary.

Stationary Cylinders.

Since v_i is identically zero, application of (11) to
perform the differentiation in the second term immediately
converts (18) to

$$(19) \quad \rho(x,t) - \rho_0 = - \frac{1}{4\pi a_0^3} \int_S \frac{\ell_j}{r} \frac{\partial r}{\partial x_i} \left[\frac{\partial p_{ij}}{\partial t} \right] dS(y)$$

$$- \frac{1}{4\pi a_0^2} \int_S \frac{\ell_j}{r^2} \frac{\partial r}{\partial x_i} \left[p_{ij} \right] dS(y).$$

28

To obtain a still more useful form, two further assumptions are appropriate. The first is that the field point is far from the cylinder relative to cylinder size ($x_i \gg y_i$). Second, cylinder size is assumed small compared to the wave length of radiated sound so that retarded time is given by $t' = t - \frac{r(x)}{a_o}$, where r is a function of x alone. Then, defining P_i as the force per unit area exerted in the i direction by the fluid on the cylinder ($P_i = \ell_j P_{ij}$) permits rewriting (19) as

$$(20) \quad \rho(x,t) - \rho_o = - \frac{1}{4\pi a_o^3} \frac{x_i}{r^2} \int_S [\frac{dP_i}{dt}] \, dS(y)$$

$$- \frac{1}{4\pi a_o^2} \frac{x_i}{r^3} \int_S [P_i] \, dS(y) .$$

This equation is the general expression applicable to stationary cylinders; however, its experimental validation requires further specification. Such specification will be addressed later in this section, following examination of the other two cases.

Non-Stationary but Rigid Cylinders.

Following Phillips[2] and Koopmann[6], simplification begins with application of the divergence theorem to the first term of (18) after ρ_o has been removed from the integral, so that

29

$$(21) \quad -\frac{\rho_o}{4\pi a_o^2} \int_S \frac{\ell_i}{r}[\frac{\partial v_i}{\partial t}] \, dS(y) = -\frac{\rho_o}{4\pi a_o^2} \int_S \frac{\partial}{\partial y_i}(\frac{1}{r}[\frac{\partial v_i}{\partial t}]) \, dV(y)$$

$$= -\frac{\rho_o}{4\pi a_o^2} \int_V \frac{1}{r}[\frac{\partial^2 v_i}{\partial y_i \partial t}] \, dV(y)$$

$$-\frac{\rho_o}{4\pi a_o^2} \int_V \frac{x_i - y_i}{r}(\frac{1}{a_o r}[\frac{\partial^2 v_i}{\partial t^2}] + \frac{1}{r^2}[\frac{\partial v_i}{\partial t}]) \, dV(y)$$

where (10) has been used to differentiate with respect to
y. Using (11) to perform the indicated differentiation in
the second term of (16) yields

$$(22) \quad \frac{1}{4\pi a_o^2} \frac{\partial}{\partial x_i} \int_S \frac{\ell_j}{r}[\rho v_i v_j + p_{ij}] \, dS(y)$$

$$= -\frac{1}{4\pi a_o^2} \int_S \ell_j \frac{x_i - y_i}{r}(\frac{1}{a_o r}[\frac{\partial}{\partial t}(\rho v_i v_j + p_{ij})]$$

$$+ \frac{1}{r^2}[\rho v_i v_j + p_{ij}]) \, dS(y),$$

and the sum of (21) and (22) is equivalent to the right side
of (18).

Rigidity implies that the first integral on the right side
of (21) is zero. Moreover, it also implies that v_i in the
second term of (21) as well as in (22) may be replaced by
$U_i + \varepsilon_{ijk} \omega_j y_k$ where U_i is the velocity of the cylinder's
center of mass and ω_j is the angular velocity of the cylinder

30

about this center.* Then, again assuming that $x_i \gg y_i$ and that $t' = t - \frac{r(x)}{a_o}$, and using the definition of P_i, this sum of (21) and (22) becomes

$$(23) \quad \rho(x,t) - \rho_o = -\frac{\rho_o x_i}{4\pi a_o^3 r^2}[\ddot{U}_i]V - \frac{\rho_o x_i}{4\pi a_o^3 r^2}\int_V [\frac{\partial^2}{\partial t^2}(\epsilon_{ijk}\omega_j y_k)]dV(y)$$

$$-\frac{\rho_o x_i}{4\pi a_o^2 r^3}[\dot{U}_i]V - \frac{\rho_o x_i}{4\pi a_o^2 r^3}\int_V [\frac{\partial}{\partial t}(\epsilon_{ijk}\omega_j y_k)]dV(y)$$

$$-\frac{\rho_o x_i}{4\pi a_o^3 r^2}\int_S \ell_j [\frac{\partial}{\partial t}((U_i + \epsilon_{ik\ell}\omega_k y_\ell)(U_j + \epsilon_{jpq}\omega_p y_q))]dS(y)$$

$$-\frac{\rho_o x_i}{4\pi a_o^2 r^3}\int_S \ell_j [(U_i + \epsilon_{ik\ell}\omega_k y_\ell)(U_j + \epsilon_{jpq}\omega_p y_q)]dS(y)$$

$$-\frac{x_i}{4\pi a_o^3 r^2}\int_S [\dot{P}_i]dS(y)$$

$$-\frac{x_i}{4\pi a_o^2 r^3}\int_S [P_i]dS(y).$$

To further simplify requires consideration of the fifth and sixth terms. Applying the divergence theorem to the integral of the sixth term, and noting that $\frac{\partial[f]}{\partial y} = [\frac{\partial f}{\partial y}]$ in

---

*Both Phillips and Koopmann omit this perhaps unusual sound field contribution resulting from rotation of a rigid cylinder in a flow. A letter noting this omission and reporting the correction developed in this paper has been sent to Professor Phillips in his capacity as an editor of the Journal of Fluid Mechanics.

(10) per the $r = r(x)$ assumption, gives

$$(24) \quad \int_S \ell_j [(U_i + \varepsilon_{ik\ell}\omega_k y_\ell)(U_j + \varepsilon_{jpq}\omega_p y_q)] dS(y)$$

$$= \int_V [\frac{\partial}{\partial y_j}((U_i + \varepsilon_{ik\ell}\omega_k y_\ell)(U_j + \varepsilon_{jpq}\omega_p y_q))] dV(y)$$

$$= \int_V [(\varepsilon_{ik\ell}\omega_k \delta_{\ell j})(U_j + \varepsilon_{jpq}\omega_p y_q)$$

$$+ (U_i + \varepsilon_{ik\ell}\omega_k y_\ell)(\varepsilon_{jpq}\omega_p \delta_{jq})] dV(y)$$

$$= \int_V [\varepsilon_{ikj}\omega_k U_j + \varepsilon_{jik}\varepsilon_{jpq}\omega_k \omega_p y_q] dV(y)$$

$$= \int_V [-\varepsilon_{ijk}U_j\omega_k + (\delta_{ip}\delta_{kq} - \delta_{kp}\delta_{iq})\omega_k \omega_p y_q] dV(y)$$

$$= \int_V [-\varepsilon_{ijk}U_j\omega_k + \omega_i\omega_j y_j - \omega_j\omega_j y_i] dV(y)$$

Similarly applying the divergence theorem to the fifth term of (23) and interchanging the order of differentiation results in an equation identical to (24) except that the retarded time derivative of the above integrand appears. In all, then, the general expression applicable to this case is

$$(25) \quad \rho(x,t) - \rho_0 = -\frac{\rho_0 x_i}{4\pi a_0^3 r^2}[\ddot{U}_i]V - \frac{\rho_0 x_i}{4\pi a_0^3 r^2}\int_V [\frac{\partial^2}{\partial t^2}(\varepsilon_{ijk}\omega_j v_k)$$

$$-\frac{\partial}{\partial t}(\varepsilon_{ijk}U_j\omega_k - \omega_i\omega_j y_j + \omega_j\omega_j y_i)]dV(y)$$

$$-\frac{\rho_0 x_i}{4\pi a_0^2 r^3}[\dot{U}_i]V - \frac{\rho_0 x_i}{4\pi a_0^2 r^3}\int_V [\frac{\partial}{\partial t}(\varepsilon_{ijk}\omega_j y_k)$$

$$-(\varepsilon_{ijk}U_j\omega_k - \omega_i\omega_j y_j + \omega_j\omega_j y_i)]dV(y)$$

$$-\frac{x_i}{4\pi a_0^3 r^2}\int_S [\dot{P}_i]dS(y) - \frac{x_i}{4\pi a_0^2 r^3}\int_S [P_i]dS(y) .$$

Within this case, the behavior of a cylinder under synchronization is of primary interest. However, before applying (25) to this phenomenon, further definitions are in order. First, let the cylinder's axis be the Z axis and let ϕ be the polar angle at the center of the cylinder (see Figure C-1). Then the local lift force in the i direction (f_i) is given by $f_i = \int_\phi P_i \frac{d}{2}d\phi$, and the total force in the i direction (F_i) is $F_i = \int_Z f_i dz$, so that $F_i = \int_S P_i dS(y)$.

Now, with synchronization, as discussed on page 17, cylinder motion and the vortex shedding process interact, and the vortex wake becomes truly two dimensional. In turn, the lift and drag forces exerted by the fluid on the cylinder are in phase along Z, and $F_i = f_i L$ as no rotation is present.

33

Then (25) becomes

$$(26) \quad \rho(x,t) - \rho_0 = - \frac{x_i}{4\pi a_0^3 r^2} [\rho_0 \ddot{U}_i V + \dot{F}_i]$$

$$- \frac{x_i}{4\pi a_0^2 r^3} [\rho_0 \dot{U}_i V + F_i].$$

As the drag force fluctuates at twice the frequency of the lift force and with fluctuation amplitude small compared to that of the lift force[2], attention is restricted to the latter. Taking x_2 as the direction of cylinder motion, replacing the subscript "2" by "L" for lift, defining θ as the angle between x_2 and r (see Figure C-1), and converting to acoustic pressure p yields

$$(27) \quad p = - \frac{\cos \theta}{4\pi r} [\frac{\rho_0 \ddot{U}_L V + \dot{F}_L}{a_0} + \frac{\rho_0 \dot{U}_L V + F_L}{r}]$$

or equivalently,

$$(28) \quad p = \frac{\partial}{\partial x_L} [\frac{F_L + \rho_0 V \dot{U}_L}{4\pi r}].$$

Koopmann[6] experimentally verified the second or near field term of (27).

Finally, it should be noted that (27) and (28) relate the phase of radiated sound to that of both lift force and cylinder motion.

Non-Rigid and Non-Stationary.

Equations (21) and (22), derived for the previous case before introduction of assumptions peculiar to that case, apply to this still more general consideration. As before, their sum represents the total sound field and also as before, the $x_i \gg y_i$ as well as the $t' = t - \frac{r(x)}{a_0}$ assumptions are made. Then again defining P_i and adding (21) and (22) yields

$$(29) \quad \rho(x,t) - \rho_0 = -\frac{\rho_0}{4\pi a_0^2 r} \int_V [\frac{\partial^2 v_i}{\partial y_i \partial t}] \, dV(y)$$

$$-\frac{\rho_0 x_i}{4\pi a_0^3 r^2} \int_V [\frac{\partial^2 v_i}{\partial t^2}] dV(y) - \frac{\rho_0 x_i}{4\pi a_0^2 r^3} \int_V [\frac{\partial v_i}{\partial t}] dV(y)$$

$$-\frac{x_i}{4\pi a_0^3 r^2} \int_S \ell_j [\frac{\partial}{\partial t}(\rho v_i v_j)] dS(y)$$

$$-\frac{x_i}{4\pi a_0^2 r^3} \int_S \ell_j [\rho v_i v_j] dS(y)$$

$$-\frac{x_i}{4\pi a_0^3 r^2} \int_S [\frac{\partial P_i}{\partial t}] dS(y) - \frac{x_i}{4\pi a_0^2 r^3} \int_S [P_i] dS(y)$$

In a manner still parallel to previous results, the last two terms are seen as far and near field contributions from the flow-caused lift force. The first term is unique to this complex case and is the source contribution resulting from cylinder deformation. The remaining terms, then, are

35

the far (second and fourth terms) and near (third and fifth terms) field dipole contributions attributable to cylinder motion.

To verify this explanation, however, it is desirable to make several assumptions which will produce tractable mathematics. Therefore, restricted cylinder deformation and motion are stipulated as follows: the only deformation is pure dilatation, and cylinder motion is such that each cross section moves as a rigid body so that the cylinder may be viewed as vibrating like a thick string.

With these assumptions in hand, the first term of (29) now will be simplified. In this term, the volume $V(y)$ refers to the volume of the cylinder; within this volume, continuity (1) holds and thus

$$\frac{\partial \rho_c}{\partial t} + v_i \frac{\partial \rho_c}{\partial y_i} + \rho_c \frac{\partial v_i}{\partial y_i} = 0$$

where ρ_c is the density of the cylinder ($\rho_c = m/V$). Uniform dilatation implies that $\frac{\partial \rho_c}{\partial y_i} = 0$, and hence $\frac{\partial v_i}{\partial y_i} = -\frac{1}{\rho_c} \frac{\partial \rho_c}{\partial t}$ for this case. Therefore,

$$-\frac{\rho_o}{4\pi a_o^2 r} \int_V \left[\frac{\partial^2 (v_i)}{\partial y_i \partial t}\right] dV(y) = \frac{\rho_o}{4\pi a_o^2 r} \int_V \left[\frac{\partial}{\partial t}(\frac{1}{\rho_c} \frac{\partial \rho_c}{\partial t})\right] dV(y).$$

Taking the derivative of the integrand gives

$$\frac{\partial}{\partial t}(\frac{1}{\rho_c} \frac{\partial \rho_c}{\partial t}) = -\frac{1}{\rho_c^2}(\frac{\partial \rho_c}{\partial t})^2 + \frac{1}{\rho_c} \frac{\partial^2 \rho_c}{\partial t^2}.$$

36

The dilatation now is assumed small so that the second order term may be ignored. Evaluating the second derivative,

$$\frac{\partial}{\partial t}\left(\frac{\partial \rho_c}{\partial t}\right) = \frac{\partial}{\partial t}\frac{\partial\left(\frac{m}{V}\right)}{\partial t} = \frac{\partial}{\partial t}\left(-\frac{m}{V^2}\frac{\partial V}{\partial t}\right) = -\frac{\rho_c}{V}\frac{\partial^2 V}{\partial t^2} \quad \text{to first order.}$$

Hence,

$$-\frac{\rho_o}{4\pi a_o^2 r}\int_V\left[\frac{\partial^2 v_i}{\partial t\partial y_i}\right]dV(y) = -\frac{\rho_o}{4\pi a_o^2 r}\int_V\left[\frac{1}{V}\frac{\partial^2 V}{\partial t^2}\right]dV(y)$$

Finally, uniform dilatation implies that the integrand is independent of y.

Thus,

$$-\frac{\rho_o}{4\pi a_o^2 r}\int_V\left[\frac{\partial^2 v_i}{\partial t\partial y_i}\right]dV(y) = -\frac{\rho_o}{4\pi a_o^2 r}\left[\frac{1}{V}\frac{d^2 V}{dt^2}\right]V$$

$$(30) \qquad = -\frac{\rho_o}{4\pi a_o^2 r}\left[\ddot{V}\right] \qquad \text{to first order.}$$

(30) is the source contribution previously reported by Fitzpatrick and Strassberg.[23]

Of the terms which in general describe cylinder motion the two surface integrals, the fourth and fifth terms of (29), are best approached first. In these terms, setting $\rho = \rho_o$ followed by subsequent application of the divergence theorem results in volume integrals, the integrands of which are of the form

37

$$[\frac{\partial}{\partial y_j} (v_i v_j)]$$

where the order of the time and space derivatives are interchanged as required.

The specific vibratory motion previously assumed now permits definition of the quantity $u_i(z,t')$, the velocity of a rigid segment, of length dz, of the cylinder (see Figure C-1). The assumption also requires that the direction of u be perpendicular to z for small amplitude motion.

Then, the integral over the volume, of this derivative, involves terms of the form

$$u_i \frac{\partial u_j}{\partial y_j} + u_j \frac{\partial u_i}{\partial y_j} ,$$

which by rigidity of the dz segment are zero unless $j = z$. However, if $j = z$, then $u_j = u_z = 0$, and therefore, the fourth and fifth terms are zero.

The remaining sound field contribution, then, results from the second and third terms of (29). Letting A be the cross sectional area of the cylinder and using the definition of u_i gives

$$(31) \quad - \frac{\rho_o x_i}{4\pi a_o^3 r^2} \int_V [\frac{\partial^2 v_i}{\partial t^2}] dV - \frac{\rho_o x_i}{4\pi a_o^2 r^3} \int_V [\frac{\partial v_i}{\partial t}] dV$$

$$= - \frac{\rho_o x_i A}{4\pi a_o^3 r^2} \int_z [\frac{\partial^2 u_i}{\partial t^2}] dz - \frac{\rho_o x_i A}{4\pi a_o^2 r^3} \int_z [\frac{\partial u_i}{\partial t}] dz.$$

38

The first of these is identical to that reported by Leehey and Hanson[25] as describing the far field contribution of cylinder vibration. The second is the corresponding near field contribution. It is also pertinent to note that if u_i is z independent, then $u_i = U_i$, and this expression reduces to the corresponding portion of that derived for a rigidly moving cylinder (27).

In all, therefore, the explanation of (29) has been shown valid for several specific cases, with results derived herein in agreement with results reported but not derived in the literature. Equation (29) is the most general expression, but reduction of it to useful form would be extremely difficult without appropriate assumptions; nevertheless, it contains the two previously addressed simpler cases.

Before addressing in detail the further application of the stationary cylinder result (20) to the present experiment, two notes should be added. First, the contribution to the sound field from either dilatation (30) or vibratory motion (31) have been shown by Leehey and Hanson[25], based on the approach of Laird and Cohen[47], to be at minimum some 25 db below that of the lift force. This emphasizes the fact that aeolian tones are not analogous to the sound produced by a plucked string; instead they are caused by the fluctuating lift force and occur with or without cylinder motion of any sort, although motion may result in their amplification.

Second, the preceding development did not account for
boundary motion (i.e., for the time dependence of the
coordinates of a surface element (dS)). A completely
rigorous mathematical development would replace (8) with
Morgans'[48] modification of the Kirchhoff solution to the
wave equation, a modification which includes boundary motion.
However, examination of Morgans' formula reveals that so
long as the Mach number (now defined as the ratio of boundary
velocity to sound speed) and the ratio of body size to sound
wavelength are small, the original Kirchhoff expression is
only insignificantly affected. Therefore, (8) is indeed a
sound basis for the above development.

APPLICATION TO THE PRESENT EXPERIMENT

The present experiment is concerned primarily with far
field sound intensity emanating from stationary cylinders.
The governing equation is that derived for uniform smooth
cylinders with the near-field term omitted.

$$(32) \quad \rho(x,t) - \rho_0 = - \frac{x_i}{4\pi a_0^3 r^2} \int_S [\dot{P_i}] \; dS(y)$$

This single term still presents difficulty in that, in
general, minute variation of cylinder diameter or slight
instability in the incoming flow cause three dimensional
effects in the vortex wake; in turn, the lift force then is
not phase invariant along the length of the cylinder. Al-
though the previous definition of f_i and F_i still apply

40

(see page 33), F_i no longer is equal to $f_i L$. Accordingly, evaluation of (32) first requires the introduction of additional concepts.

In the three term sum on the right side of (32), only the second or $i = 2$ term (see Figure C-1) is of significant magnitude. Retaining only this term, replacing the subscript 2 by L for lift, using the definition of f_i, and converting to acoustic pressure (p) permits (32) to be rewritten as

$$(33) \quad p = - \frac{1}{4\pi a_o} \frac{\cos \theta}{r} \int_0^L \dot{f}_L(z,t') \, dz.$$

Following Graham,[49] the local lift force, regardless of its phase variation with z, is assumed to be narrowband and sinusoidal. Then $\dot{f}_L = \omega f_L e^{i\pi/2}$, and

$$(34) \quad p = - \frac{\omega}{4\pi a_o} \frac{\cos \theta}{r} e^{i\pi/2} \int_0^L f_L(z,t') \, dz.$$

However, (34) cannot be verified because of f_L's varying phase. Therefore, attention is focused on the mean square pressure amplitude,

$$(35) \quad p^2 = \frac{\omega^2}{16\pi^2 a_o^2} \frac{\cos^2\theta}{r^2} \int_{z_1=0}^L \int_{z_2=0}^L \overline{f_{L_1}(z_1,t) f_{L_2}(z_2,t)} \, dz_1 dz_2,$$

where the bar indicates a time average and where the statistics of the local lift force are assumed invariant with z and t. That is, the local lift force is assumed stationary in the statistical sense (which is not to be confused with

41

the cylinder remaining stationary in the physical sense).
Of course $\overline{F_L^2}$, the mean square lift force, is given by

$$(36) \qquad \overline{F_L^2} = \int_0^L \int_0^L \overline{f_{L_1}(z_1,t) f_{L_2}(z_2,t)} \, dz_1 dz_2 \; .$$

The problem then is to evaluate

$$(37) \qquad p^2 = \frac{\omega^2}{16\pi^2 a_o^2} \; \frac{\cos^2\theta}{r^2} \; \overline{F_L^2} \; .$$

To this end, as suggested by Frenkiel[24], define the correlation function $R(\gamma)$ by

$$(38) \qquad R(\gamma) = \frac{\overline{f_{L_1}(z_1,t) f_{L_2}(z_2,t)}}{\overline{f_L^2}}$$

where $R(\gamma)$ is a function of $\gamma = z_2 - z_1$ alone (see Figure C-2). Define the correlation length (ℓ_c) by

$$(39) \qquad \ell_c = \int_{-L}^L R(\gamma) \, d\gamma.$$

Then

$$(40) \qquad \ell_c = 2 \int_0^L R(\gamma) \, d\gamma$$

as $R(\gamma)$, by virtue of its definition, is an even function.
Let $\overline{\gamma}$ be the centroid of the area under the right half of the correlation curve (the plot of $R(\gamma)$ vs γ).

42

$$
(41) \qquad \overline{\gamma} = \frac{\int_0^L \gamma R(\gamma)\,d\gamma}{\int_0^L R(\gamma)\,d\gamma} = \frac{\int_0^L \gamma R(\gamma)\,d\gamma}{\ell_c/2}
$$

Then, substituting $R(\gamma)$ into the integral of (36) yields

$$
(42) \qquad \overline{F_L^2} = \int_0^L \int_0^L \overline{f_{L_1}(z_1,t)f_{L_2}(z_2,t)}\,dz_1 dz_2
$$

$$
= \int_0^L \int_0^L \overline{f_L^2}\,R(\gamma)\,dz_1 dz_2 \ .
$$

As f_L is stationary, $\overline{f_L^2}$ may be removed from the integral, and the problem becomes the evaluation of $\int_0^L \int_0^L R(\gamma)\,dz_1 dz_2$. To accomplish this evaluation, substitute $\gamma + z_1$ for z_2.

$$
\int_0^L \int_0^L R(\gamma)\,dz_1 dz_2 = \int_{z_1=0}^L \int_{\gamma=-z_1}^{L-z_1} R(\gamma)\,d\gamma\,dz_1
$$

Now integrate by parts with respect to z_1;

$$
\text{let } \tilde{u} = \int_{\gamma=-z_1}^{L-z_1} R(\gamma)\,d\gamma \qquad\qquad d\tilde{v} = dz_1,
$$

so that

$$
d\tilde{u} = \frac{d\tilde{u}}{dz_1}\,dz_1 \qquad\qquad\qquad \tilde{v} = z_1 .
$$

Using Liebnitz' rule to evaluate $\frac{d\tilde{u}}{dz_1}$, noting that $R(\gamma)$ is a function of γ alone, gives $\frac{d\tilde{u}}{dz_1} = R(-z_1) - R(L - z_1)$, and

43

so the integral is

$$\int_0^L \int_0^L R(\gamma)\,dz_1\,dz_2 = [z_1 \int_{\gamma=-z_1}^{L-z_1} R(\gamma)\,d\gamma]_{z_1=0}^{L}$$

$$+ \int_0^L z_1 R(L-z_1)\,dz_1 - \int_0^L z_1 R(-z_1)\,dz_1$$

Substituting γ for $L-z_1$ and for $-z_1$ respectively in the latter two integrals gives

$$\int_0^L \int_0^L R(\gamma)\,dz_1\,dz_2 = L \int_{-L}^0 R(\gamma)\,d\gamma - \int_L^0 (L-\gamma) R(\gamma)\,d\gamma - \int_0^{-L} \gamma R(\gamma)\,d\gamma$$

$$= 2L \int_0^L R(\gamma)\,d\gamma - 2\overline{\gamma} \int_0^L R(\gamma)\,d\gamma$$

since $R(\gamma)$ is even and $\gamma R(\gamma)$ is odd. Finally, using the definitions of ℓ_c and $\overline{\gamma}$,

$$(43) \qquad \int_0^L \int_0^L R(\gamma)\,dz_1\,dz_2 = (L-\overline{\gamma})\,\ell_c$$

Hence, $\overline{F_L^2}$ has been shown to be given by

$$(44) \qquad \overline{F_L^2} = \overline{f_L^2}\,(L-\overline{\gamma})\,\ell_c\ .$$

With synchronization, the flow is correlated (i.e., two dimensional).

44

$$R(\gamma) = 1, \quad 0 \le \gamma \le L. \qquad \ell_c = 2L, \quad \overline{\gamma} = \frac{\ell_c}{4} = \frac{L}{2}$$

and

$$\overline{F_L^2} = \overline{f_L^2} \, L^2$$

as required.

In a highly uncorrelated flow, $R(\gamma)$ is approximately $\ell_c \, \delta(\gamma)$, $\overline{\gamma} = 0$, and $\overline{F_L^2} = \overline{f_L^2} L \ell_c$. Thus ℓ_c and $\overline{\gamma}$ are the factors accounting for the reduction in F_L caused by phase variation in f_L. The total lift force is that which would be produced by a shorter cylinder of length $\sqrt{(L-\overline{\gamma}) \ell_c}$, having in-phase lift forces. Alternatively, ℓ_c may be considered an effective length, with $\overline{\gamma}$ a first order correction term. Physically, then, ℓ_c is about twice the length over which f_L is approximately phase invariant.

Substituting (44) into (37) yields

$$(45) \qquad p^2 = \frac{\omega^2}{16 \pi^2 a_o^2} \, \frac{\cos^2\theta}{r^2} \, \overline{f_L^2}(L - \overline{\gamma}) \, \ell_c,$$

and the acoustic intensity I is

$$(46) \qquad I = \frac{\omega^2}{16\pi^2 a_o^3 \rho_o} \, \frac{\cos^2\theta}{r^2} \, \overline{f_L^2}(L - \overline{\gamma}) \, \ell_c.$$

To express I in the form more often seen in the literature, define the root mean square local lift coefficient

45

$$(47) \qquad C_L = \frac{\sqrt{\overline{f_L^2}}}{\frac{1}{2}\rho_o U^2 d}$$

Then, substituting $\frac{2\pi S U}{d}$ for ω yields the desired form that was verified experimentally by Leehey and Hanson[25] at two discrete Reynolds numbers.

$$(48) \qquad I(\omega) = \frac{1}{16}\frac{\rho_o}{a_o^3}\frac{\cos^2\theta}{r^2}C_L^2 U^6 s^2 (L-\bar{\gamma})\ell_c$$

As noted previously, in the current experiment, F_L is measured vice f_L. Therefore, for this experiment, the appropriate equation is

$$(49) \qquad I = \frac{\omega^2}{16\pi^2\rho_o a_o^3}\frac{\cos^2\theta}{r^2}\overline{F_L^2}$$

which was obtained directly from (37). Of course, by the above development, (49) is equivalent to (48) for uniform smooth cylinders, but it has the additional advantage of applicability to any stationary rigid cylinder, regardless of the relationship between F_L and f_L for that cylinder.

NEW APPLICATIONS

The previous results apply only to uniform smooth cylinders. Although the present experiment involves cylinders of this type, it also studies other configurations. In particular, it is concerned with cylinders on which

uniform smooth sections are divided at regular intervals
by fins or notches (see Figure C-3). Accordingly, this
section extends the previously developed results to such
cylinders. Following this extension it also briefly
addresses the more complex case of a cylinder with a
sinusoidal surface (see Figure C-4).

Regularly Divided Cylinders.

As (49) is valid for any rigid stationary cylinder, it
of course is applicable for the subclass of periodically
divided cylinders. Application of (49), then, only requires
that F_L be related to both f_L and measurable correlation
factors. However, the determination of this relation first
requires further definition. This definition, in turn,
will be followed by a development paralleling that used
to obtain (44).

Let the cylinder of length L be divided by M partitions
into M+1 segments each of length L'. (L' = L/(M+1)).

Between partitions, define $R_w(\gamma)$ by

(50) $$R_w(\gamma) = \frac{\overline{f_{L_1}(z_1,t) f_{L_2}(z_2,t)}}{\overline{f_L}^2},$$

z_1 and z_2 within the same partition. As f_L is stationary,
$R_w(\gamma)$ is a function of $\gamma = z_2 - z_1$ alone. Similarly define
ℓ_{c_w} and $\overline{\gamma}_w$:

47

$$(51) \qquad \ell_{C_W} = 2 \int_0^{L'} R_W(\gamma)\, d\gamma$$

$$(52) \qquad \overline{\gamma}_W = \frac{\int_0^{L'} \gamma R_W(\gamma)\, d\gamma}{\ell_{C_W}/2}$$

Across partitions, define γ by $\gamma = z_2 - z_1$ with the stipulation that γ in the interval $((n-1)L', (n+1)L')$ implies that z_1 and z_2 are in segments separated by n partitions, n a positive integer (see Figure C-3).

Subject to this stipulation, $R_A(\gamma)$, defined by

$$(53) \qquad R_A(\gamma) = \frac{\overline{f_{L_1}(z_1,t)\, f_{L_2}(z_2,t)}}{\overline{f_L}^2}\;,$$

is a function of γ alone.

Define:

$$(54) \qquad \ell_{C_A} = 2 \int_0^{L} R_A(\gamma)\, d\gamma$$

$$(55) \qquad \overline{\gamma}_A = \frac{\int_0^{L} \gamma R_A(\gamma)\, d\gamma}{\ell_{C_A}/2}$$

$$(56) \qquad \ell_{C_A}' = 2 \int_0^{L'} R_A(\gamma)\, d\gamma$$

$$(57) \qquad \overline{\gamma}_A' = \frac{\int_0^{L'} \gamma R_A(\gamma)\, d\gamma}{\ell_{C_A}'/2}$$

By definition, as before

$$(36) \qquad \overline{F_L{}^2} = \int_0^L \int_0^L \overline{f_{L_1} f_{L_2}} \, dz_1 dz_2 \; .$$

Expanding each component integral of (36) into the sum of integrals over segments within partitions gives

$$(58) \qquad \overline{F_L{}^2} = \sum_{i=0}^{M} \int_{z_1=iL'}^{(i+1)L'} \int_{z_2=iL'}^{(i+1)L'} \overline{f_{L_1} f_{L_2}} \, dz_1 dz_2$$

$$+ \sum_{\substack{i=0 \\ i \neq j}}^{M} \sum_{j=0}^{M} \int_{z_1=iL'}^{(i+1)L'} \int_{z_2=jL'}^{(j+1)L'} \overline{f_{L_1} f_{L_2}} \, dz_1 dz_2$$

As $R_w(\gamma)$ must be of identical form within each segment, the first sum of (37) is equivalent to the sum of (M+1) integrals over any segment, say the first; thus,

$$\sum_{i=0}^{M} \int_{z_1=iL'}^{(i+1)L'} \int_{z_2=iL'}^{(i+1)L'} \overline{f_{L_1} f_{L_2}} \, dz_1 dz_2$$

$$= (M+1) \int_0^{L'} \int_0^{L'} \overline{f_{L_1} f_{L_2}} \, dz_1 dz_2$$

$$= (M+1) \int_0^{L'} \int_0^{L'} \overline{f_L{}^2} \, R_w(\gamma) \, dz_1 dz_2 ,$$

where (50) has been applied. Comparison of the last
expression with (42) reveals an exact parallel, and
therefore

$$(59) \quad \sum_{i=0}^{M} \int_{z_1=iL'}^{(i+1)L'} \int_{z_2=iL'}^{(i+1)L'} \overline{f_{L_1} f_{L_2}} \, dz_1 dz_2$$

$$= \overline{f_L^2} (M+1)(L' - \overline{\gamma}_w) \, \ell_{c_w}$$

is immediately obtained.

It remains, then, to evaluate the second term of (58).
Applying (53) and removing $\overline{f_L^2}$ from the integral permits
expression of this second term (Y) as

$$Y = \sum_{\substack{i=0 \\ i \neq j}}^{M} \sum_{j=0}^{M} \int_{z_1=iL'}^{(i+1)L'} \int_{z_2=jL'}^{(j+1)L'} \overline{f_{L_1} f_{L_2}} \, dz_1 dz_2$$

$$= \overline{f_L^2} \sum_{\substack{i=0 \\ i \neq j}}^{M} \sum_{j=0}^{M} \int_{z_1=iL'}^{(i+1)L'} \int_{z_2=jL'}^{(j+1)L'} R_A(\gamma) \, dz_1 dz_2$$

Substituting $\gamma + z_1$ for z_2,

$$\frac{Y}{\overline{f_L^2}} = \sum_{\substack{i=0 \\ i \neq j}}^{M} \sum_{j=0}^{M} \int_{z_1=iL'}^{(i+1)L'} \int_{\gamma=jL'-z_1}^{(j+1)L'-z_1} R_A(\gamma) \, d\gamma dz_1 .$$

Integrating by parts with respect to z_1, let

$$\tilde{u} = \int_{jL'-z_1}^{(j+1)L'-z_1} R_A(\gamma)\,d\gamma \qquad d\tilde{v} = dz_1 \; ,$$

so that

$$d\tilde{u} = \frac{d\tilde{u}}{dz_1}\,dz_1 \qquad\qquad \tilde{v} = z_1 \; .$$

Using Liebnitz' rule to evaluate $\frac{d\tilde{u}}{dz_1}$ gives

$$\frac{d\tilde{u}}{dz_1} = R_A(jL'-z_1) - R_A((j+1)L'-z_1) \; ,$$

whence

$$\frac{Y}{f_L{}^2} = \sum_{\substack{i=0 \\ i \neq j}}^{M} \sum_{j=0}^{M} \Big\{ \Big[z_1 \int_{jL'-z_1}^{(j+1)L'-z_1} R_A(\gamma)\,d\gamma \Big]_{z_1=iL'}^{z_1=(i+1)L'}$$

$$- \int_{iL'}^{(i+1)L'} z_1\,R_A(jL'-z_1)\,dz_1$$

$$+ \int_{iL'}^{(i+1)L'} z_1\,R_A\left((j+1)L'-z_1\right)\,dz_1$$

Substituting γ for $(jL'-z_1)$ and $((j+1)L'-z_1)$ respectively
in the last two integrals gives:

$$(60) \quad \frac{Y}{f_L{}^2} = \sum_{\substack{i=0 \\ i \neq j}}^{M} \sum_{j=0}^{M} \left\{ (i+1)L' \int_{(j-i-1)L'}^{(j-i)L'} R_A(\gamma)\,d\gamma \right.$$

$$- iL' \int_{(j-i)L'}^{(j-i+1)L'} R_A(\gamma)\,d\gamma$$

$$+ jL' \int_{(j-i)L'}^{(j-i-1)L'} R_A(\gamma)\,d\gamma$$

$$- (j+1)L' \int_{(j-i+1)L'}^{(j-i)L'} R_A(\gamma)\,d\gamma$$

$$+ \int_{(j-i+1)L'}^{(j-i)L'} \gamma R_A(\gamma)\,d\gamma$$

$$- \int_{(j-i)L'}^{(j-i-1)L'} \gamma R_A(\gamma)\,d\gamma \Bigg\}$$

Consider first the last two terms of (60). In the fifth let $k = j+1$; then

$$(61) \quad \sum_{\substack{i=0 \\ i \neq j}}^{M} \sum_{j=0}^{M} \int_{(j-i+1)L'}^{(j-i)L'} \gamma R_A(\gamma)\,d\gamma$$

$$= \sum_{i=0}^{M} \sum_{\substack{k=1 \\ k \neq (i+1)}}^{M+1} \int_{(k-i)L'}^{(k-i-1)L'} \gamma R_A(\gamma)\,d\gamma$$

Changing the dummy index on the right from k to j and subtracting the last term of (60) from the right side of (61) gives:

$$(62) \quad \sum_{\substack{i=0 \\ i \neq j}}^{M} \sum_{j=0}^{M} \left[\int_{(j-i+1)L'}^{(j-i)L'} \gamma R_A(\gamma) d\gamma \right. $$

$$- \int_{(j-i)L'}^{(j-i-1)L'} \gamma R_A(\gamma) d\gamma$$

$$= \sum_{i=0}^{M-1} \int_{[M-(i-1)]L'}^{(M-i)L'} \gamma R_A(\gamma) d\gamma + \sum_{i=1}^{M} \int_{0}^{-L'} \gamma R_A(\gamma) d\gamma$$

$$- \sum_{i=1}^{M} \int_{-iL'}^{-(i+1)L'} \gamma R_A(\gamma) d\gamma - \sum_{i=0}^{M-1} \int_{-L'}^{0} \gamma R_A(\gamma) d\gamma$$

$$= -\left(\int_{0}^{L} \gamma R_A(\gamma) d\gamma - \int_{0}^{L'} \gamma R_A(\gamma) d\gamma \right) + M \int_{0}^{L'} \gamma R_A(\gamma) d\gamma$$

$$-\left(\int_{0}^{L} \gamma R_A(\gamma) d\gamma - \int_{0}^{L'} \gamma R_A(\gamma) d\gamma \right) + M \int_{0}^{L'} \gamma R_A(\gamma) d\gamma$$

(since $\gamma R_A(\gamma)$ is an odd function)

$$= 2(M+1) \int_{0}^{L'} \gamma R_A(\gamma) d\gamma - 2 \int_{0}^{L} \gamma R_A(\gamma) d\gamma$$

$$= (M+1) \, \overline{\gamma}_A' \, \ell_{c_A}' - \overline{\gamma}_A \, \ell_{c_A}$$

Similarly, for the first four terms of (60), now denoted by X, interchange i and j in the third and fourth terms. Then, noting that $R_A(\gamma)$ is an even function gives:

53

$$X = 2 \sum_{\substack{i=0 \\ i \neq j}}^{M} \sum_{j=0}^{M} [(i+1)L' \int_{[j-(i+1)]L'}^{(j-i)L'} R_A(\gamma) d\gamma$$

$$- iL' \int_{(j-i)L'}^{[j-(i-1)]L'} R_A(\gamma) d\gamma].$$

Then, in the first term on the right, using the substitution $k = i+1$ to obtain new limits and then replacing the dummy index k by i gives

$$X = 2 \sum_{\substack{j=0 \\ j \neq i-1}}^{M} \sum_{i=1}^{M+1} i \int_{(j-i)L'}^{(j-(i-1))L'} R_A(\gamma) d\gamma$$

$$- 2 \sum_{\substack{j=0 \\ i \neq j}}^{M} \sum_{i=0}^{M} i \int_{(j-i)L'}^{[j-(i-1)]L'} R_A(\gamma) d\gamma.$$

Performing the indicated subtraction, again noting that $R_A(\gamma)$ is even and using the definitions of ℓ_{c_A} and ℓ_{c_A}', results in

(63) $$X = (M+1)L'(\ell_{c_A} - \ell_{c_A}') = L(\ell_{c_A} - \ell_{c_A}')$$

Combining (60), (62) and (63) reveals that

$$\frac{Y}{f_L^2} = (L - \overline{\gamma}_A) \ell_{c_A} - (M+1)(L' - \overline{\gamma}_A') \ell_{c_A}'$$

54

Therefore upon including the result of (59), (58) has been shown to be

$$(64) \quad \overline{F_L^2} = \overline{f_L^2}((M+1)(L'-\overline{\gamma}_w)\ell_{c_w} - (M+1)(L'-\overline{\gamma}_A')\ell_{c_A}'$$

$$+ (L-\overline{\gamma}_A)\ell_{c_A}).$$

It should be noted that (64) reduces correctly to the previous smooth cylinder result (44) because in the absence of periodic divisions, $R_A(\gamma) = R(\gamma)$, $\ell_{c_A} = \ell_c$, $\overline{\gamma}_A = \overline{\gamma}$, $\ell_{c_w} = \ell_{c_A}'$ and $\overline{\gamma}_w = \overline{\gamma}_A'$. Moreover, (64) is intuitively satisfying in that the correlation factor is the sum of correlation within divisions and correlation across divisions, less that portion of across-division correlation which is counted too often in the formation of this sum.

Finally, using (64) in (49) yields the expression

$$(65) \quad I(\omega) = \frac{\omega^2}{16\pi^2\rho_o a_o^3} \frac{\cos^2\theta}{r^2} \overline{f_L^2}[(M+1)(L'-\overline{\gamma}_w)\ell_{c_w}$$

$$- (M+1)(L'-\overline{\gamma}_A')\ell_{c_A}' + (L-\overline{\gamma}_A)\ell_{c_A}]$$

for the sound intensity radiated from a regularly divided cylinder.

The derivation of (65) assumed that periodic divisions only affected the phase of f_L. If, on the other hand,

cylinder-flow interactions causing amplitude variation in f_L are present as well, then (65) is not totally appropriate. Although this equation could still serve to approximate the radiated intensity, it should be used with great caution in such cases.

Sinusoidal Cylinders

The case of a cylinder with a sinusoidal surface (see Figure C-4a) is still more complicated. Variation of diameter with z implies variation of both the local Strouhal number and the local Reynolds number. Therefore, as lift coefficient is Reynolds number dependent, both the frequency and the amplitude of the local lift force vary along the cylinder's length. In addition, as in the previously considered cases, phase variation with z also occurs.

In order to reduce complexity somewhat, phase variation will be ignored in what follows; that is, the local lift forces at two cross sections of equal diameter (points A and B in Figure C-4a) will be assumed in phase. Similarly, in order to avoid consideration of where in the sinusoid the cylinder terminates, the cylinder will be assumed scaled so that it is of minimum diameter at each end. To simplify algebraic manipulation, the cylinder will be idealized in that the diameter will be permitted to be zero (Figure C-4b) but rigidity will remain postulated.

If the cylinder is considered to be divided into short segments (dz) over which the lift force is of constant frequency and amplitude, then the radiated sound should be

56

the superposition of the sound produced by each segment.
That is, the sound should exhibit a frequency spectrum
extending to the infinitely high frequency associated with
zero diameter, with sound amplitude frequency dependent.

Mathematically,

$$(33) \qquad p = - \frac{1}{4\pi a_o} \frac{\cos \theta}{r} \int_{-L/2}^{L/2} \dot{f}_L(z,t)\,dz$$

applies. As f_L is assumed narrowband within any segment
dz,

$$\dot{f}_L = i\,\omega\,f_{L_o}\,e^{i\omega t}$$

where f_{L_o} is the local lift force amplitude. Therefore,
noting that ω itself is z dependent,

$$(66) \qquad p = -\frac{i}{4\pi a_o} \frac{\cos \theta}{r} \int_{-L/2}^{L/2} \omega\, f_{L_o}\, e^{i\omega t}\,dz.$$

Now,

$$\omega = \frac{2\pi \overline{U} S}{d} \qquad \text{and} \qquad f_{L_o} = C_L \frac{1}{2} \rho \overline{U}^2 d$$

by the definitions of S and C_L.

Often C_L exhibits a power relation with Reynolds number.
Assuming such a relation yields, with K and n serving as
constants,

57

$$C_L = K R_e^n = K \bar{U}^n d^n / \nu^n$$

or

$$\omega \, f_{L_o} = \frac{\rho K \pi \bar{U}^{n+3} S}{\nu^n} d^n ,$$

and

$$(67) \quad p = - \frac{i \rho K \bar{U}^{n+3} S}{4 a_o \nu^n} \frac{\cos \theta}{r} \int_{-L/2}^{L/2} d^n e^{i \frac{2\pi \bar{U} S t}{d}} dz$$

Now, the previous assumption was that $d = D \sin z$ where D is the maximum cylinder diameter. Thus,

$$(68) \quad p = - \frac{i \rho K \bar{U}^{n+3} S}{4 a_o \nu^n} \frac{\cos \theta}{r} \int_{-L/2}^{L/2} D^n \sin^n z \, e^{i \frac{2\pi \bar{U} S}{D \sin z} t} dz$$

To evaluate the integral, let $\omega = \frac{2\pi \bar{U} S}{D \sin z}$; then

$$(69) \quad p = \frac{i \rho K}{a_o \nu^n D} 2^{n-1} \pi^{n+1} (\bar{U}^2 S)^{n+2} \int_{-\infty}^{\infty} \frac{e^{i\omega t} \, d\omega}{\omega^{n+1} \sqrt{\omega^2 - (\frac{2\pi \bar{U} S}{D})^2}}$$

where positive ω actually varies from $\frac{2\pi \bar{U} S}{D}$ to infinity.

Examination of the integral in (69) immediately reveals that it is an inverse Fourier transform.[50] As such, the integrand, less the $e^{i\omega t}$ factor, provides the frequency spectrum of p. This spectrum is plotted in Figure C-5 as a function of the parameter n which relates lift coefficient

to Reynolds number. The infinite frequency, present in this idealized case corresponds to zero cylinder diameter, while the minimum frequency is the Strouhal frequency of maximum diameter.

Evaluation of the integral to obtain a closed form expression for p as a time function involves using the appropriate transform tables.[50,51] Cursory examination of these tables indicates that the resulting p is a summation of Hankel functions of varying frequency, each term of which in the asymptotic limit of time is a sinusoid.

However, the algebraic details of this process are not included herein for two reasons. First, (69) describes an idealized case; it ignores phase variation, represents a rigid cylinder with zero diameter and specified end conditions, and is dependent upon a constant power relation between lift coefficient and Reynolds number. Second and more important, observations reported later in this paper indicate that non-uniform diameter cylinders may not be treated in terms of superposition of independent segments. The non-uniformity introduces shadowing and other effects which cause interdependence between similar cylinder sections as well as relatively unpredictable cylinder-flow interactions. In these cases, mathematical models based upon independence serve poorly for both lift force and sound field predictions, and therefore, the lengthy algebraic manipulation required for complete evaluation of the integral in (69) is not an appropriate effort.

II. <u>INSTRUMENTATION</u>

In order to measure simultaneously the intensity of the radiated sound and the total lift force believed to be the cause of this sound, it is necessary to have a wind tunnel providing an open jet which discharges into an anechoic chamber. As the Naval Postgraduate School already had an excellent anechoic facility, construction of an open jet wind tunnel sufficiently portable to move into the chamber was the proper approach. This section addresses the design and construction of this wind tunnel and describes the other instrumentation necessary to perform the intended experiment. It includes discussion of wind tunnel and anechoic chamber characteristics, stands for cylinders and lift force measurements, equipment for correlation length measurements, the rationale for cylinders selected, and the instrumentation unique to the case of a synchronized cylinder.

ANECHOIC CHAMBER

The anechoic chamber is of room within a room construction. Its 12' thick concrete outer wall, measuring 37' X 24' X 25' is separated from the 6" thick concrete inner well by a 2" blanket of fiberglass and cork. The chamber is completely sealed except for a single door, two 20" X 14" window ducts, in each of which are mounted four $\frac{1}{4}$" thick glass panes, and for two small ducts for passage of electric cable. The door, windows and cable ducts lead to an anteroom in which appropriate

60

instrumentation may be located (see Figures C-6 and C-7).
Attached to the inner chamber wall, floor, and ceiling as
well as to the inside of the door are 40" deep fiberglass
wedges. A floor of 225 wire cables, each stretched to a
tension of 150 to 200 pounds, horizontally crosses the
chamber, leaving a working area above the grid of
27' X 14' X 11'.

The chamber is 99% non-reflective at frequencies above
100 Hz, and it provides excellent sound isolation (measured
background noise is plotted in Figure C-8). The chamber is
used extensively and was available for only 4 weeks for
conduct of this experiment.

WIND TUNNEL

Wind tunnel design was constrained by several factors.
First, anechoic chamber availability necessitated conducting
all flow measurements outside this facility and then moving
the tunnel into the chamber to gather sound field data.
Therefore, the tunnel was built in detachable sections each
sufficiently small to permit passage through standard
$83\frac{1}{2}$" X $32\frac{1}{2}$" doorways. Second, economics dictated that the
tunnel be constructed of inexpensive commercially available
materials, and third, the tunnel had to provide good laminar
flow.

Accordingly, the tunnel was designed to provide maximum
contraction consistent with maximum allowable dimensions.

An open jet tunnel (see Figures C-9 to 11) consists of an air source, a plenum chamber to permit the air to settle and to isolate the output from direct source flow, screens to reduce large eddies to small turbulent cells, and a contraction to reduce these cells to laminar streamlines.

The air source was an in-house Navy surplus blower unit originally built by Wagner Electric Corporation. Its 23" X 13 3/4" output provided 83.3 ft^3/sec volume flow when discharging into atmospheric pressure. However, excessively high pressure at the output caused fan instability.

Ductwork provided the sealed passage from blower to plenum chamber. Its cross-section at one end matched blower output dimensions and at the other matched those of the anechoic chamber windows. It was constructed of slotted angle-iron covered with 6 mil thick polyethylene sheet, commercially called Visqueen; the sheet in turn was sealed with 10 mil indoor-outdoor vinyl tape.

The 8' X 8' X 83" plenum chamber also was constructed of angle-iron. Interior to this chamber, a 3' X 4', 3/4" plywood board was mounted 10" back from the ductwork termination as a baffle. The plenum chamber's side walls were Visqueen sealed with 10 mil vinyl tape. However, the pressure on these large wall sections caused a substantial shear force at the tape/Visqueen interface, and as a result, leaks created by creep of the tape appeared. To prevent this leakage, additional angle iron beams were installed several inches from the original structural beams so that

each Visqueen sheet was taped to metal instead of to other Visqueen sections. The small gaps between adjacent beams were then closed with strips of $\frac{1}{2}$" plywood which were bolted to the angle iron (see Plate D-1).

To prevent the plenum chamber from lifting off the ground, a solid floor of two 4' X 8' plywood sheets bolted to angle iron was installed. A door was built into one end of the chamber to provide access to the chamber interior. Finally, body putty filler, commercially sold for automobile body repair, was applied to seal the small gaps between abutting wooden sections.

The wooden screen support section (see Figures C-12 and C-13) provided a rigid structure for mounting 10 screens as well as the contraction. The previously mentioned consideration of restricting dimensions to that of a doorway limited the maximum screen cross section to 5' X 5'. The screen itself was common window screen rigidly fastened to the bottom of the wooden support frame. At the top, each screen was stapled to a wooden strip which in turn was connected by five 4" turnbuckles to the top wooden support. Tightening the turnbuckles compensated for screen sag.

The rear legs of this support section were attached to slots in the plenum chamber floor, with the slots then sealed with body putty. The downstream legs rested outside the chamber. In addition, extension beams termed "paws" were bolted to these legs to prevent the support structure

63

from tipping over and crushing the contraction. On the outside of the 5' X 5' frame, 120 hanger bolts were mounted to hold the contraction. For added support a vertical wooden brace, which just touched a contraction cross-sectional strength member, was bolted to the "paws."

For the best flow, it was necessary to make the jet itself as small as possible. Initial determination indicated that a 3" by 10" jet was the minimum allowable size as 3" provided a 6:1 tunnel to cylinder diameter ratio for a 1/2" cylinder and 10" furnished the initial estimate of 20d maximum correlation length. Therefore, a 120:1 contraction ratio resulted. Again, doorway size limited the contraction length to 30".

The contraction itself was designed by drawing smooth curve cross sections matching the extreme dimension of 60" X 60" and 3" X 10". The curves were drawn so as to cause maximum reduction of cross section at the upstream end and to gradually taper to a straight section near the jet output (see Figures C-14 and 15). Templates for contraction side walls were derived using descriptive geometry techniques so that the projections of contraction side wall intersections on the plane of a screen were straight lines. The technique, illustrated in Figure C-16, was implemented numerically; to accomplish this calculation, the side cross sections of figures C-14 and 15 were divided into segments each matched by a curve of the form ae^{-bx}. Then simple integration permitted plotting of the template curves.

64

Contraction construction was begun by building six wooden frames, each matched to a different screen-plane contraction cross section. These cross sections were those located at 6" intervals along the axis of the contraction as indicated in Figures C-14 and 15. In the first cross section frame, which measured 5' X 5', holes for hanger bolts were drilled at locations corresponding to those of the screen support structure. The wooden frames were then joined by wooden ribs contoured to match the cross sections of the side walls. Additional ribs following the corner contours also were attached.

Four sections of commercially available 60 mil thick fiberglass sheet then were cut to conform to the side wall templates. These sheets were glued with fiberglass resin to the inside of the wooden frame and rib contraction structure with remaining gaps sealed with body putty. Thus, the interior of the contraction was smooth sheet while all its structure was exterior to this sheet (see Plate D-2).

Before attaching the contraction, a vinyl gasket was fitted over the hanger bolts on the screen support structure. Then the four end Visqueen sheets, each of which already had one end taped to a corner angle iron beam of the plenum chamber, were fitted over this gasket. Mounting the contraction on the hanger bolts and tightening down thereby held the Visqueen sheets as well. Thus, the entire screen support structure, except for the downstream legs, "paws" and brace, effectively was inside the plenum chamber. Again,

65

any weak points, such as where the Visqueen had to be cut
to fit around the downstream legs, were well sealed with
vinyl tape and body putty.

Wind tunnel speed was controlled by regulating the
input flow to the blower. The tunnel provided a 0 to 150
ft/sec open jet at its mouth. However, near the maximum
speed, fan instability occurred, and at the higher speeds,
the plenum chamber developed leaks on occasion. Therefore,
the tunnel generally was operated at speeds below 110 ft/sec.

Jet velocity was uniform over almost the entire 3" by
10" section (see Figure C-17) for a downstream distance
approaching 2 inches. Further downstream the effect of a
spreading shear layer, caused by the jet mixing with sur-
rounding still air, reduced this area of uniform velocity.
By 15" downstream this constant velocity cross section was
reduced to a 2" by 6" area as shown in Figure C-18.

The jet turbulence level was less than 0.5% at the
tunnel mouth, a low level for an open jet but a high tur-
bulence level compared to that typically measured in closed
tunnels (see Figure C-19). As expected, the turbulence
level steadily increased downstream (see Figures C-20 to
C-25). Therefore, it was apparent that comparison of
measurements sensitive to turbulence level would only
have validity if these measurements were made on cylinders
located at equal downstream distances.

Relocation of the tunnel within the anechoic chamber
necessitated disassembly, reassembly and some slight

66

modifications. The only tunnel component too heavy to carry by hand was the blower which required a hydraulic lift for its relocation. Blower weight precluded its placement on the chamber's wire cable floor; thus the blower was placed in the anteroom (see Figures C-26 and C-27).

The remainder of the tunnel was reassembled within the anechoic chamber and connected to the blower by a 14' extension of the ductwork. The only other modification to the wind tunnel itself was the replacement of the Visqueen plenum chamber ceiling with two 4' X 8', $\frac{1}{2}$" plywood sheets bolted to angle iron. This replacement was necessary as a Visqueen ceiling would have expanded into the overhead anechoic chamber wedges.

The anechoic chamber required some safety additions caused by the presence of the tunnel. To prevent flaking of fiberglass wedges at the far wall, Visqueen sheets, virtually transparent acoustically, were hung over the area of direct jet impingement. In addition, an output duct to provide an exit for the air entering the chamber in the tunnel jet, was set into the other anechoic chamber window. A filter was mounted on the anteroom side of this exit duct to trap any fiberglass particles stirred up by the flow. This precaution insured that air in the anteroom would be safe to breathe; however, a gas mask was worn when it was necessary to enter the chamber during tunnel operation or during the first two hours after tunnel shutdown.

67

The jet was checked following tunnel installation within the chamber for both velocity uniformity and turbulence level. No substantial differences from the values previously measured (Figures C-17 to C-25) were observed. However, as shown in Figure C-8, anteroom noise from the fan and other sources was coupled through the ducts into the chamber, raising background levels above those previously measured.

CYLINDER STANDS AND MEASUREMENT OF F_L

The cylinder stand assembly both supported the various cylinders and served to measure total lift force. It also permitted placement of all except skewed cylinders at the tunnel mouth. The assembly is illustrated in Figure C-28.

Metal caps with close tolerance holes drilled to the various cylinder diameters supported the respective cylinders; set screws provided rigidity in the mechanical cylinder-cap contact. Each cap was threaded in its interior and held to one of two 3/8" threaded shafts by a nut. The shafts, in turn, were screwed into the two mechanical impedance heads and also held by nuts. 3/8" bolts connected the impedance heads to two small 3/8" thick aluminum plates which, in turn, were bolted to a 14" X 14" X $1\frac{1}{2}$" steel plate. Finally, the steel plate was supported by a large wooden stand which was grooved to support the slide mechanism used for hot wire anemometer measurements behind the cylinder (see Plate D-3).

End caps were required to eliminate spanwise flow and the resultant drop in base pressure suction.[45] As the metal

support caps were found experimentally to be insufficiently large to serve in this capacity, sets of masonite end caps unique to each cylinder diameter were added. These 3" X 5" caps effectively extended the tunnel side walls past the cylinder. In each rectangular cap a hole for cylinder passage was drilled. Then a wooden clamp mechanism was attached to hold the end cap to the adjacent metal cap. Any small remaining holes were sealed with masking tape on the side of the cap exterior to the flow and with modelling clay on the flow side.

With this symmetric arrangement, one half the total lift force on the cylinder could be read at the force output of either impedance head. However, as impedance heads measure differential force, this equating of their outputs to $F_L/2$ was predicated on their lower side being a mechanical ground. Although relatively massive, the steel plate was not such a ground as it exhibited flexural vibrations over the frequencies of interest. Therefore, resin impregnated felt damping material was placed on the upper side of the steel plate and was held down by smaller aluminum plates bolted to the steel. This material also was inserted between the aluminum plates to which the impedance heads were attached and the steel.

Measurements of impulse and steady state support response then revealed that flexural vibrations of the steel plate were negligible. Yet, steady state frequency response still was not completely flat as resonances occurred at cylinder

69

vibration frequencies and at the natural frequencies of the wooden stand. Nevertheless, large windows of flat response did exist over the frequency range of interest.

The increased length of the skewed cylinder precluded support in the above manner. Therefore, an additional wooden stand was constructed to support this cylinder; the aluminum plates, to which the impedance heads were attached were bolted directly to this stand. The skew angle was varied by rotating the entire stand with respect to the wind tunnel axis.

At different skew angles, different cylinder lengths were exposed to the 10" wide flow. This required the end caps to be located at different points along the cylinder at each skew angle. Accordingly, larger masonite caps with body putty hardened on one side were used. The caps were drilled to permit cylinder passage through a hole in both masonite and putty at angles from zero to forty-five degrees to the cap. In mounting, the cap was moved to the desired cylinder location and held with a generous amount of modelling clay applied to the side exterior to the flow. Any small remaining hole was sealed on the flow side with a small quantity of clay.

HOT WIRE ANEMOMETERS

Velocity and wake measurements were made with TSI hot wire anemometers to which DISA probes were connected. The probe sensing elements were 5 micron platinum plated tungsten

wire. Each combination of probe and anemometer was calibrated with a TSI calibrator; a representative calibration curve appears as Figure C-29.

For any hot wire anemometer measurements, particularly those in the wake of a body, the first consideration is whether to mount the probes parallel or perpendicular to the flow. Kovasznay[13] reported that disturbances from probes mounted parallel to the flow propagate upstream, thereby effecting the phenomenon under study. On the other hand, Ballou[36] experienced similar difficulties with probes perpendicularly mounted. In view of this ambiguity, the probes in this study were mounted so as to minimize construction and alignment difficulties, namely perpendicular to the flow.

With this mounting, velocity was measured at the tunnel output ahead of the cylinder. For wake measurements, the probes were supported by a slide mechanism (see Plate D-3) which permitted controlled probe motion both along the cylinder axis and in the vertical. The slide mechanism, in turn, slid along grooves in the wooden stand in the upstream-downstream direction. As such, three dimensional motion of each probe was possible.

Probe position parallel to the cylinder axis was read from a meter stick along which slid two pointers, one connected to each probe holder. Probe holder thickness limited minimum probe separation to 3/8". Vertical probe position also was read on a pointer/metal rule arrangement; however,

71

motion in this direction could be extremely well controlled
by the threaded drive of the probe holder. Small up and
downstream motion was read to 1/100 mm on dial indicators
located in the wooden groove, while approximate position
in this direction again was read on a pointer/meter stick
arrangement.

MICROPHONE

A 2" long 9/16" diameter SONY ECM-16 electret condenser
microphone was used for sound measurements. It was calibrated
in the anechoic chamber against a B&K microphone whose
response was both known and verified with a piston phone.
The resultant calibration curve appears as Figure C-30.

For beam pattern measurement, the microphone was mounted
on a four foot boom which was driven by an electric motor
attached to the cylinder support stand. Motor drive con-
trol and motor shaft angular position readout were located
in the chamber anteroom (see Figure C-31). This arrangement
permitted rotation of the microphone at constant 4 foot
distance from and at fixed aspect to the cylinder, in the
plane perpendicular to the cylinder axis. As the boom only
could be driven from the wind tunnel structure to the chamber
floor grid, rotation was limited to 180°.

In order to measure surface pressure fluctuation on
synchronized cylinders (which are discussed below), the
microphone alternatively was mounted within an interior-to-
the-cylinder cavity which was connected to the surface by a

72

pinhole. As illustrated in Figure C-32, the cavity was formed by inserting two threaded metal pieces into a length of interior cylinder threads. The first piece held the microphone with a set screw. The second piece, when tightened, prevented travel of the first and also furnished exposed threads for attachment of the remaining portion of each cylinder. Both pieces were of minimum weight as cylinders used for synchronization were weight critical.

The design of this arrangement was based upon the concept of a Helmholtz resonant cavity, the resonant frequency of which is given by Kinsler and Frey[52] as $\omega_o = a_o \sqrt{\frac{s}{\ell' V'}}$, where s is the area of the cavity entrance cross section, V' is the cavity volume, and ℓ' is the sum of entrance length and 1.2 times the radius of the entrance. Using the dimensions provided in Figure C-32 in this formula yields a resonance frequency of $\frac{\omega_o}{2\pi} = 273$ Hz.

For determination of cavity bandwidth, an estimate of losses through the cavity entrance was required. Acoustic losses were modelled by considering the cavity entrance as a pipe and using formulas provided in Kinsler and Frey.[52] These losses thereby were found to be negligible, less than 2×10^{-3} db. Viscous losses were assumed to be those characteristic of pipe flow, and were calculated using formulas given by Schlichting.[26] These losses, in turn, permitted estimation of the system quality factor (Q') as 2.5, and thus, by the definition of Q', the bandwidth was estimated as about 100 Hz.

73

The amplitude response of the microphone within the cavity was measured in the anechoic chamber and is shown in Figure C-30. The calculated values of resonant frequency and bandwidth are seen as good estimates. The secondary resonance at 450 Hz was verified carefully and was determined to be real, although neither predictable nor easily explainable. The phase response of the microphone cavity system was not measured as various difficulties encountered in obtaining synchronization precluded the necessity for such measurement.

CYLINDERS

Cylinders were selected to test various aspects of the theory of aerodynamic sound as well as the extension of the theory developed in Section I.

The original wind tunnel design assumed cylinder diameters from $\frac{1}{4}$ to $\frac{1}{2}$ an inch. However, larger diameters raised the fundamental flexural resonance of the cylinder, thereby facilitating lift force measurement. Accordingly, a 1" diameter cylinder also was used and the range of Reynolds number covered thus was broadened. The hollow steel tube $\frac{1}{4}$" cylinder and aluminum tube $\frac{1}{2}$" and 1" cylinders were polished on a lathe with progressively finer paper, terminating the effort with wet 600 paper. A $\frac{1}{4}$" aluminum tube cylinder was discarded when its lack of rigidity became apparent.

To determine sensitivity to polishing, a $\frac{1}{2}$" cylinder
roughened with 36D paper until its surface exhibited
grooves also was used. The other cylinders described
below, however, were all polished to the wet 600 paper level.

The finned cylinder (see Figure C-33) was designed to
permit attachment of from zero to four $2\frac{1}{4}$" ($4\frac{1}{2}$ diameter)
fins. It consisted of a 1/8" shaft, threaded at each end,
over which fit $\frac{1}{2}$" diameter 2" long sections, each of which
had a 1/8" hole bored through its center. Two 2" sections
also were threaded on their interior side. The fins, simi-
larly having a centered 1/8" hole, were held by adjacent
2" sections, while all middle sections and fins were main-
tained in a rigid configuration by tightening the two
threaded end sections on the threaded shaft.

Three different notched cylinders (see Figure C-33)
were used. The first was effectively, two 5" long cylinders
as it consisted of two sections of diameter $\frac{1}{2}$" and 3/8"
respectively. The second also provided 5" of each diameter,
but in alternate 1" sections. Measurements recorded for
this second notched cylinder indicated that longer 3/8"
sections were desirable; accordingly, the third notched
cylinder shown in Figure C-33 also was made. However, only
sound field data were recorded for this third notched ver-
sion, while both lift force and sound field were measured
for the first two.

Splitter plates placed behind the continuous $\frac{1}{2}$" cylinder
were of two lengths, $1\frac{1}{2}$" (3d) and 3" (6d). The plates were

75

adjacent to but not attached to the rear of the cylinder. Instead, they were supported by a wooden shaft arrangement which mounted to the steel plate as shown in Figure C-34.

Finally, the cylinder used for the skewed case was simply a $\frac{1}{2}$" diameter, polished, 17" long aluminum tube, with the additional length provided to permit the cylinder to traverse the entire 10" flow at various angles.

SYNCHRONIZATION

As outlined in the introduction, for synchronization it is necessary for the vortex shedding frequency to be near the natural frequency of the mechanical system consisting of the cylinder and a compliant mount. In addition, the amplitude of motion must be sufficiently large, usually 0.1d or greater, for cylinder movement to control the vortex shedding process.[8,27-29,31]

Ignoring lift force amplification, lift force magnitude, at specified flow velocity, is determined by the quantity of flow intercepted. As such, the amplitude of cylinder oscillation in the lift direction is determined by cylinder diameter and the mass, compliance and losses of the cylinder and mount mechanical system. That is, for springs of small mass and for constant $\bar{U}$, amplitude is a function of cylinder d and m, spring k and system Q.

Griffen[27-29] has modelled the case of a synchronized cylinder, providing a mathematical approach to these qualitative concepts. Moreover, his von der Pol oscillator[53] model has furnished experimentally proven predictions of

synchronization-associated phenomena such as lift force amplification. His model involves rather lengthy calculations and is mentioned here only as a basis for design of cylinder and support for achieving synchronization in the present effort.

Griffen defines several parameters including those noted above. Then, from constraints imposed by the simultaneous requirements that the lift force be the forcing function for simple harmonic cylinder motion and that this same force satisfy the von der Pol equation as adjusted with three non-dimensional parameters, he obtains appropriate conditions and relationships governing the various parameters involved. Specifically, his results indicate that synchronization can only occur with certainty if the damping ratio (α) is between 0.5 and 1.1, where α is defined by $\alpha = \frac{1}{2Q\mu}$ and $\mu = \frac{\rho_0 L d^2}{8\pi^2 S^2 m}$ (μ is essentially the ratio of the mass of displaced fluid to that of the cylinder).

This limitation on α, for specified values of ρ_0, L and S, translates directly into limitations governing the relationships among m, d and Q. In Figure C-35 these translated limitations are plotted for the present case, $L = 10"$ and $S = .21$. The division of the figure into two sections is for clarity only; it prevents overlap of the mass limits applicable to different diameters.

Diameter selection, then, involved balancing several constraints. Cylinders had to be sufficiently small to fit within the jet; therefore, a maximum d of $1\frac{1}{2}"$ was

77

selected. The cylinder also had to support the interior microphone and had to represent achievable m, Q combinations. For Q's of 300 - 400, an interval deemed achievable, examination of Figure C-35 revealed that allowable mass for a tubular cylinder increased rapidly with diameter. Accordingly, problems associated with minimizing mass would be mitigated by choosing maximum allowable d, and thus, the $1\frac{1}{2}$" diameter became firm. It then remained to reduce the mass of cylinder sections, springs, microphone, and cavity boundaries to 100 grams.

As the intention was to skew synchronized cylinders, several different lengths appropriate to different skew angles were needed. Therefore, three different configurations were required; each consisted of the 7" A section of Figure C-32 and the cavity boundary pieces. The remaining sections were B pieces of the figure, of length $4\frac{1}{2}$", 7" and 10", so that total cylinder lengths were $11\frac{1}{2}$", 14" and 17".

Cylinder section reduction was accomplished by etching the aluminum cylinder section interiors using a 7 percent potassium hydroxide solution. In this process it was important that interior cylinder section threads used for microphone cavity support not be damaged. Therefore, a $1\frac{1}{2}$" long threaded aluminum plug with an "O" ring seal behind a thickened aluminum disk at its forward end was fabricated (see Figure C-32). After threads of both cylinder sections and plug were greased with silicone, the plug was inserted

78

within the cylinder section, and the resulting assembly was placed plug side down in a water bath to a level 1" below the open cylinder end.

The 7% potassium hydroxide solution then was poured inside the cylinder section to a level 1" below the open end. The undissolved 1" end thereby was preserved at full rigidity for mounting in an end cap. The assembly was monitored every 6 to 12 hours, by pouring out the solution, rinsing and weighing, in order to prevent formation of a hole or weak spot at local cylinder metal inhomogeneities. Sufficient reduction required about 20 to 30 hours for each section, and upon process completion, total cylinder assembly weights were 90 grams for the $11\frac{1}{2}$" length, 105 grams for the 14" and 120 for the 17".

To support the cylinder and microphone assembly, the mechanism illustrated in Figures C-36 and C-37 was constructed and bolted to a wooden stand which rested on the floor. The cylinder assembly thereby was supported by two leaf springs which were held to Plates B of the figures by tightening down Plates A. Plates B were grooved to permit motion relative to Plates C, and Plate D was similarly grooved to allow travel of Plates C. This arrangement, then, provided all adjustment necessary for accommodation of different cylinder lengths. Moreover, it permitted adjustment of exposed spring length, thereby providing the mechanism for varying cylinder assembly natural frequency.

79

For the $11\frac{1}{2}"$ cylinder, natural frequency was determined by measuring impulse response, with a capacitive probe, at the extremes of spring adjustment, and was found to vary from 30 to 140 Hz.

Subsequently, one final minimum mass, unthreaded, one piece, 2" diameter cylinder was fabricated. This cylinder was reduced in a 7 percent potassium hydroxide solution to a mass of 40 grams.

III. MEASUREMENT TECHNIQUES AND RAW DATA

This section discusses the techniques employed in
gathering total lift force, correlation function and sound
intensity data and reports the data obtained. It includes
a description of the electronics applicable to each type
of measurement. It also addresses problems encountered
in obtaining synchronization and the rationale for abandoning
this effort. Finally, it reports specific wake measurements
made to confirm an hypothesis suggested by the results of
Section IV.

TOTAL LIFT FORCE (F_L)

A voltage proportional to total lift force was available
at the force output of either impedance head (see Figure
C-28). This voltage was amplified and inserted into a wave
analyzer equipped with a self-contained frequency sweep
feature and into an oscilloscope (see Figure C-38). The
10 Hz bandwidth wave analyzer provided a 1 Hz per second
sweep through frequencies above 20 Hz; it also furnished
two DC output signals, one proportional to frequency and
one to filtered amplitude, so that plots of $F_L/2$ vs fre-
quency, samples of which appear as Figures C-39 and C-40,
were automatically generated on the x-y plotter.

Frequency accuracy of the wave analyzer was verified
on an independent counter, while its amplitude response
was confirmed with a second wave analyzer.

81

To insure that the selected impedance head indeed provided a measure of $F_L/2$, the second impedance head force output also was processed through these same electronics both initially and on randomly chosen occasions thereafter. After accounting for the different calibration of the second head, no significant shape or amplitude deviations were observed on any of the resulting corroborative plots.

Determination of the $F_L/2$ magnitudes listed in Tables B-1 athrough B-17 from the $F_L/2$ vs frequency plots followed one of two procedures. The first was used when the Strouhal frequency fell within a flat response window, well separated from cylinder and stand resonances; it consisted of listing the value of $F_L/2$ read directly from the plot. For example, the 440 mV $F_L/2$ magnitude read from Figure C-39 is the seventh entry in Table B-3.

The second method, neither as direct nor as accurate, was used when the Strouhal frequency was near a stand or cylinder resonance. In such cases, an approximate calibration of the non-level system frequency response was developed. The calibration then was used to adjust the subject $F_L/2$ value, and an appropriate error interval was assigned to this adjusted result.

For example, in Figure C-40a, the 347 Hz Strouhal frequency is near the 322 Hz cylinder flexural vibration resonance, and therefore, the 1700 mV response at 347 Hz requires adjustment. Conversely, the 443 Hz F_L frequency $\smallsmile$ in Figure C-40b is well above the 322 Hz resonance; thus the

82

plotted response at the latter frequency may be attributed primarily to turbulence-borne flow noise. As such, Figure C-40b essentially provides a white noise system response in the vicinity of 322 Hz, and the 3:1 amplitude increase over background at this frequency is the desired calibration. Returning, then, to the 1700 mV value of Figure C-40a and applying this inferred calibration results in an adjusted $F_L/2$ of 567 mV. Finally, the error inherent in this approximate procedure justifies the ± 100 mV uncertainty interval assigned to the corresponding $\overline{U}$ = 84.3 entries in Table B-7.

In general, at high flow velocities, $F_L/2$ was sufficiently large to facilitate application of either of the above methods. A typical high velocity response signal at the amplifier output appears as Plate D-4.

Plate D-5, on the other hand, is an example of the multi-resonant, small amplitude $F_L/2$ response, characteristic of low flow velocities. For such velocities, the Stouhal frequency often was within the envelope of the 30, 60, 90 Hz stand resonance series, necessitating application of the indirect method. The inherent inaccuracy thus introduced, compounded by the small magnitude of $F_L/2$, resulted in the relatively large error intervals assigned to low velocity force values obtained in this manner. Large error intervals also were assigned to values determined with the direct method in that low velocity $F_L/2$ amplitude, even when located within a flat response window, was little above background noise.

In all, then, assignment of error intervals was somewhat subjective. No errors were recorded for method one, and those assigned to method two $F_L/2$ values depended on this author's evaluation of the accuracy of inferred calibration and of the signal-to-noise ratio present.

Similar general statements apply to the various types of cylinder considered. Either method of reading $F_L/2$ was most easily applied to uniform and finned cylinders. For notched cylinders, response curves were complicated by excitation at two Strouhal frequencies. Moreover, the response for the multinotched cylinder was of small amplitude. The addition of splitter plates to otherwise uniform cylinders also reduced lift force amplitude. Finally, the multi-resonant stand which supported the skewed cylinder minimized the extent of flat response windows, causing application of method two to be the rule instead of the exception.

CORRELATION FUNCTION $(R(\gamma))$

As discussed in Section II, $R(\gamma)$ is a measure of lift force phase variation along the cylinder axis for an idealized single tone vortex shedding process. In real aeolian tone generation, neither the lift force nor the vortices are pure tones, but rather an unsteady band about the Strouhal frequency; $R(\gamma)$ then is the statistical measure of average phase variation.

Although some researchers have determined $R(\gamma)$ through direct simultaneous measurement of the phase of the local

84

lift force at different cylinder locations,[37,39,40] most
have determined this function by comparison of velocity
variation, the corresponding parameter, in the vortex
wake.[6,25,36,38,42] This latter technique, used in the
current experiment, is easier to implement, but it is based
on the not totally verified assumption that phase and ampli-
tude variation in the vortex wake, caused by three dimen-
sional effects in the flow, correspond one to one with
similar lift force variation on the cylinder.

Implementation of the wake measurement technique requires
determination of three values, the mean square velocity
variation at each of two locations, both at equal distance
behind the cylinder, and the time average of the product
of the two velocity variations. Equivalently, the three
values actually used are the two mean square anemometer
voltages from two correctly located and aligned probes,
$\overline{A^2(t)}$ and $\overline{B^2(t)}$, and the time averaged product of the two,
$\overline{A(t)B(t)}$. $R(\gamma)$ then may be calculated by forming the quotient
$\overline{AB}\Big/\sqrt{\overline{A^2}\,\overline{B^2}}$ which, by the assumption noted above, is
equivalent to equation (38).

Examination of this quotient reveals that the $R(\gamma)$
value obtained is sensitive to the extraneous turbulent
noise sensed by each probe. This undesired noise increases
denominator values without substantially effecting the time-
averaged numerator. Accordingly, both probes must be located
to minimize this noise, restricting probe output to the

85

desired statistical variation of velocity characteristics of a turbulent vortex wake.

In this experiment, the proper probe location was found by traversing the wake in three dimensions until a relatively noise-free signal (see Plate D-6) was obtained. The correct probe location typically was on the outer side of the vortex street at a point about 1 diameter from the wake center and from 1 to 3 diameters behind the cylinder. This position was not the point of maximum RMS velocity variation which generally was 2 diameters behind the cylinder and 0.6 diameters from the wake center.

When the probe was placed at the maximum RMS velocity location, the signal exhibited noise spikes (see Plate D-7) caused by the extraneous turbulent noise which was characteristic of the center wake. As flow velocity increased, both maximum RMS and noise-free position moved closer to the cylinder, but both maintained their respective 0.6 and 1 diameter distance from the wake center.

Consistent measurement also required proper probe alignment, the maintenance of constant cylinder to probe distance as probe position varied in the z direction (see Figure C-1). To obtain such alignment, the probes were placed 9 inches apart, and the slide mechanism was adjusted until probe to cylinder distance as measured with a metal rule was equal for both hot wires. Fine alignment was then accomplished electronically using the auto-correlation technique discussed below. This latter technique insured

exact alignment as an unchanging auto-correlation with probe
position change in the z direction requires constant signal-
to-noise ratio and constant sum of signal and noise power,
two criteria which are satisfied simultaneously only if
probe location relative to the cylinder is unchanged.

Once determined, probe alignment relative to the cylinder
was maintained by setting two dial indicators, one mounted
relative to each end of the probe support slide mechanism.
When $\overline{U}$ was increased, the entire slide mechanism was moved
toward the cylinder, with alignment insured by equal position
change indication on both dials. Alignment at the new loca-
tion nevertheless was again verified by auto-correlation.

Measurement of the voltages $\overline{A^2(t)}$, $\overline{B^2(t)}$ and $\overline{A(t)B(t)}$
was accomplished with the electronics of Figure C-41.

The Saicor correlator internally converted each analog
input signal to 400 discrete data points which were digitally
processed to provide auto-correlation of either input or
cross-correlation of the two. It terminated the length of
input signal at 400 times the sampling interval. In the
present use, sampling rate was set at 50 to 100 times the
Strouhal frequency as the factor of two specified by the
sampling theorem required modification to account for the
increased bandwidth caused by unsteady input and correlator
induced finite signal duration. Thus, for a 100 Hz Strouhal
frequency, a 0.1 to 0.2 ms sampling interval was selected
and 4 to 8 cycles of wake signal were processed.

The device's non-destructive readout consisted of 400 correlation function points and a DC voltage for oscilloscope synchronization. Each of the 400 discrete voltages also could be addressed individually so that in this experiment the $\tau = 0$ correlation function value was read on a digital voltmeter.

In this manner, the correlator was used to perform auto and cross correlation of two time signals; the space correlation, $R(\gamma)$, was calculated from the $\tau = 0$ time correlation values. Specifically, for a particular probe separation (γ), auto-correlation of A(t) provided $R_{AA}(\tau) = \frac{1}{T} \int_0^T A(t)A(t+\tau)\,dt$, the $\tau = 0$ value of which, by definition, is $\overline{A^2(t)}$. Similarly, B(t) auto-correlation provided the discrete value $\overline{B^2(t)}$.

Cross correlation generated $R_{AB}(\tau) = \frac{1}{T} \int_0^T A(t)B(t+\tau)\,dt$, which is $\overline{A(t)B(t)}$ when evaluated at $\tau = 0$. These three distinct values together provided the information required to calculate $R(\gamma) = \frac{\overline{AB}}{\sqrt{\overline{A^2}\ \overline{B^2}}}$ for this single value of γ, and three more $\tau = 0$ time correlation values were necessary for calculation of each subsequent single $R(\gamma)$ curve data point.

Although only $\tau = 0$ time correlation values thereby were recorded, the entire autocorrelated time signal, as described previously, was used for alignment. In addition, the auto-correlated time signal provided a measure for precise determination of the optimum signal-to-noise probe

location. In this manner, two signals from almost identical probe positions, each appearing relatively noise-free on the oscilloscope as in Plate D-6, were differentiated. The signal from the location of greater noise, when autocorrelated, exhibited a definite noise envelope which decayed in several cycles (see Plate D-8), while the optimum signal-to-noise ratio signal was characterized by nearly equal amplitude peaks as in Plate D-9.

Similarly, although only $\tau = 0$ values were recorded, the entire cross correlation of the two time signals also provided useful qualitative information. As probe separation was increased, the two probe outputs not only grew progressively out of phase but tended to become unrelated in phase as well. Plate D-10 is a typical $R_{AB}(\tau)$ correlator output for small probe separation. It exhibits well defined peaks and a $\tau = 0$ value of amplitude near that of the peaks. For large γ, a poorly defined time cross correlation, as magnified and reproduced in Plate D-11, was typical. Criteria like those shown in these plates permitted using cross correlation outputs to obtain an immediate estimate of $R(\gamma)$ curve shape and to determine bounds on the quantity of numerical data thus required.

For each cylinder, the above methods of alignment, probe positioning and $R(\gamma)$ calculation were used to obtain a set of $R(\gamma)$ curves (for example, see Figures C-42 and C-43). High confidence is placed in those results applicable to uniform and finned cylinders. However, as vortex strength

89

was proportional to lift force magnitude, wake signals
corresponding to attenuated lift forces were of reduced
signal-to-noise ratio, and therefore, degraded measurement
precision affected the $R(\gamma)$ curves for other cylinders.
In addition, other effects which contributed to non-uniform
cylinder measurement difficulties require further explanation.

With notched cylinders, a shadowing effect, wherein
the $\frac{1}{2}$" flow regime extended over adjacent 3/8" sections, was
observed. This effect was illustrated by plotting wake
frequency scans generated by mounting a single probe in
the wake of the two-notched cylinder near the diameter
discontinuity and then sweeping frequency on the wave
analyzer. The strength of the $d = \frac{1}{2}$" Strouhal frequency
behind the 3/8" section at various z coordinate locations
indicated the extent of the shadowing. Within 1/4" of
the diameter discontinuity, shadowing was strong; it was
still present, although weaker, over the next 1/4" but no
shadowing appeared behind the remaining $4\frac{1}{2}$" of the 3/8"
diameter section.

The 3/8" section of the two-notched cylinder thus was
sufficiently long to permit this effect to be disregarded.
Moreover, as correlation values for non-uniform cylinders
were otherwise obtained with high confidence, no further
$R(\gamma)$ measurements were made for this cylinder. However, on
the regular multinotched cylinder, each 1" long, 3/8" d
section was shadowed by two adjacent $\frac{1}{2}$" d sections, leaving
virtually no unaffected 3/8" length over which the usual

flow pattern could develop. Therefore, meaningful $R(\gamma)$ data could not be obtained.

On the other hand, measurements behind the $\frac{1}{2}$" sections did yield $R(\gamma)$ curves (for example see Figure C-44). Finally, the expectation of shadowing effecting 3/8" d section sound generation dictated the fabrication of a cylinder whose small diameter sections were long enough to provide some unshadowed 3/8" portion (see Figure C-33e).

As expected, the placement of a splitter plate behind uniform cylinders disrupted vortex formation and made location of a noise-free wake position difficult. In most cases, the wake position ultimately accepted was characterized by a poor signal-to-noise ratio; as such, the usual calculation provided only an upper bound on $R(\gamma)$.

To compensate, $R(\gamma)$ also was calculated by replacing the noise-influenced denominator by the largest numerator value measured. A renormalized $R(\gamma)$, based on the assumption that a noise-free signal would have yielded a unity $R(\gamma)$ value at minimum probe separation, thereby was obtained. In subsequent calculations all quantities derived from $R(\gamma)$ were computed twice, with resulting differences considered as error intervals.

For the 3d splitter plate, the location of best signal to noise was about 3 diameters past the rear edge of the plate (6d in back of cylinder). This position qualitatively agrees with that reported by Apelt and West[54] who determined that a regular vortex street was established immediately

91

(i.e., one diameter) downstream of a 3d plate at a Reynolds number of 10^4.

The 2d quantitative difference may be explained in terms of splitter plate alignment and attachment. Apelt and West carefully aligned their plate by mounting it in a groove at the rear of the cylinder and then adjusting the cylinder to equalize pressure at equal distance from the forward stagnation point. In the present experiment, the plate was aligned visually, with a small gap remaining between it and the cylinder.

Apelt and West further reported that for plates longer than five diameters, the high vorticity shear layers became reattached to the plate 5d downstream of the cylinder, and that a well formed vortex street shed by the combined body (consisting of cylinder and plate) appeared well downstream, about 17 diameters from the cylinder.

In the current experiment, a similar vortex street was observed 15 diameters downstream when the 6d splitter plate was placed behind the $\frac{1}{2}$" cylinder. The signal at this 15 d location was strong; however, as this position was 8" from the tunnel mouth, the turbulent noise in the flow also was strong, and the signal-to-noise ratio was poor. A weak signal at the basic cylinder Strouhal frequency also was observed at a position of little noise, above the plate about 4d past the cylinder. As this position provided a higher signal-to-noise ratio, it was used for $R(\gamma)$ measurement.

The monotonic increase in turbulence with downstream
distance similarly degraded $R(\gamma)$ measurement for the skewed
cylinder. If this cylinder had been mounted with one end
at the tunnel mouth and the other end extending downstream,
then flow of different turbulence level would have accompanied
each skew angle. To preclude this undesirable condition, it
was necessary to center the cylinder, regardless of skew,
at the position the cylinder midpoint occupied at the largest
skew angle of 45°. Accordingly, in all cases, the cylinder
center was 5" from the tunnel mouth, and all $R(\gamma)$ measure-
ments were made with probes located in a downstream region
of comparatively poor signal-to-noise ratio. However, signal
degradation was not as severe as that experienced with
splitter plates or with regular multiple notches; the curves
for skew all were normalized to the usual factor, $\sqrt{\overline{A^2}\ \overline{B^2}}$,
used for uniform cylinders.

Finally, skew introduced one additional complication.
As measurement required that the probes be equidistant from
the cylinder, the positioning of one probe downstream of the
second necessarily accompanied large skew angles. Accordingly,
for small γ, one probe was in the wake of the other. Never-
theless, degradation at the downstream probe was slight,
even at the minimum separation of 3/8", compared to the
signal-to-noise reduction common to both probes, and the
degradation quickly disappeared as γ was increased.

RADIATED SOUND INTENSITY (I)

The intensity of radiated sound was recorded using the electronics of Figure C-45. Two types of recording were made. For the first, the microphone was held stationary 4 feet above and pointing toward the cylinder; microphone position was remotely indicated in the anechoic chamber anteroom by a light which was connected to a microswitch on the shaft of the microphone boom motor. The 4 foot distance was sufficiently large to be considered far field in that the difference in path length from the closest and furthest point on the cylinder to the microphone, at the highest frequency of interest (1 KHz), was less than 1/30 of a wave length. Data recorded for this case were plots of sound intensity vs frequency, obtained with the frequency sweep feature of the wave analyzer.

For the second, the wave analyzer filter was maintained at the frequency of maximum sound intensity, while the microphone, always pointing toward and four feet from the cylinder, was rotated on its boom through at least 120° in the plane which perpendicularly bisected the cylinder. The boom motor was controlled remotely from the anteroom where a voltage proportional to motor shaft position was connected to the x-y plotter. Beam patterns in one plane resulted.

Plots obtained included background noise 4 feet above the cylinder. Other unrecorded background noise measurements indicated that noise was usually independent of

94

microphone position. The single exception was caused by the contraction serving as a baffle, for the area in the vicinity of the tunnel mouth, for blower high frequency sound which propagated into the chamber through the duct work. Vibrations of the stand which supported the cylinder, boom motor and microphone boom were sensed by the microphone and also appear as background noise.

The generalizations which characterized the F_L plots apply equally well to these sound field data. Large amplitude sound fields occurring at large flow velocities were (for example, see Figure C-46) well above background noise, while small intensities which accompanied low velocities were often in the noise and frequently near stand vibration frequencies. For the latter, often the only information obtained was an upper bound on I. Sound intensity values read from these plots are listed in Tables B-18 to B-34.

In all cases, beam patterns obtained confirmed the validity of theoretically predicted dipole fields. Their consistency permitted their use in identification of low level sound in that small intensity peaks exhibited dipole patterns while noise spikes from either background noise or from microphone support resonances were not directional. For example, in Figure C-47, beam patterns permitted separation of the aeolian tone which was coincident with the 120 Hz stand vibration overtone from candidate sound fields at 80 and 110 Hz.

95

MICROCOPY RESOLUTION TEST CHART
NATIONAL BUREAU OF STANDARDS 1963

Unrecorded sound field measurements at positions out-
side the plane of the perpendicular bisector of the cylinder
further confirmed the existence of dipole fields.

In general, then, sound fields were obtained in a direct
manner with few unexpected results. A single anomaly
appeared at 165 Hz for the cylinder with small splitter
plate at $\overline{U} = 50.6$ ft/sec. This anomaly, although confirmed
by immediate repetition of the measurement, nevertheless
exhibited the clarity of an extraneous electrical signal.
As it appeared in no other case, it was considered an
unimportant exception whose cause did not merit detailed
investigation.

SYNCHRONIZATION

Perhaps the most logical explanation of the abandonment
of the effort to achieve synchronization is provided by a
narrative detailing both the series of failures and the
single success which occurred in the course of this
experiment.

The initial attempt to obtain synchronization was made
with the $11\frac{1}{2}"$ long, 90 gram, $1\frac{1}{2}"$ diameter cylinder which
contained the cavity-mounted microphone in its interior.
Several different flow velocities were selected, with
springs adjusted (see Figures C-36 and C-37) to match
system natural vibration frequency to measured Strouhal
frequency for each. In no case did synchronization occur.

In the belief that the lack of synchronization was attributable to excessive mass, the microphone was removed. However, synchronization still was not observed. Further chemical reduction of cylinder mass to 75 grams similarly failed to improve the situation.

Examination of Figure C-35 then indicated that the difficulty was not excessive mass, but rather that the Q of the cylinder-spring system was too small. However, use of the lowest loss leaf springs available did not yield the required Q of 225. Therefore, to confirm the high loss hypothesis, a 2" tubular aluminum cylinder with no internal microphone cavity was chemically reduced to 40 grams. Use of this cylinder, per Figure C-35, lowered the required Q value to the 85 to 140 range.

The previously used large $1\frac{1}{2}$" interior diameter end caps could not be used to support the 2" cylinder. Accordingly, 2" diameter light weight end caps were fabricated. These new caps were insufficiently large to prevent loss of base pressure suction and the resultant decrease in both lift force and Strouhal frequency.[45] Therefore, a 100 ft/sec tunnel velocity produced only a 45 Hz frequency for shed vortices; the natural vibration frequency of the cylinder-spring system was adjusted to this measured value.

With this configuration, irregular synchronization finally was observed. The cylinder visibly oscillated in the vertical direction for several seconds, but as the 3" tunnel mouth was not infinite relative to the 2" cylinder,

97

the oscillation grew to an amplitude of about 1/8 diameter and then abruptly stopped. The entire cycle then repeated. Synchronization was confirmed by connecting amplified anomometer probe signals directly to the oscilloscope and observing Lissajous figures for maximum probe separation. As the flow and cylinder motion synchronized, a rather noisy ellipse abruptly was transformed into a straight line tilted to approximately 45 degrees; then, after several seconds, the transformation process reversed.

This partial success validated the attribution of the original failure to low system Q, and it indicated that synchronization could have been obtained, for a 100 gram system, if cylinder diameter had been somewhat larger than 2". In view of the 3" tunnel mouth, however, two alternatives were available, constructing a new larger-sized contraction terminating in a 10" X 10" jet or obtaining a lower-loss spring mounting such as that provided by a taut-wire support configuration.

On the other hand, in the current experiment, the primary motivation for pursuing synchronization was to provide sufficient sound amplitude to insure quantitative measurement of the effect of cylinder skew, an amplitude already obtained with a fixed cylinder. Therefore, although synchronization was still desirable for accomplishing a sound pressure vs lift force phase comparison, it had been downgraded to a tangential goal. Moreover, the partial success both had satisfied experimental curiosity directed toward

observation of the phenomena and had confirmed diagnosis of the failures encountered. Accordingly, time and funding limitations obstructing further pursuit of synchronization were accepted, and the effort was abandoned.

ADDITIONAL WAKE MEASUREMENT

To support the existence of the effect reported and discussed in the following section, it was necessary to measure velocity variation in the wake at a location fixed relative to the position occupied by a variety of $\frac{1}{2}$" cylinders. Therefore, a single anemometer probe was rigidly attached to the support stand at a position which placed its sensing element in a reasonably low noise region of the wake. Frequency scans of the probe output were recorded with uniform, finned and multiple notched cylinders sequentially mounted on the stand; moreover, the same two flow velocities, 48 and 88 ft/sec., were selected for each cylinder.

IV. EXPERIMENTAL RESULTS

This section reports and discusses the results obtained during this research. It is divided into two subsections. The first addresses uniform cylinders, reporting Strouhal number, lift coefficient, correlation length and sound intensity; it also compares these experimentally determined values with the reports of earlier investigations or with theory. The second subsection discusses non-uniform cylinders, comparing values obtained for the above parameters with corresponding uniform cylinder values. This subsection also describes a lift force amplification/attenuation effect first identified in this experiment. It then explains the origin of this effect and discusses reports in the literature which, although not specifically identifying the effect, nevertheless support its existence.

UNIFORM CYLINDERS

Strouhal numbers obtained for uniform cylinders are plotted in Figure C-48. The source of each measured frequency-lift force, vortex wake or radiated sound — is as noted. With one exception, no significant variation unique to any of the four cylinders used ($\frac{1}{4}$", $\frac{1}{2}$" smooth, $\frac{1}{2}$" finned with no fins attached, or 1") was observed. The exception is the apparent rise at higher Reynolds number resulting from the 1" cylinder data.

100

The best fit value, .201, is only slightly lower than the .205 to .21 mean reported in the literature. This agreement lends confidence to the experimental configuration used, particularly to the effectiveness of the end caps.

Initially, the various measurements discussed in the preceding two sections were attempted with no end caps; the loss of base pressure suction caused by spanwise flow[21,45] resulted in catastrophic reduction of both Strouhal frequency and total lift force. Addition of end caps, on the other hand, reduced spanwise flow as evidenced by the present Strouhal frequency being within 4 percent of the mean value obtained in closed test sections with sealed cylinder penetrations at the side walls. As such, lift forces herein obtained similarly should be only slightly less than those reported previously.

Correlation length (ℓ_c) and the centroid of the one-sided correlation curve ($\bar{\gamma}$) were calculated per equations (40) and (41) from measured $R(\gamma)$ curve values. All integrations were performed numerically using one diameter abscissa intervals. Results are listed in Tables B-1 through B-3 and are plotted in Figure C-49.

Figure C-50 compares the current values with those reported in the literature.[2,25,32,33,36-42] Although the present results are somewhat higher than the previous mean, high confidence nevertheless may be placed in them.

As noted in Section I, ℓ_c is an approximate measure of twice the physical distance over which f_L is of relatively

101

constant phase. Accordingly, visual observations[2,32,33,38,41]
are indicative of $\ell_c/2$, and the corresponding reported
values have been doubled on the figure for comparison.

Several observers[40,49] question the measurements of
Prendegast[39] and El Baroudi.[42] The latter were among the
first obtained, and they contradict the concept of correla-
tion length not increasing as vortex turbulence increases
with Reynolds number. In addition, Prendegast's results
were based on measured $R(\gamma)$ values which remained non-zero
at extremely large γ.

As noted in the last section, the effect of measurement
difficulty is to decrease $R(\gamma)$, thereby causing a similar
decrease in calculated ℓ_c and $\overline{\gamma}$. Therefore, the location
of current values at or above already reported magnitudes
adds to their credibility. Moreover, these values agree
rather well with the recent careful measurements of Ballou[36]
and Leehey and Hansen.[25] These two observations, then,
coupled with the consistency herein obtained over several
cylinder diameters, support the high confidence assigned.

Total lift force was calculated by modifying the raw
voltage data listed in Tables B-1 to B-3 and B-5 to account
for impedance head calibration and F_L-electronics gain
factors. This process yielded F_L in pounds. Then equations
(44) and (47) as well as the already obtained ℓ_c and $\overline{\gamma}$
values were used to compute the local lift forces (f_L) and
local lift coefficients (C_L) listed in these same tables.

Local lift coefficients are plotted in Figure C-51. As observed in the last section, small magnitude lift force amplitudes associated with low velocities are highly uncertain. With one exception, the values obtained over the entire range appear independent of cylinder and diameter variation. The apparent C_L decrease characterizing 1" cylinder data may be attributable to inadequacy of the 3:1 ratio of tunnel size to cylinder diameter.

The best fit to the data of Figure C-51 is duplicated and compared to reported C_L values[6,21,25,43,44,55-57] in Figure C-52. The current data exhibit the C_L increase with Reynolds number common to the other observations. The sharp knee at $R = 2.1 \times 10^4$ may be an artifact or may be attributable to the 3" tunnel width becoming more significant as vortex strength increased.

The previously reported data exhibit considerable scatter. Gerrard partially explained this scatter by clarifying the increase of lift force with the turbulence level of the incoming flow.[43,44] His explanation reconciled his results with those of Schwage,[56] Keefe,[21] and Bishop and Hassen;[57] however, the greater of the two low turbulence C_L values reported by Leehey and Hansen[25] is too large to fit Gerrard's pattern.

All results shown except the current values and that of Koopmann[6] are for closed test sections. Koopmann's point represents synchronization, with accompanying lift force amplification, and a 3 percent incoming flow turbulence

level. The small magnitude lift force exhibited again is an exception to the other data.

In view of this scatter of reported data, as well as similar scatter in data reported for higher Reynolds numbers,[55] the present results appear credible. If they deviate from previous values, such deviation is downward, and corresponds in direction to the slight Strouhal number decrease discussed above.

Predicted sound field intensities, listed in Tables B-1 to B-3 and B-5, were calculated by inserting already obtained F_L and ω data into equation (49). Measured sound intensities from Tables B-18 to B-20 and B-22 are compared with these predicted values in Figures C-53 to C-55. Agreement is not only excellent, but so consistent that a best fit line could be drawn to both predicted and measured intensities for two different $\frac{1}{2}$" cylinders in Figure C-54.

NON-UNIFORM CYLINDERS

Except for the irregular multinotched cylinder (Figure C-33e), both total lift force and radiated sound were measured for all non-uniform cylinders. Only radiated sound was measured for the exception. Values of total lift force and of predicted sound intensities obtained by using these F_L values in Equation (49) are listed in Tables B-4 and B-5 to B-17. Measured sound intensities are listed in Tables B-21 and B-23 to B-35. Predicted and measured values are compared in Figures C-56 through C-67 where, for

reference, the best fit line for $\frac{1}{2}$" uniform cylinders from Figure C-54 is repeated.

Agreement between predicted and measured sound is excellent except for the skewed cylinder at zero skew angle. In this anomalous case, measured sound is not only lower than predicted but also lower than the reference. This unexplainable shortfall, unfortunately not discovered until after the wind tunnel was disassembled, is assumed to be a transitory systematic measurement error.

Disregarding this single exception, the overwhelming consistent agreement exhibited on the other eleven figures totally confirms the theory of aerodynamic sound. Regardless of the specific non-uniformity of each particular cylinder, be it roughness, fins, splitter plates, skew or notches, and regardless of the relation between each sound intensity and the corresponding $\frac{1}{2}$" uniform cylinder reference intensity, predicted and radiated sound values agree completely.

The extent of this agreement is particularly significant in view of the current naval and oceanographic applications noted in the introduction. It demonstrates that F_L and I now may be used almost interchangeably as their direct Equation (49) relationship has been validated experimentally. Moreover, this agreement shows that reduction of lift force, by any means, leads to a corresponding reduction in radiated sound, with the correspondence quantitatively described by Equation (49).

105

Having accomplished this confirmation of Lighthill's theory
and having noted the implications of this confirmation,
the primary objective of this research has been satisfied.
Examination of lift force and correlation length variation
thus becomes the focus of remaining interest.

Roughened cylinder C_L and ℓ_c values, calculated in the
usual manner and listed in Table B-4, are plotted on Figures
C-68 and C-69 respectively. These figures, together with
Figure C-56 indicate that roughening reduces total lift
force by adding sufficient three dimensionality to decrease
the correlation factor, $(L - \overline{\gamma}) \ell_c$ (see Equation (44)). Local
lift force also may be reduced, but the measured reduction
is too slight to clarify any substantial effect. Similarly,
unplotted Strouhal number data fall within the scatter
measured for uniform cylinders (Figure C-48) and average
.198, only slightly below the .201 measured reference.

Correlation factors for the four-finned cylinder were
calculated by applying Equation (64) to measured $R(\gamma)$
curves, using one diameter abscissa intervals for numerical
integration. Results appear in Table B-7 and on Figure
C-63. The uniform $\frac{1}{2}$" cylinder correlation factor, $(L - \overline{\gamma}) \ell_c$,
also is shown as a reference.

As recorded on the $R(\gamma)$ curves, the vortex wake behind
a cylinder section bounded by adjacent fins was highly two
dimensional, exhibiting nearly constant phase between adja-
cent fins and some phase correlation across fins. Neverthe-
less, the resulting correlation factor, when compared to the

106

no fin case, showed a decrease. This indicates that the increase in local two-dimensionality did not compensate for the reduction in large γ axial coherence caused by the introduction of fins.

Correlation data were not recorded for the two-finned cylinder. Therefore, the approximate correlation factor shown in the figure was obtained by averaging four fin and uniform cylinder values.

Strouhal numbers for these finned cylinders again fell within the uniform cylinder scatter shown in Figure C-48. Average values were .205 and .197 for the two and four fin cases respectively. The latter figure perhaps should be larger in view of the measured increased in wake two dimensionality. However, the amount of data recorded for the four-finned case together with the appearance of the expected result for the two-finned cylinder mitigate this observed contradiction.

The expectation of local lift force remaining independent of wake two-dimensionality predicts, in view of decreased correlation factor, a decrease in total lift force. However, as indicated on Figures C-57 and C-58, F_L in fact increased. C_L values calculated from Equations (47) and (64) and plotted on Figure C-71 identify the cause of this increase. Local lift force indeed showed a dependence on the local two-dimensionality of the flow. This initially unexpected phenomenon will be discussed further later in this subsection.

107

For the cylinder with splitter plates, ℓ_c and C_L values, calculated in the usual manner, are listed in Tables B-8 and B-9 and plotted in Figures C-72 and C-73. These figures indicate that the reduction in total lift force shown on Figure C-59 resulted from decreases in both local lift force and correlation values. Figures C-59 and C-73 also indicate that the decrease is greater for the larger plate, particularly at lower Reynolds numbers. The contrary trend shown for low Re on Figure C-72 is based on uncertain data, in view of the poor anomometer probe signal-to-noise ratios discussed in the previous section. As such, this contra-indication is considered insubstantial.

The Reynolds number dependence is explainable in terms of Gerrard's formation length[44], which is defined as the distance in back of the cylinder where fluid from outside the wake first crosses the wake axis. This length, in effect, is that over which virtually no interaction occurs between opposite vorticity regions of the wake. Therefore, insertion of a splitter plate of length less than the formation length should have little effect on the flow. Formation length decreases as Reynolds number increases.[44]

For the present case, the large splitter plate extended past the uniform cylinder formation length at all Reynolds numbers considered. The small plate similarly exceeded the less than 2d[44] formation length characterizing Reynolds numbers above 8×10^3. However, below this Re, formation length increased almost to the 3d extent of the smaller

108

plate, minimizing the plate's influence on the vortex formation process.

Observed Strouhal numbers averaged 68 and 46 percent of the .201 uniform cylinder value for the small and large plate respectively. These values, compare favorably with the 76 and 36 percent figures reported by Apelt and West[54] for similarly scaled but more precisely mounted plates.

Skewed cylinder measurements herein reported were made to determine the applicability of superposition to flow over a cylinder in the presently considered Reynolds number regime. This determination was motivated by verbal reports that superposition, in spite of the non-linearity of the governing Navier-Stokes equation, nevertheless predicted correct experimental values.

To accomplish this portion of the experiment, the usual quantities were measured for skew angles, β, of zero and 45 degrees and at four intermediate angles of about 10, 21, 31 and 39 degrees. Results obtained then were compared with those for uniform cylinders, with appropriate modified parameters such as $U^* = \overline{U} \cos \beta$, $Re^* = \frac{U^* d}{\nu}$ and $S^* = \frac{\omega d}{2 \pi U^*}$ used to provide a reasonable corresponding basis. In general, these results confirmed the applicability of superposition at small skew angles, but they also indicated an attenuation of ℓ_c, $\overline{\gamma}$, S^*, C_L, and F_L which grew more significant as skew angle was increased.

This conclusion is exemplified by the sound intensity curves of Figures C-61 through C-65 and by the average

109

Strouhal numbers listed in Table B-36. Moreover, it may be applicable to the ℓ_c and $\bar{\gamma}$ values of Figures C-74 to C-79, which were computed from measured $R(\gamma)$ values using Equations (40) and (41). On the other hand, the results shown for ℓ_c and $\bar{\gamma}$ also were attenuated by poor signal-to-noise ratios as discussed in Section III, and therefore, the magnitude of the shortfall attributable to superposition is not clear.

If these correlation values in fact had been larger, then the C_L values listed in Tables B-12 through B-17 and plotted in Figures C-80 through C-85 would have been smaller than shown (see Equations (44) and (47)). As such, the indicated C_L values represent upper bounds and thus affirm the previously stated conclusion.

Further consideration of the Strouhal number values of Table B-36 motivated additional comparison. Recognizing that the factor ω/ω_s was consistently about equal to or less than $\cos \beta$ dictated examination of the resultant data with ω/ω_s replacing $\cos \beta$ as the factor for computing effective normal flow velocity. Accordingly, the previous C_L and I results were replotted against $U^{**} = \bar{U} \, \omega/\omega_s$ and $Re^{**} = \dfrac{U^{**}d}{\nu}$ as shown in Figures C-86 through C-95. On the other hand, the previously mentioned measurement uncertainty obviated the necessity to replot ℓ_c and $\bar{\gamma}$ values.

As the figures indicate, employment of this new effective skew angle, $\cos^{-1} \omega/\omega_s$, postpones the apparent introduction

110

of the departure from superposition, but it does not alter the basic conclusion. Application of superposition predicts experimentally correct results at small skew angles but is increasingly inappropriate as skew becomes more severe.

The two-notched cylinder (Figure C-33c), as indicated in the previous section, is essentially two 5 inch long cylinders with different diameters. As such, the total lift force measured for the $\frac{1}{2}$" section should be lower than that of the 10 inch reference. Figure C-66 exhibits this result and also indicates reasonable 3/8" section lift force magnitude.

Although correlation quantities were not measured for this cylinder, ℓ_c and $\bar{\gamma}$ values appropriate to each diameter were determined from the uniform normal cylinder curves of Figure C-49. These values then were used, together with the 5" length, in Equations (44) and (47) to calculate the C_L values listed in Table B-10 and plotted in Figure C-96. Results agree with those already obtained for 10" cylinders. Similarly, measured Strouhal numbers averaged .201, the previous uniform cylinder mean value.

Results for the regular multi-notched cylinder, on the other hand, are not so amenable to direct interpretation. Although radiated sound again agreed with predicted values (see Figure C-67), the magnitudes of both F_L and I as well as those of correlation parameters and S, as discussed in detail below, were smaller than expected for $\frac{1}{2}$" sections. The 3/8" sections showed similar agreement between predicted

111

and measured sound intensity, but the strong shadowing effect precluded measurement of correlation function.

Nevertheless, Strouhal frequencies, based upon wake measurements as well as lift force and sound field data, were measured for 3/8" sections. The values obtained matched those measured on this same cylinder for $\frac{1}{2}$" sections, with neither set exhibiting any more scatter than the corresponding data of Figure C-48. The average Strouhal number of .183 was 1G percent less than the uniform cylinder value.

An estimate of the effect of shadowing was obtained by comparing the f_L predicted from uniform cylinder C_L with the F_L measured for 3/8" sections. The comparison assumed that 3/8" sections were phase independent, a reasonable assumption in view of the failure to observe other than random phase relationships during the shadowing — aborted attempt to measure 3/8" section $R(\gamma)$. As enumerated in Table B-11, the square of the effective length was obtained by dividing the square of measured F_L by five times the square of predicted f_L (see Equation (64)). The result was an effective length averaging .3d per 1" long section, with a standard deviation of about .05d. Therefore, because of shadowing, each 1" long, 3/8" diameter section radiated sound as if it was an unshadowed section about 1/8" in length.

The $\frac{1}{2}$" section $R(\gamma)$ values of .25 at minimum probe separation and the similarly weak but consistently 180° out-of-phase values between separated sections are subject

112

to two interpretations. The first treats the intervening 3/8" sections as periodic divisions (see Figure C-44 (a) and (b)) and applies Equation (64) to compute a correlation factor of 2.865. The second assumes that shadowing effectively causes the lift force to be applied along the entire cylinder. Then, sketching in the unmeasured portion of the $R(\gamma)$ curve (Figure C-44(c)) permits calculation of ℓ_c and $\overline{\gamma}$. The resulting correlation factor, $\sqrt{(L - \overline{\gamma}) \ell_c}$, of 2.5 agrees relatively well with that obtained by the first method.

C_L values based upon measured F_L and the above 2.865 correlation factor are listed in Table B-11 and plotted in Figure C-97. As indicated, they are only 40% of uniform cylinder values, a reduction which corresponds mathematically to the two orders of magnitude decrease in radiated sound shown in Figure C-67. Moreover, this decrease is unaffected by any $R(\gamma)$ measurement inaccuracies caused by poor signal-to-noise ratios and spanwise flow between $\frac{1}{2}$" sections. As for previous cylinders for which $R(\gamma)$ measurement difficulties were encountered, underestimating correlation factors implies that C_L values based upon these factors are upper bounds.

To obtain reasonable lengths of unshadowed 3/8" sections, as noted earlier, the irregular multinotched cylinder was fabricated toward the end of this experiment, and for this cylinder, only radiated sound was measured. Results, plotted

113

in Figure C-98 were used together with an estimate of correlation factor to obtain an estimate of C_L.

For the four 1 3/4" long, 3/8"d sections two estimates of correlation factor were made. Both assumed phase independence between sections as well as an unshadowed length of about 2d within each section, with the latter value inferred from the shadowed length computation for the regular multinotched cylinder. The first estimate, 4.47, followed from Equation (64) and the stipulation that within each section, correlation was identical to the $R_w(\gamma)$ curve characterizing $\frac{1}{2}$" sections of the regular multinotched cylinder. The second estimate, 6.76, resulted from the assumption of a within-section effective length identical to the .65L value obtained for uniform $\frac{1}{2}$" cylinders.

Substitution of these estimates and measured I values into Equations (44), (47) and (49) provided the 3/8" section C_L values listed in Table B-37 and plotted in Figure C-99. As shown, lift coefficients still are slightly below uniform cylinder results.

Similarly, these same two methods were used to obtain correlation factor estimates for the three 1" long, $\frac{1}{2}$"d sections. However, in this case inter-section phase independence was not an assumption but was determined from crude wake measurements which indicated no phase relationships between separated sections. Values obtained are listed in Table B-37 together with resultant C_L values, and the latter are also plotted in Figure C-92. Again, a slight decrease

114

from uniform cylinder results is indicated, but comparison with Figure C-97 reveals that this decrease is not nearly so severe as that measured for the regular multinotched cylinder.

Finally, the proximity of irregular multinotched and uniform cylinder C_L values is paralleled by the .204 mean Strouhal number measured for the former.

The difference in lift force attenuation between these two multinotched cylinders may be understood in terms of the mechanism of vortex shedding as explained by Gerrard.[44]

"The growing vortex continues to be fed by circulation from the shear layer until the vortex becomes strong enough to draw the other shear layer across the wake. The approach of oppositely-signed vorticity in sufficient concentration cuts off further supply of circulation to the vortex, which then ceases to increase in strength. We may speak of the vortex as being shed from the body at this stage."[44]

On both irregular multinotched and uniform cylinders, this mechanism applied. Their Strouhal numbers agreed, and C_L differentials between these cylinders were small. Moreover, as discussed below, small decreases in vortex wake two-dimensionality in back of the 2d lengths of $\frac{1}{2}$" sections on the irregular multinotched cylinder may have caused the small f_L reduction observed.

On the regular multi-notched cylinder, however, where $\frac{1}{2}$" sections were not phase independent, Gerrard's mechanism apparently was modified. The same 180° phase reversal

115

existed between $\frac{1}{2}$" sections as existed between opposite
cylinder sides on a uniform cylinder. In addition, the
Strouhal number decrease observed implied the presence of
spanwise flow. Therefore, one may conclude that in Ger-
rard's description the oppositely-signed vorticity, which
caused shedding, flowed to the top of one $\frac{1}{2}$" section from
the bottom of that section and, in lesser quantity, from
the top of adjacent sections as well. This between-section
flow interaction, similar to the usual opposite-side-of-
the-cylinder interaction, thus disrupted the vortex shedding
process and caused lift force attenuation.

This significant magnitude effect, wherein strong span-
wise interaction introduced large lift force attenuation,
may be generalized, in view of the previously reported
results for other cylinders, to the observation that the
magnitude of local lift force is dependent upon the two-
dimensionality of the vortex wake.

On the irregular multinotched cylinder, f_L attenuation,
although small, was nevertheless present. Moreover, the
L/d ratio of two for each section was hardly large enough
to justify considering each section as an infinitely long
uniform cylinder. As such, some wake three-dimensionality
must have been present.

In addition, some lift force attenuation accompanied
increased three-dimensionality for both the roughened and
the skewed cylinder, particularly at large skew angles for
the latter. Although the magnitude of the observed attenuation

116

could be considered to fall within experimental error, the
trend nevertheless exhibited supports the above generalization.

More importantly, the greatly increased wake two-dimen-
sionality observed for finned cylinders was accompanied by
large lift force amplification. This large magnitude
result together with above discussed regular multinotched
cylinder measurements clearly indicates that f_L is monotonic
with local two-dimensionality in the vortex wake.

This conclusion, although previously not stated so
explicitly, nevertheless is supported by several reports
in the literature. Among those reporting lift force ampli-
fication, Keefe[21] mounted 5d fins on an otherwise uniform
cylinder and varied fin spacing between 25 and 3d. At
large separation, the fins had virtually no effect on f_L,
but as separation was decreased, f_L was amplified, with the
amount of amplification per unit separation decrease more
significant at small spacing. Amplification factors of
1.2 and 1.5 were observed at 5 and 3d separation respectively.

Other researchers[8,27-30,58-62] also noted an increase
in f_L with increasing two-dimensionality, but such increase
accompanied synchronization. Nevertheless, the reports of
lift force amplification were so numerous that Schmidt[63]
suggested the necessity for a correction to measured local
lift force to account for the relationship between correla-
tion length and the finite extent of the force transducers
used for f_L measurement. This correction is not applicable to
the current experiment wherein F_L, not f_L, is measured.

117

In general, reports of lift force attenuation[6,21,25] pertain to the previously addressed reduction of both f_L and S which accompanies the loss of base pressure suction. In turn, this loss is well known to be caused by spanwise flow,[45] a three dimensional phenomenon. On the other hand, no reports of measurements such as those herein obtained for multinotched cylinders are known to this author. As such, it appears that the literature does not as completely support the coupling of lift force attenuation and increased wake three dimensionality as it does the lift force amplification phenomenon.

It appears, therefore, that measurement of local lift force is required to complement previously discussed results regarding this effect. For such measurement, a short-length cylindrical force transducer with equal diameter cylindrical attachments fabricated so as to provide finned and notched cylinders is required. The appropriate measurements then could be made by placing the cylinder/transducer body in flow and recording force transducer output.

Unfortunately, in the present case, time and funding limitations precluded pursuing this task which, while serving to quantify the observed effect, nevertheless is tangential to the already attained primary experimental objective of validating the theory of aerodynamic sound for cylinders in flow. On the other hand, a qualitative, yet expeditious and inexpensive confirmation of the above dis-cussed effect was accomplished in the measurement discussed at the end of Section III.

118

This measurement of velocity variation, u', in the vortex wake, at a position fixed relative to different equal diameter cylinders, was made for two flow velocities, 48 and 88 feet per second. Results obtained indicated that u' was virtually identical for irregular multinotched and uniform cylinders; u' doubled with the addition of fins and decreased by forty percent from the uniform cylinder value for the regular multinotched cylinder.

As f_L and u' definitely are related monotonically, these data qualitatively agree with the previous results regarding amplification and attenuation of local lift force. The near quantitative agreement, however, may well be fortuitous as the exact numerical relation between f_L and u' is not clear.

Bernoulli's law is inapplicable to determination of this relation as the conditions for its use are not satisfied. Moreover, experimental data relating surface pressure to u' apparently appear in only a single reference. Goldstein's[64] report of data recorded by Schiller and Linke indicates that over the limited Reynold's number range 4 to 6×10^3, an increase in u' by a factor of 1.25 is accompanied by a corresponding 1.4 factor increase in C_L. Extrapolation of this linear relation to other Reynolds numbers is not clearly justifiable, particularly in view of the shadowing and other flow effects applicable to these multinotched cylinders; however, this limited information does support somewhat the one-to-one relationship obtained for the additional wake measurement herein reported.

In all, in spite of these uncertainties, the experimental evidence available, within the current results or synthesized from the literature, does support the existence of the effect. Local lift force indeed appears to increase monotonically with vortex wake two-dimensionality, or equivalently, with reduction of spanwise flow.

V. CONCLUSIONS

This experimental effort originally was focused toward validating the theory of aerodynamic sound. However, several tangential paths were explored in the course of the research, and therefore, the conclusions reached extend beyond the original scope.

1. The theory of aerodynamic sound as applied to cylinders is correct. Radiated sound predictions based on measured total lift force agree overwhelmingly with measured sound intensity.

2. Reduction of lift force, by any means, correspondingly reduces radiated sound intensity.

3. The herein derived extension of this theory to periodically divided cylinders also is correct. Lift coefficients calculated from measured total force and correlation values form a consistent pattern and agree with applicable results in the literature.

4. The magnitude of local lift force varies monotonically with the two-dimensionality of the vortex wake behind the cylinder. This effect is supported qualitatively by the results herein obtained and by reports in the literature.

5. Installing a microphone within a Helmholtz resonant cavity is a feasible method of measuring surface pressure variation at a point on a cylinder. Use of this method first requires careful calibration of both the phase and the amplitude of the microphone-cavity system.

6. Reports of incoming flow turbulence, cylinder end conditions, cylinder roughness, and vortex-wake two-dimensionality should accompany reports of measured lift force. The need for turbulence data first was addressed by Gerrard,[43,44] and several observers[21,45,54] showed the need for specification of end conditions. The additional requirements are indicated by the current results.

VI. SUGGESTED FURTHER RESEARCH

The present experiment opens a new area of inquiry,
the study of the effect reported in Section IV and summarized
in the fourth conclusion of Section V. Quantification of
this effect requires simultaneous measurement of local lift
force and correlation parameters for a variety of uniform,
finned and notched cylinders, the fabrication of which was
discussed in Section IV. However, exhaustive quantification
further requires that the spacing of fins and notches,
relative to the force transducer used, be variable.

In addition, information gained from searching the
literature and from reading papers in related areas also
suggests areas for further inquiry. First, although Light-
hill's theory correctly predicts the magnitude of radiated
sound, no clear understanding of the phase relationship
between radiated sound pressure and surface pressure varia-
tion on the cylinder has been attained. Experimental deter-
mination of this phase relationship would be facilitated
by use of a synchronized cylinder.

Similarly, a synchronized cylinder is necessary for
study of the second related area, the effect of skew on
synchronization. Little is known regarding the combination
of these two phenomena.

Finally, $R(\gamma)$ traditionally has been determined using
one of two techniques, the measurement of phase relations

123

in the vortex wake or the phase comparison of the outputs
of two or more cylinder-mounted force transducers. Although
these two distinct methods have resulted in values which
exhibit general agreement, proof of their equivalence
awaits the equality of experimental results obtained
simultaneously with each method.

124

VII. REFERENCES

1. V. Strouhal 1878 *Annalen Physik und Chemie Bd 5*. 216-51

2. O. M. Phillips 1956 *Journal of Fluid Mechanics 1*. "The Intensity of Aeolian Tones"

3. Lord Rayleigh 1879 *Philosophical Magazine 7*. 149-62

4. Lord Rayleigh 1896 *The Theory of Sound Vol. II*. London: MacMillan

5. F. Allborn 1902 *Agh Geb Naturwiss Bd 17*.

6. G. H. Koopman 1969 *Wind Induced Vibrations and their Associated Sound Fields*. Washington, D.C.: Catholic University

7. H. Bénard 1908 *Academie des Sciences Comptes Rendues T. 147*. 839-42

8. G. H. Koopmann 1967 *Journal of Fluid Mechanics 28*. "The Vortex Wakes of Vibrating Cylinders at Low Reynolds Numbers"

9. T. Von Karman 1912 *Physikolische Zeitschrift Bd 13*. "Über der Mechanismus des Flüssigkeitsund Luftwiderstandes"

10. W. F. Durand Ed. 1943 *Aerodynamic Theory No. 1 Div. D*. (Giacommelli and Pistolesi) : Durand Reprinting Committee

11. Lord Rayleigh 1915 *Philosophical Magazine 29-6*. "Aeolian Tones"

12. E. F. Relf 1921 *Philosophical Magazine 42-6*. "On the Sound Emitted by Wires of Circular Section when Exposed to Air Current"

13. L. S. G. Kovasznay 1949 *Proceedings of the Royal Society A198*. "Hot Wire Investigation of the Wake Behind Cylinders at Low Reynolds Numbers"

14. A. Roshko 1953 *NACA TN2913*. "On the Development of Turbulent Wakes from Vortex Streets"

15. J. H. Gerrard 1955 *Proceedings of the Royal Society B68*. "Measurement of the Sound from Circular Cylinders in an Air Stream"

16. E. Z. Stowell and A. F. Deming 1936 Journal of the Acoustic Society of America 7. "Vortex Noise from Rotating Cylindrical Rods"

17. E. Y. Yudin 1947 NACA TN1136. (Translation of Zhur Tekh Fiz 14,561 (1944))

18. M. J. Lighthill 1952 Proceedings of the Royal Society A211. "On Sound Generated Aerodynamically, I General Theory"

19. N. Curle 1955 Proceedings of the Royal Society A231. "The Influence of Solid Boundaries upon Aerodynamic Sound"

20. B. Etkin, G. K. Korbacher and R. T. Keefe 1956 UTIA Report 39. "Acoustic Radiation from a Stationary Cylinder in a Fluid Stream (Aeolian Tones)" Toronto: University of Toronto

21. R. T. Keefe 1961 UTIA Report 76. "An Investigation of the Fluctuating Forces Acting on a Stationary Circular Cylinder in a Subsonic Stream and of the Associated Sound Field" Toronto : University of Toronto

22. M. J. Lighthill 1962 Proceedings of the Royal Society A267. "The Bakerian Lecture 1961, Sound Generated Aerodynamically"

23. H. M. Fitzpatrick and M. Strassberg 1957 Naval Hydrodynamic Publication 515 National Academy of Science. "Hydrodynamic Sources of Sound" Washington, D.C.

24. F. N. Frenkiel 1959 Advances in Applied Mechanics Vol. III. "Turbulent Diffusion" New York Academic Press

25. P. Leehey and C. E. Hanson 1971 Journal of Sound and Vibration 13. "Aeolian Tones Associated with Resonant Vibrations"

26. H. Schlicting 1968 Boundary Layer Theory New York: McGraw Hill

27. O. M. Griffen and C. W. Votaw 1972 Journal of Fluid Mechanics 51. "The Vortex Sheet in the Wake of a Vibrating Cylinder"

28. O. M. Griffen, R. A. Skop and G. H. Koopmann 1973 Journal of Sound and Vibration 31. "The Vortex Excited Resonant Vibrations of Circular Cylinders"

29. O. M. Griffin 1973 Journal of Sound and Vibration 27. "A Model for the Vortex-Excited Resonant Response of Bluff Cylinders"

30. N. Ferguson and G. V. Parkinson 1967 American Society of Mechanical Engineers Paper 67, Vibration - 31. "Surface and Wake Flow Phenomena of the Vortex-Excited Oscillation of a Circular Cylinder"

31. N. Ferguson and G. V. Parkinson 1967 Journal of Engineering for Industry. "Surface and Wake Flow Phenomena of the Vortex Excited Oscillation of A Circular Cylinder"

32. J. H. Gerrard 1961 Journal of Fluid Mechanics 11. "An Experimental Investigation of the Oscillating Lift and Drag of a Circular Cylinder Shedding Turbulent Vortices"

33. J. S. Humphreys 1960 Journal of Fluid Mechanics 9. "On a Circular Cylinder in a Steady Wind at Transition Reynold Numbers"

34. R. L. Goldman 1958 Shock and Vibration Bulletin Part II. Washington, D.C. : Naval Research Laboratory

35. Y. C. Fung 1960 Journal of Aerospace Sciences 27. "Fluctuating Lift and Drag acting on a Cylinder in Flow at Supercritical Reynolds Numbers"

36. C. L. Ballou 1967 MIT Engineering Projects Laboratory Report 76028-2. "Investigation of the Wake Behind a Cylinder at Coincidence of a Natural Frequency of Vibration of the Cylinder and the Vortex Shedding Frequency" Boston : Massachusetts Institute of Technology

37. J. H. Gerrard 1958 ARC 19,844 "Measurements of the Fluctuating Pressure on the Surface of a Circular Cylinder, Part I - Cylinder of 1" Diameter"

38. F. R. Hama 1957 Journal of Aeronautical Sciences 24. "Three Dimensional Vortex Patterns Behind a Circular Cylinder"

39. V. Prendegast 1958 UTIA TN23. "Measurement of Two-Point Correlations of the Surface Pressure on a Circular Cylinder" Toronto : University of Toronto

40. L. V. Schmidt 1965 Journal of Aircraft 2. "Measurement of Fluctuating Air Loads on a Circular Cylinder"

41. M. S. Macovsky 1958 David Taylor Model Basin Report 1190.
"Vortex-Induced Vibration Studies" Carderock, Maryland:
US Navy

42. M. Y. El Baroudi 1960 UTIA TN31.
"Measurement of Two-Point Correlations of Velocity Near
a Circular Cylinder Shedding a Karman Vortex Street"
Toronto : University of Toronto

43. J. H. Gerrard 1965 Journal of Fluid Mechanics 22.
"A Disturbance - Sensitive Reynolds Number Range of the
Flow Past a Circular Cylinder"

44. J. H. Gerrard 1966 Journal of Fluid Mechanics 25.
"The Mechanics of the Vortex Formation Region of
Vortices Behind Bluff Bodies"

45. P. W. Bearman 1965 Journal of Fluid Mechanics 21.
"Investigation of the Flow Behind a Two-Dimensional
Model with a Blunt Trailing Edge and Fitted with
Splitter Plates"

46. J. A. Stratton 1941 Electromagnetic Theory.
New York: McGraw Hill

47. P. T. Laird and H. Cohen 1952 Journal of the Acoustic
Society of America 24. "Directionality Patterns for
Acoustic Radiation from a Source on a Rigid Cylinder"

48. W. R. Morgans 1930 Philosophical Magazine 9-7.
"The Kirchhoff Formula Extended to a Moving Surface"

49. C. Graham 1966 MIT Engineering Projects Laboratory Report
76028-1. "A Survey of Correlation Length Measurements
of the Vortex Shedding Process Behind a Circular Cylinder"
Boston : Massachusetts Institute of Technology

50. G. A. Campbell and R. M. Foster 1948 Fourier Integrals.
Princeton : D. Van Nostrand

51. 1965 Handbook of Mathematical Functions.
U. S. Department of Commerce National Bureau of Standards

52. L. E. Kinsler and A. R. Frey 1962 Fundamentals of Acoustics.
New York : John Wiley and Sons

53. N. Minorsky 1962 Non-Linear Oscillations.
Princeton : D. Van Nostrand

54. C. J. Apelt and G. S. West 1975 Journal of Fluid Mechanics
71. "The Effects of Wake Splitter Plates on Bluff-Body
Flow in the Range $10^4 < R < 5 \times 10^4$, Part 2"

128

55. J. H. Lienhard 1966 WSU Technical Extension Service Bulletin 300. "Synopsis of Lift, Drag and Vortex Frequency Data for Rigid Circular Cylinders" : Washington State University

56. W. Weaver Jr. 1961 ASCE Proceedings 87 No. EM-1. "Wind Induced Bivrations of Antenna Members"

57. R. E. D. Bishop and A. Y. Hassan 1964 Proceedings of the Royal Society A277. "The Lift and Drag Forces on a Circular Cylinder in a Flowing Fluid"

58. R. E. D. Bishop and A. Y. Hassan 1964 Proceedings of the Royal Society A277. "The Lift and Drag Forces on a Circular Cylinder Oscillating in a Flowing Fluid"

59. O. M. Griffen 1972 Journal of Engineering for Industry, May. "Flow Near Self-Excited and Forced Vibrating Circular Cylinders"

60. O. M. Griffen 1971 Journal of Applied Mechanics, Dec. "The Unsteady Wake of an Oscillating Cylinder at Low Reynolds Number"

61. V. C. Mei and I. G. Curie 1969 Physics of Fluids 12. "Flow Separation on a Vibrating Circular Cylinder"

62. G. H. Toebes 1969 Journal of Basic Engineering, Sept. "The Unsteady Flow and Wake Near an Oscillating Cylinder"

63. L. V. Schmidt 1970 Journal of Spacecraft and Rockets 7. "Influence of Spatial Correlation upon Load Resolution"

64. S. Goldstein Ed. 1938 Modern Developments in Fluid Dynamics, Vol. II. Oxford Press

APPENDIX A: GLOSSARY

A	Cross-sectional area of cylinder
$A(t)$	Anemometer output voltage: first probe
a_o	Speed of sound
$B(t)$	Anemometer output voltage: second probe
C_L	Root-mean-square local lift coefficient
d	Cylinder diameter
D	Maximum diameter — sinusoidal cylinder
F_i	Total force on cylinder in i direction
F_L	Total lift force on cylinder
f_i	Local force in i direction
f_L	Local lift force
f_{L_1}	Local lift force at $z = z_1$
f_{L_2}	Local lift force at $z = z_2$
f_{L_o}	Local lift force amplitude-sinusoidal cylinder
I	Radiated Sound intensity
k	Spring constant
L	Cylinder length
L'	Length between divisions-periodically divided cylinder
$L_\perp$	Perpendicular distance between end caps - skewed cylinder
ℓ_i	Direction cosine of the outward normal from the fluid
ℓ'	Effective entrance length — Helmholtz resonant cavity
ℓ_c	Correlation length

ℓ_{c_W}	Intra-section correlation length — periodically divided cylinder
ℓ_{c_A}	Inter-section correlation length — periodically divided cylinder
ℓ_{c_A}'	Correlation length adjustment — periodically divided cylinder
M	Number of divisions — periodically divided cylinder
Ma	Mach Number
m	Cylinder mass
$\vec{n}$	Outward normal from the fluid
P_i	Force per unit area in the i direction exerted by the fluid on the cylinder
$P(\omega)$	Fourier transform of p — sinusoidal cylinder
P_{ij}	Compressive stress tensor
p	Acoustic pressure
Q	Quality factor of cylinder-spring system for synchronization
Q'	Quality factor of Helmholtz resonant cavity
$R(\gamma)$	Correlation function
$R_W(\gamma)$	Intra-section correlation function — periodically divided cylinder
$R_A(\gamma)$	Inter-section correlation function — periodically divided cylinder
$R_{AA}(\tau)$	Autocorrelation in time of first anemometer output
$R_{BB}(\tau)$	Autocorrelation in time of second anemometer output
$R_{AB}(\tau)$	Cross correlation in time of first and second anemometer outputs
R_e	Reynolds number
R_e^*	Reynolds number-skewed cylinder; modified for skew angle
R_e^{**}	Reynolds number-skewed cylinder; modified for effective skew angle

$\vec{r}$	$\vec{x} - \vec{y}$: Vector from body to field point
S	Strouhal number; also body surface as in an integral
S*	Strouhal number-skewed cylinder: modified for skew angle
s	Area of Helmholtz resonant cavity entrance
T_{ij}	Instantaneous applied stress
T	Duration of signal for correlation
t	Time
$\bar{U}$	Speed of undisturbed flow
U*	$\bar{U}$ modified for skew angle-skewed cylinder
U**	$\bar{U}$ modified for effective skew angle-skewed cylinder
U_i	Velocity of center of mass of the cylinder in i direction
U_L	Velocity of center of mass of the cylinder in the direction of lift
$u_i(z,t)$	Velocity of a dz section: non-rigid cylinder
u'	Root-mean square velocity variation in vortex wake
V	Cylinder volume
V'	Helmholtz resonant cavity volume
v_i	Fluid velocity vector
x_i	Vector from origin to field point
y_i	Vector from origin to a point in the source region; usually a body coordinate
z	x_3 direction or coordinate (along axis of cylinder)
α	Damping ratio for synchronization
β	Skew angle
γ	Separation distance along cylinder; $(z_2 - z_1)$
$\bar{\gamma}$	Centroid of area under one-sided $R(\gamma)$ curve

132

$\bar{\gamma}_w$	Centroid of area under one-sided $R_w(\gamma)$ curve
$\bar{\gamma}_A$	Centroid of area under one-sided $R_A(\gamma)$ curve
$\bar{\gamma}_A'$	Centroid adjustment to $\bar{\gamma}_A$
θ	Angle between x_2 direction and r
μ	Mass ratio for synchronization
ν	Kinematic viscosity
ρ	Fluid density
ρ_o	Mean fluid density
ρ_c	Cylinder density
τ	Time coordinate of correlator output
ϕ	Polar circumferential angle at center of cylinder
ω	Strouhal frequency; measured Strouhal frequency
ω_s	Predicted Strouhal frequency
ω_o	Resonant frequency of Helmoltz cavity
ω_i	Angular velocity vector for cylinder rotation

APPENDIX B

TABLES

TABLE B-1. AMPLIFIED IMPEDANCE HEAD OUTPUT ($F_L/2$), CORRELATION PARAMETERS, LIFT COEFFICIENT AND PREDICTED SOUND INTENSITY FOR THE UNIFORM 1/2" CYLINDER

$\bar{U}$ (ft/sec)	$\omega/2\pi$ (Hz)	$F_L/2$ (mV)	ℓ_c (d's)	$\bar{\gamma}$ (d's)	$f_L \times 10^{-3}$ (lbs/ft)	$C_L \times 10^{-2}$	$Re \times 10^3$	Predicted I (db re: 20μPa)
91.5	448	400	10.2	3.1	62.23	15.25	23.83	72.0
91.5	448	600	10.2	3.1	93.34	22.87	23.83	75.5
80.9	399	500	10.2	3.1	68.30	34.13	21.07	72.9
78.6	377	400	10.2	3.1	62.23	20.66	20.47	70.5
72.0	347	330	10.2	3.1	51.34	20.31	18.75	68.1
72.0	347	350	10.2	3.1	54.45	21.55	18.75	68.6
58.0	276	150	10.2	3.1	23.34	14.23	15.10	59.2
58.0	276	180	10.2	3.1	28.00	17.08	15.10	60.8
49.4	231	100	10.24	3.12	15.54	13.06	12.86	54.2
48.1	251	120	10.31	3.14	18.59	16.48	12.53	56.5
36.0	166	42	11.81	3.53	6.15	9.74	9.38	43.8
31.3	155	30	12.72	3.80	4.27	8.94	8.15	40.3
31.3	155	35	12.72	3.80	4.98	10.43	8.15	41.6
30.9	144	30	12.81	3.83	4.26	9.15	8.05	39.6
15.4	73	4.2	17.21	5.85	.55	4.75	4.01	16.6
15.4	73	5.25	17.21	5.85	.69	5.94	4.01	18.6
9.6	51	.5	19.98	7.29	.06	1.43	2.50	-5.0
9.6	51	1.5	19.98	7.29	.19	4.28	2.50	4.6

TABLE B-2. AMPLIFIED IMPEDANCE HEAD OUTPUT ($F_L/2$), CORRELATION PARAMETERS, LIFT COEFFICIENT AND PREDICTED SOUND INTENSITY FOR THE UNIFORM 1/4" CYLINDER

$\overline{U}$ (ft/sec)	$\omega/2\pi$ (Hz)	$F_L/2$ (mV)	ℓ_c (d's)	$\overline{\gamma}$ (d's)	$f_L \times 10^{-3}$ (lbs/ft)	$C_L \times 10^{-2}$ —	$Re \times 10^3$ —	Predicted I (db re: $20\mu Pa$)
105.9	907	210	10.2	3.1	44.22	16.18	13.8	72.5
105.9	907	157	10.2	3.1	33.06	12.09	13.8	70.0
100.0	853	160	10.25	3.11	33.61	13.79	13.0	69.6
91.5	837	125	10.43	3.19	26.06	12.77	11.91	67.3
73.7	643	58	11.68	3.51	11.48	8.67	9.60	58.3
73.1	667	60	11.72	3.51	11.85	9.10	9.52	59.0
55.8	520	50	13.46	4.12	9.29	12.25	7.27	55.2
55.8	520	35	13.46	4.12	6.51	8.57	7.27	52.1
52.8	462	32	13.82	4.29	5.88	8.66	6.88	50.3
52.8	462	39	13.82	4.29	7.17	10.55	6.88	52.0
48.9	464	20	14.35	4.50	3.62	6.21	6.37	46.3
48.9	464	30	14.35	4.50	5.43	9.32	6.37	49.8
35.8	305	8	16.37	5.40	1.37	4.40	4.66	34.7
35.8	305	12	16.37	5.40	2.06	6.59	4.66	38.2
35.1	336	8	16.48	5.49	1.37	4.56	4.57	35.5
35.1	336	12	16.48	5.49	2.06	6.85	4.57	39.0
31.0	303	5	17.20	5.83	.84	3.60	4.04	30.5
31.0	303	8	17.20	5.83	1.35	5.75	4.04	3 .
27.9	274	4.5	17.80	6.16	.75	3.95	3.63	28.7
27.9	274	5.5	17.80	6.16	.92	4.82	3.63	30.5
17.6	162	1.6	20.50	7.53	.25	3.36	2.29	15.2
12.1	119	.35	22.63	8.12	.05	1.49	1.58	-0.7
12.1	119	.70	22.63	8.12	.10	2.92	1.58	5.3
11.8	103	<1	22.82	8.21	<.15	<4.47	1.54	<7.2
9.3	90	@.225	24.31	9.42	.03	1.60	1.21	<-7.0
6.5	64	<.1	26.30	10.41	<.01	<1.42	.85	<-17.0

135

TABLE B-3. AMPLIFIED IMPEDANCE HEAD OUTPUT ($F_L/2$),
CORRELATION PARAMETERS, LIFT COEFFICIENT
AND PREDICTED SOUND INTENSITY FOR THE
1" CYLINDER

U (ft/sec)	$\omega/2\pi$ (Hz)	$F_L/2$ (mV)	ℓ_c (d's)	$\overline{\gamma}$ (d's)	$f_L \times 10^{-3}$ (lbs/ft)	$C_L \times 10^{-2}$ —	$Re \times 10^3$ —	Predicted I (db re: 20μPa)
113.8	296	700	10.2	3.1	85.22	6.75	59.27	73.2
103.6	286	500	10.2	3.1	60.87	5.82	53.96	70.0
103.6	286	700	10.2	3.1	85.22	8.14	53.96	72.9
101.6	249	620	10.2	3.1	75.48	7.50	52.90	70.7
90.3	235	500	10.2	3.1	60.87	7.66	47.03	68.3
90.3	235	700	10.2	3.1	85.22	10.72	47.03	71.2
83.7	216	440	10.2	3.1	53.56	7.84	43.60	66.5
74.0	184	400	10.2	3.1	48.69	9.12	38.50	64.2
74.0	184	325	10.2	3.1	39.56	7.41	38.50	62.4
61.0	153	260	10.2	3.1	31.65	8.72	31.77	58.9
61.0	153	200	10.2	3.1	24.35	6.71	31.77	56.6
57.0	137	250	10.2	3.1	30.43	9.61	29.70	57.6
42.2	108	170	10.2	3.1	20.70	11.92	22.00	52.2
32.9	76	80	10.2	3.1	9.74	9.23	17.10	42.6
32.9	76	40	10.2	3.1	4.87	4.61	17.10	36.6
32.0	81	45	10.2	3.1	5.48	5.49	16.70	38.1
32.0	81	80	10.2	3.1	9.74	9.75	16.70	43.1
17.9	47	20	11.83	3.55	2.34	7.48	9.32	26.4
11.7	30	8	14.60	4.61	.92	6.90	6.09	14.5
11.7	30	6	14.60	4.61	.69	5.65	6.09	12.0

TABLE B-4. AMPLIFIED IMPEDANCE HEAD OUTPUT ($F_L/2$),
CORRELATION PARAMETERS, LIFT COEFFICIENT
AND PREDICTED SOUND INTENSITY FOR THE
ROUGHENED 1/2" CYLINDER

U (ft/sec)	$\omega/2\pi$ (Hz)	$F_L/2$ (mV)	ℓ_c (d's)	$\overline{\gamma}$ (d's)	$f_L \times 10^{-3}$ (lbs/ft)	$C_L \times 10^{-2}$ –	$Re \times 10^3$ –	Predicted I (db re: $20\mu Pa$)
103.0	440	800	6.0	2.21	158.2	30.58	26.82	77.9
103.0	440	675	6.0	2.21	133.4	25.80	26.82	76.4
88.4	376	425	6.02	2.27	84.03	22.06	23.02	71.0
80.6	354	330	6.05	2. 6	66.39	20.96	20.99	68.3
65.3	310	180	6.20	2.37	35.17	16.92	17.01	61.9
56.0	236	110	6.41	2.43	21.17	13.85	14.58	55.2
43.9	201	62	6.83	2.56	11.60	12.35	11.42	48.8
40.4	167	52	6.99	2.61	9.63	12.11	10.52	45.7
32.8	145	27	7.70	2.97	4.82	9.18	8.54	38.8
22.2	97	10	9.23	3.59	1.66	6.91	5.78	26.7
22.2	97	7.5	9.23	3.59	1.24	5.18	5.78	24.2
13.2	63	4	12.08	4.58	.60	7.05	3.44	15.0
13.2	63	2	12.08	4.58	.30	3.52	3.44	8.9
11.5	46	3	12.92	4.88	.44	6.80	2.99	9.7
11.5	46	0.5	12.92	4.88	.07	1.13	2.99	-5.8

137

TABLE B-5. AMPLIFIED IMPEDANCE HEAD OUTPUT ($F_L/2$), CORRELATION PARAMETERS, LIFT COEFFICIENT AND PREDICTED SOUND INTENSITY FOR THE 1/2" FINNED CYLINDER WITH NO FINS ATTACHED

$\bar{U}$ (ft/sec)	$\omega/2\pi$ (Hz)	$F_L/2$ (mV)	ℓ_c (d's)	$\bar{\gamma}$ (d's)	$f_L \times 10^{-3}$ (lbs/ft)	$C_L \times 10^{-2}$ —	$Re \times 10^3$ —	Predicted I (db re: 20μPa)
110.0	526	500	10.2	3.1	77.79	13.19	28.65	75.3
93.2	479	475	10.2	3.1	73.90	17.83	24.01	74.0
84.3	383	300	10.2	3.1	46.67	13.47	21.95	67.5
82.8	358	600	10.2	3.1	93.34	27.93	21.56	74.1
64.8	318	225	10.2	3.1	35.00	17.10	16.87	64.0
64.8	318	300	10.2	3.1	46.67	22.80	16.87	66.5
57.0	275	150	10.2	3.1	23.34	14.73	14.84	59.2
57.0	275	180	10.2	3.1	28.00	17.68	14.84	60.8
29.2	140	28	13.21	3.99	3.93	9.46	7.60	38.8
17.7	85	<10	16.41	5.45	<1.32	<8.65	4.61	<25.5
12.0	58	1	18.76	6.59	.13	1.83	3.12	2.2
12.0	58	3	18.76	6.59	.39	5.50	3.12	13.7
10.5	50*	1	19.51	6.99	.13	2.39	2.73	0.9
10.5	50*	3	19.51	6.99	.38	7.16	2.73	10.4

*Uncertain

TABLE B-6. AMPLIFIED IMPEDANCE HEAD OUTPUT ($F_L/2$),
CORRELATION PARAMETERS, LIFT COEFFICIENT
AND PREDICTED SOUND INTENSITY FOR THE
FINNED CYLINDER WITH TWO FINS

U (ft/sec)	$\omega/2\pi$ (Hz)	$F_L/2$ (mV)	Correlation Factor (d^2)	$C_L \times 10^{-2}$ -	$Re \times 10^3$ -	Predicted I (db re: 20μPa)
104.0	486	820	135.9	27.25	27.08	78.9
92.2	438	620	136.1	26.21	24.01	75.6
87.8	400	500	136.3	23.28	22.86	73.0
69.7	334	300	138.0	22.02	18.15	67.0
60.1	272	250	138.9	24.61	15.65	63.6
60.1	272	200	138.9	19.68	15.65	61.6
41.6	200	120	149.9	23.73	10.83	54.5
41.6	200	80	149.9	15.82	10.83	51.0
32.0	158	45	159.6	14.57	8.33	44.0
28.7	143	30	163.8	11.92	7.47	39.6
24.1	125	19	170.0	10.51	6.28	34.5
21.4	91	18	174.8	12.46	5.57	31.2
21.4	91	11	174.8	7.61	5.57	26.9
19.5	105	9	178.1	7.43	5.08	26.4
19.5	105	7	178.1	5.78	5.08	24.3
13.1	61	.5	193.2	.88	3.41	-3.4
13.1	61	10	193.2	17.57	3.41	22.6

139

TABLE B-7. AMPLIFIED IMPEDANCE HEAD OUTPUT $(F_L/2)$, CORRELATION PARAMETERS, LIFT COEFFICIENT AND PREDICTED SOUND INTENSITY FOR THE FINNED CYLINDER WITH FOUR FINS

U (ft/sec)	$\omega/2\pi$ (Hz)	$F_L/2$ (mV)	Correlation Factor (d^2)	$C_L \times 10^{-2}$ —	$Re \times 10^3$ —	Predicted I (db re: $20\mu Pa$)
107.1	482	850	97.0	31.52	27.89	79.2
94.3	443	750	99.8	35.37	24.56	77.4
90.1	407	720	100.1	37.14	23.46	76.3
89.3	382	700	100.2	36.74	23.26	75.5
84.3	347	667	102.0	38.94	21.95	74.4
84.3	347	467	102.0	27.26	21.95	71.1
64.0	292	473	106.9	46.80	16.67	69.7
64.0	292	273	106.9	27.01	16.67	65.0
57.0	254	245	109.1	30.25	14.84	62.8
50.6	229	210	111.8	32.50	13.18	60.6
45.7	208	120	113.7	22.58	11.90	54.9
45.7	208	150	113.7	28.22	11.90	56.8
40.3	180	120	115.8	28.77	10.49	53.6
37.7	173	95	116.5	25.95	9.82	51.3
33.6	157	70	119.0	23.81	8.75	47.8
27.2	135	42	123.2	21.43	7.08	42.0
23.0	108	20	126.1	14.11	5.99	33.6
14.8	75	5	134.3	8.25	3.85	18.4
14.8	75	7	134.3	11.55	3.85	21.3
10.9	42	<2	140.2	<5.96	2.84	<5.4
7.3	35-40*	<2	148.1	<12.92	1.90	<9.8

*Uncertain

140

TABLE B-8. AMPLIFIED IMPEDANCE HEAD OUTPUT ($F_L/2$),
CORRELATION PARAMETERS, LIFT COEFFICIENT
AND PREDICTED SOUND INTENSITY FOR THE
1/2" CYLINDER FITTED WITH THE SMALL
SPLITTER PLATE

U (ft/sec)	$\omega/2\pi$ (Hz)	$F_L/2$ (mV)	ℓ_c (d's)	$\bar{\gamma}$ (d's)	$f_L \times 10^{-3}$ (lbs/ft)	$C_L \times 10^{-2}$ -	$Re \times 10^3$ -	Predicted I (db re: 20μPa)
92.3	283	50	6.23	1.96	9.63	2.32	24.04	50.0
85.6	268	40	6.23	1.96	7.71	2.16	22.29	48.6
82.6	252	38.3	6.23	1.96	7.38	2.22	21.51	46.6
67.6	237	24	6.23	1.96	4.62	2.08	17.60	42.0
67.6	237	30	6.23	1.96	5.78	2.59	17.60	44.0
63.0	175	27	6.24	1.96	5.20	2.69	16.41	40.4
54.6	150	20	6.40	1.96	3.80	1.81	14.22	38.0
49.4	166	12	6.58	1.99	2.25	1.89	12.86	32.2
46.5	139	12	6.70	2.01	2.23	2.12	12.11	31.4
38.7	130	11.5	7.18	2.14	2.07	2.94	10.08	30.4
32.8	120	9	8.10	2.47	1.55	2.78	8.54	27.6
26.6	87	6*	9.78	3.10	.97*	2.84*	6.93	21.3*
26.6	87	10*	9.78	3.10	1.62*	4.73*	6.93	25.7*
18.2	60	7*	12.85	4.25	1.00*	6.28*	4.74	19.5*
18.2	60	10*	12.85	4.25	1.43*	8.88*	4.74	22.6*
11.1	48	<4	16.92	5.75	<.53	<8.79	2.89	<12.6

*Uncertain

141

TABLE B-9. AMPLIFIED IMPEDANCE HEAD OUTPUT ($F_L/2$), CORRELATION PARAMETERS, LIFT COEFFICIENT AND PREDICTED SOUND INTENSITY FOR THE 1/2" CYLINDER FITTED WITH THE LARGE SPLITTER PLATE

U (ft/sec)	$\omega/2\pi$ (Hz)	$F_L/2$ (mV)	ℓc (d's)	$\bar{\gamma}$ (d's)	$f_L \times 10^{-3}$ (lbs/ft)	$C_L \times 10^{-2}$ -	$Re \times 10^3$ -	Predicted I (db re: 20μPa)
97.1	215	42.5	4.80	1.60	9.24	2.01	25.29	46.2
97.1	215	56	4.80	1.60	12.17	2.65	25.29	48.6
90.3	202	41	4.80	1.61	8.91	2.24	23.52	45.3
82.6	179	37.5	4.80	1.63	8.16	2.45	21.51	43.5
65.1	155	20	4.80	1.69	4.36	2.11	16.95	36.8
57.9	142	17	4.83	1.70	3.69	2.26	15.08	34.6
51.7	126	14	5.08	1.71	2.97	2.26	13.46	31.9
37.2	73	9	6.49	1.97	1.70	2.52	9.69	23.3
30.1	69	6	7.76	2.53	1.05	2.38	7.84	19.3
30.1	69	8	7.76	2.53	1.40	3.18	7.84	21.8
23.6	55	4	9.77	3.50	.64	2.37	6.15	13.8
23.6	55	8	9.77	3.50	1.29	4.74	6.15	19.8
16.7	38*	<3*	12.66	4.89	<.44*	<3.26*	4.35	<8.1*
11.2	25*	<2*	16.00	6.47	<.28*	<4.54*	2.92	<0.9*

*Uncertain

TABLE B-10a. AMPLIFIED IMPEDANCE HEAD OUTPUT ($F_L/2$),
CORRELATION PARAMETERS, LIFT COEFFICIENT
AND PREDICTED SOUND INTENSITY FOR THE
TWO-NOTCHED CYLINDER: 1/2" SECTION

U (ft/sec)	$\omega/2\pi$ (Hz)	$F_L/2$ (mV)	Uniform Cylinder ℓ_c (d's)	γ (d's)	$f_L \times 10^{-3}$ (lbs/ft)	$C_L \times 10^{-2}$ —	$Re \times 10^3$ —	Predicted I (db re: 20μPa)
104.0	444	433	10.2	3.1	105.4	19.99	27.08	72.6
104.0	444	650	10.2	3.1	158.3	30.01	27.08	76.1
90.1	388	370	10.2	3.1	90.08	22.76	23.46	70.1
84.3	346	280	10.2	3.1	68.17	19.68	21.95	66.7
70.6	310	200	10.2	3.1	48.69	20.04	18.39	62.8
62.2	280	120	10.2	3.1	29.22	15.49	16.20	57.5
62.2	280	145	10.2	3.1	35.30	18.72	16.20	59.1
57.2	271	120	10.2	3.1	29.22	18.32	14.90	57.2
51.8	242	80	10.2	3.1	19.48	14.90	13.49	52.7
42.1	201	34	10.9	3.28	8.11	9.39	10.96	42.7
39.6	182	30	11.4	3.39	7.06	9.23	10.31	41.7
33.2	154	22	12.4	3.70	5.08	9.46	8.65	37.5
31.4	143	15	12.7	3.81	3.46	7.19	8.18	33.6
26.6	120	10	13.8	4.28	2.29	6.66	6.93	28.5
24.8	125	9	14.3	4.46	2.07	6.89	6.46	28.0
24.1	111	9	14.4	4.52	2.07	7.31	6.28	26.9
22.8	103	4.5	14.8	4.69	1.04	4.09	5.94	20.3
16.8	86	3.25	16.8	5.59	.77	5.61	4.38	15.9
16.7	83	2.75	16.8	5.62	.65	4.82	4.35	14.1
9.0	43	<3.5	20.0*	5.00*	<.71	<18.1	2.34	<10.5

*If $(L-\bar{\gamma})\ell_c > L^2$, use L^2 as the correlation factor.

TABLE B-10b. AMPLIFIED IMPEDANCE HEAD OUTPUT ($F_L/2$), CORRELATION PARAMETERS, LIFT COEFFICIENT AND PREDICTED SOUND INTENSITY FOR THE TWO-NOTCHED CYLINDER: 3/8" SECTION

$\overline{U}$ (ft/sec)	$\omega/2\pi$ (Hz)	$F_L/2$ (mV)	Uniform Cylinder ℓ_c (d's)	$\overline{\gamma}$ (d's)	$f_L \times 10^{-3}$ (lbs/ft)	$C_L \times 10^{-2}$ —	$Re \times 10^3$ —	Predicted I (db re: 20μPa)
104.0	613	250	10.2	3.1	66.64	16.85	20.31	70.6
104.0	613	350	10.2	3.1	93.30	23.59	20.31	73.6
90.1	532	200	10.2	3.1	53.28	17.98	17.60	67.5
90.1	532	300	10.2	3.1	79.92	26.97	17.60	71.0
84.3	478	163	10.2	3.1	43.45	16.72	16.46	64.8
84.3	478	203	10.2	3.1	54.11	20.83	16.46	66.7
70.6	430	100	10.2	3.1	26.66	14.63	13.79	59.6
62.2	392	84	10.4	3.14	22.22	15.71	12.15	57.3
57.2	382	60	10.8	3.25	15.66	13.09	11.17	54.1
51.8	311	45	11.4	3.41	10.36	10.74	10.12	49.9
42.1	253	26	12.7	3.79	6.44	9.92	8.22	43.3
39.6	243	20	13.1	3.95	4.91	8.57	7.73	40.7
33.2	211	14	14.3	4.45	3.38	8.40	6.48	37.3
31.4	236	8	14.6	4.60	1.93	5.35	6.13	32.5
26.6	181	8	15.6	5.09	1.92	7.43	5.20	30.2
24.8	179	6	16.1	5.29	1.44	6.39	4.84	27.6
24.1	163	6	16.3	5.38	1.44	6.76	4.71	26.7
22.8	146	3	16.7	5.55	.72	3.77	4.45	19.8
16.8	123	1.5	18.5	6.48	.36	3.52	3.28	12.3
16.7	109	1.3	18.5	6.50	.31	3.05	3.26	10.0
9.0	58	<3.25	26.7*	6.67*	<.66	<22.41	1.76	<12.4

*If $(L-\overline{\gamma})\ell_c > L^2$, use L^2 as the correlation factor.

144

TABLE B-11a. AMPLIFIED IMPEDANCE HEAD OUTPUT $(F_L/2)$, CORRELATION PARAMETERS, LIFT COEFFICIENT AND PREDICTED SOUND INTENSITY FOR THE REGULAR MULTI-NOTCHED CYLINDER: 1/2" SECTIONS

U (ft/sec)	$\omega/2\pi$ (Hz)	$F_L/2$ (mV)	Correlation Factor (d^2)	$f_L \times 10^{-3}$ (lbs/ft)	$C_L \times 10^{-2}$ -	$Re \times 10^3$ -	Predicted I (db re: 20µPa)
115.0	494	42	2.865	50.7	7.86	30.0	53.3
115.0	494	50	2.865	60.3	9.36	30.0	54.8
115.0	449	34.3	2.865	41.4	6.42	30.0	50.7
98.0	460	32.5	2.865	39.2	8.38	25.5	50.4
88.9	420	29.0	2.865	35.0	9.08	23.2	48.7
85.4	380	22.5	2.865	27.15	7.64	22.6	45.6
*62.9	277	13.3	2.865	16.02	8.32	16.4	38.3
*61.2	248	10.0	2.865	12.07	6.61	15.9	34.8
*61.2	248	7.5	2.865	9.05	4.96	15.9	32.3
*60.1	280	8	2.865	9.65	5.48	15.7	33.9
*60.1	280	11	2.865	13.27	7.54	15.7	36.7
*60.1	234	8.75	2.865	10.56	6.00	15.7	33.2
*60.1	271	8	2.865	9.65	5.48	15.7	33.7
*60.1	271	12	2.865	14.50	8.22	15.7	37.2
**49.4	235	5	2.865	6.03	5.07	12.9	28.3
**46.4	225	4.5	2.865	5.43	5.17	12.1	27.0
**46.4	225	3.0	2.865	3.62	3.45	12.1	23.5
**37.9	178	2.25	2.865	2.72	3.88	9.9	19.0
**29.2	147	1	2.865	1.21	2.90	7.6	10.3
**29.2	147	2.5	2.865	3.02	7.26	7.6	18.2
**23.5	111	1.1	2.865	1.33	4.93	6.1	8.7
**10.9	46	$\leq$1	2.865	1.21	<20.8	2.8	<0.2

*Uncertain entries in this row

**Very uncertain entries in this row

TABLE B-11b. AMPLIFIED IMPEDANCE HEAD OUTPUT $(F_L/2)$, UNIFORM CYLINDER C_L, CALCULATED EFFECTIVE LENGTH AND PREDICTED SOUND INTENSITY FOR THE REGULAR MULTINOTCHED CYLINDER: 3/8" SECTIONS

U (ft/sec)	$\omega/2\pi$ (Hz)	$F_L/2$ (mV)	$Rex10^3$	Uniform Cylinder $C_L x10^{-2}$	Effective Length (d)	Predicted I (db re: 20 μPa)
115	617	21	22.5	22.5	.30	49.2
98	600	15	19.1	21.0	.31	46.0
88.9	521	12.2	17.4	19.1	.34	43.0
88.9	556	11	17.4	19.1	.31	42.7
85.4	522	6.25	16.7	18.3	.20	37.2
* 62.9	368	3.5	12.3	13.8	.27	29.1
* 61.2	359	3.5	12.0	13.6	.29	28.9
* 60.1	350	3	11.7	13.3	.26	27.4
* 60.1	350	4	11.7	13.3	.35	29.9
* 49.4	332	3	9.6	11.2	.46	26.9
* 46.4	300	2	9.1	10.5	.37	22.5
* 46.4	300	4	9.1	10.5	.74	28.5
* 37.9	233	1	7.4	8.65	.34	14.3
* 37.9	233	2	7.4	8.65	.67	20.3
* 29.2	180	.6	5.7	6.85	.43	7.6
* 29.2	180	1	5.7	6.85	.72	12.0
* 23.5	149	≤1	4.6	5.6	<.77	≤10.4
**10.9	+	<1	2.1	2.7	<13.1	+

* Entries in this row are uncertain

** Extremely uncertain

+ Cannot be determined

TABLE B-12. AMPLIFIED IMPEDANCE HEAD OUTPUT ($F_L/2$),
CORRELATION PARAMETERS, LIFT COEFFICIENT
AND PREDICTED SOUND INTENSITY FOR THE
SKEWED CYLINDER AT NORMAL ($\beta = 0°$) INCIDENCE

$\overline{U}$ (ft/sec)	$\omega/2\pi$ (Hz)	$F_L/2$ (mV)	ℓ_c (d's)	$\overline{\gamma}$ (d's)	$C_L \times 10^{-2}$ -	$Re \times 10^3$ -	Predicted I (db re: 20μPa)
90.9	466	500	8.9	2.83	20.51	23.67	74.3
70.6	338	270	8.9	2.83	18.36	18.39	66.1
50.9	241	120	8.9	2.83	15.70	13.26	56.2
35.8	169	42	10.4	3.20	10.39	9.32	44.0
17.7	88	5.5	14.0	4.59	5.01	4.61	20.6
17.7	81	2	14.0	4.59	1.82	4.61	11.1

147

TABLE B-13. FORCE, CORRELATION AND FREQUENCY PARAMETERS, AND PREDICTED I FOR SKEWED CYLINDERS: $\beta = 10.9°$

$\overline{U}$ (ft/sec)	$\overline{U} \cos \beta$ (ft/sec)	$Re \times 10^3 \cdot \cos \beta$	$\omega/2\pi$ (Hz)	ω/ω_s -	$\overline{U} \cdot \omega/\omega_s$ (ft/sec)	$Re \times 10^3 \cdot \omega/\omega_s$ -
99.2	97.4	25.37	472	.991	96.3	25.11
82.3	80.8	21.05	402	1.018	79.9	21.09
70.6	69.3	18.05	333	.983	68.6	17.72
53.3	52.3	13.63	286	1.118	51.8	15.11
53.3	52.3	13.63	209	.817	51.8	11.30
42.9	42.1	10.97	172	.835	41.7	9.32
34.3	33.7	8.77	171	1.039	33.3	9.30
24.8	24.4	6.34	115	.966	24.1	6.24
17.7	17.4	4.53	90	1.059	17.2	4.79
17.7	17.4	4.53	48	.565	17.2	2.61

$\overline{U}$ (ft/sec)	$F_L/2$ (mV)	Measured ℓ_c (d's)	Measured $\overline{\gamma}$ (d's)	$C_L \times 10^{-2}$ -	Skewed Cylinder Normal Incidence ℓ_c (d's)	Skewed Cylinder Normal Incidence $\overline{\gamma}$ (d's)	$C_L \times 10^{-2}$ -	Predicted I (db re: 20μPa)
99.2	500	7.6	2.8	19.31	2.83	17.86	74.4	8.9
82.3	320	7.6	2.8	17.96	2.83	16.61	69.1	8.9
70.6	250	7.7	2.8	18.95	2.83	17.64	65.3	8.9
53.3	105	7.75	2.8	13.93	2.83	13.01	56.5	8.9
53.3	150	7.75	2.8	19.90	2.83	18.59	56.9	8.9
42.9	85	7.85	2.8	17.29	2.99	15.89	50.2	9.4
34.3	40	8.4	3.1	12.39	3.48	11.15	43.6	10.6
24.8	20	9.5	3.35	11.19	3.90	10.00	34.2	12.3
17.7	1	10.5	3.55	1.05	4.59	.94	6.0	14.0
17.7	6	10.5	3.55	6.32	4.59	5.65	15.8	14.0

148

TABLE B-14. FORCE, CORRELATION AND FREQUENCY PARAMETERS, AND PREDICTED I FOR SKEWED CYLINDERS: $\beta = 21.2°$

$\bar{U}$ (ft/sec)	$\bar{U}\cos\beta$ (ft/sec)	$Re\times10^3 \cdot\cos\beta$ —	$\omega/2\pi$ (Hz)	ω/ω_s —	$\bar{U}\cdot\omega/\omega_s$ (ft/sec)	$Re\times10^3\cdot\omega/\omega_s$ —
85.8	80.0	20.83	328	.796	76.4	17.75
61.6	57.4	14.96	259	.876	54.8	14.05
48.6	45.3	11.80	229	.982	43.3	12.41
39.6	36.9	9.62	171	.900	35.3	9.29
32.2	30.0	7.82	130	.841	28.7	7.06
32.2	30.0	7.82	130	.841	28.7	7.06
23.4	21.8	5.68	112	.997	20.8	6.07
15.4	14.4	3.74	55	.744	13.7	2.95
15.4	14.4	3.74	55	.744	13.7	2.95

		Measured			Skewed Cylinder Normal Incidence			Predicted I
$\bar{U}$ (ft/sec)	$F_L/2$ (mV)	ℓ_c (d's)	$\bar{\gamma}$ (d's)	$C_L\times10^{-2}$ —	ℓ_c (d's)	$\bar{\gamma}$ (d's)	$C_L\times10^{-2}$ —	(db re: 20µPa)
85.8	350	6.3	2.3	20.57	2.83	17.54	68.1	8.9
61.6	142	6.4	2.4	16.12	2.83	13.82	58.2	8.9
48.6	95	6.5	2.4	17.18	2.90	14.88	53.7	8.9
39.6	60	6.5	2.4	16.36	3.00	13.53	47.2	9.8
32.2	20	6.5	2.5	8.27	3.79	6.61	35.2	10.9
32.2	25	6.5	2.5	10.34	3.79	8.26	37.2	10.9
23.4	9	6.7	2.6	6.96	4.02	5.27	27.0	12.6
15.4	3.75	6.8	2.7	6.61	4.82	4.77	13.2	14.7
15.4	7.5	6.8	2.7	13.23	4.82	9.54	19.2	14.7

$\overline{U}$ (ft/sec)	$\overline{U}\cos\beta$ (ft/sec)	$Rex10^3 \cdot \cos\beta$ —	$\omega/2\pi$ (Hz)	ω/ω_s —	$\overline{U}\cdot\omega/\omega_s$ (ft/sec)	$Rex10^3 \cdot \omega/\omega_s$ —
88.0	75.9	19.76	336	.795	69.4	18.21
80.9	69.8	18.16	285	.734	63.8	15.49
68.1	58.7	15.29	255	.780	53.7	13.82
54.3	46.8	12.19	190	.729	42.8	10.30
42.8	36.9	9.61	155	.754	33.8	8.41
39.6	34.1	8.89	149	.784	31.2	8.09
39.6	34.1	8.89	149	.784	31.2	8.09
32.2	27.8	7.23	127	.822	25.4	6.89
25.7	22.2	5.77	104	.843	20.3	5.64
25.7	22.2	5.77	104	.843	20.3	5.64
17.7	15.3	3.97	73	.859	14.0	3.96
17.7	15.3	3.97	73	.859	14.0	3.96

		Measured			Skewed Cylinder Normal Incidence			Predicted I
$\overline{U}$ (ft/sec)	$F_L/2$ (mV)	ℓ_c (d's)	$\overline{\gamma}$ (d's)	$C_L x10^{-2}$ —	ℓ_c (d's)	$\overline{\gamma}$ (d's)	$C_L x10^{-2}$ —	(db re: 20μPa)
88.0	200	5.15	1.88	13.63	2.83	10.60	63.5	8.9
80.9	140	5.15	1.88	11.28	2.83	8.77	59.0	8.9
68.1	65	5.15	1.88	7.41	2.83	5.76	51.3	8.9
54.3	60	5.15	1.88	10.75	2.83	8.36	48.1	8.9
42.8	50	5.15	1.88	14.42	2.99	10.95	44.7	9.4
39.6	30	5.15	1.88	10.13	3.00	7.54	39.9	9.8
39.6	45	5.15	1.88	15.19	3.00	11.30	43.5	9.8
32.2	19	5.15	1.88	9.65	3.79	6.94	34.6	10.9
25.7	6	5.15	1.88	4.78	3.83	3.27	22.8	12.1
25.7	17	5.15	1.88	13.54	3.83	9.25	31.9	12.1
17.7	0.8	5.15	1.88	1.34	4.59	.87	2.3	14.0
17.7	1.2	5.15	1.88	2.01	4.59	1.30	5.8	14.0

TABLE B-16. FORCE, CORRELATION AND FREQUENCY PARAMETERS, AND PREDICTED I FOR SKEWED CYLINDERS: $\beta = 38.8°$

$\bar{U}$ (ft/sec)	$\bar{U} \cos \beta$ (ft/sec)	$Rex10^3 \cdot \cos \beta$ –	$\omega/2\pi$ (Hz)	ω/ω_s –	$\bar{U} \cdot \omega/\omega_s$ (ft/sec)	$Rex10^3 \cdot \omega/\omega_s$ –
92.4	72.1	18.77	288	.649	57.7	15.61
85.1	66.4	17.28	261	.639	53.1	14.13
85.1	66.4	17.28	261	.639	53.1	14.13
79.6	62.1	16.17	259	.678	49.7	14.02
79.6	62.1	16.17	259	.678	49.7	14.02
62.2	48.5	12.63	189	.633	38.8	10.25
62.2	48.5	12.63	189	.633	38.8	10.25
52.8	41.2	10.72	158	.623	32.9	8.56
52.8	41.2	10.72	158	.623	32.9	8.56
34.7	27.1	7.05	91	.546	21.7	4.94
34.7	27.1	7.05	91	.546	21.7	4.94
22.3	17.4	4.53	63	.589	13.9	2.67
22.3	17.4	4.53	63	.589	13.9	2.67
15.4	12.0	3.13	47	.636	9.6	2.54

$\bar{U}$ (ft/sec)	Measured				Skewed Cylinder Normal Incidence			Predicted I
	$F_L/2$ (mV)	ℓ_c (d's)	$\bar{\gamma}$ (d's)	$C_L x10^{-2}$ –	ℓ_c (d's)	$\bar{\gamma}$ (d's)	$C_L x10^{-2}$ –	(db re: 20μPa)
92.4	115	4.9	1.76	8.88	2.83	6.75	57.3	8.9
85.1	100	4.9	1.76	9.10	2.83	6.92	55.3	8.9
85.1	140	4.9	1.76	12.74	2.83	9.69	58.2	8.9
79.6	75	4.9	1.76	7.81	2.83	5.94	52.7	8.9
79.6	110	4.9	1.76	11.45	2.83	8.71	56.0	8.9
62.2	40	4.9	1.76	6.83	2.83	5.19	44.5	8.9
62.2	80	4.9	1.76	13.65	2.83	10.38	50.5	8.9
52.8	35	4.9	1.76	8.28	2.83	6.29	41.8	8.9
52.8	50	4.9	1.76	11.82	2.83	8.99	44.9	8.9
34.7	10	4.9	1.76	5.47	3.45	3.87	26.1	10.6
34.7	20	4.9	1.76	10.93	3.45	7.73	32.1	10.6
22.3	4.4	4.9	1.76	5.83	4.14	3.82	15.8	12.8
22.3	8.8	4.9	1.76	11.67	4.14	7.64	21.8	12.8
15.4	<4	4.9	1.76	<11.15	4.82	<6.93	<12.4	14.7

TABLE B-17. FORCE, CORRELATION AND FREQUENCY PARAMETERS, AND PREDICTED I FOR SKEWED CYLINDERS: $\beta = 45°$

$\bar{U}$ (ft/sec)	$\bar{U} \cos\beta$ (ft/sec)	$Re \times 10^3 \cdot \cos\beta$	$\omega/2\pi$ (Hz)	ω/ω_s -	$\bar{U} \cdot \omega/\omega_s$ (ft/sec)	$Re \times 10^3 \cdot \omega/\omega_s$ —
100.0	70.7	18.41	320	.667	59.4	17.36
92.4	65.3	17.01	264	.595	54.9	14.31
92.4	65.3	17.01	264	.595	54.9	14.31
71.4	50.5	13.15	214	.624	42.4	11.59
71.4	50.5	13.15	214	.624	42.4	11.59
61.6	43.6	11.34	173	.585	36.6	9.39
61.6	43.6	11.34	173	.585	36.6	9.39
51.8	36.6	9.54	138	.555	30.8	7.48
51.8	36.6	9.54	138	.555	30.8	7.48
36.2	25.6	6.67	102	.587	21.5	5.54
36.2	25.6	6.67	102	.587	21.5	5.54
22.8	16.1	4.20	60	.548	13.5	3.26
22.8	16.1	4.20	60	.548	13.5	3.26
16.3	11.5	3.00	40	.511	9.7	2.29

	Measured				Skewed Cylinder Normal Incidence			Predicted I
$\bar{U}$ (ft/sec)	$F_L/2$ (mV)	ℓ_c (d's)	$\bar{\gamma}$ (d's)	$C_L \times 10^{-2}$ -	ℓ_c (d's)	$\bar{\gamma}$ (d's)	$C_L \times 10^{-2}$ -	(db re: 20μPa)
100.0	70	3.4	1.38	6.17	2.83	3.92	53.9	8.9
92.4	60	3.6	1.41	6.03	2.83	3.94	50.9	8.9
92.4	90	3.6	1.41	9.04	2.83	5.91	54.5	8.9
71.4	40	3.9	1.82	6.50	2.83	4.39	45.6	8.9
71.4	45	3.9	1.82	7.32	2.83	4.94	46.6	8.9
61.6	25	3.9	1.82	5.45	2.83	3.68	39.7	8.9
61.6	30	3.9	1.82	6.54	2.83	4.42	41.2	8.9
51.8	10	3.9	1.82	3.10	2.83	2.09	29.7	8.9
51.8	15	3.9	1.82	4.64	2.83	3.13	33.3	8.9
36.2	4	3.9	1.82	2.53	3.19	1.60	19.2	10.3
36.2	8	3.9	1.82	5.06	3.19	3.20	25.2	10.3
22.8	3	3.9	1.82	4.80	4.05	2.78	12.0	12.7
22.8	6	3.9	1.82	9.60	4.05	5.56	18.1	12.7
16.3	<3	3.9	1.82	<9.41	4.73	<5.19	<8.5	14.4

TABLE B-18.   MEASURED SOUND INTENSITY FOR THE
                UNIFORM 1/2" CYLINDER

U (ft/sec)	$\omega/2\pi$ (Hz)	Recorded I (db)	Microphone Sensitivity (db re: $1V/10^5$ μPa)	I Radiated from Cylinder (db re: 20μPa)
102.3	463	−31.0	−75.1	78.1
88.9	396	−41.0	−75.3	68.3
80.3	367	−39.3	−75.4	70.1
51.5	247	−48.5	−75.8	61.3
44.7	209	−61.5	−75.9	48.4
33.7	167	−70.4	−76.9	40.5
21.4	120	−76.0	−78.5	36.5
19.0	104	−92.4	−79.1	20.7
16.1	80*	<−90	−80.6*	<24.6*

*Uncertain

TABLE B-19. MEASURED SOUND INTENSITY FOR THE 1/4" CYLINDER

U (ft/sec)	$\omega/2\pi$ (Hz)	Recorded I (db)	Microphone Sensitivity (db re: $1V/10^5 \mu Pa$)	I Radiated from Cylinder (db re: 20 μPa)
94.1	956	−42.0	−74.4	66.4
88.9	867	−42.0	−74.6	66.6
80.3	787	−48.3	−74.7	60.4
75.7	761	−51.0	−74.7	57.7
63.8	640	−55.0	−74.9	53.9
48.9	501	−66.5	−75.1	42.6
31.1	307	−68.0*	−75.7	41.7*
21.8	212*	<−91*	−75.9*	<18.9
15.5	144*	<−87*	−77.6*	<24.6*
11.7	104*	<−96*	−79.1*	<17.1*
9.2	92*	<−91*	−79.6*	<22.6*

*Uncertain

TABLE B-20. MEASURED SOUND INTENSITY FOR THE 1" CYLINDER

U (ft/sec)	$\omega/2\pi$ (Hz)	Recorded I (db)	Microphone Sensitivity (db re: $1V/10^5 \mu Pa$)	I Radiated from Cylinder (db re: 20 μPa)
91.5	249	-34.0	-75.9	75.9
84.0	219	-39.0	-76.0	71.0
66.9	181	-46.0	-76.6	64.6
57.9	150	-52.5	-77.3	59.2
33.0	87	-72.0	-80.0	42.0
21.4	55	<-76*	-84.7	<42.7*
13.3	32*	<-83*	-93.0*	<44*

*Uncertain

155

TABLE B-21.   MEASURED SOUND INTENSITY FOR THE
ROUGHENED 1/2" CYLINDER

U (ft/sec)	ω/2π (Hz)	Recorded I (db)	Microphone Sensitivity (db re: 1V/10⁵ μPa)	I Radiated from Cylinder (db re: 20 μPa)
90.2	435	-36.7	-75.2	72.9
79.2	384	-44.0	-75.4	65.4
57.9	249	-50.8	-75.8	59.0
45.9	184	-62.8	-76.6	47.8
28.0	120	-76.0	-78.5	36.5
14.2	94	<-80*	-79.7	<33.7*

*Uncertain

TABLE B-22. MEASURED SOUND INTENSITY FOR THE
FINNED CYLINDER WITH NO FINS ATTACHED

U (ft/sec)	$\omega/2\pi$ (Hz)	Recorded I (db)	Microphone Sensitivity (db re: 1V/10⁵ μPa)	I Radiated from Cylinder (db re: 20 μPa)
88.9	428	-35.6	-75.2	73.8
74.5	377	-40.6	-75.3	68.7
50.2	247	-49.2	-75.9	60.7
34.3	182	-64.0	-76.6	46.6
21.4	123	-74.0	-78.4	38.4
9.2	46*	<-91*	-87.2*	<30.2*

*Uncertain

TABLE B-23. MEASURED SOUND INTENSITY FOR THE CYLINDER WITH 2 FINS

U (ft/sec)	$\omega/2\pi$ (Hz)	Recorded I (db)	Microphone Sensitivity (db re: 1V/10⁵ µPa)	I Radiated from Cylinder (db re: 20 µPa)
88.9	421	-34.1	-75.3	75.2
79.2	361	-39.0	-75.4	70.4
49.7	237	-51.0	-75.9	58.9
37.5	187	-61.9	-76.3	48.4
21.6	126	-77.0	-78.3	35.3
10.1	52	<-86*	-85.1	<33.1*

*Uncertain

TABLE B-24. MEASURED SOUND INTENSITY FOR THE CYLINDER WITH FOUR FINS

U (ft/sec)	$\omega/2\pi$ (Hz)	Recorded I (db)	Microphone Sensitivity (db re: $1V/10^5 \mu Pa$)	I Radiated from Cylinder (db re: $20 \mu Pa$)
90.2	418	-33.0	-75.3	76.3
81.5	363	-35.5	-75.4	73.9
53.2	244	-47.8	-75.8	62.0
37.1	179	-61.1	-76.6	49.5
28.3	133	-71.0	-78.0	41.0
16.1	81	<-90*	-80.4	$\leq$21.4*

*Uncertain

159

TABLE B-25. MEASURED SOUND INTENSITY FOR THE
1/2" CYLINDER WITH SMALL SPLITTER PLATE

U (ft/sec)	$\omega/2\pi$ (Hz)	Recorded I (db)	Microphone Sensitivity (db re: $1V/10^5$ μPa)	I Radiated from Cylinder (db re: 20 μPa)
102.3	363	-56	-75.3	53.3
91.5	322	-58	-75.6	51.6
88.9	292	-61	-75.7	48.7
86.4	280	-62	-75.7	47.7
68.0	232	-70	-75.9	39.9
50.6	179*	-73*	-76.7*	37.7*
43.1	135*	-78*	-77.9*	33.9*
26.2	86*	-89*	-80.1*	25.1*

*Uncertain

TABLE B-26. MEASURED SOUND INTENSITY FOR THE 1/2" CYLINDER WITH LARGE SPLITTER PLATE

U (ft/sec)	ω/2π (Hz)	Recorded I (db)	Microphone Sensitivity (db re: 1V/10^5 µPa)	I Radiated from Cylinder (db re: 20 µPa)
103.7	226	-62	-75.9	47.9
103.7	252	-62	-75.8	47.8
91.5	195	-64	-76.2	46.2
87.7	185	-67	-76.4	43.4
68.0	167	-72	-77.0	39.0
55.1	116	-78	-78.7	34.7
43.1	90	-86.5*	-79.9	27.4*

*Uncertain

TABLE B-27.   MEASURED SOUND INTENSITY FOR THE TWO-NOTCHED CYLINDER

U (ft/sec)	$\omega/2\pi$ (Hz)	Recorded I (db)	Microphone Sensitivity (db re: $1V/10^5$ μPa)	I Radiated from Cylinder (db re: 20 μPa)
(a) 1/2" SECTIONS				
90.2	441	−41.0	−75.3	68.3
74.5	373	−49.0	−75.5	60.5
43.1	246	−65.0	−75.9	44.9
20.7	90	−85.0*	−79.9	28.9*
(b) 3/8" SECTIONS				
90.2	597	−37.5	−75.0	71.5
74.5	507	−45.0	−75.1	64.1
43.1	330*	−66.0*	−75.6*	43.6*
20.7	130	<−92.0*	−77.6	<19.6*

*Uncertain

162

TABLE B-28.   MEASURED SOUND INTENSITY FOR THE
REGULAR MULTINOTCHED CYLINDER

$\bar{U}$ (ft/sec)	$\omega/2\pi$ (Hz)	Recorded I (db)	Microphone Sensitivity (db re: $1V/10^5 \mu Pa$)	I Radiated from Cylinder (db re: $20\mu Pa$)
(a) 1/2" SECTIONS				
99.5	484	-58.5	-75.1	50.6
91.5	437	-62.0	-75.2	47.2
85.2	384	-65.0	-75.3	44.3
(b) 3/8" SECTIONS				
99.5	600	-63	-75.0	46.0
91.5	549	-66	-75.0	43.0
85.2	528	<-71	-75.1	<38.1

TABLE B-29. MEASURED SOUND INTENSITY FOR THE
IRREGULAR MULTINOTCHED CYLINDER

Ū (ft/sec)	ω/2π (Hz)	Recorded I (db)	Microphone Sensitivity (db re: 1V/10⁵ µPa)	I Radiated from Cylinder (db re: 20 µPa)
(a) 1/2" SECTIONS				
90.8	484	-56	-75.1	53.1
87.1	439	-58	-75.2	51.2
74.5	385	-61	-75.3	48.3
57.9	241	-73	-75.9	36.9
(b) 3/8" SECTIONS				
90.8	633	-54	-74.9	54.9
87.1	575	-60	-75.0	49.0
74.5	498	-62	-75.1	47.1
57.9	325	-74	-75.6	35.6

TABLE B-30. MEASURED SOUND INTENSITY FOR THE
SKEWED CYLINDER AT NORMAL INCIDENCE ($\beta = 0°$)

$\bar{U}$ (ft/sec)	$\omega/2\pi$ (Hz)	Recorded I (db)	Microphone Sensitivity (db re: $1V/10^5$ μPa)	I Radiated from Cylinder (db re: 20 μPa)
95.5	464	-42	-75.1	67.1
87.7	401	-45	-75.3	64.3
80.9	360	-49	-75.4	60.4
50.2	243	-59	-75.8	50.8
25.1	124	-81*	-78.4	31.4*
10.4	47*	<-88*	-86.8*	<32.8*

*Uncertain

TABLE B-31.   MEASURED SOUND INTENSITY FOR THE SKEWED
              CYLINDER: $L_\perp$ = 9 7/16"; β = 9.8°

$\overline{U}$ (ft/sec)	$\omega/2\pi$ (Hz)	Recorded I (db)	Microphone Sensitivity (db re: $1V/10^5 \mu Pa$)	I Radiated from Cylinder (db re: 20 µPa)	$\overline{U} \cos \beta$ (ft/sec)	$\overline{U} \cdot (\omega/\omega_g)$ (ft/sec)
88.9	393	-38.0	-75.3	71.3	87.6	88.1
76.3	347	-41.0	-75.5	68.5	75.2	75.6
44.7	224	-59.0	-75.9	50.9	44.0	44.3
34.0	163	-66.7	-76.9	44.2	33.5	33.7
21.4	107	-83.0*	-79.0	30.0*	21.0	21.1
11.9	47*	<-87.0*	-86.8*	<33.8*	11.7	11.7

* Uncertain

TABLE B-32. MEASURED SOUND INTENSITY FOR THE SKEWED CYLINDER: $L_\perp$ = 9 9/16"; β = 22.1°

U (ft/sec)	$\omega/2\pi$ (Hz)	Recorded I (db)	Microphone Sensitivity (db re: 1V/10⁵µPa)	I Radiated from Cylinder (db re: 20 µPa)	$U \cos\beta$ (ft/sec)	$\bar{U} \cdot (\omega/\omega_s)$ (ft/sec)
86.4	370	−40.5	−75.4	68.9	80.1	77.3
70.1	319	−46	−75.6	63.6	65.0	62.7
47.2	201	−56	−76.1	54.1	43.7	42.2
34.3	148	−68	−77.5	43.5	31.8	30.7
25.1	102	−79*	−79.3	34.3*	23.3	22.5
11.5	48	<−87*	−86.4	<33.4*	10.7	10.3

*Uncertain

167

TABLE B-33. MEASURED SOUND INTENSITY FOR THE SKEWED
CYLINDER: $L_\perp = 9\ 3/8"$; $\beta = 32.6°$

$\bar{U}$ (ft/sec)	$\omega/2\pi$ (Hz)	Recorded I (db)	Microphone Sensitivity (db re: $1V/10^5\ \mu Pa$)	I Radiated from Cylinder (db re: 20 μPa)	$\bar{U} \cos \beta$ (ft/sec)	$\bar{U} \cdot (\omega/\omega_g)$ (ft/sec)
91.5	373	−46.5	−75.4	62.9	77.1	75.3
87.1	322	−48.0	−75.5	61.5	73.4	71.7
71.3	290	−52.5	−75.5	57.2	60.5	59.1
48.9	188	−65	−76.3	45.3	41.2	40.2
34.7	142	−74*	−77.7	37.7*	29.2	28.6
22.2	78	<−89*	−80.7	<25.7*	18.7	18.3

*Uncertain

168

TABLE B-34. MEASURED SOUND INTENSITY FOR THE SKEWED
CYLINDER: $L_\perp$ = 9 3/8"; β = 39.6°

$\bar{U}$ (ft/sec)	$\omega/2\pi$ (Hz)	Recorded I (db)	Microphone Sensitivity (db re: 1V/10^{5}µPa)	I Radiated from Cylinder (db re: 20µPa)	$\bar{U}\cos\beta$ (ft/sec)	$\bar{U}\cdot(\omega/\omega_g)$ (ft/sec)
93.5	305	−51	−75.6	58.6	72.1	63.8
85.2	264*	−55	−75.8*	54.8*	65.7	58.1
74.5	263*	−57	−75.8*	52.8*	57.4	39.2
49.7	162*	−71	−76.9*	39.9*	38.3	33.9
37.1	119*	−76*	−78.5*	36.5*	28.6	25.3
21.8	81*	<−89*	−80.4*	<25.4*	16.8	14.9

*Uncertain

169

TABLE B-35. MEASURED SOUND INTENSITY FOR THE SKEWED CYLINDER: $L_\perp$ = 9 3/4"; β = 45°

U (ft/sec)	$\omega/2\pi$ (Hz)	Recorded I (db)	Microphone Sensitivity (db re: 1v/(10⁵ µPa)	I Radiated from Cylinder (db re: 20µPa)	$\bar{U} \cos \beta$ (ft/sec)	$\bar{U} \cdot (\omega/\omega_s)$ (ft/sec)
92.2	282	−56	−75.7	53.7	65.2	59.8
81.5	261	−59.5	−75.8	50.3	57.6	52.9
78.0	246	−62	−75.8	47.8	55.2	50.6
49.7	150	−74*	−77.6	37.6*	35.1	32.3
48.9	154	−73*	−77.2	38.2*	34.6	31.7
34.3	107*	<−82*	−79.0	<31.0*	24.3	22.3
21.8	75*	<−90*	−81.0	<25*	15.4	14.1

*Uncertain

TABLE B-36. COMPARISON OF ω/ω_s WITH $\cos \beta$ FOR SKEWED
CYLINDERS

β (degrees)	$\cos \beta$	ω/ω_s*	$(\omega/\omega_s)/\cos \beta$
9.8	.985	.991	1.006
10.9	.982	.971	.989
10.9	.982	.967	.985
21.2	.932	.890	.955
21.2	.932	.884	.948
22.1	.927	.895	.965
30.4	.863	.789	.914
30.4	.863	.734	.851
32.6	.842	.823	.977
38.8	.779	.624	.801
38.8	.779	.623	.800
39.6	.771	.682	.885
45.0	.707	.649	.918
45.0	.707	.594	.840
45.0	.707	.582	.823

*Average ω/ω_s for all recorded data in a set.

TABLE B-37. ESTIMATION OF C_L FROM MEASURED I FOR THE
IRREGULAR MULTINOTCHED CYLINDER

U (ft/sec)	Rex10^3 —	Measured I (db re: 20 μPa)	ω/2π (Hz)	Correlation Factor(1) (d^2)	Correlation Factor (2) (d^2)	C_Lx10^{-2} from C.F.(1)	C_Lx10^{-2} from C.F.(2)
(a) 1/2" SECTIONS							
90.8	23.11	53.1	484	5.07	3.30	12.37	15.95
87.1	22.68	51.2	439	5.07	3.30	11.76	15.00
74.5	19.40	48.3	385	5.07	3.30	13.74	16.87
57.9	15.08	36.9	241	5.07	3.30	8.15	11.26
(b) 3/8" SECTIONS							
90.8	17.73	54.9	633	6.76	4.47	13.73	16.88
87.1	17.01	49.0	575	6.76	4.47	8.35	10.27
74.5	14.55	47.1	498	6.76	4.47	10.58	13.02
57.9	11.31	35.6	325	6.76	4.47	7.09	8.72

172
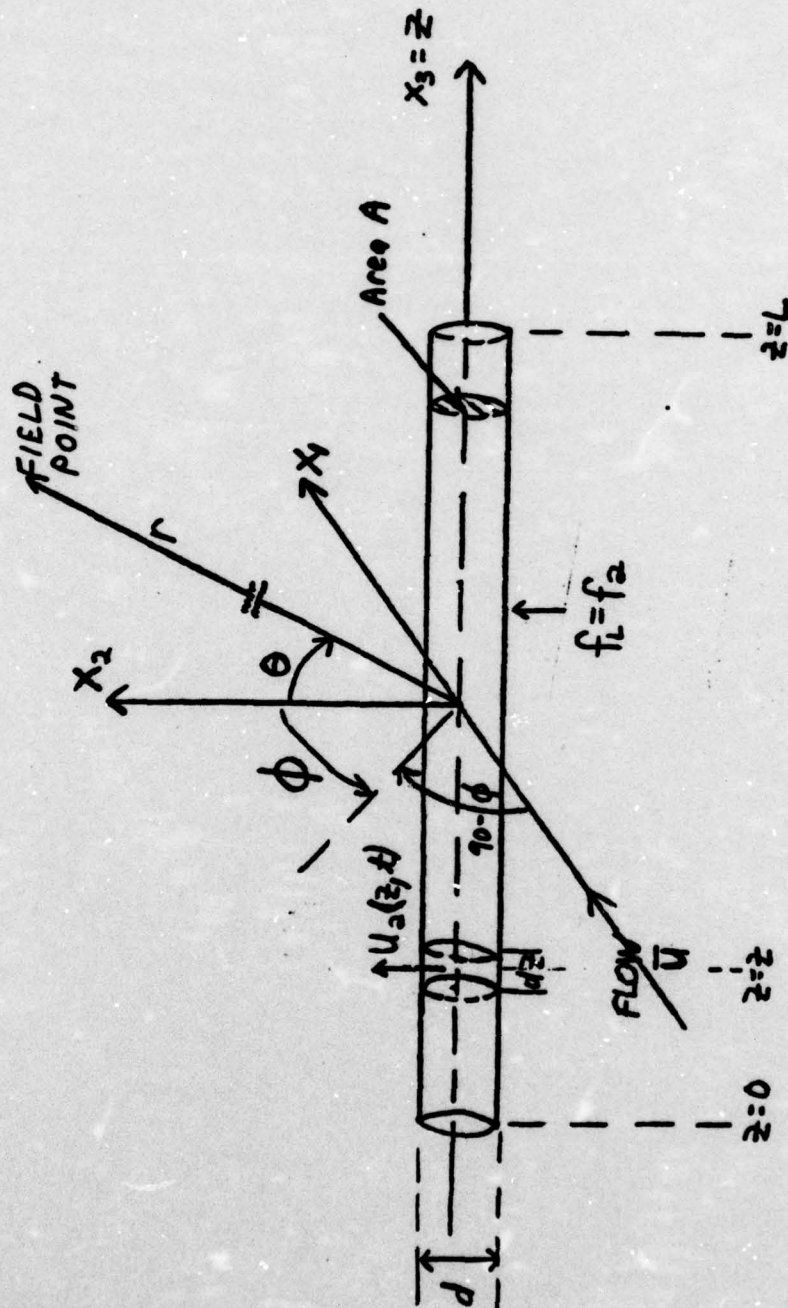
FIGURE C-1. CYLINDER COORDINATES
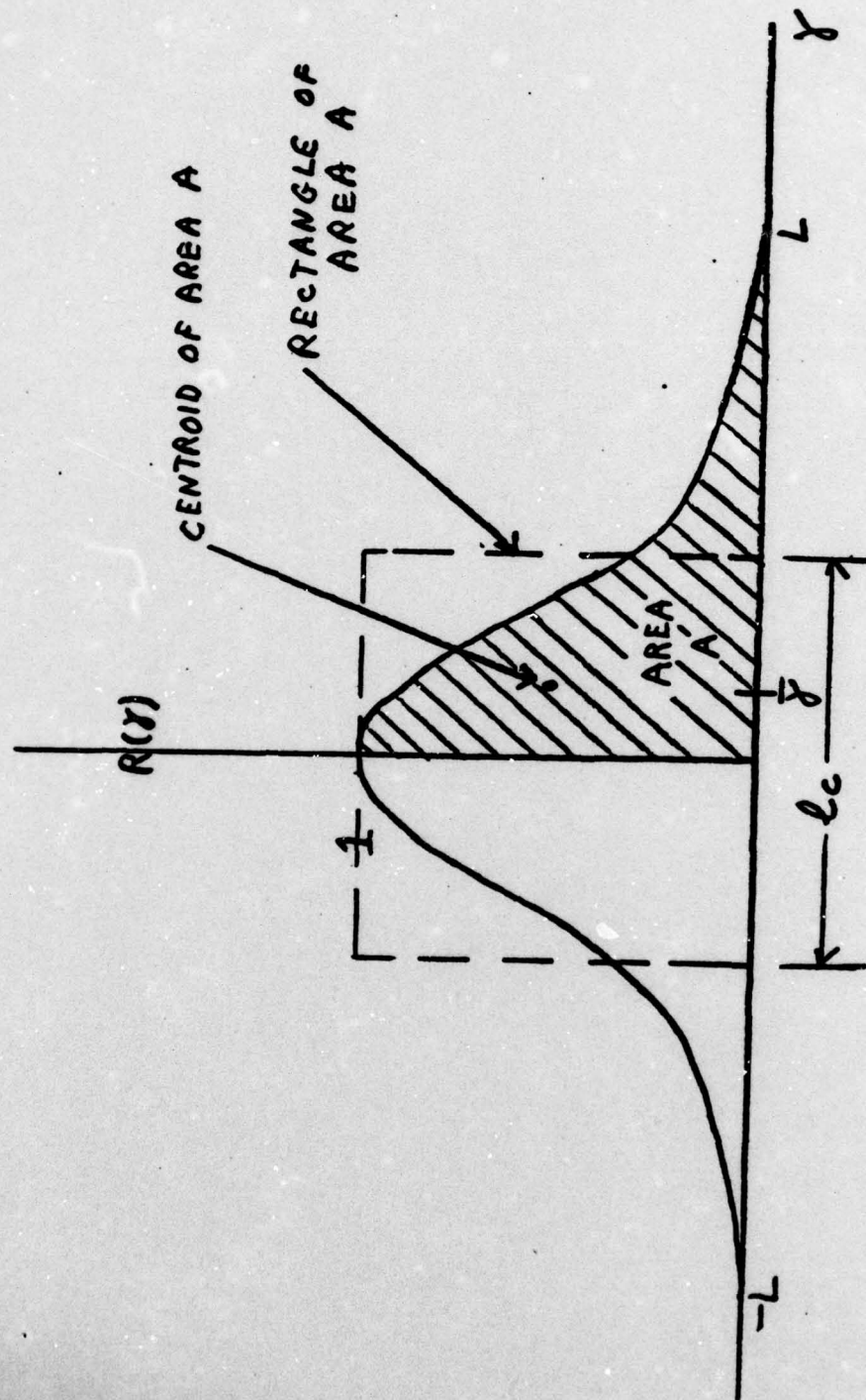
FIGURE C-2. CORRELATION FUNCTION
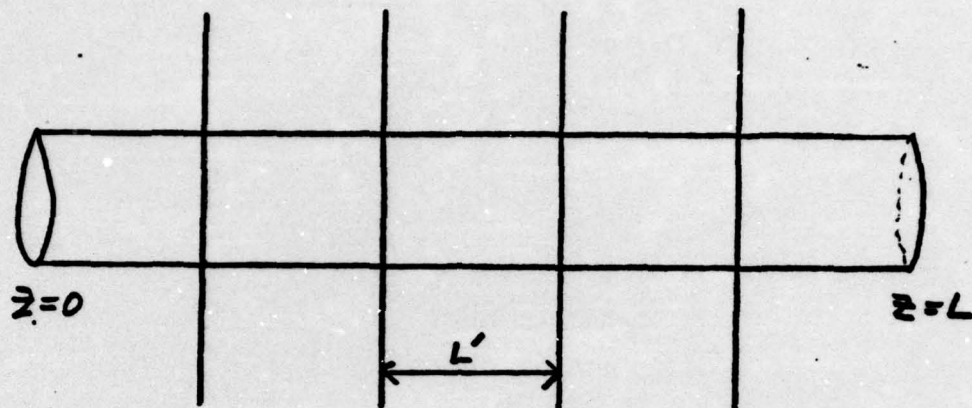
z_1, z_2 locations

γ in $(0, 2L')$
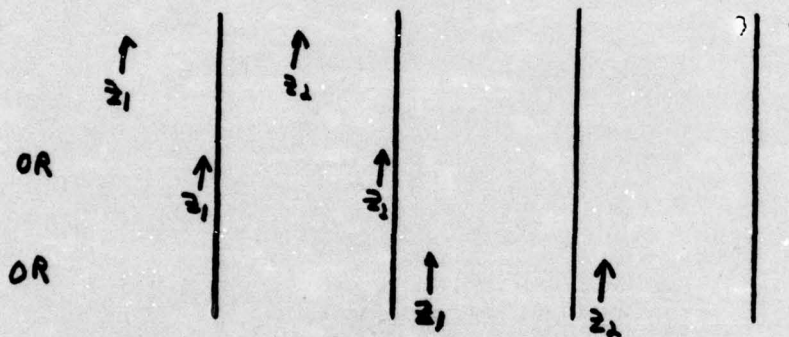
γ in $(L', 3L')$
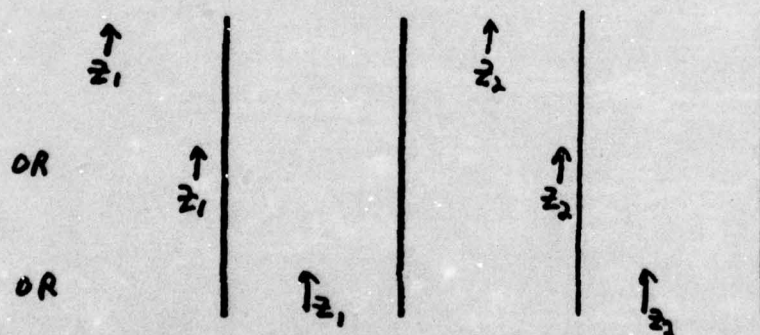
FIGURE C-3. PERIODICALLY DIVIDED CYLINDER
$M = 4$, $L' = L/5$

175
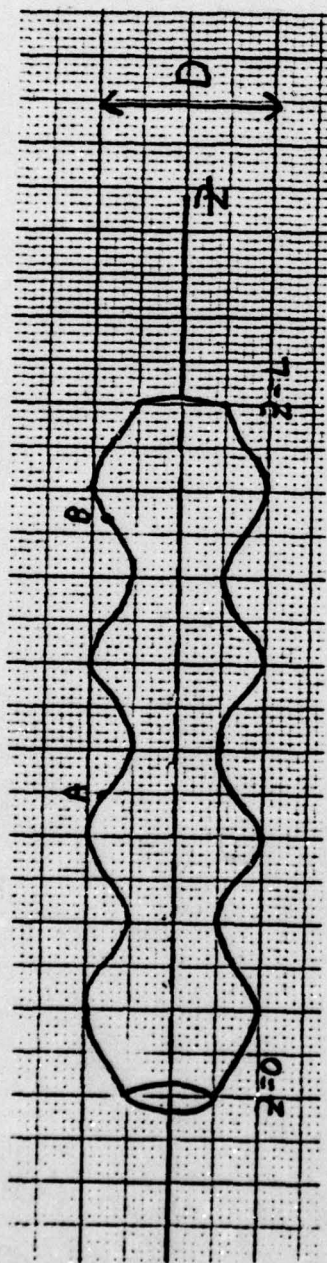
(a) ACTUAL
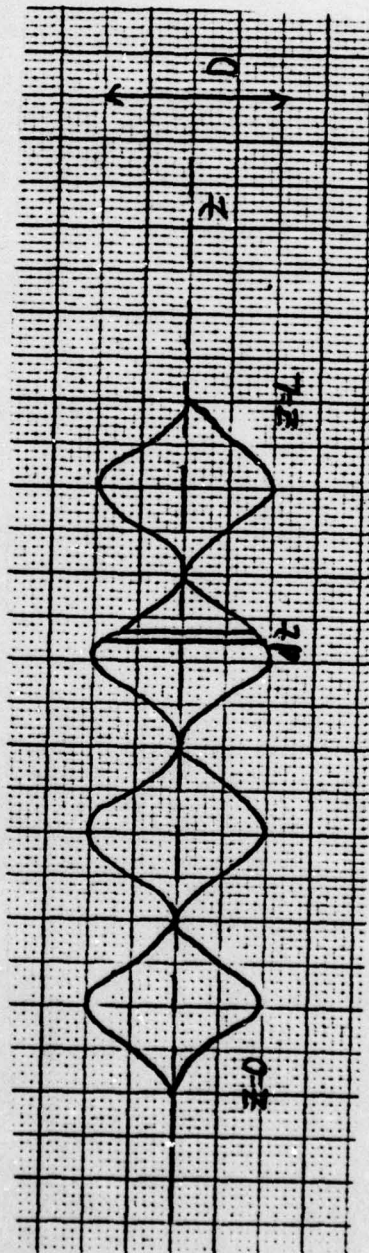
(b) IDEALIZED

FIGURE C-4. SINUSOIDAL CYLINDERS

176
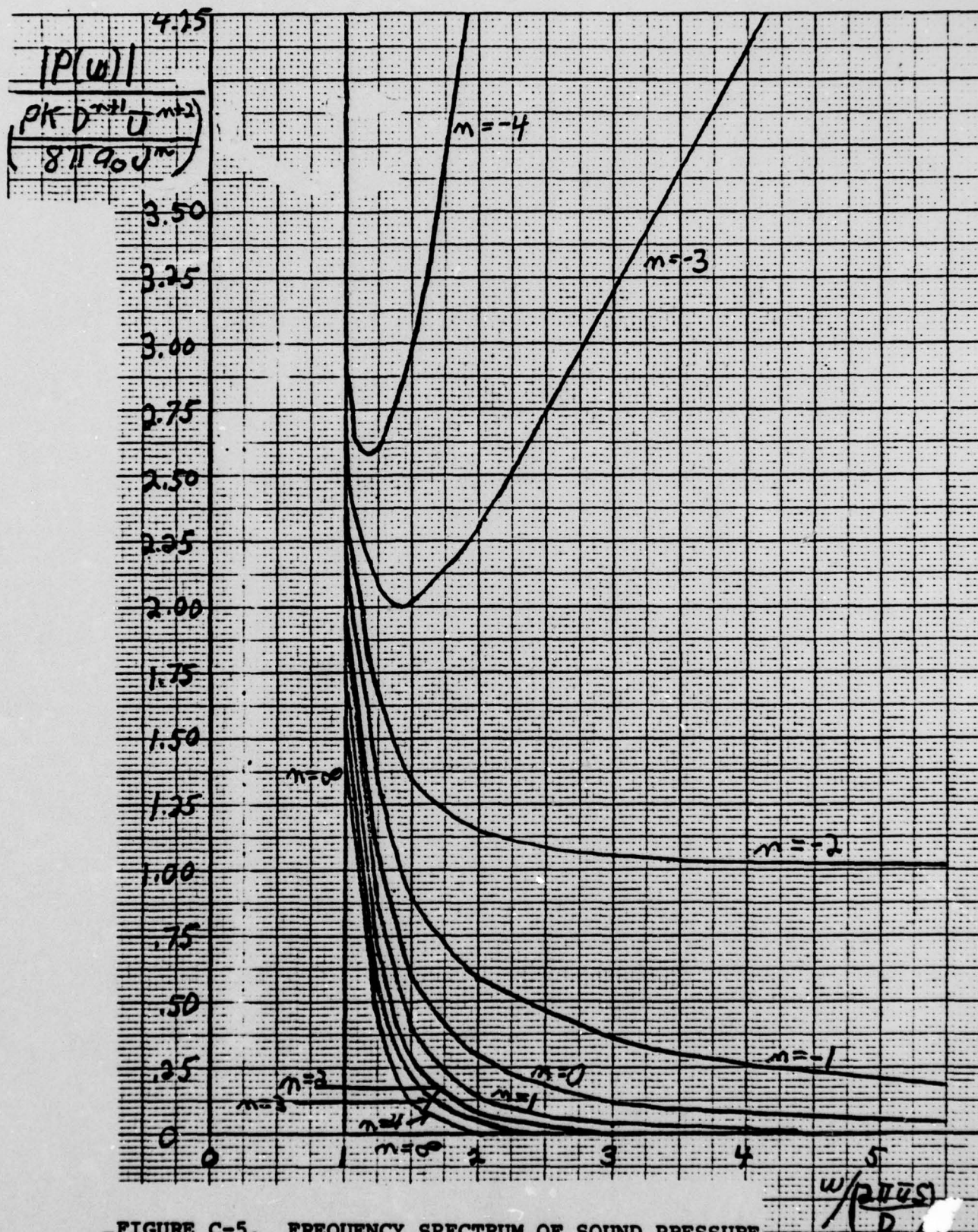
FIGURE C-5. FREQUENCY SPECTRUM OF SOUND PRESSURE RADIATED FROM IDEALIZED SINUSOIDAL CYLINDER
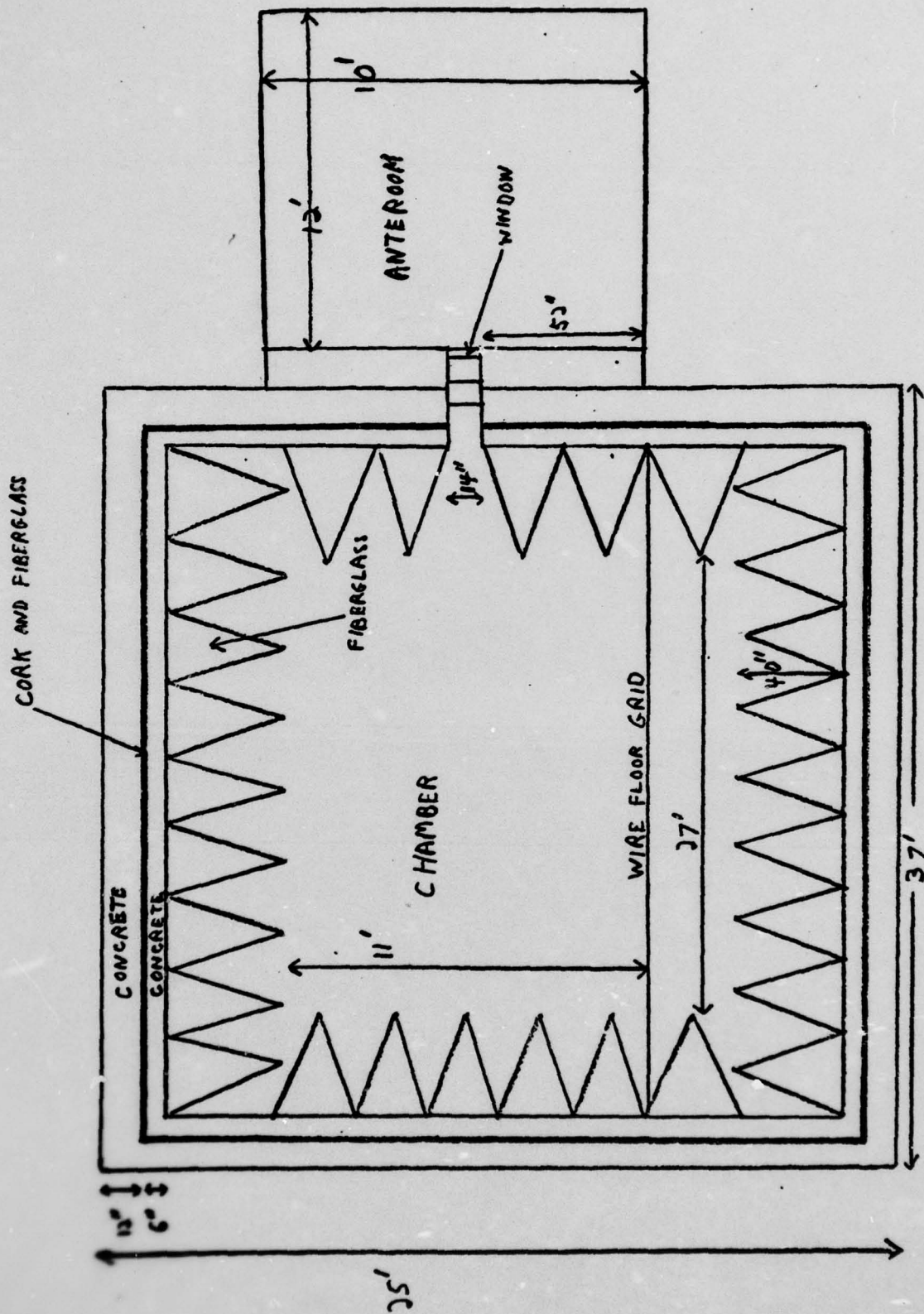
FIGURE C-6. ANECHOIC CHAMBER: SIDE VIEW

178
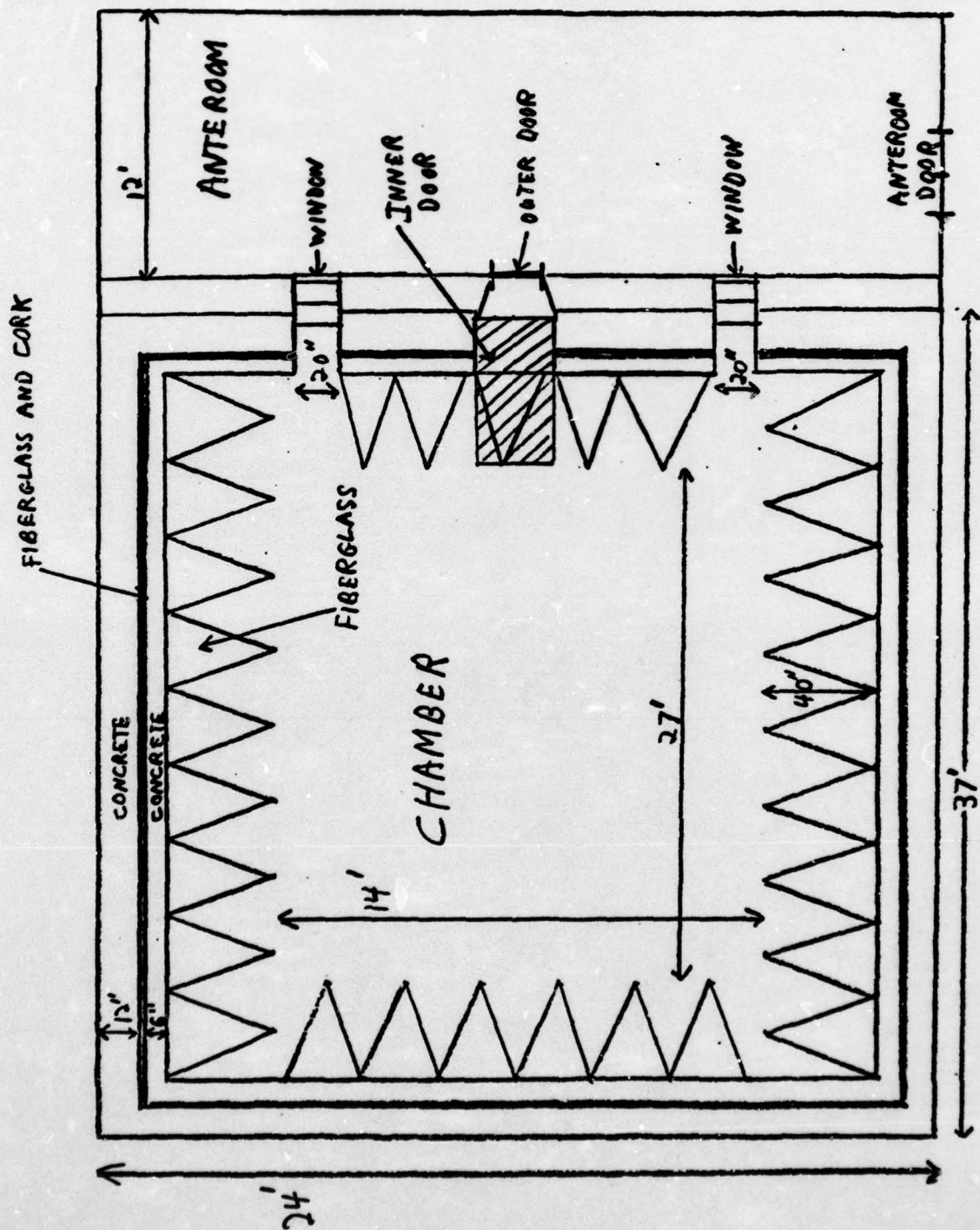
FIGURE C-7. ANECHOIC CHAMBER: TOP VIEW

179
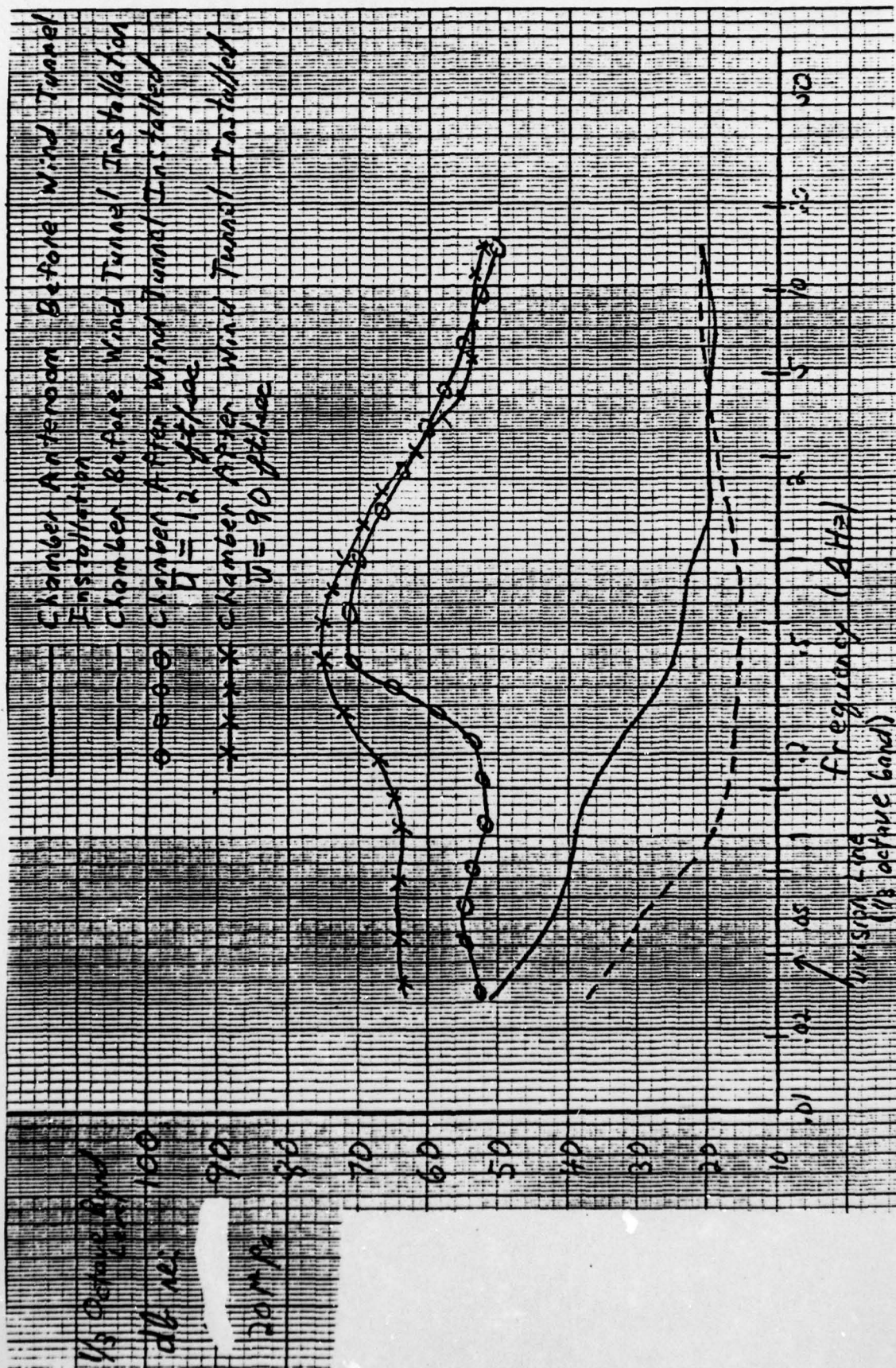
FIGURE C-8. ANECHOIC CHAMBER BACKGROUND NOISE IN 1/3 OCTAVE BAND LEVELS AS READ ON A SOUND LEVEL METER

180
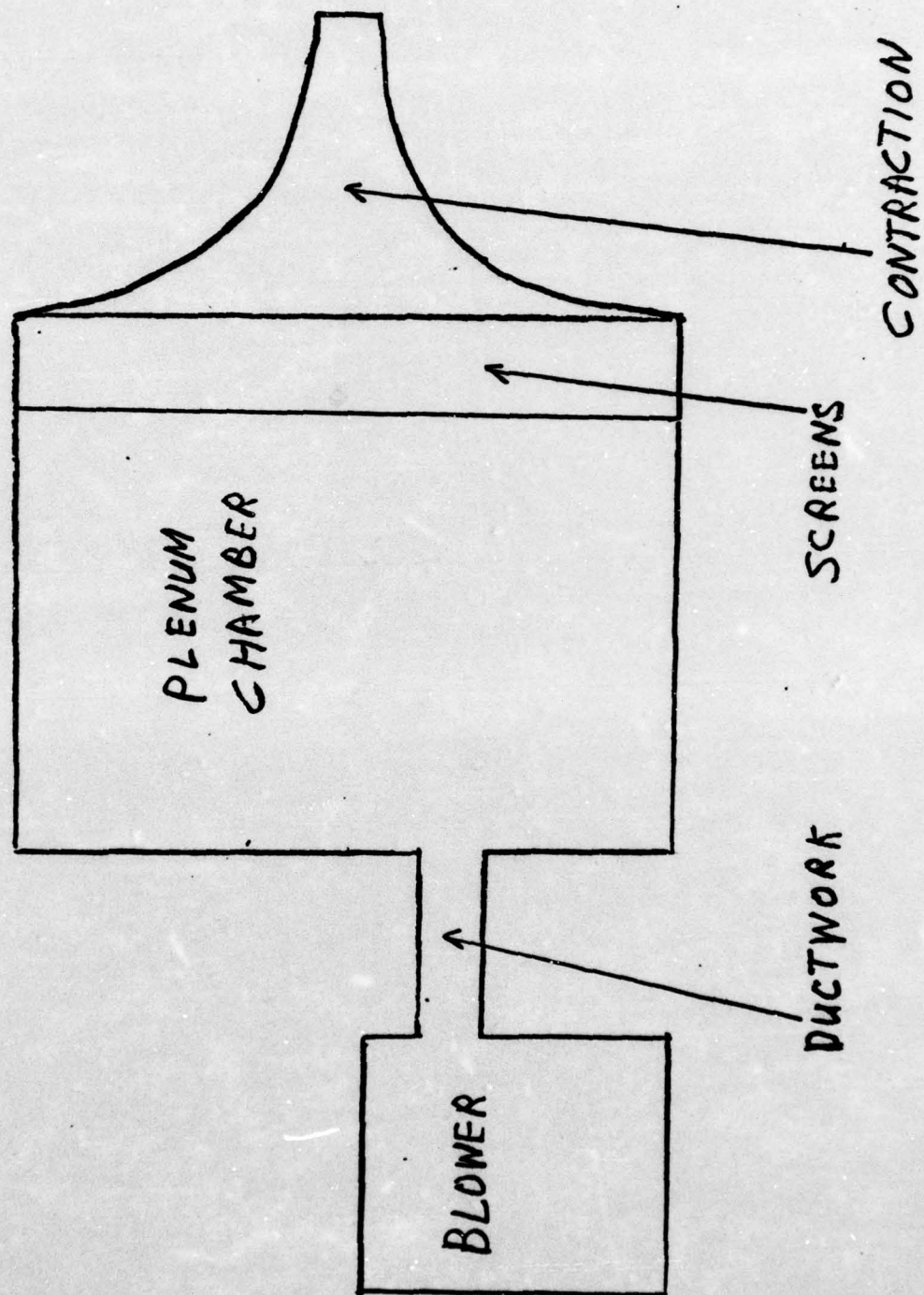
FIGURE C-9. WIND TUNNEL SCHEMATIC
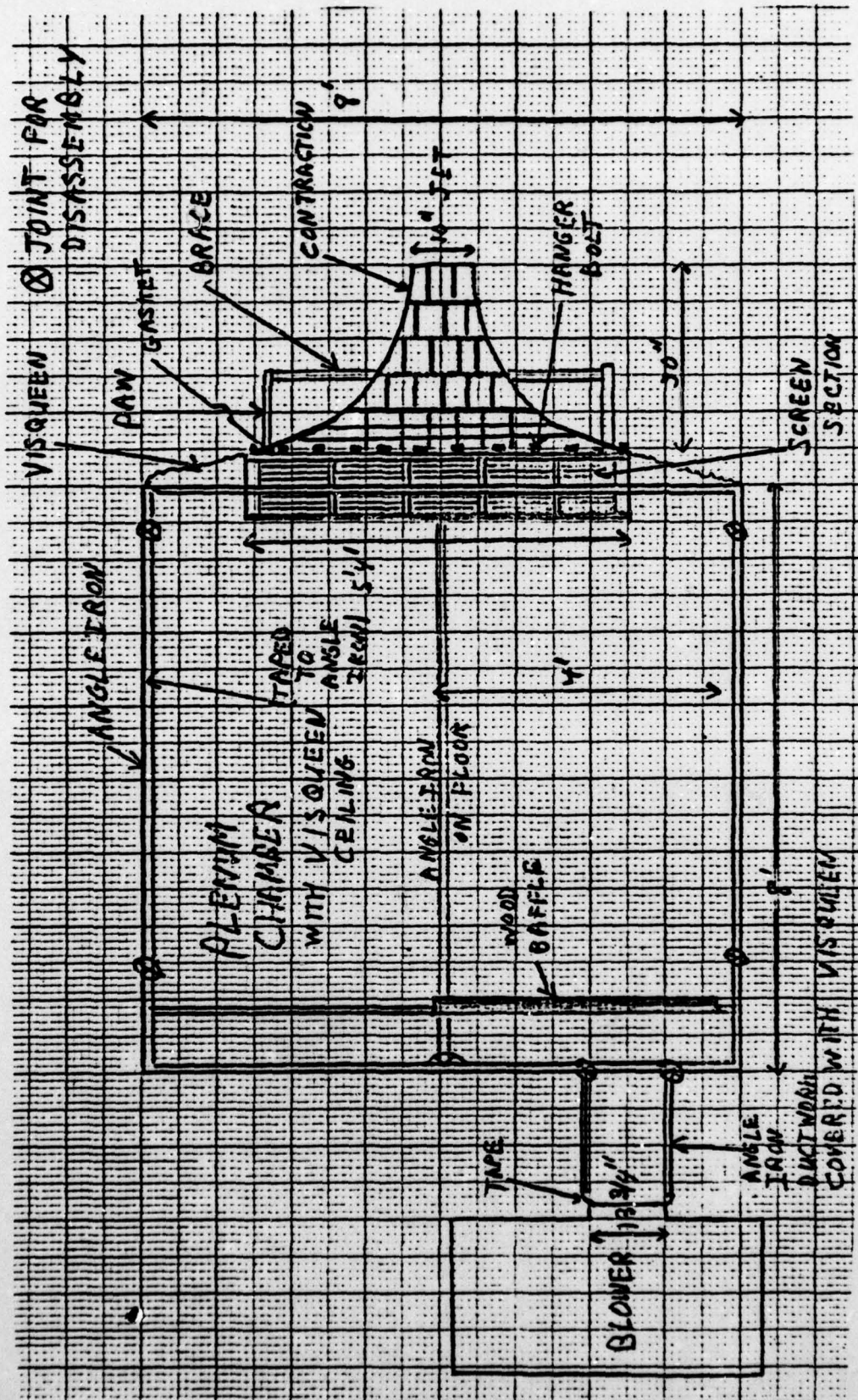
FIGURE C-10. WIND TUNNEL: TOP VIEW
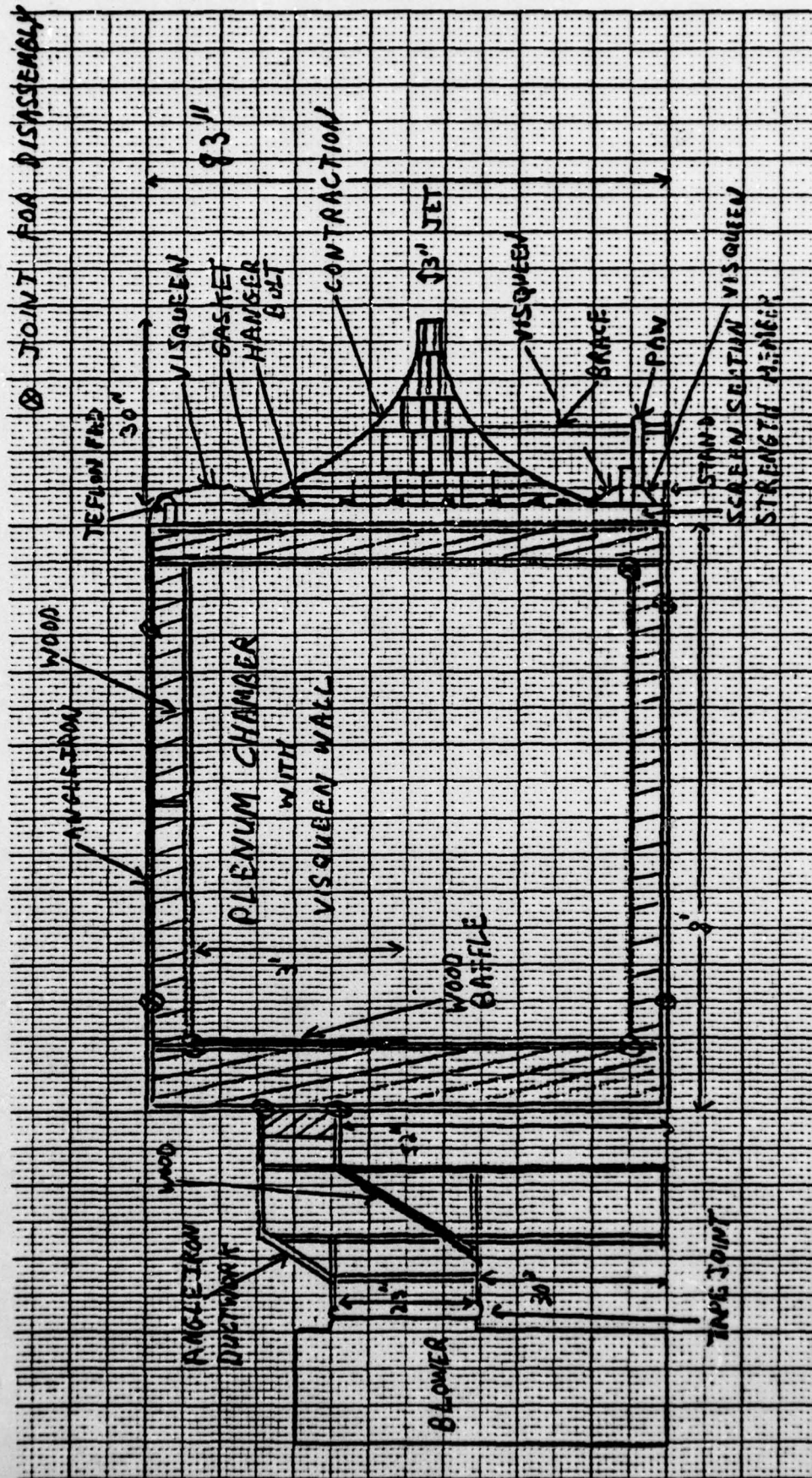
FIGURE C-11. WIND TUNNEL: SIDE VIEW

FIGURE C-12. SCREEN SECTION: SIDE VIEW

184
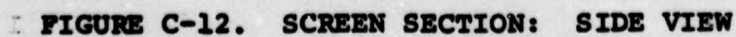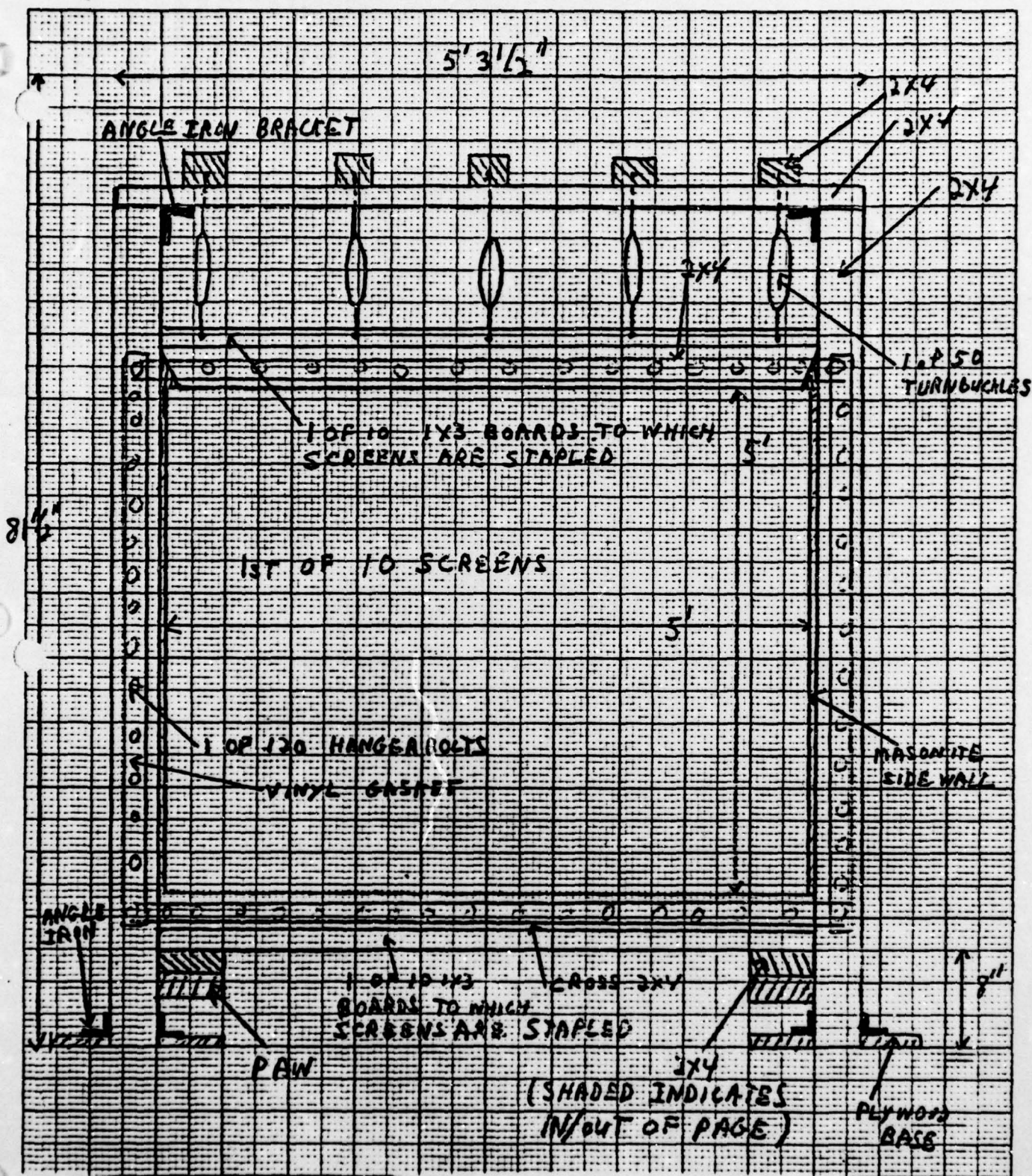
FIGURE C-13. SCREEN SECTION: FRONT VIEW

185
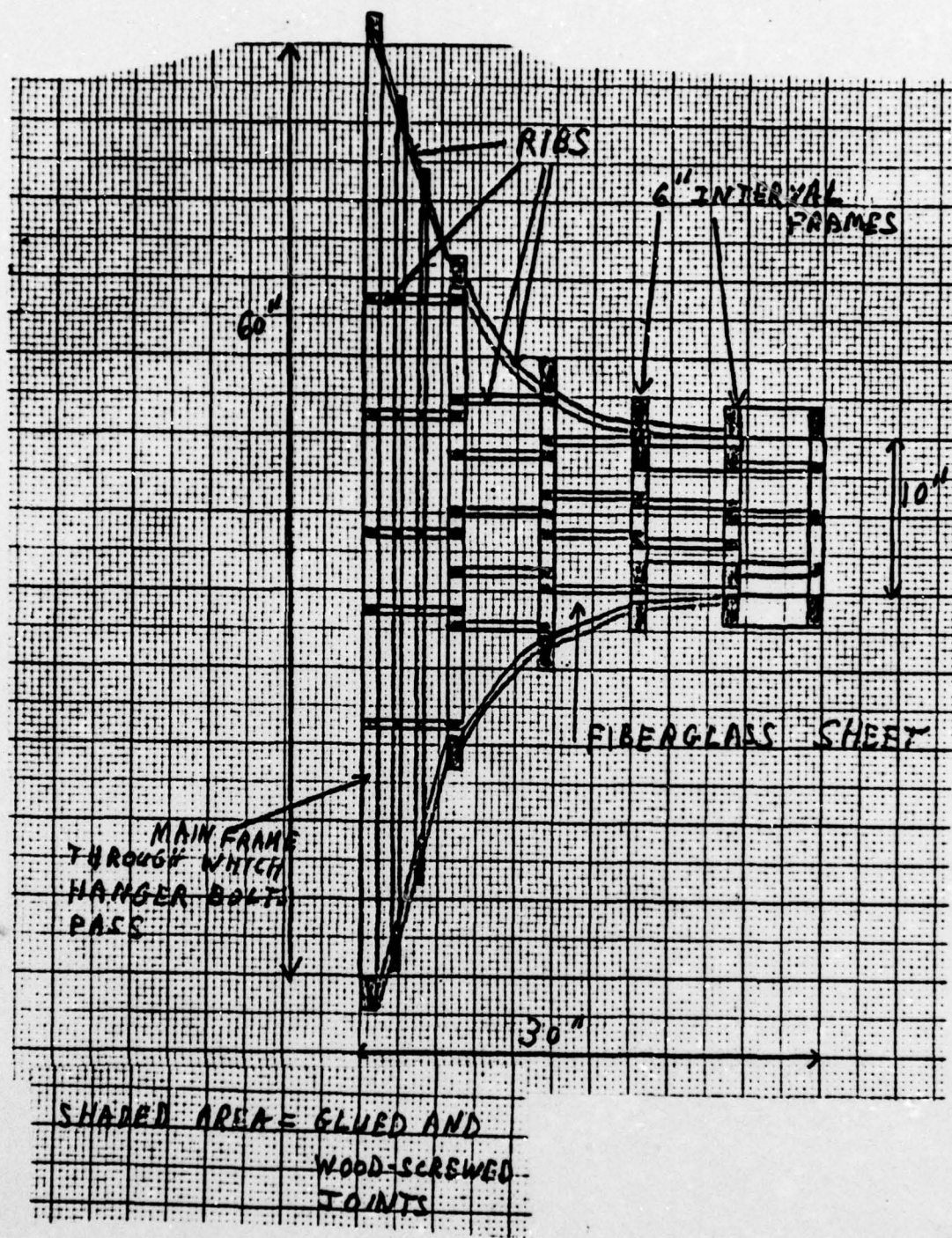
FIGURE C-14. WIND TUNNEL CONTRACTION: TOP VIEW
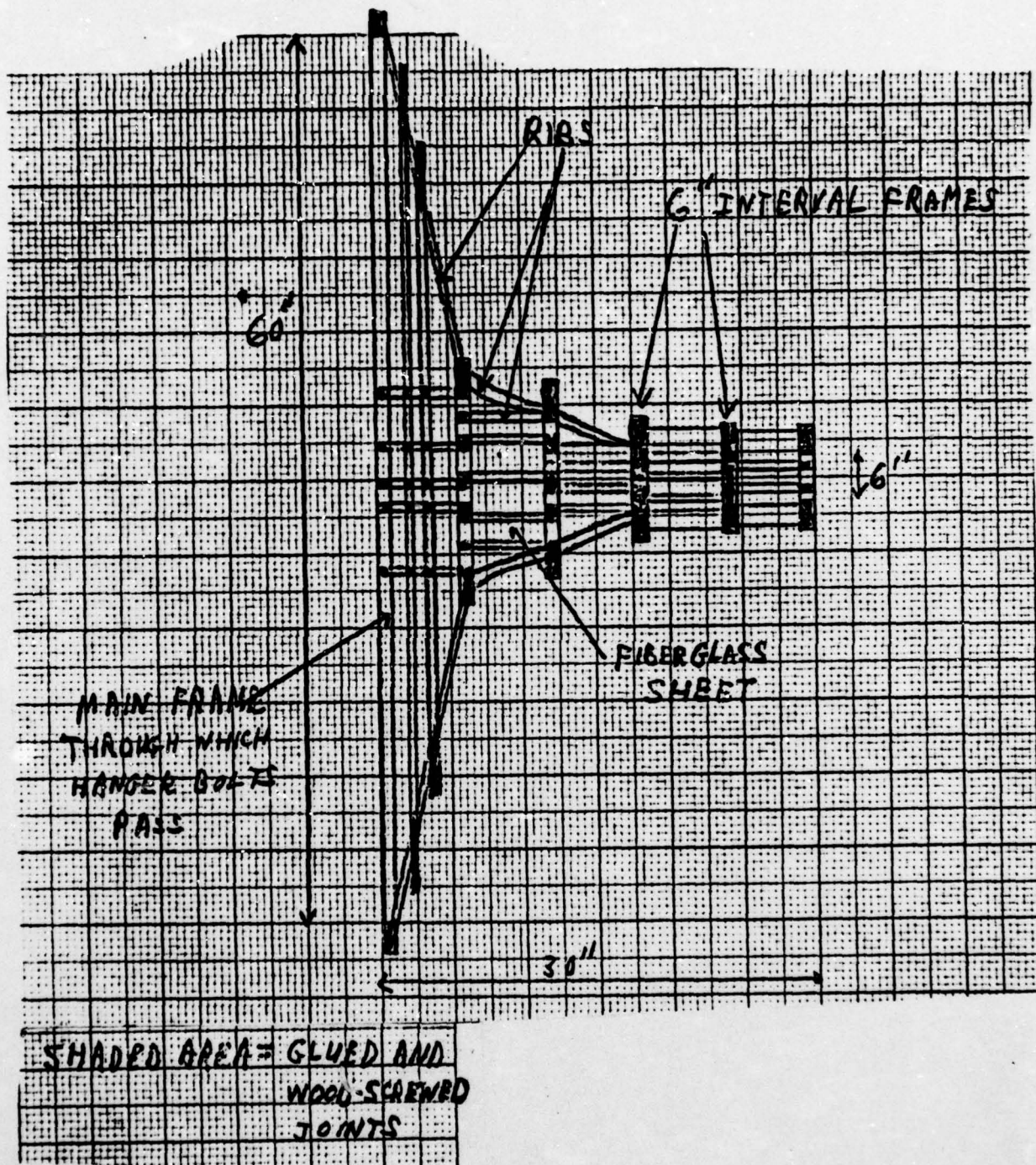
FIGURE C-15. WIND TUNNEL CONTRACTION: SIDE VIEW

187

FIGURE C-16.

DESCRIPTIVE GEOMETRY FOR WIND TUNNEL DESIGN

① DRAW BOX OF EXTREME DIMENSIONS AND SYMMETRY LINE
② DRAW CROSS SECTION ∠ (30" LONG WITH 10" JET) (DRAW ANY SMOOTH CURVE)
③ OBTAIN CROSS SECTION β FROM ∠ AS FOLLOWS.
   FOR EACH POINT ON OY, MEASURE A, PROJECT OY POINT
   TO SYMMETRY LINE AND ON TO OY. OY P IS DISTANCE
   A FROM OY POINT.
④ OBTAIN TEMPLATE FOR WALL, L, d, AS FOLLOWS.
   FOR EACH POINT ON OY, PROJECT TO CROSS SECTION
   β AND MEASURE DISTANCE β ALONG CURVE β
   PROJECT TO SYMMETRY LINE AND ON TO OX.
   THE CORRESPONDING POINT ON THE β CURVE
   IS DISTANCE β FROM OX POINT.
⑤ OBTAIN TEMPLATE γ FROM CROSS SECTION
   ∠ USING THE METHOD OF STEP 4.

188

Distance across (inches)

(a) 1/8" FROM TOP OF JET
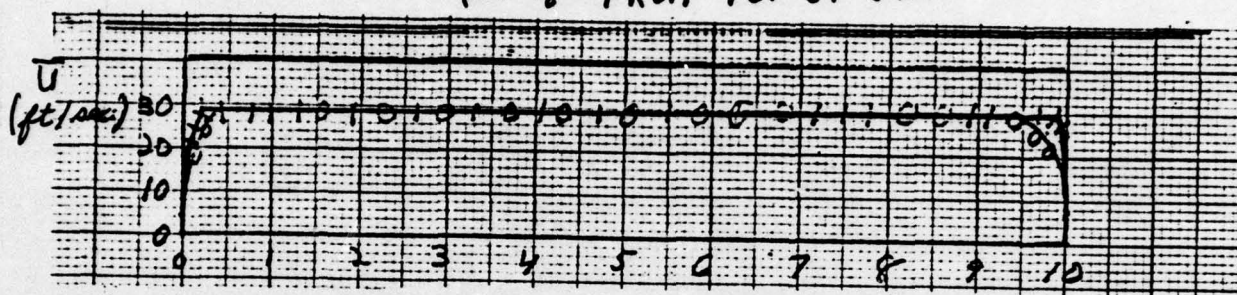
Distance across (inches)

(b) 1/2" FROM TOP OF JET
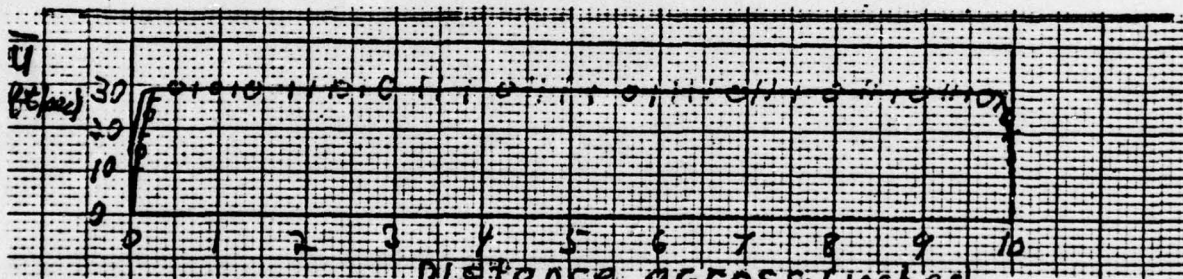
Distance across (inches)

(c) 1" FROM TOP OF JET
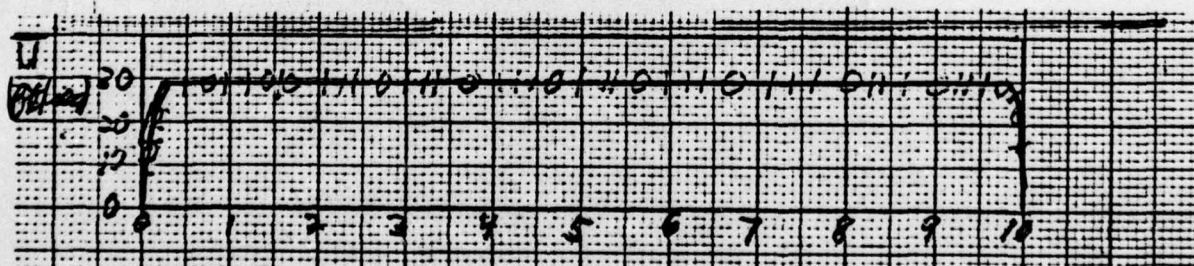
Distance across (inches)

(d) 1 1/2" FROM TOP OF JET

	1/8" from mouth
	1" from mouth
	2" from mouth

FIGURE C-17.   WIND TUNNEL VELOCITY PROFILES FOR $\bar{U} = 29$ FT/SEC
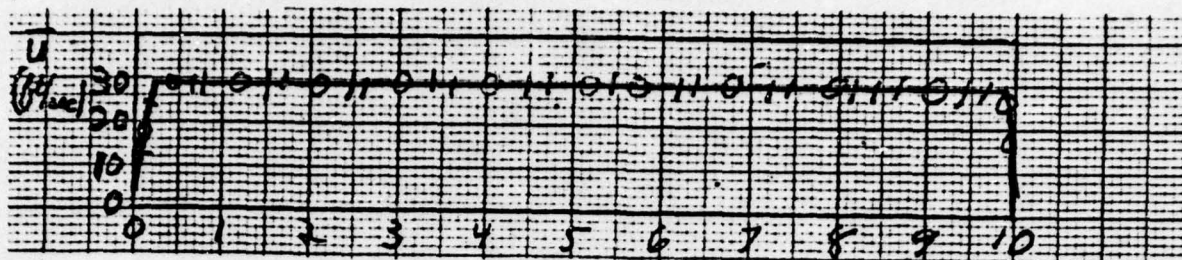
Distance across (inches)

(e) 2" FROM TOP OF JET

Distance across (inches)

(f) 2½" FROM TOP OF JET
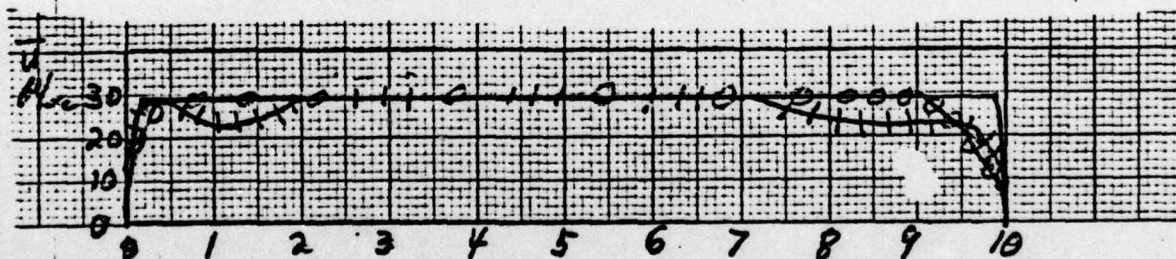
Distance across (inches)

(g) 2⅞" FROM TOP OF JET

—————— ⅛" from mouth
+++++ 1" from mouth
ooooo 2" from mouth

FIGURE C-17   (Continued)

190
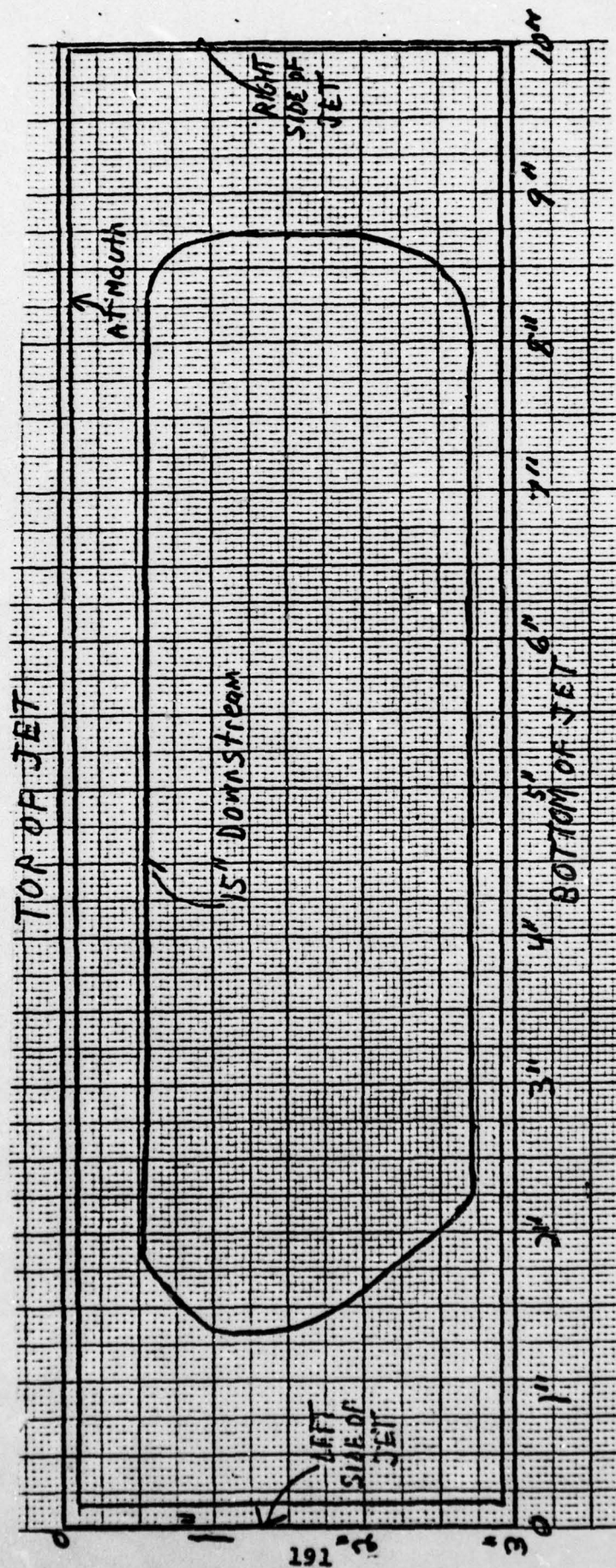
FIGURE C-18. WIND TUNNEL VELOCITY CONTOURS (BOUNDARY OF CONSTANT Ū AREA) AT Ū = 29 FT/SEC

END

DATE
FILMED

3-77

AD
A035994

MICROCOPY RESOLUTION TEST CHART
NATIONAL BUREAU OF STANDARDS 1963
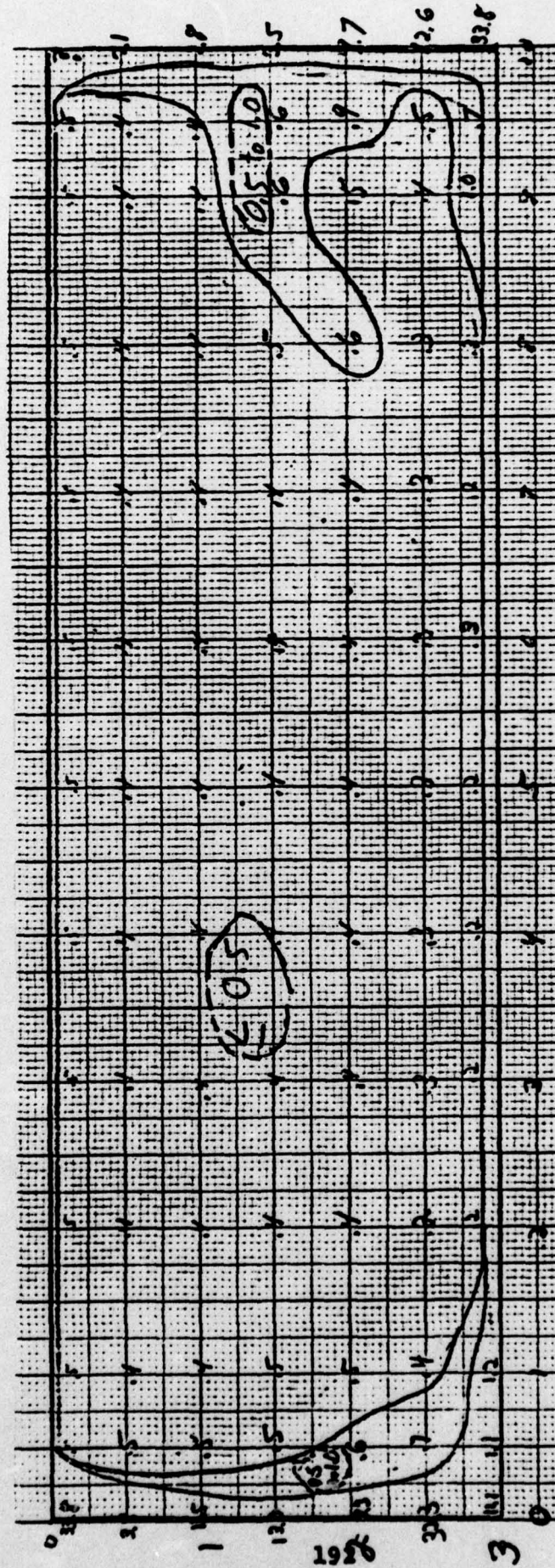
FIGURE C-19. WIND TUNNEL TURBULENCE
CONTOURS: 1/8" FROM MOUTH (U = 29 FT/SEC)
(numbers in percent):
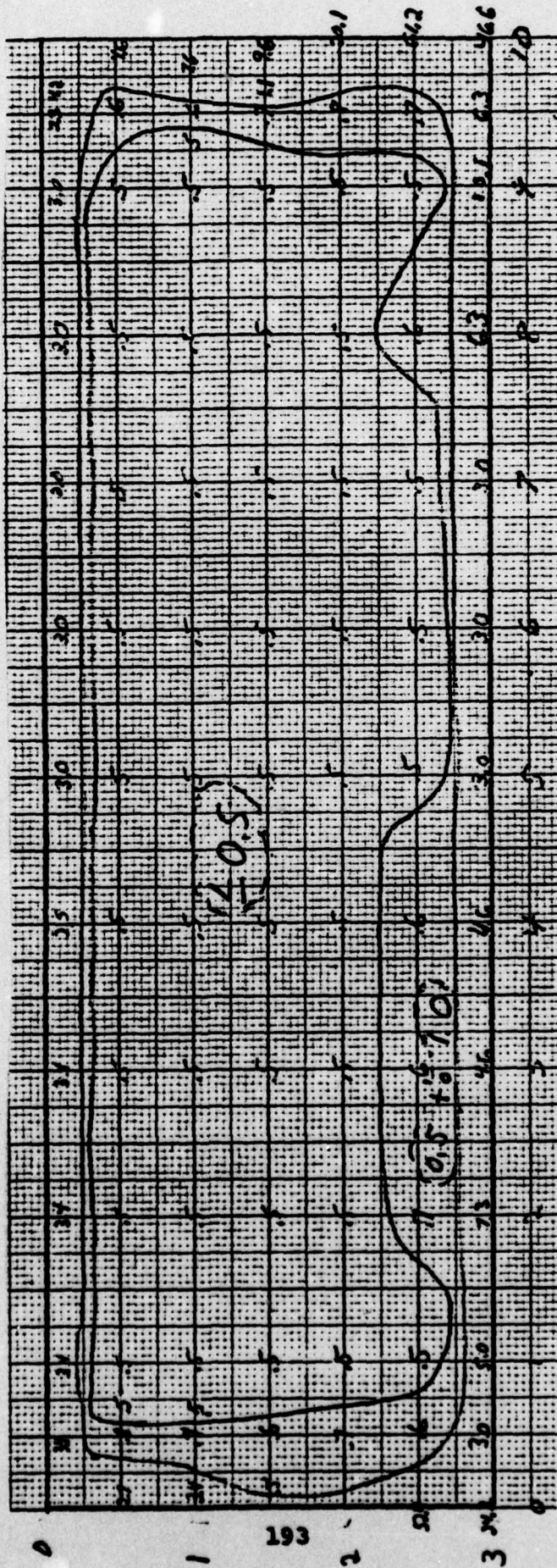
FIGURE C-20. WIND TUNNEL TURBULENCE CONTOURS:
1" FROM MOUTH ($\bar{U}_\infty$ = 29 FT/SEC)
(numbers in percent)

FIGURE C-21. WIND TUNNEL TURBULENCE CONTOURS:
2" FROM MOUTH ($\bar{U}$ = 29 FT/SEC)
(numbers in percent)
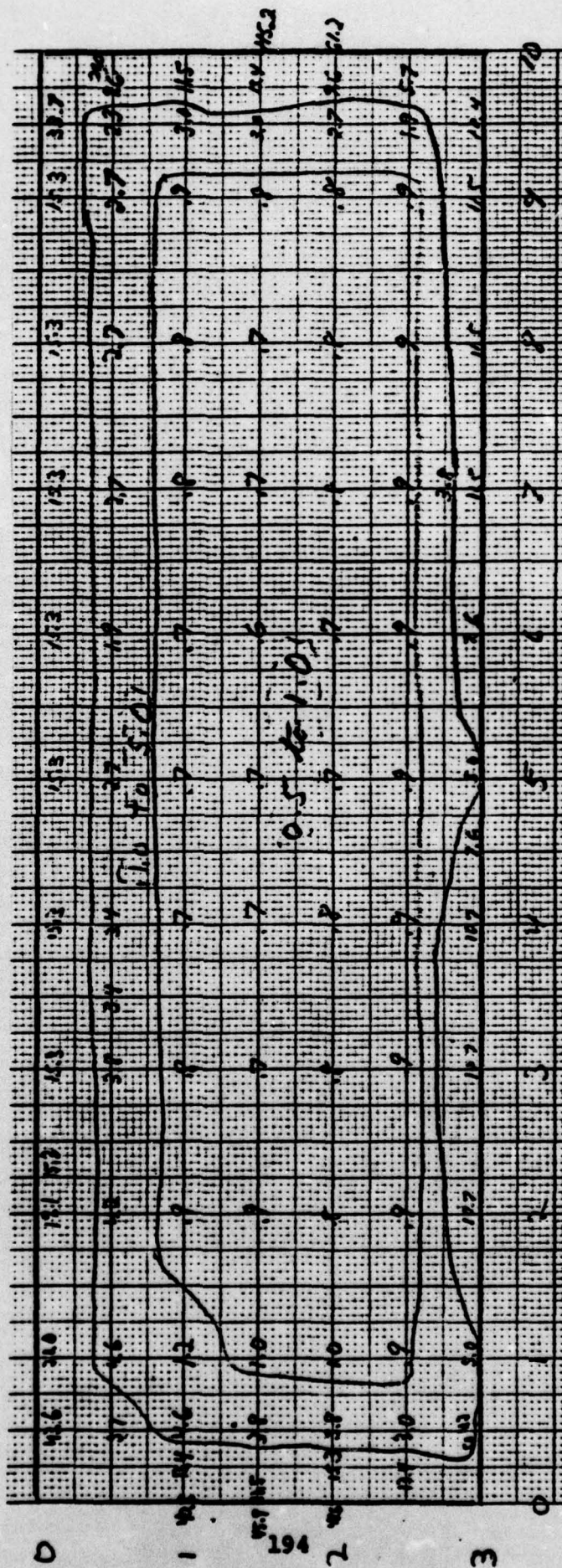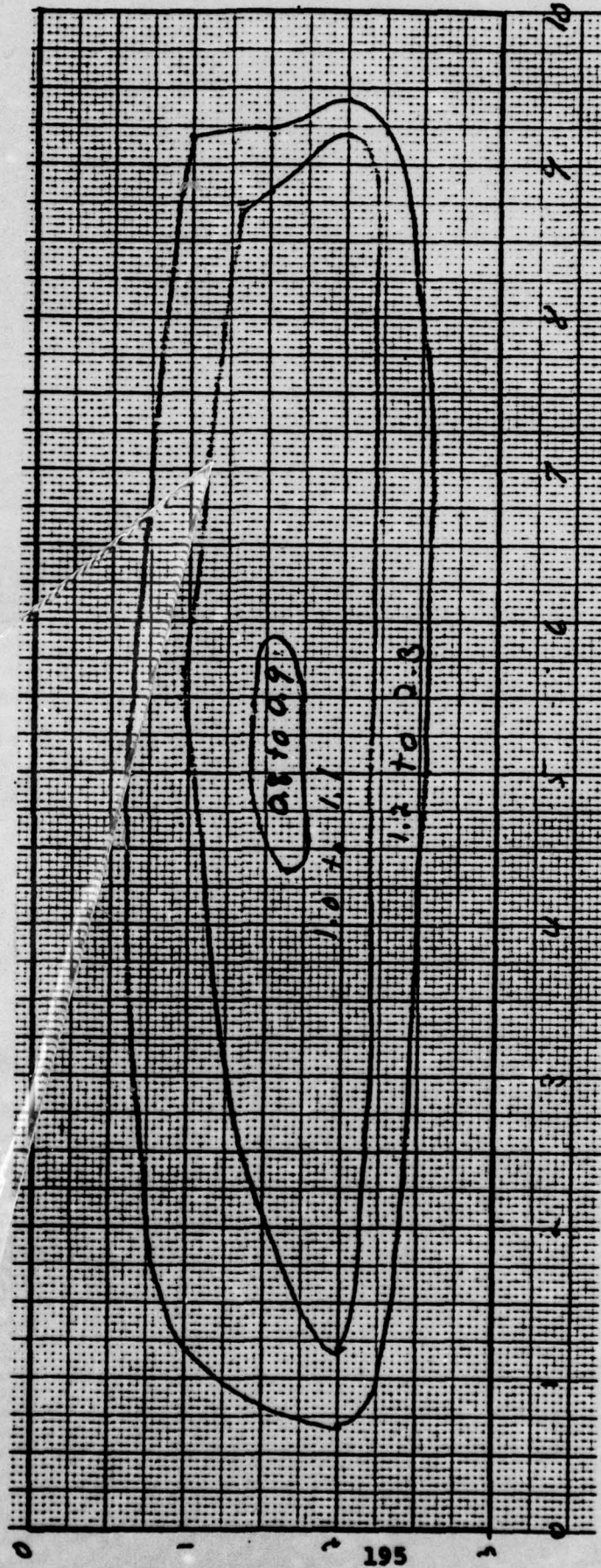
FIGURE C-22. WIND TUNNEL TURBULENCE CONTOURS:
3" FROM MOUTH (Ū = 29 FT/SEC)
(numbers in percent)
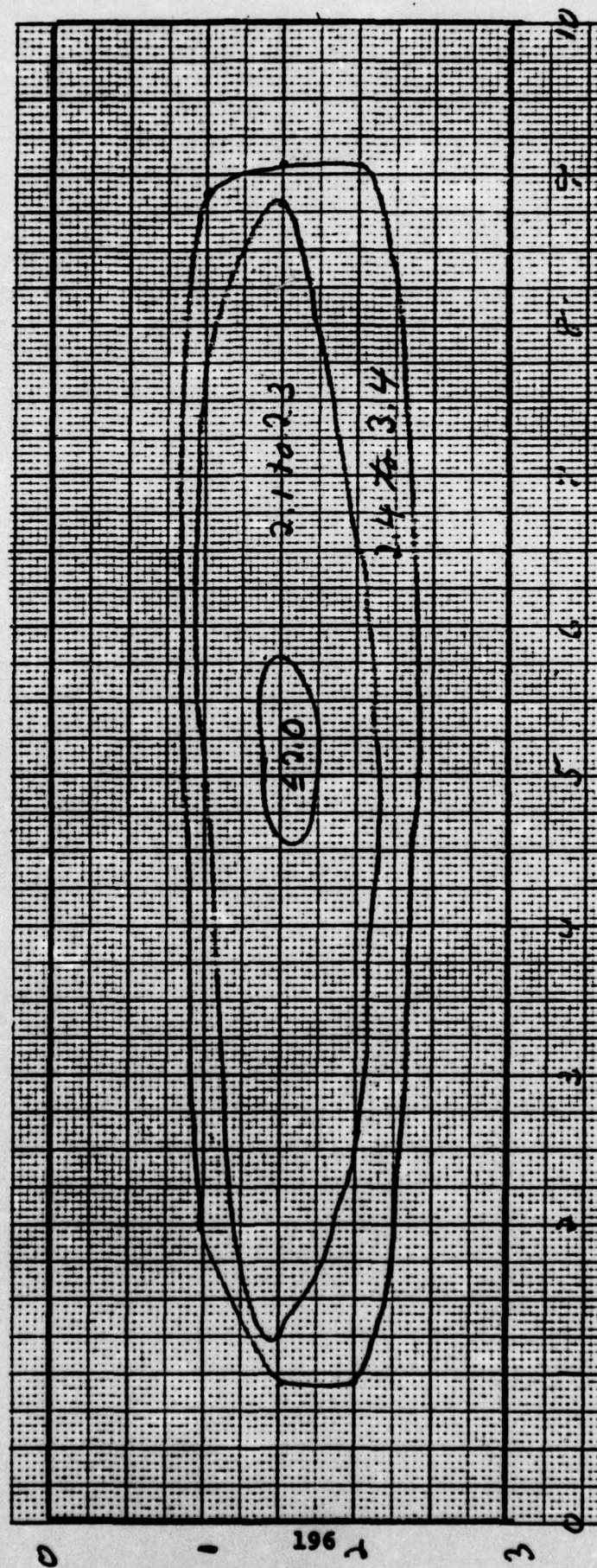
FIGURE C-23. WIND TUNNEL TURBULENCE CONTOURS:
5" FROM MOUTH ($\bar{U}$ = 29 FT/SEC)
(numbers in percent)
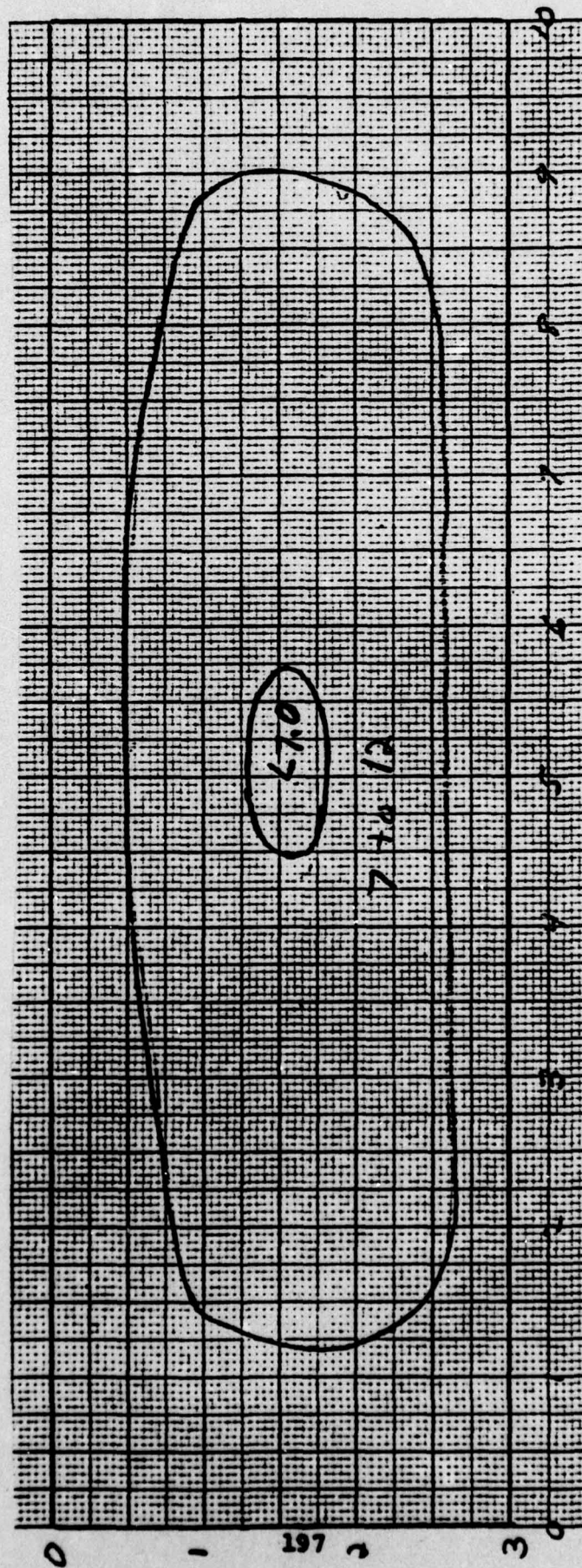
FIGURE C-24. WIND TUNNEL TURBULENCE CONTOURS (APPROXIMATE):
15" FROM MOUTH ($\bar{U}$ = 29 FT/SEC)
(numbers in percent)
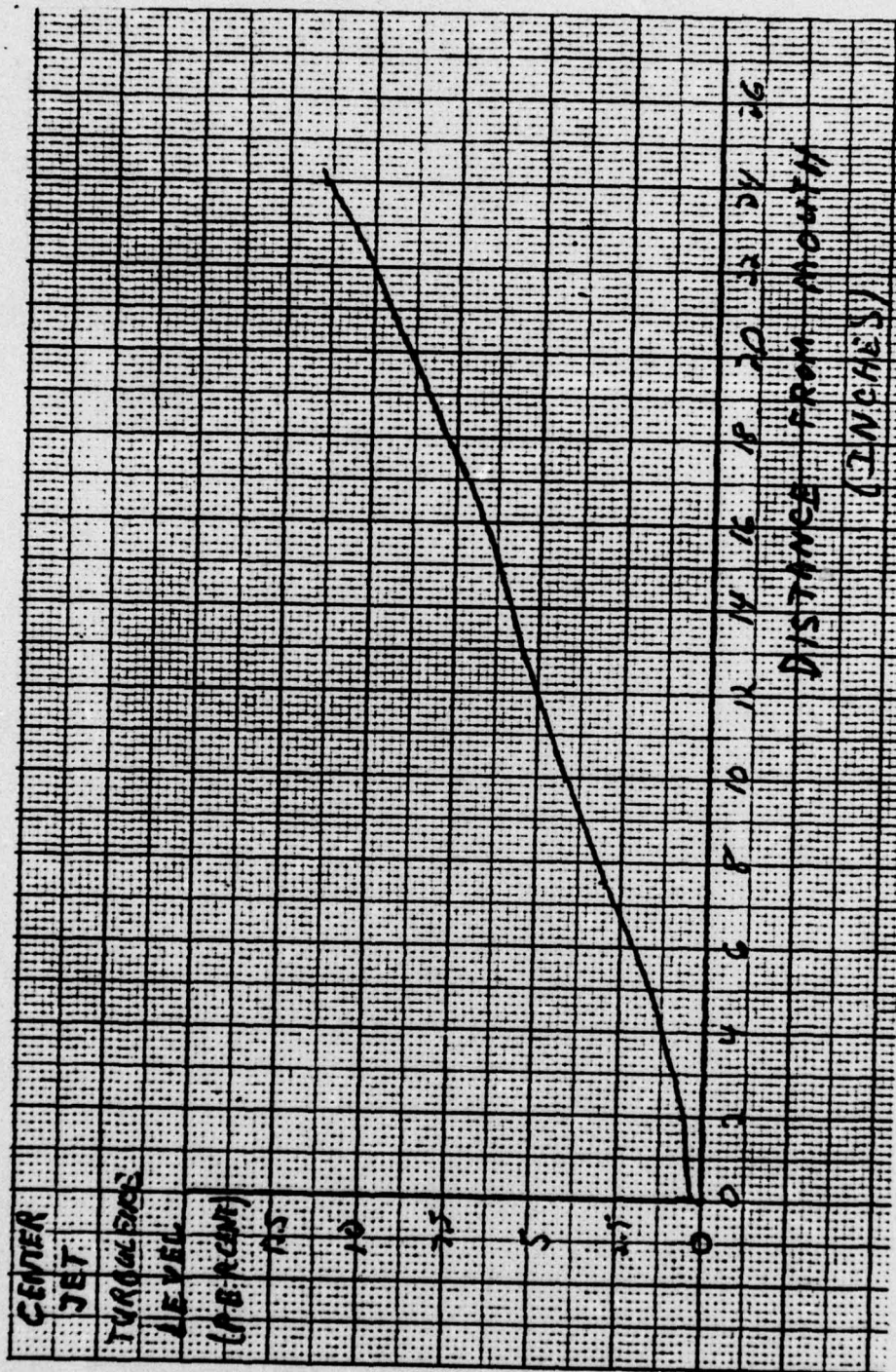
FIGURE C-25. WIND TUNNEL TURBULENCE LEVEL AT CENTER JET

ANTE ROOM

BLOWER

DUCTWORK

DUCTWORK SUPPORT

CONCRETE WALLS AND FIBERGLASS WEDGES OF CHAMBER

DUCT WORK

WORKING SECTION OF CHAMBER

11'

PLENUM CHAMBER

SCREEN SECTION

WIRE FLOOR GRID

8'

27'

VISQUEEN WALL PROTECTION

CONTRACTION

JET

37'

15'

25'
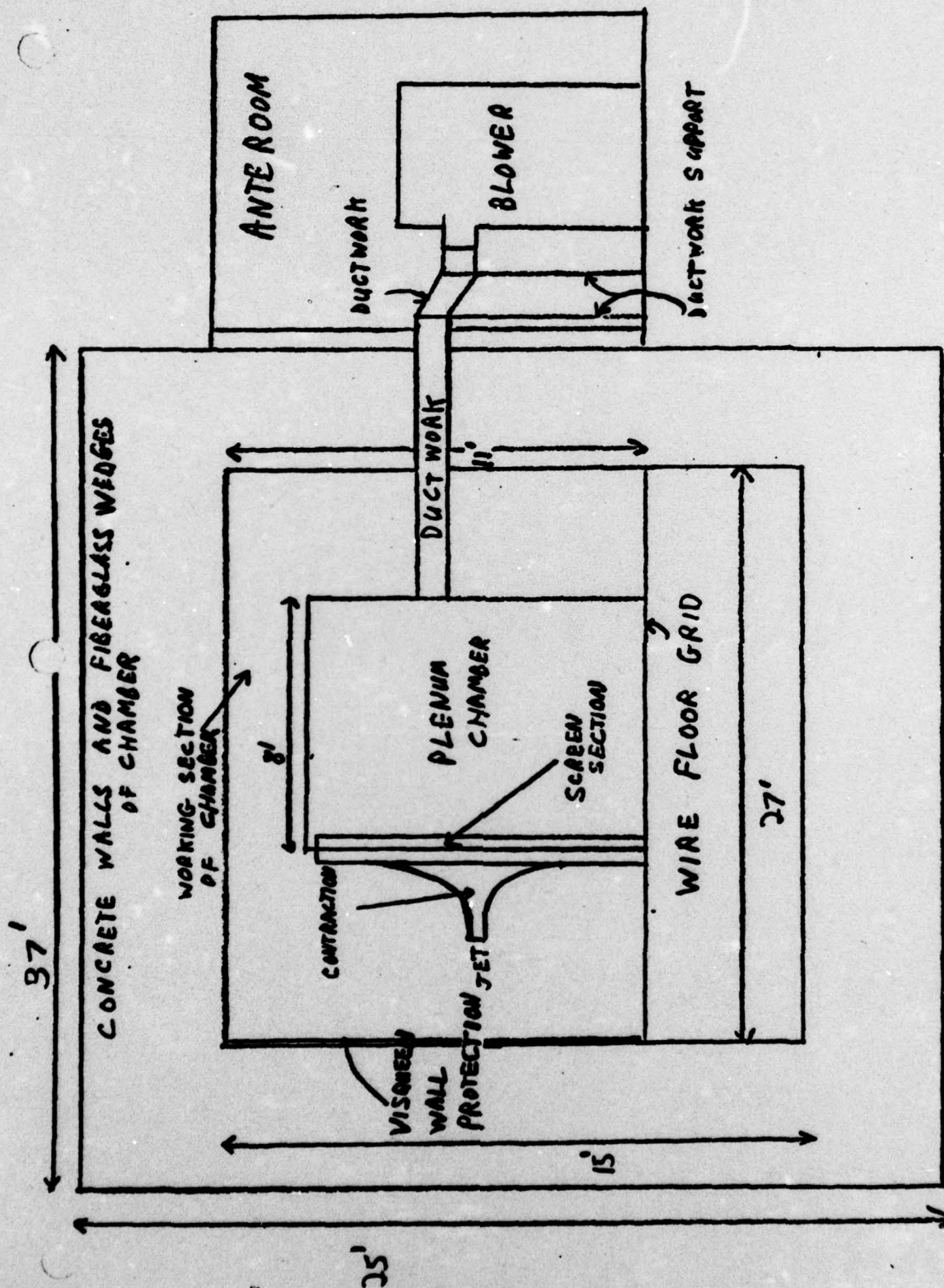
FIGURE C-26. WIND TUNNEL IN ANECHOIC CHAMBER: SIDE VIEW

199
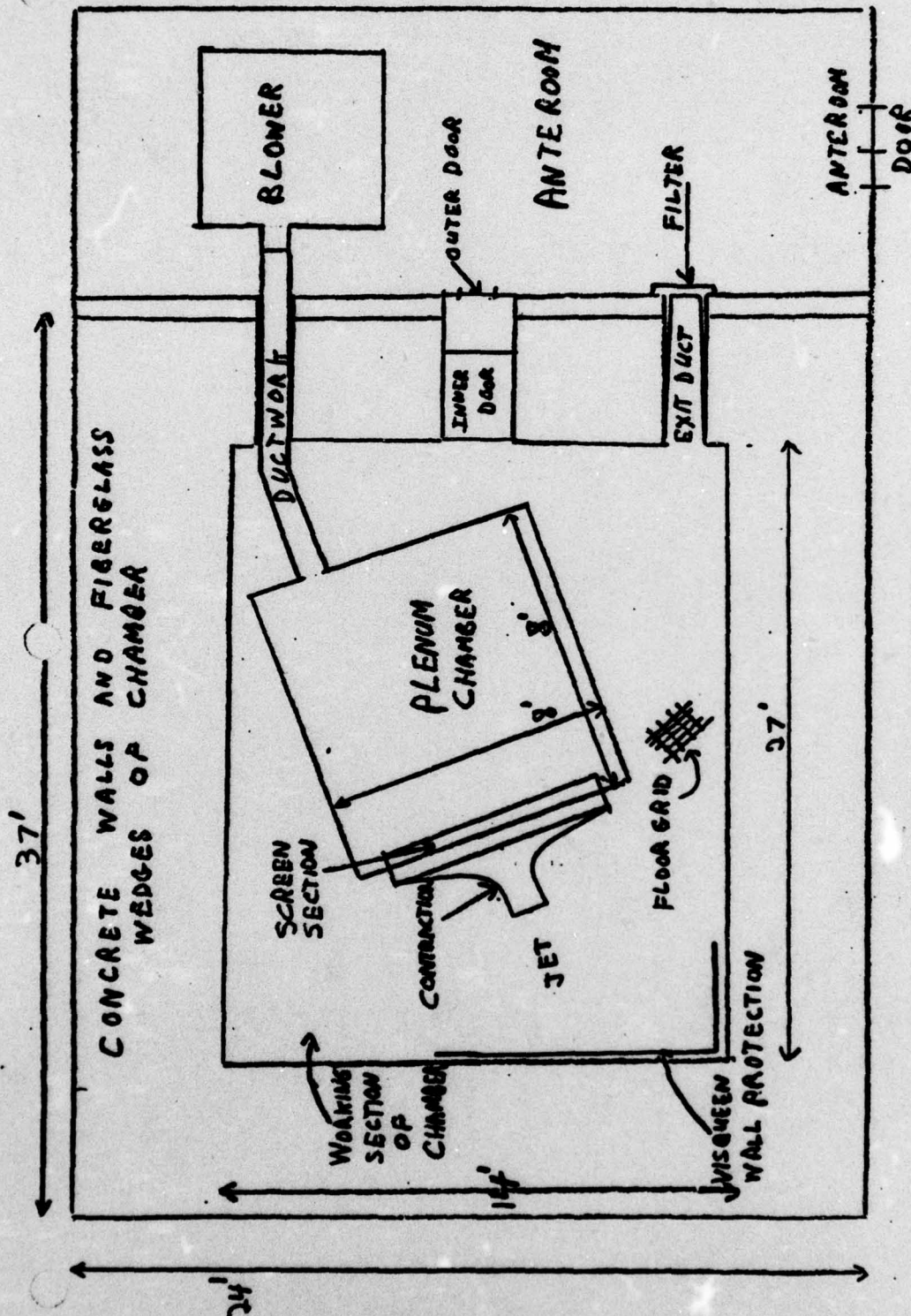
FIGURE C-27. WIND TUNNEL IN ANECHOIC CHAMBER: TOP VIEW

200
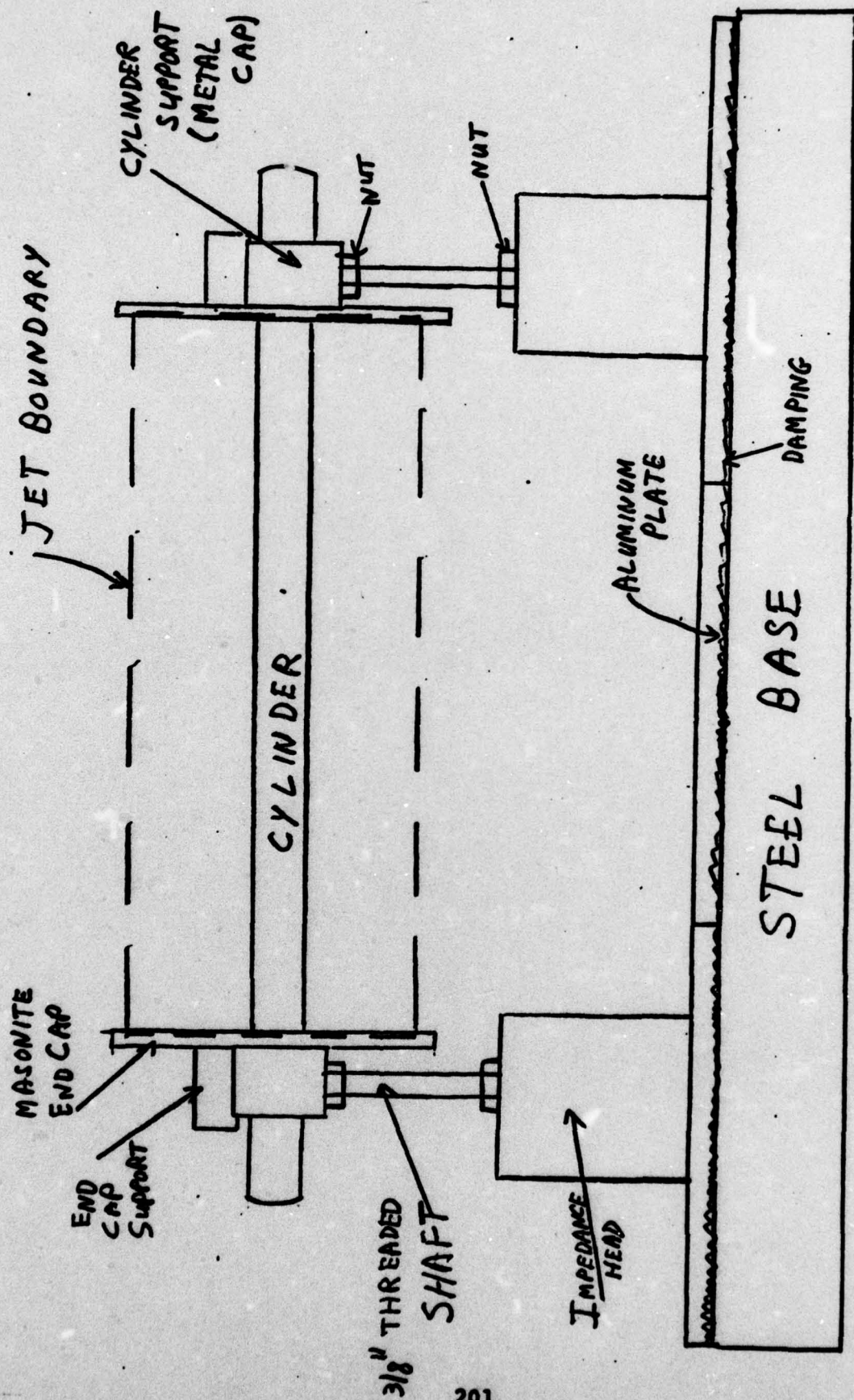
FIGURE C-28. CYLINDER SUPPORT STAND
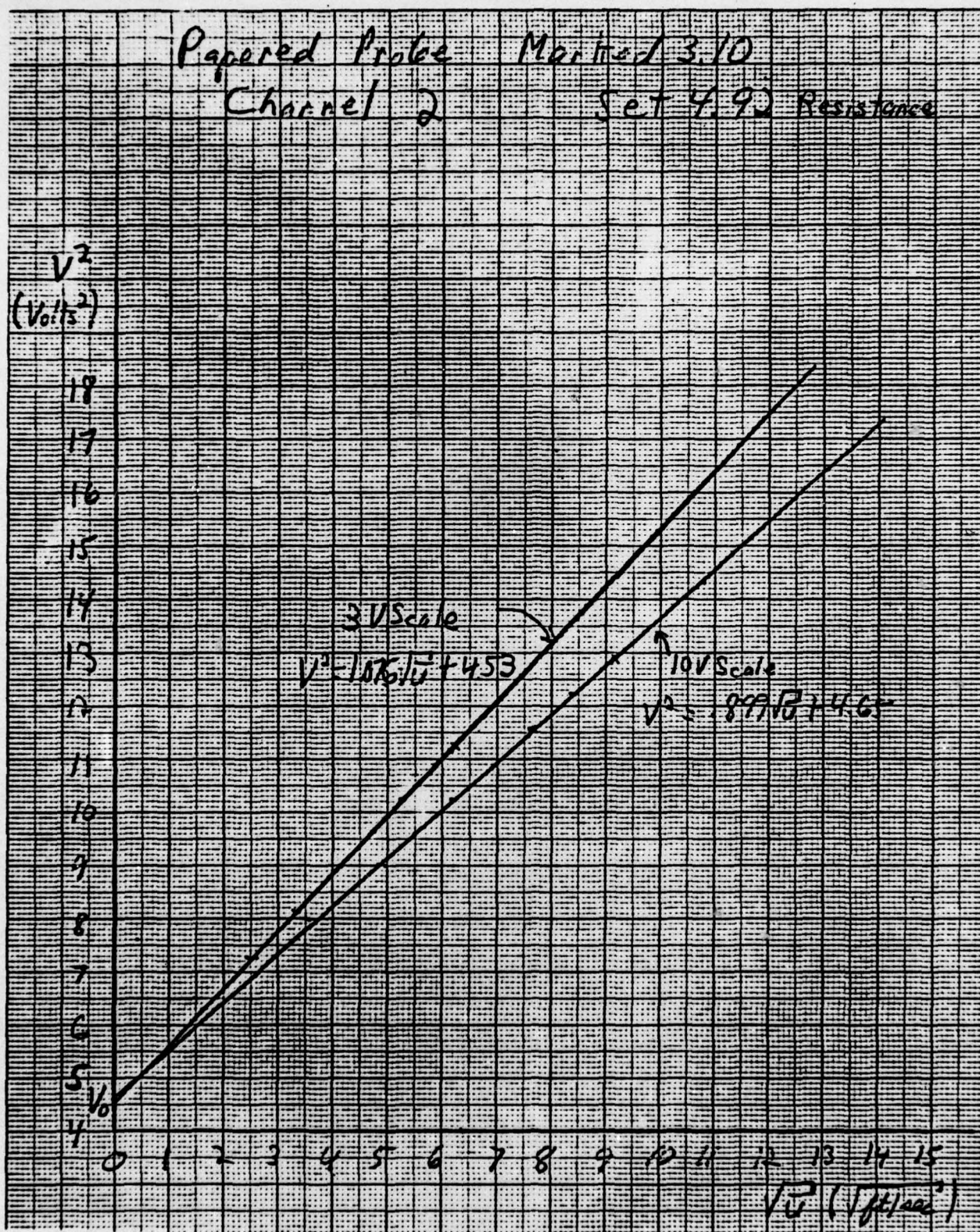
FIGURE C-29. HOT WIRE ANEMOMETER CALIBRATION CURVE

202
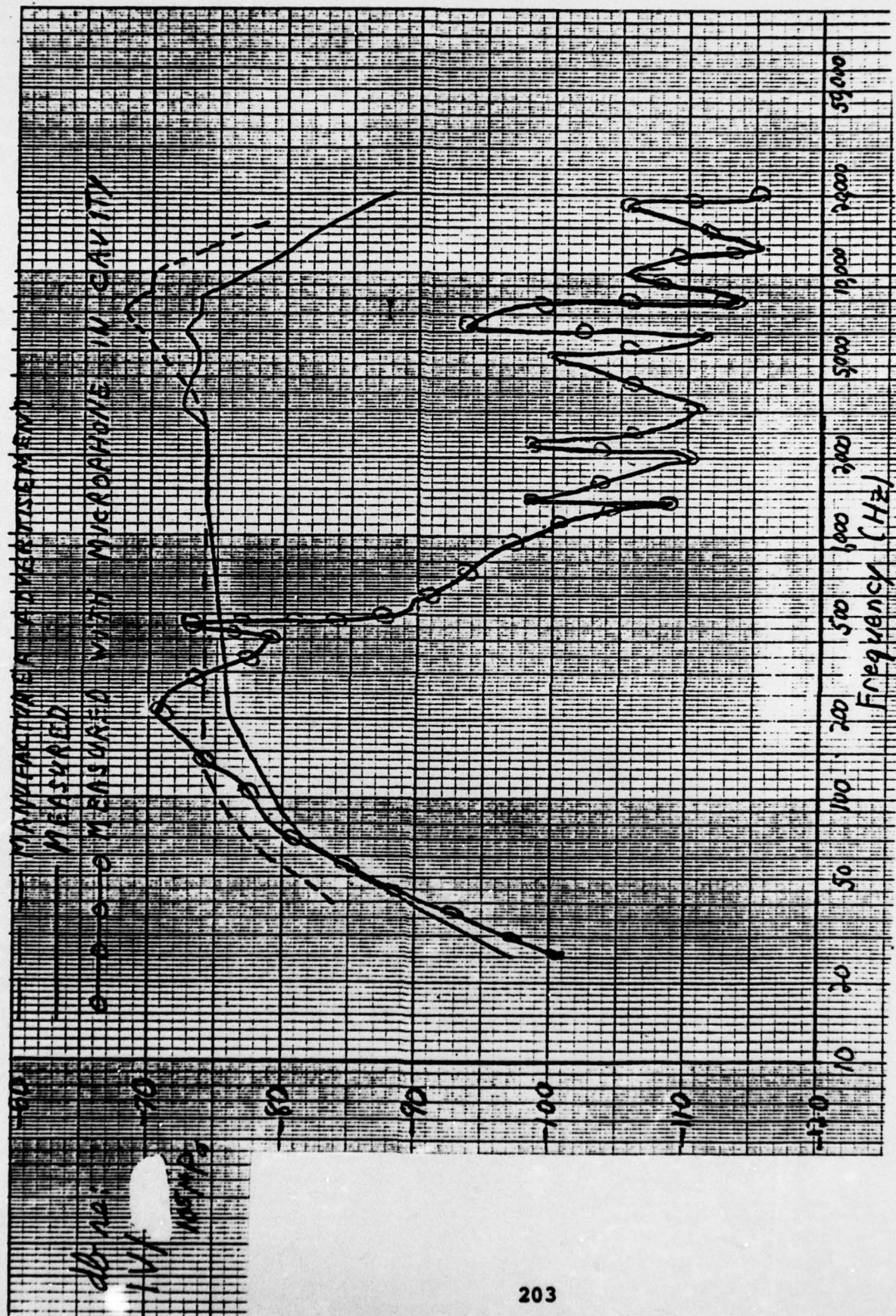
FIGURE C-30. MICROPHONE SENSITIVITY

203
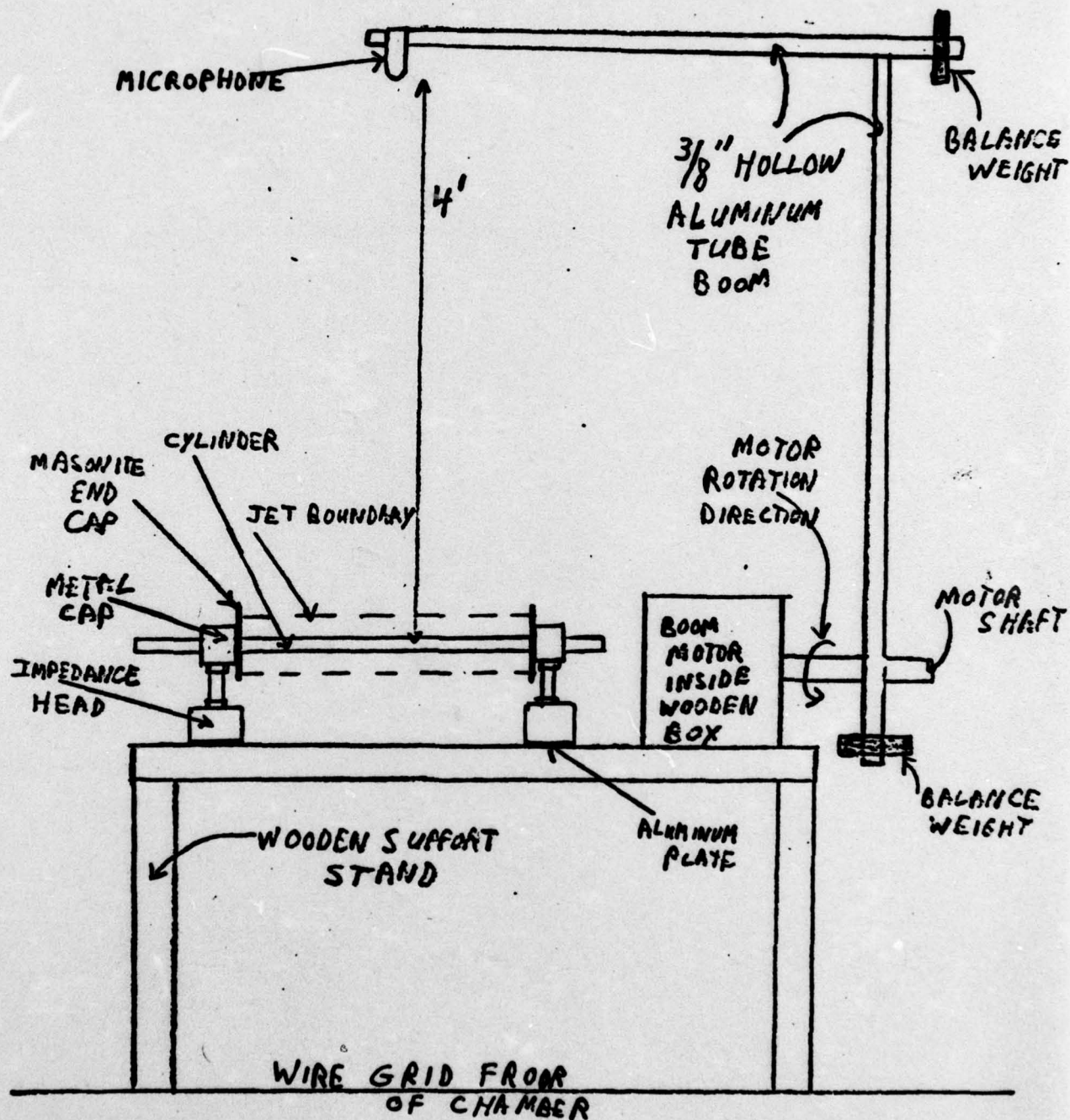
FIGURE C-31. MICROPHONE AND MOUNTING BOOM IN ANECHOIC CHAMBER

204

FIGURE C-32. MICROPHONE IN CAVITY INTERIOR TO CYLINDER

SHAFT
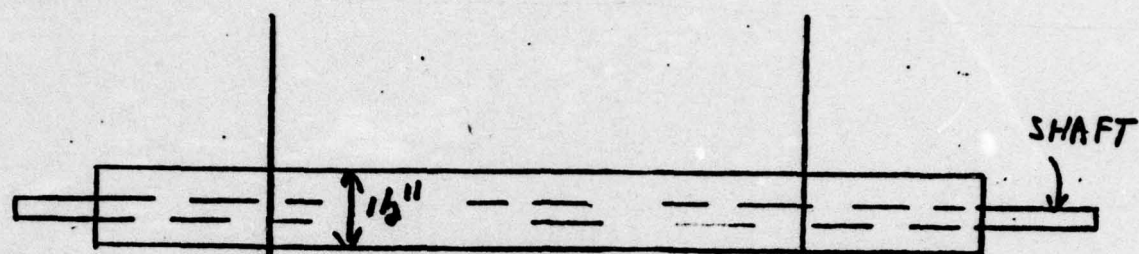
(a) CYLINDER WITH
TWO FINS

SHAFT
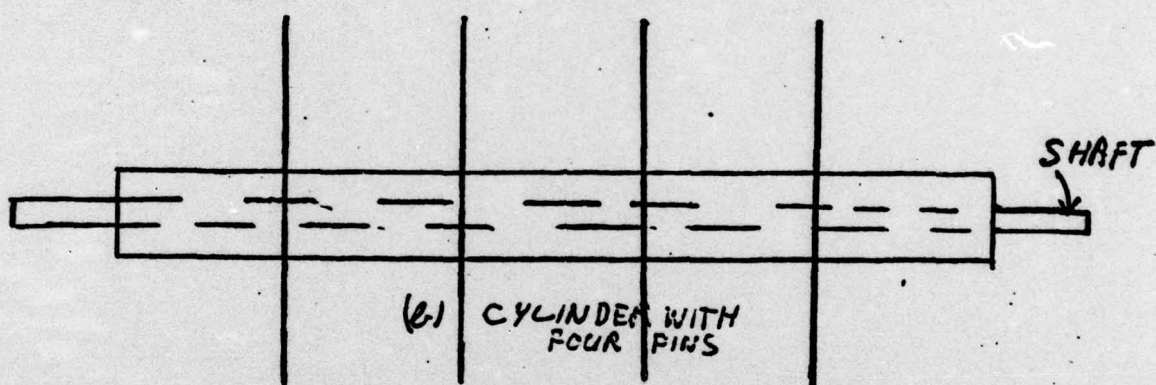
(b) CYLINDER WITH
FOUR FINS
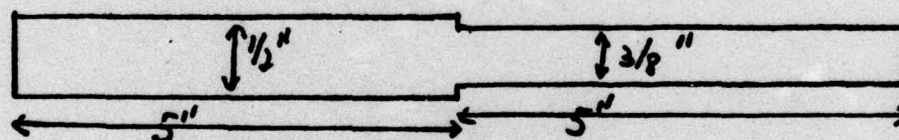
(c) TWO NOTCHED
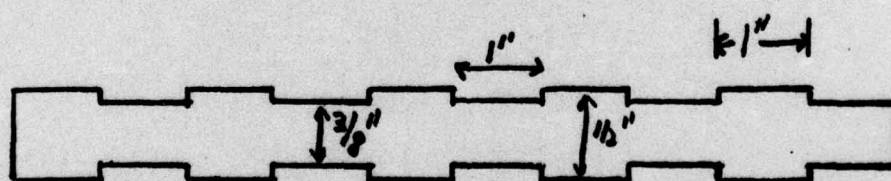
(d) REGULAR MULTINOTCHED

(e) IRREGULAR MULTINOTCHED

FIGURE C-33. CYLINDERS

206
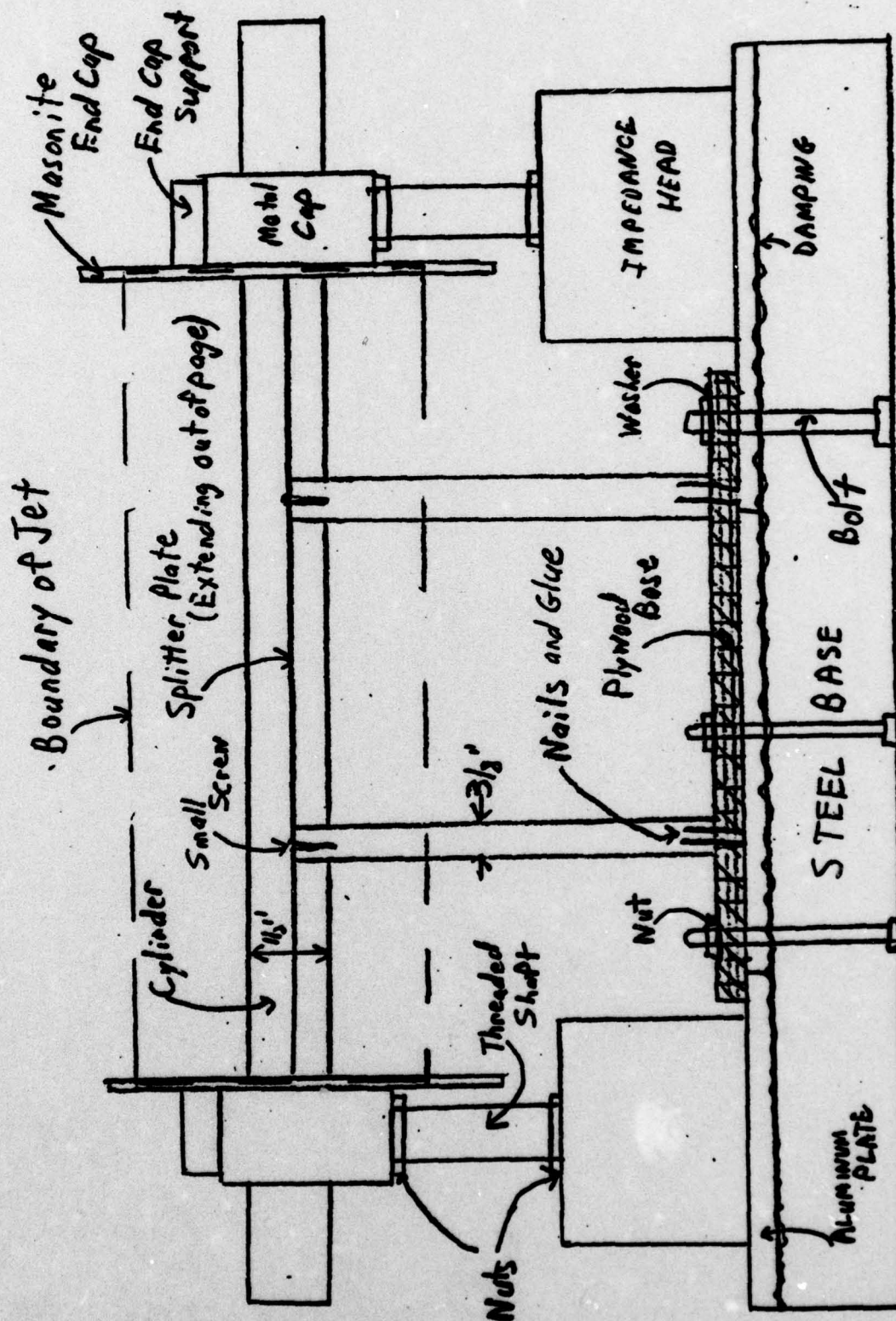
FIGURE C-34. SPLITTER PLATE SUPPORT
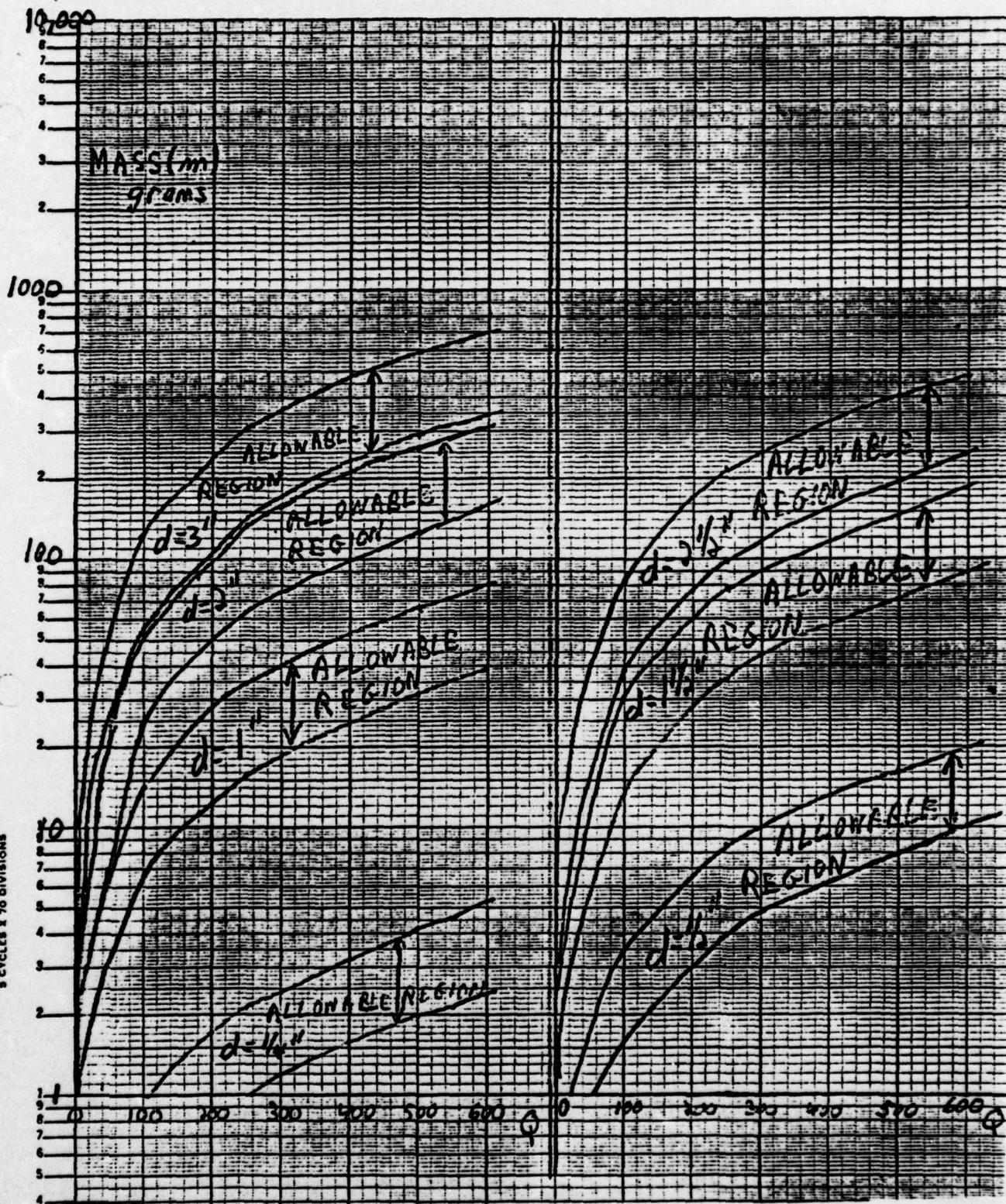
FIGURE C-35. M-Q PLOT FOR SYNCHRONIZATION

Figuren End Cap Extension

Hoop

Metal End Cap

Cylinder

10"

17"

Leaf Spring

A

B

C

Bolt

PLATE D.

Nut

Wooden Support Stand

Stand

FLOOR

Notch

Plate

Plate c

Stand Leg

209

FIGURE C-36. CYLINDER SUPPORT FOR SYNCHRONIZATION

PLATE A

3½"

Spreader Leaf Spring

PLATE B

4½"

5"

4"

Threaded holes for Plate A's Bolts

Recessed Grooves for bolts into Plate C — provides movement in indicated direction.

PLATE C (has 4 threaded holes on bottom to accept bolts from Plate D)

4"

4"

Threaded holes to accept bolts from Plate B

PLATE D (Base Plate)

Recessed Grooves through which bolts into Plate C pass. Provides motion of Plate C in direction indicated

4"

8¼"

28¾"

(A) Aluminum Plates – Disassembled: Top View

FIGURE C-37. STAND FOR SYNCHRONIZATION: DETAIL

210

Cylinder

Visqueen End Cap Extension

End Cap

Set Screw

1½″

Plate A

Bolt

3½″

1½″

Screw Leaf Spring

Ring to hold Visqueen

Plate B

1½″

Bolt

1½″

4″

Plate C

4″

Bolts

Base Plate D

1½″
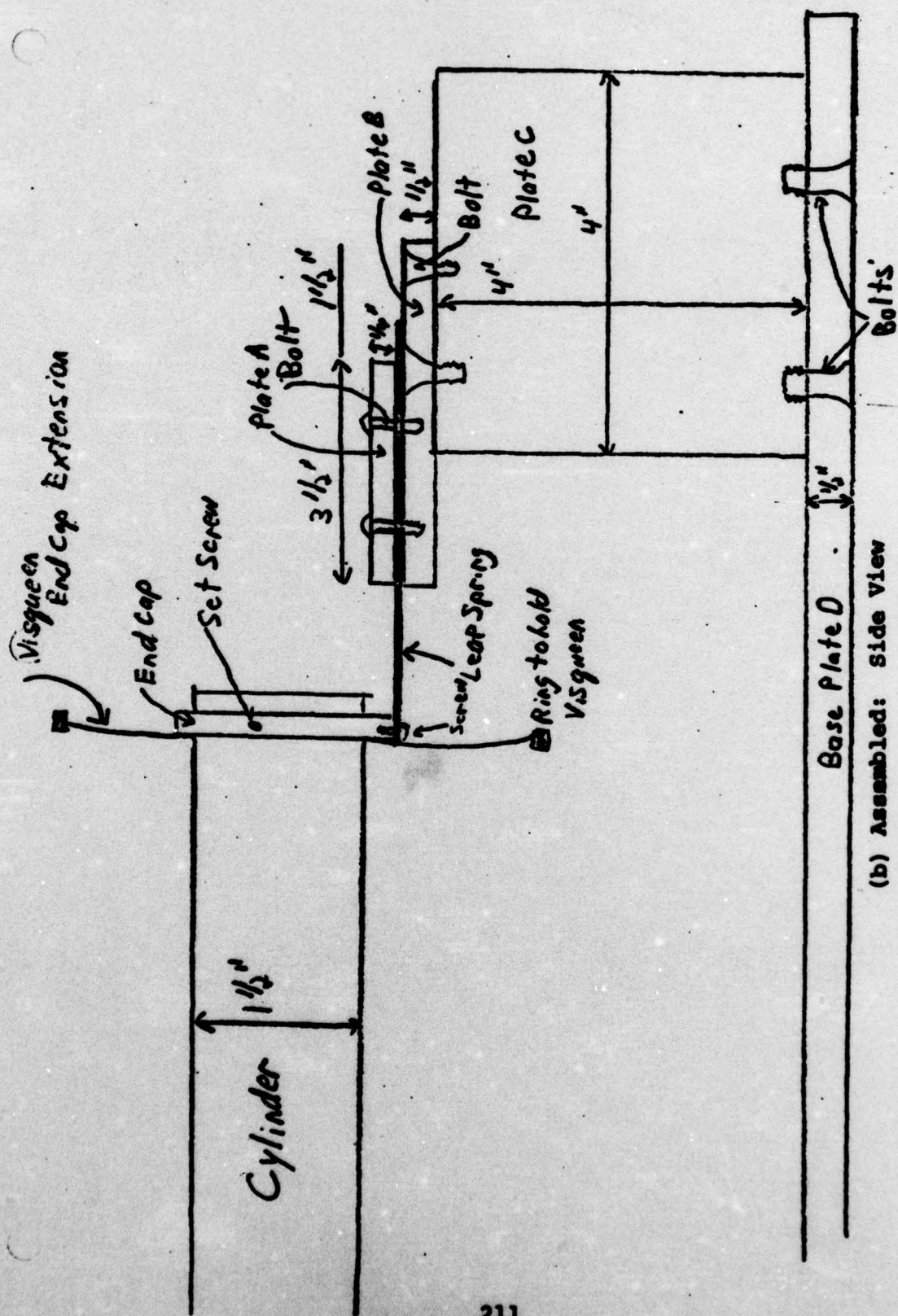
(b) Assembled: Side View

FIGURE C-37   (Continued)

211

IMPEDANCE HEAD

AMPLIFIER

OSCILLOSCOPE

SWEEPING WAVE ANALYZER

WAVE ANALYZER
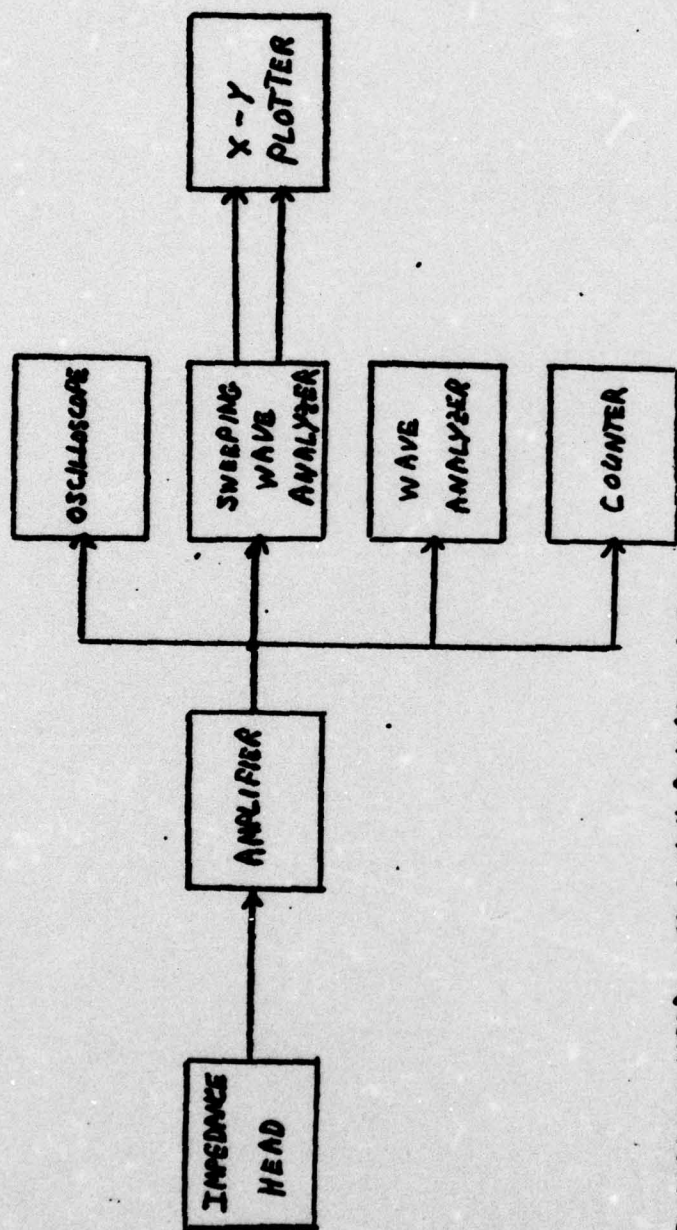
COUNTER

X-Y PLOTTER

IMPEDANCE HEAD: WILCOXON RESEARCH Z820
AMPLIFIER: H/P 465A
OSCILLOSCOPE: H/P 120A
{ WAVE ANALYZER: H/P 3570A
{ SWEEPING LOCAL OSCILLATOR: H/P 3594A
WAVE ANALYZER: H/o 302A
COUNTER: H/P 5245C
X-Y PLOTTER: VARIAN F-80

FIGURE C-38. ELECTRONICS FOR TOTAL LIFT FORCE MEASUREMENT

212
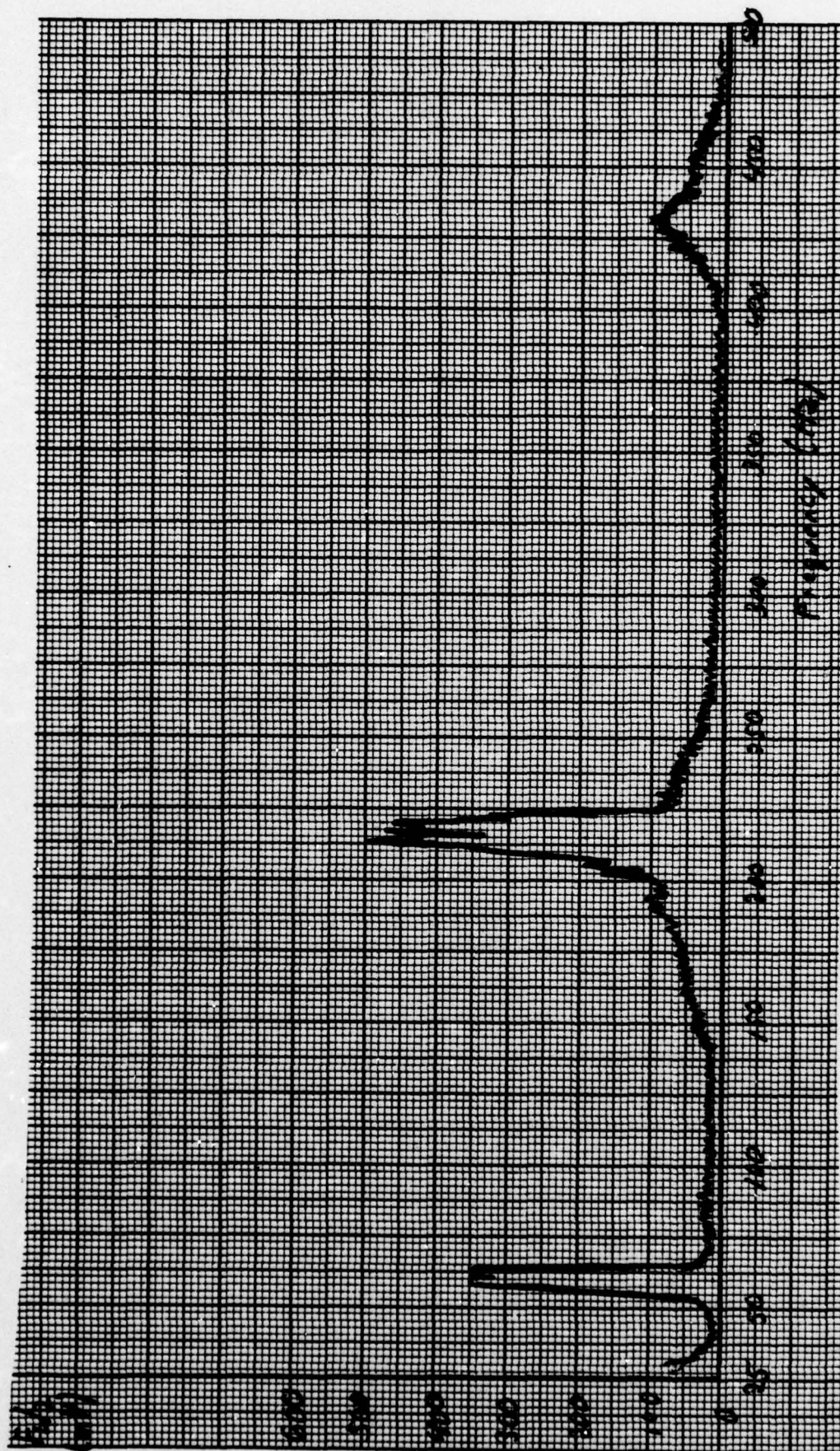
FIGURE C-39. VOLTAGE OUTPUT REPRESENTING $F_L/2$ VS FREQUENCY
$\bar{U}$ = 83.7 FT/SEC; 1" CYLINDER

213
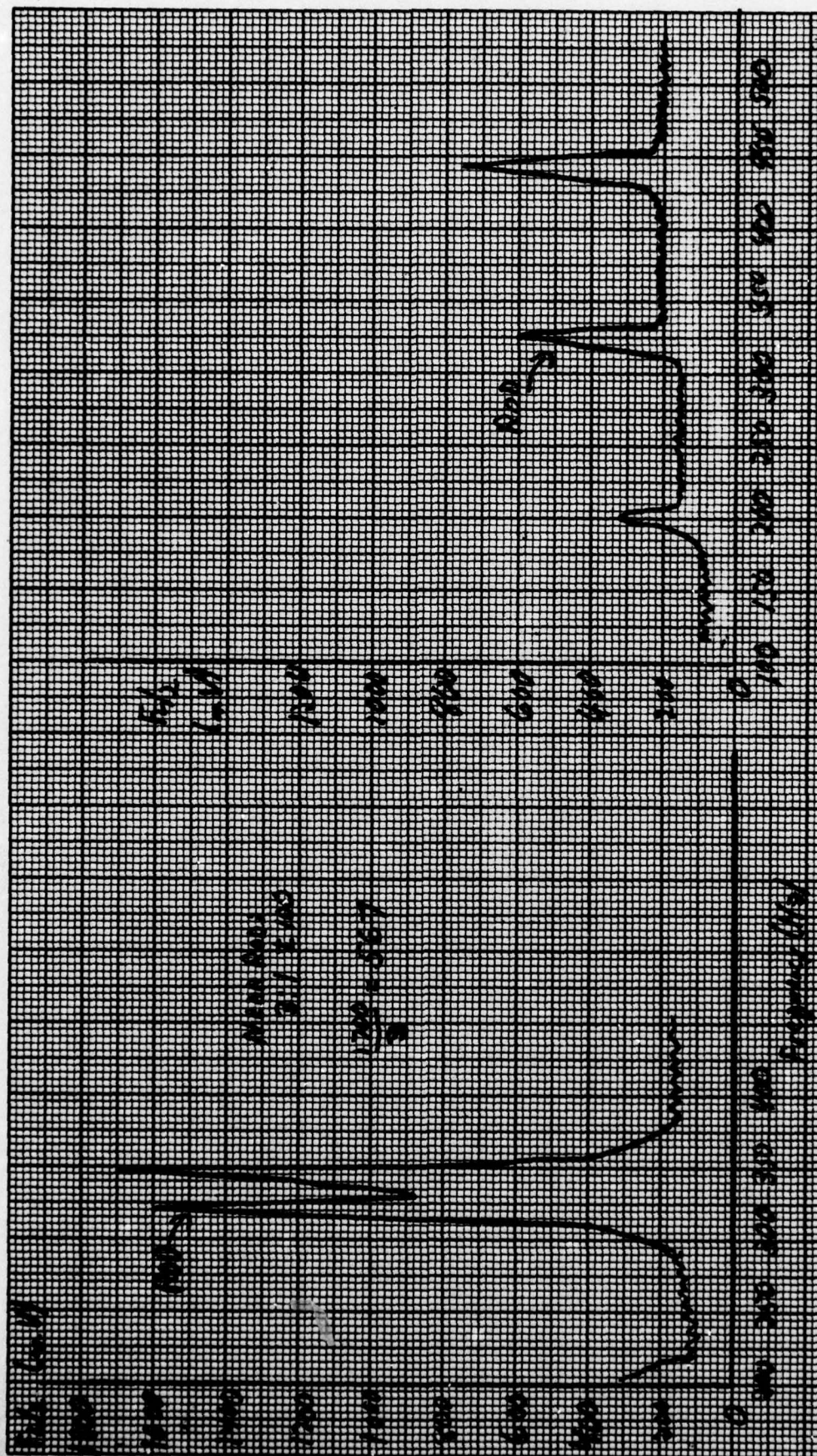
(a) U = 84.3 FT/SEC

(b) Ū = 94.3 FT/SEC

FIGURE C-40.   VOLTAGE OUTPUT REPRESENTING $F_L/2$ VS FREQUENCY:
CYLINDER WITH FOUR FINS

214
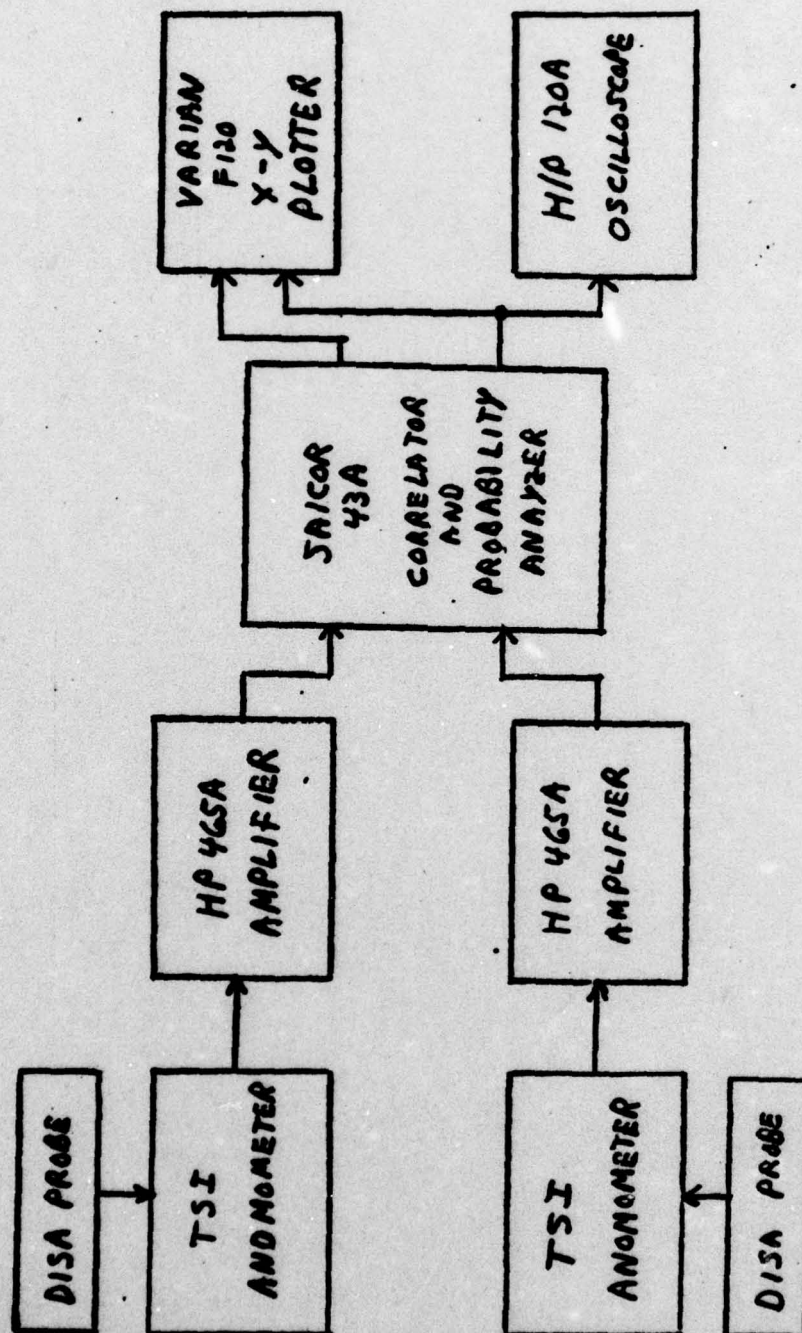
FIGURE C-41. ELECTRONICS FOR WAKE CORRELATION MEASUREMENT
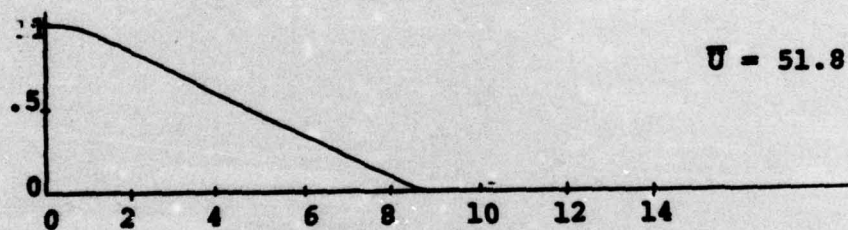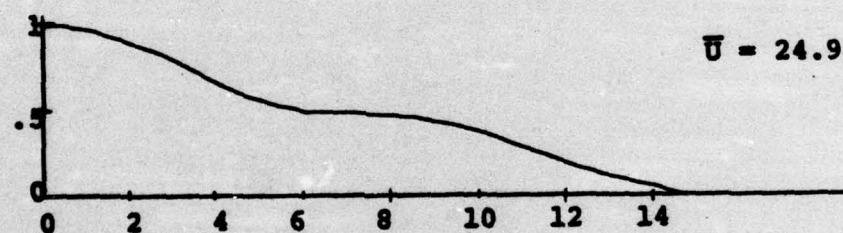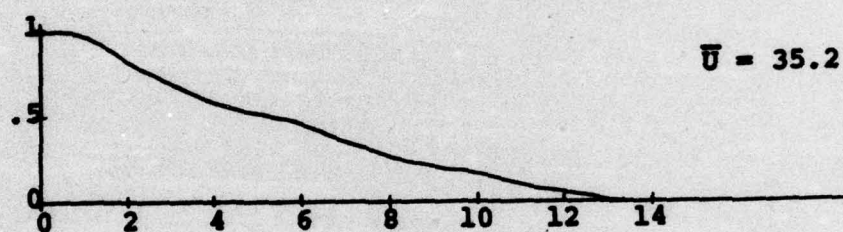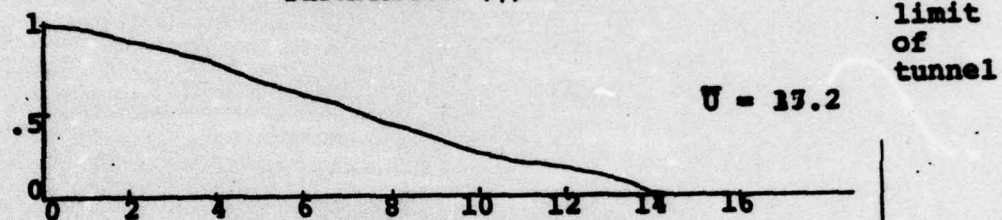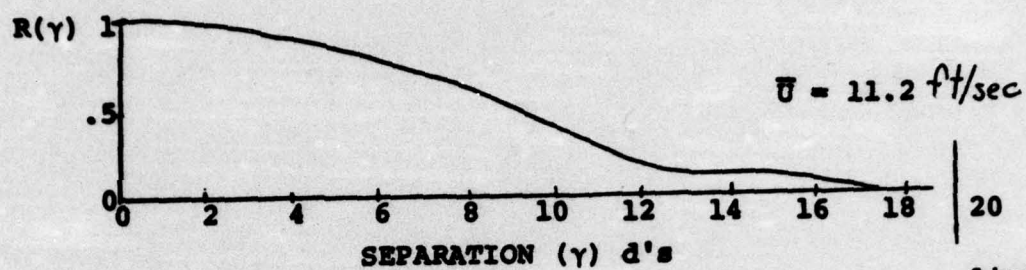
FIGURE C-42. CORRELATION FUNCTION: UNIFORM 1/2" CYLINDER
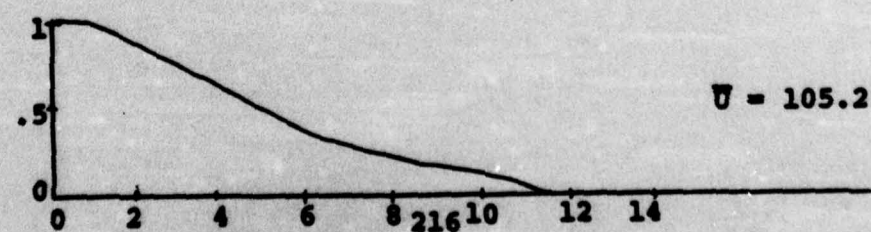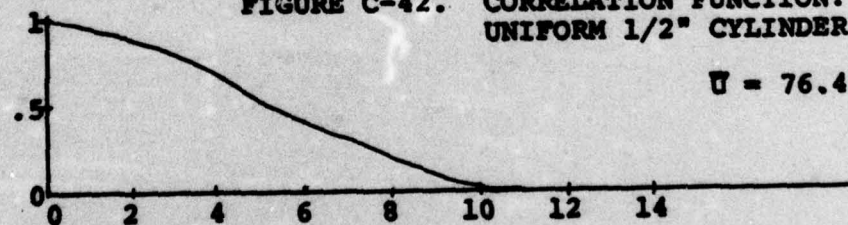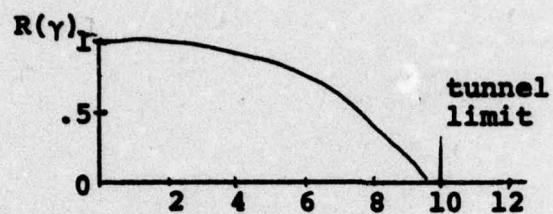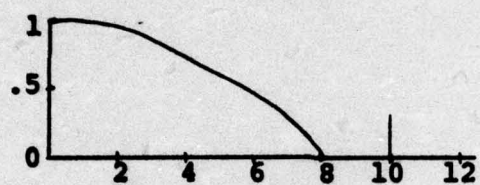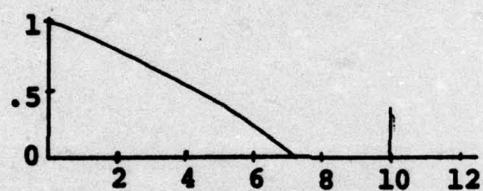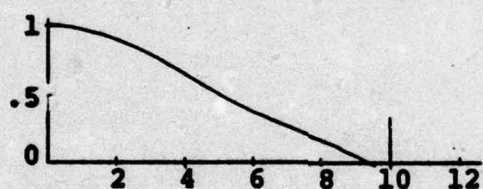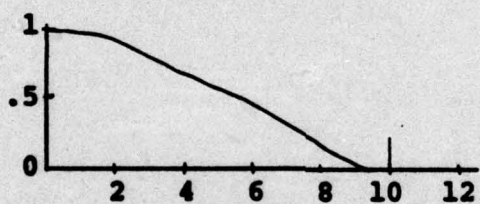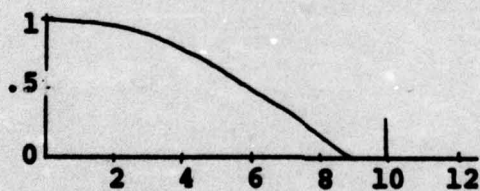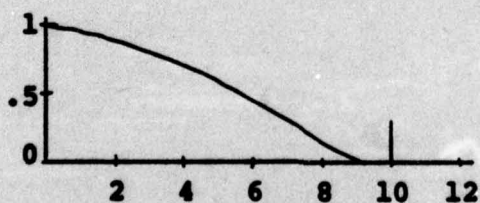
FIGURE C-43. CORRELATION FUNCTION: UNIFORM 1" CYLINDER

217
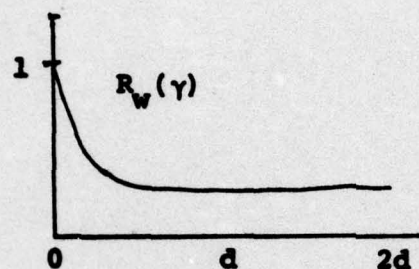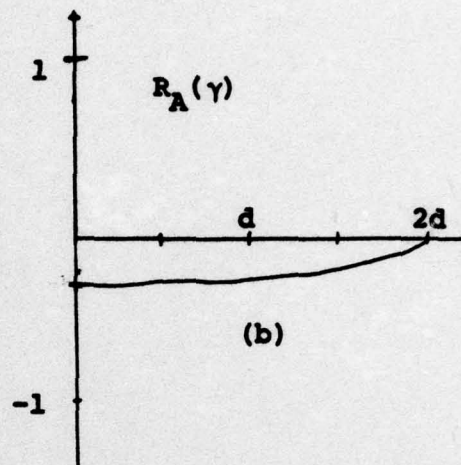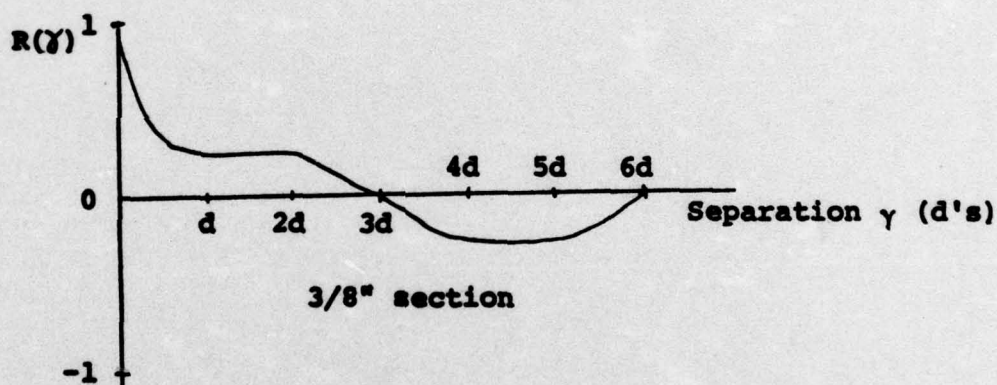
FIGURE C-44. CORRELATION FUNCTIONS: REGULAR
MULTINOTCHED CYLINDER: 1/2" SECTIONS
$\overline{U}$ = 75 FT/SEC

218
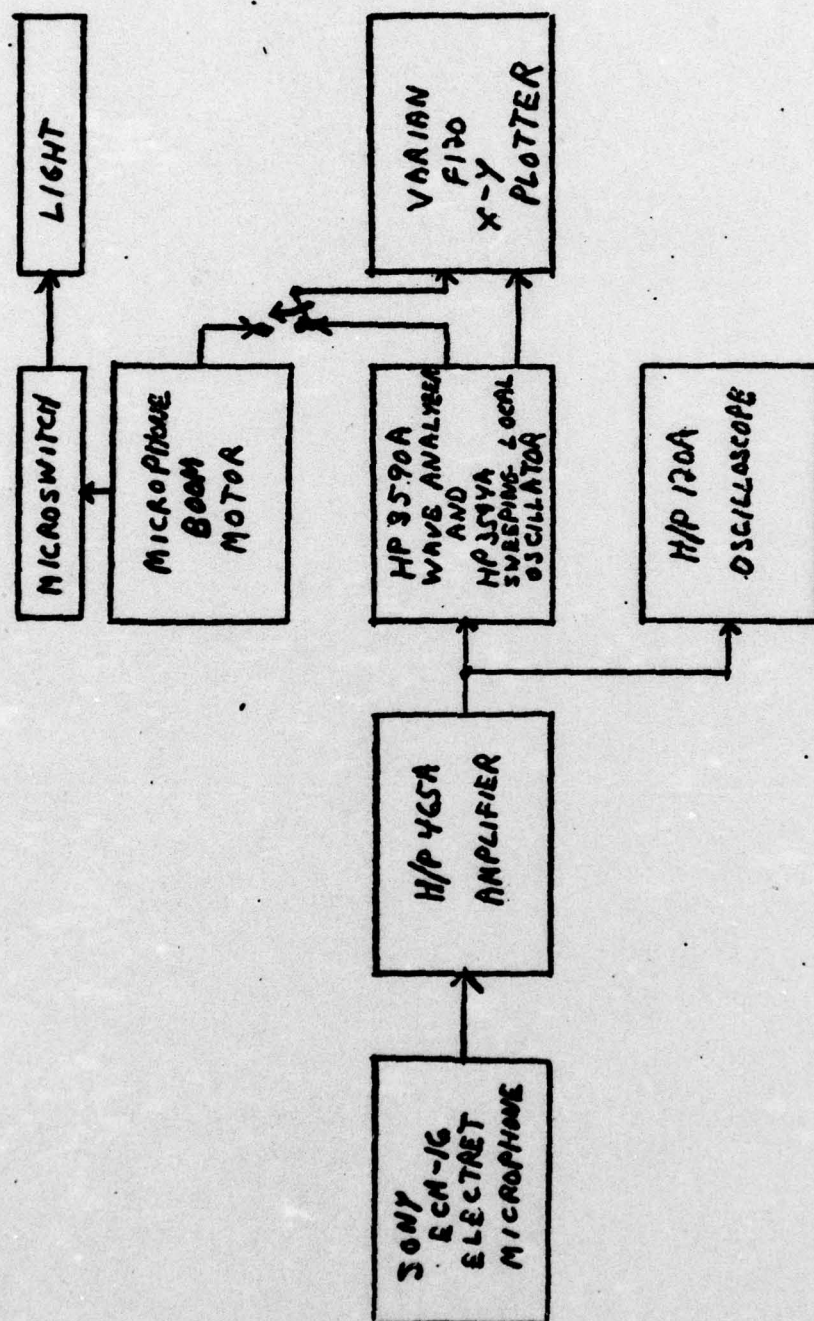
FIGURE C-45. ELECTRONICS FOR SOUND INTENSITY MEASUREMENT
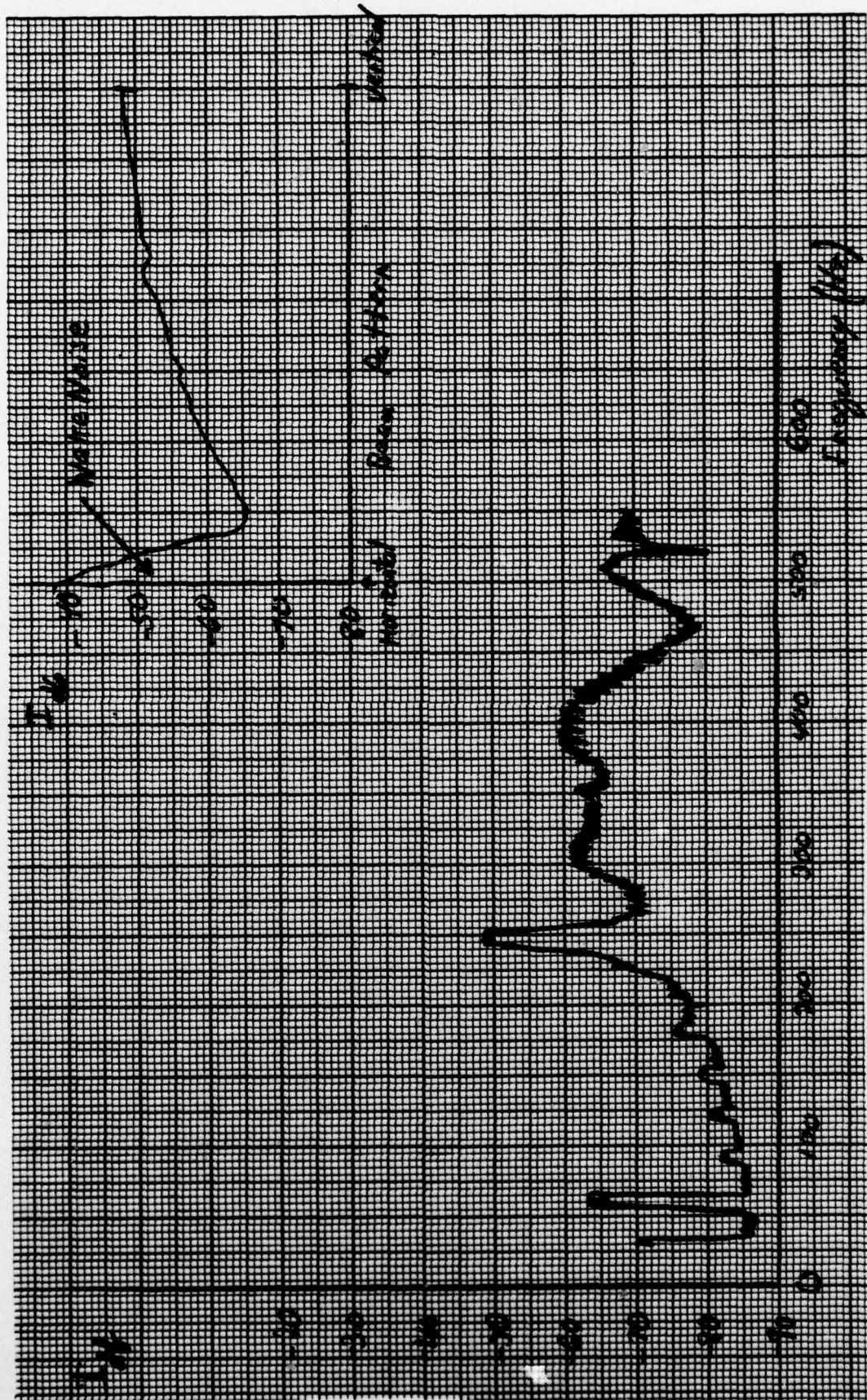
FIGURE C-46. MEASURED I: UNIFORM 1/2" CYLINDER; $\bar{U}$ = 51.5 FT/SEC

220
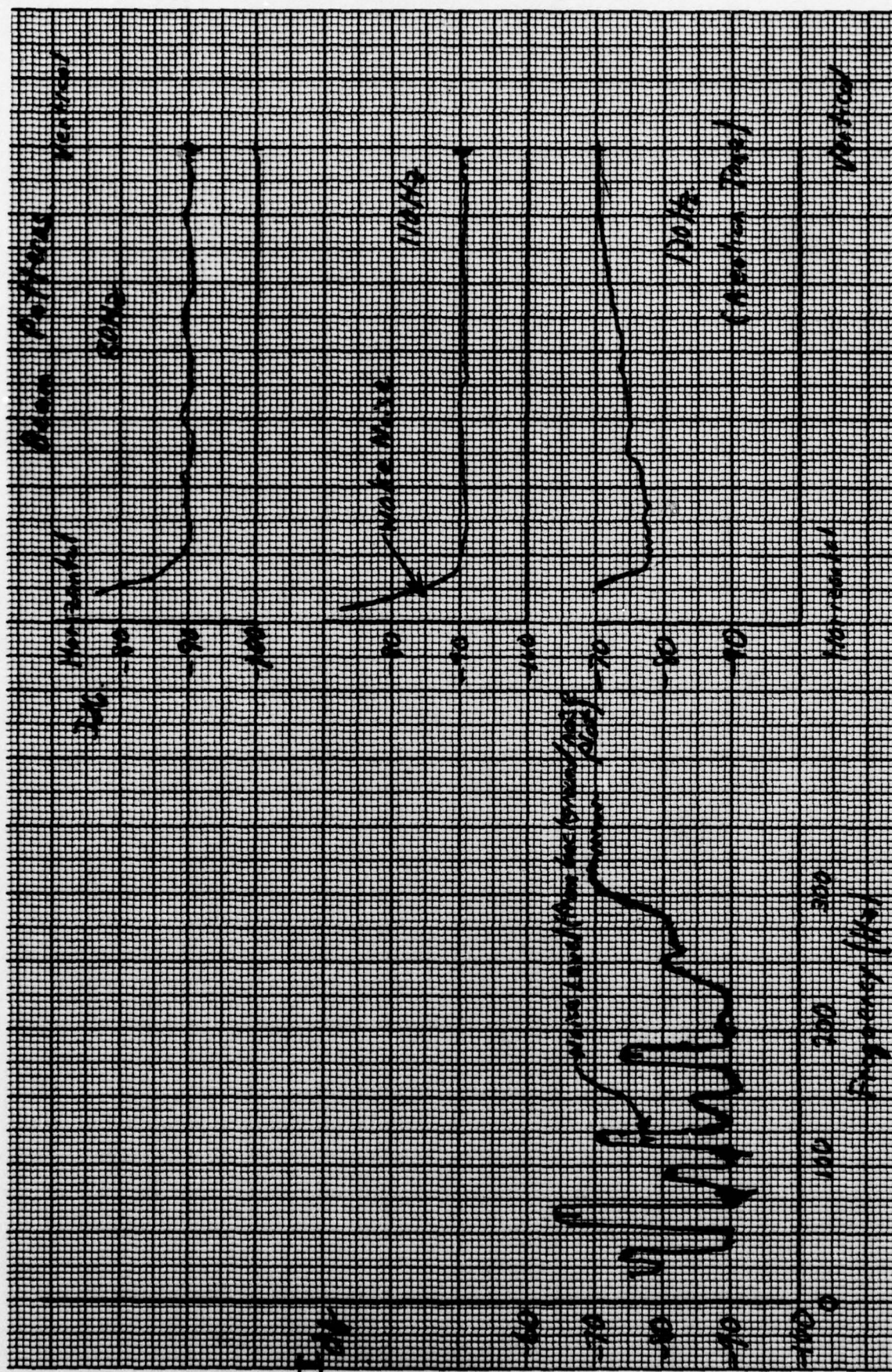
FIGURE C-47. MEASURED I: ROUGHENED 1/2" CYLINDER: $\bar{U}$ = 28 FT/SEC

221
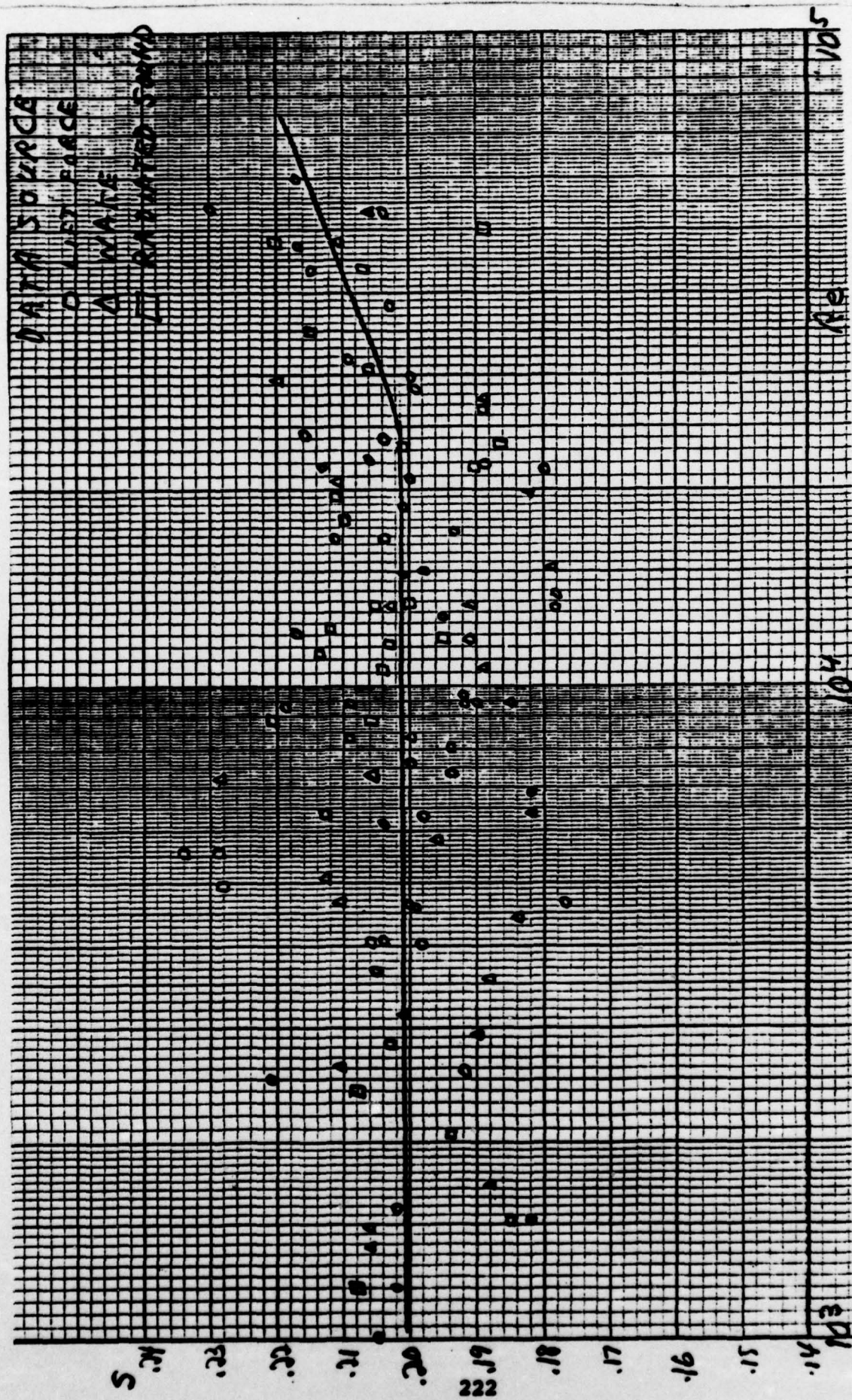
FIGURE C-48. STROUHAL NUMBER(S) VS REYNOLDS NUMBER (Re) FOR UNIFORM CYLINDER

222
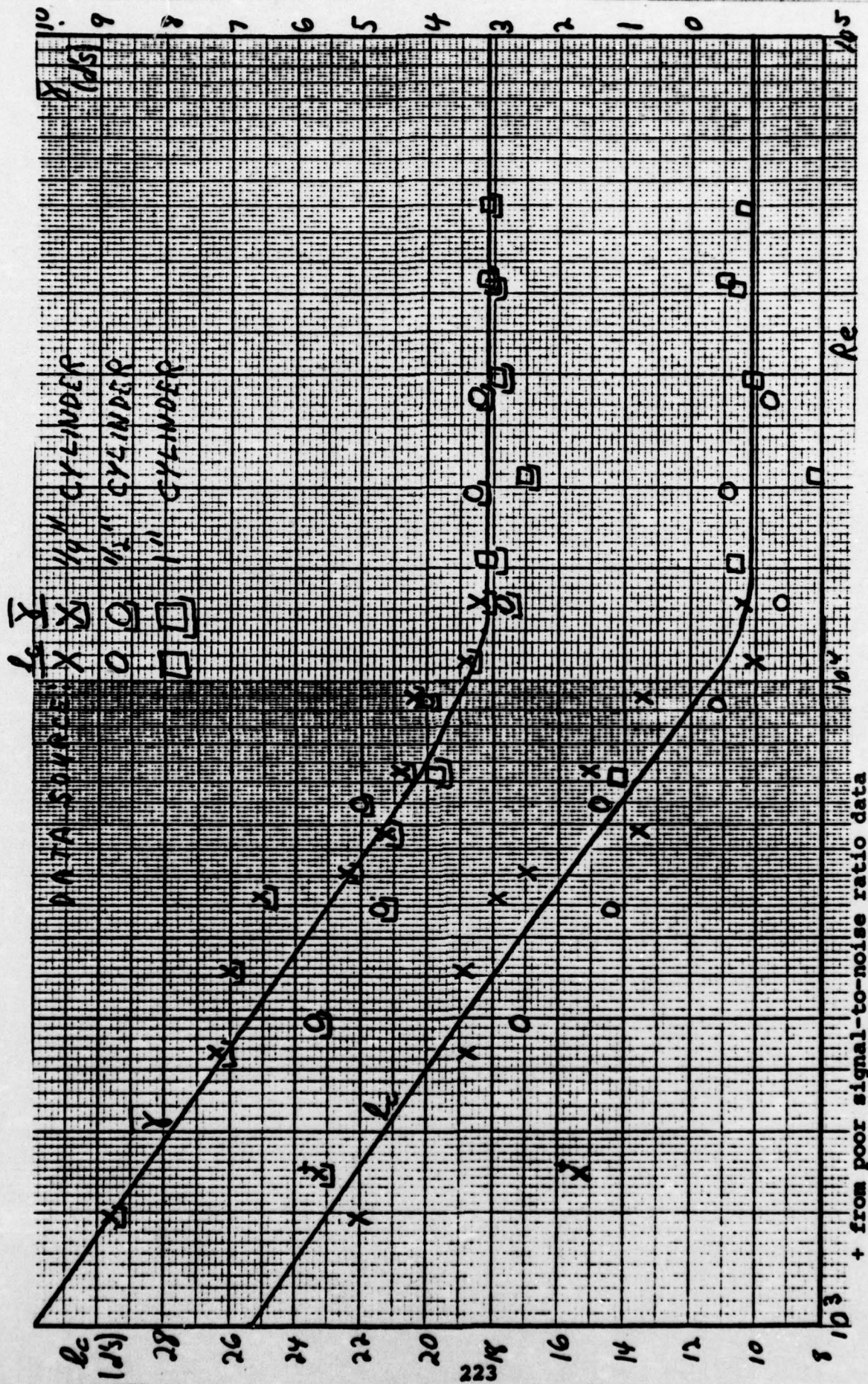
FIGURE C-49. CORRELATION LENGTH AND CENTROID OF ONE-SIDED CORRELATION CURVE
VS REYNOLDS NUMBER FOR UNIFORM CYLINDERS

223
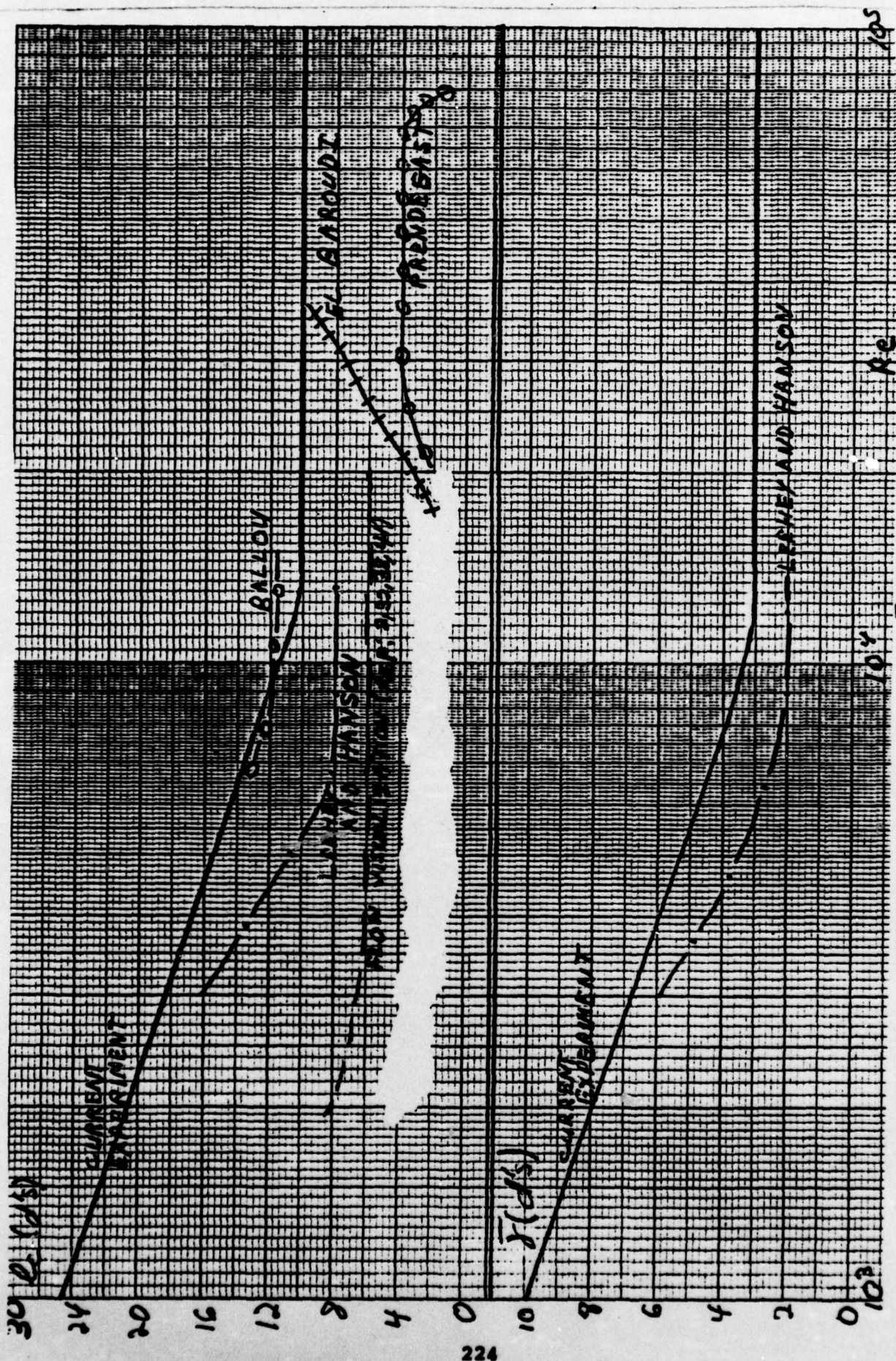
FIGURE C-50.   COMPARISON OF CURRENT l_c AND $\bar{\gamma}$ VALUES WITH PREVIOUS REPORTS

FIGURE C-51
C_L: UNIFORM CYLINDERS

225

FIGURE C-52
COMPARISON OF MEASURED
C_L WITH PREVIOUS RESULTS
IN THE LITERATURE
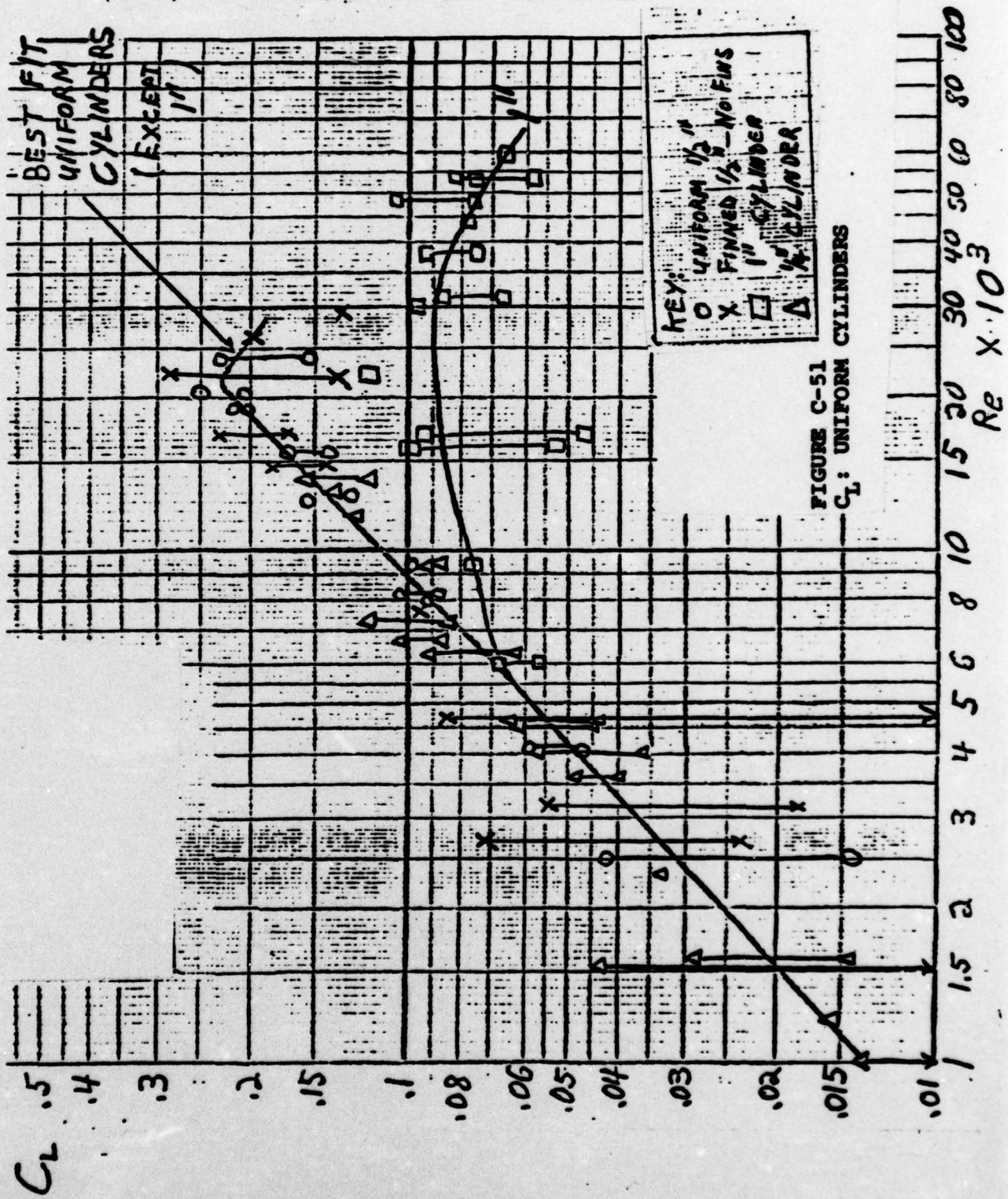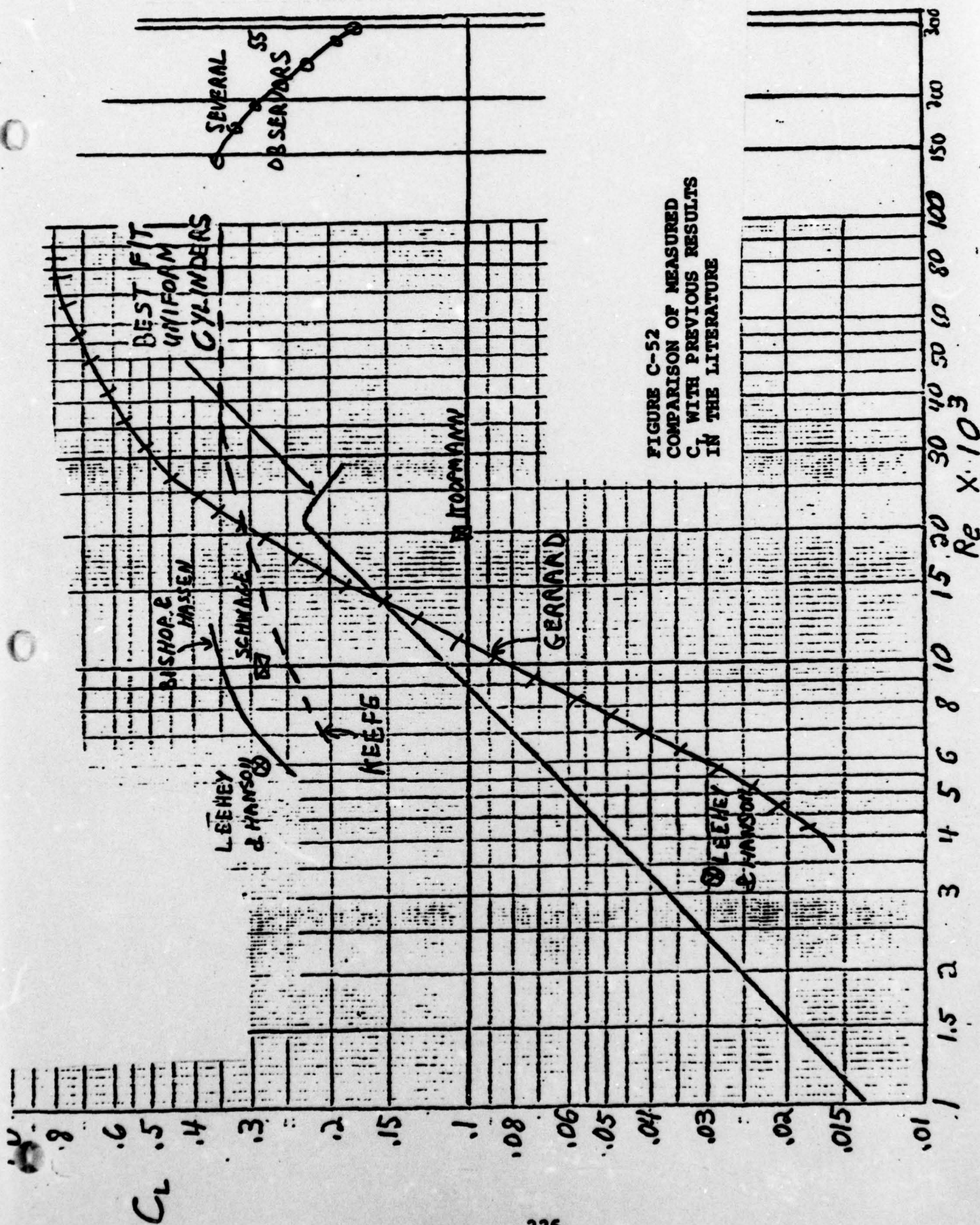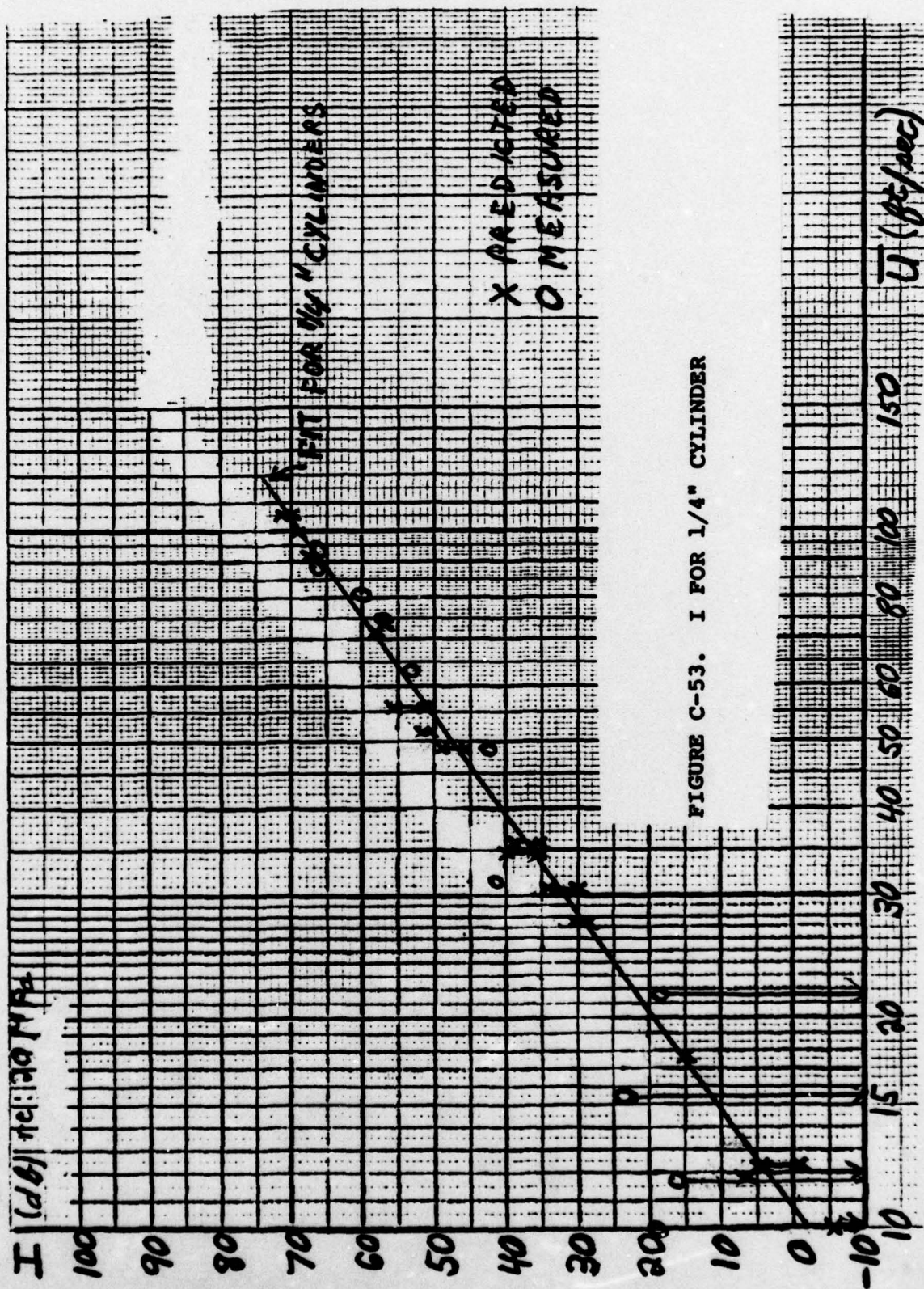
FIGURE C-53. I FOR 1/4" CYLINDER
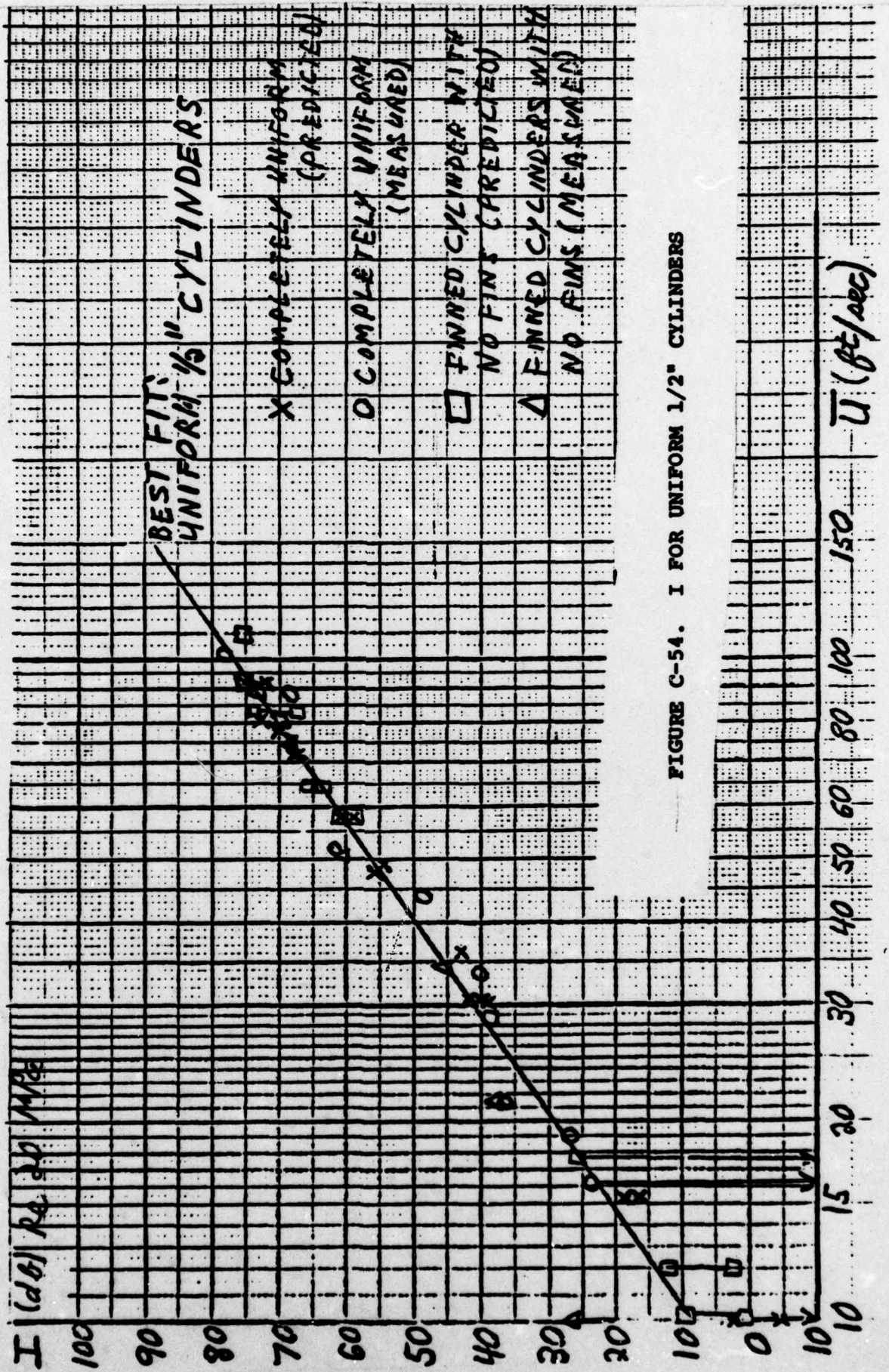
FIGURE C-54.   I FOR UNIFORM 1/2" CYLINDERS

228
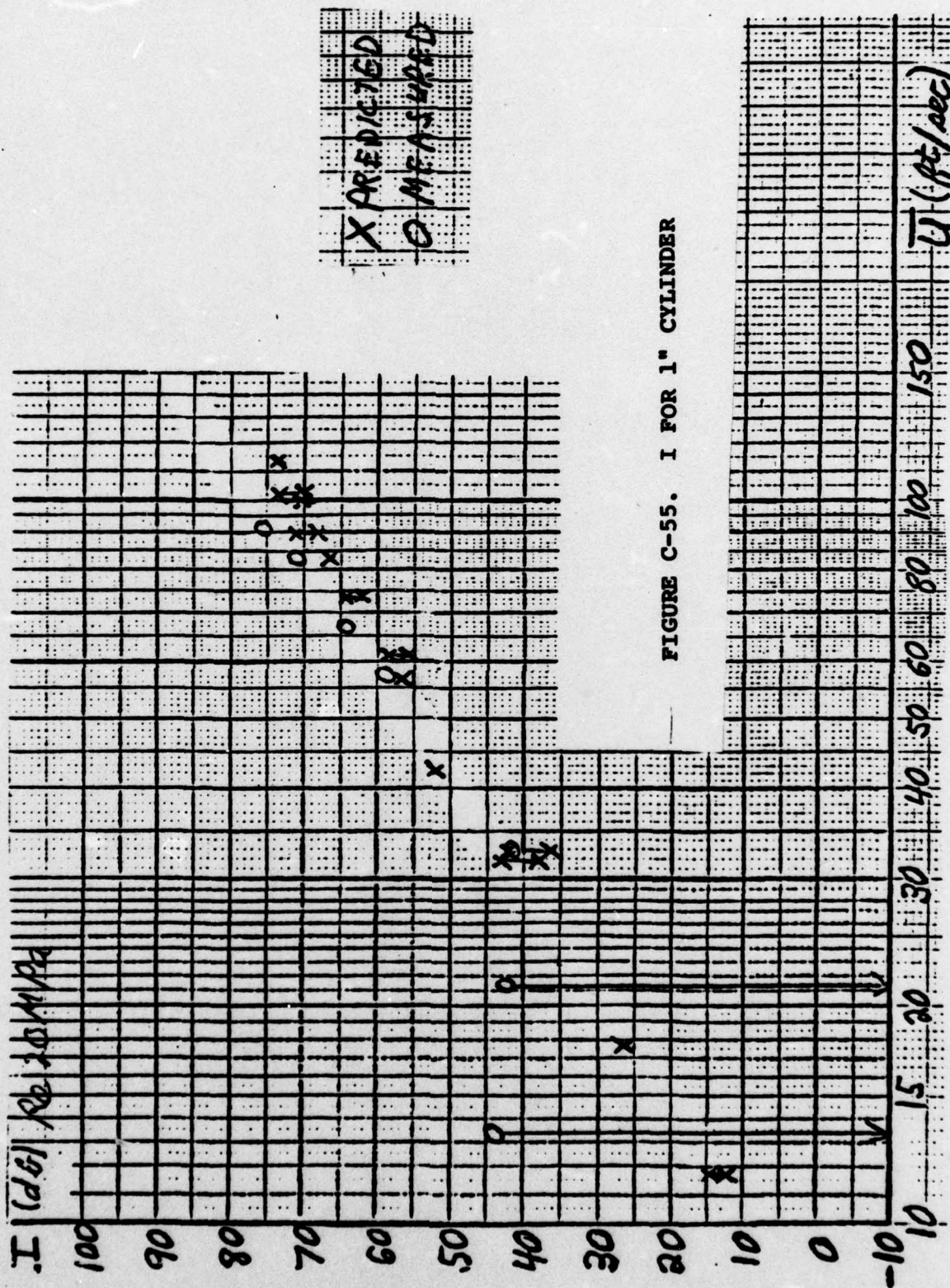
FIGURE C-55. I FOR 1" CYLINDER
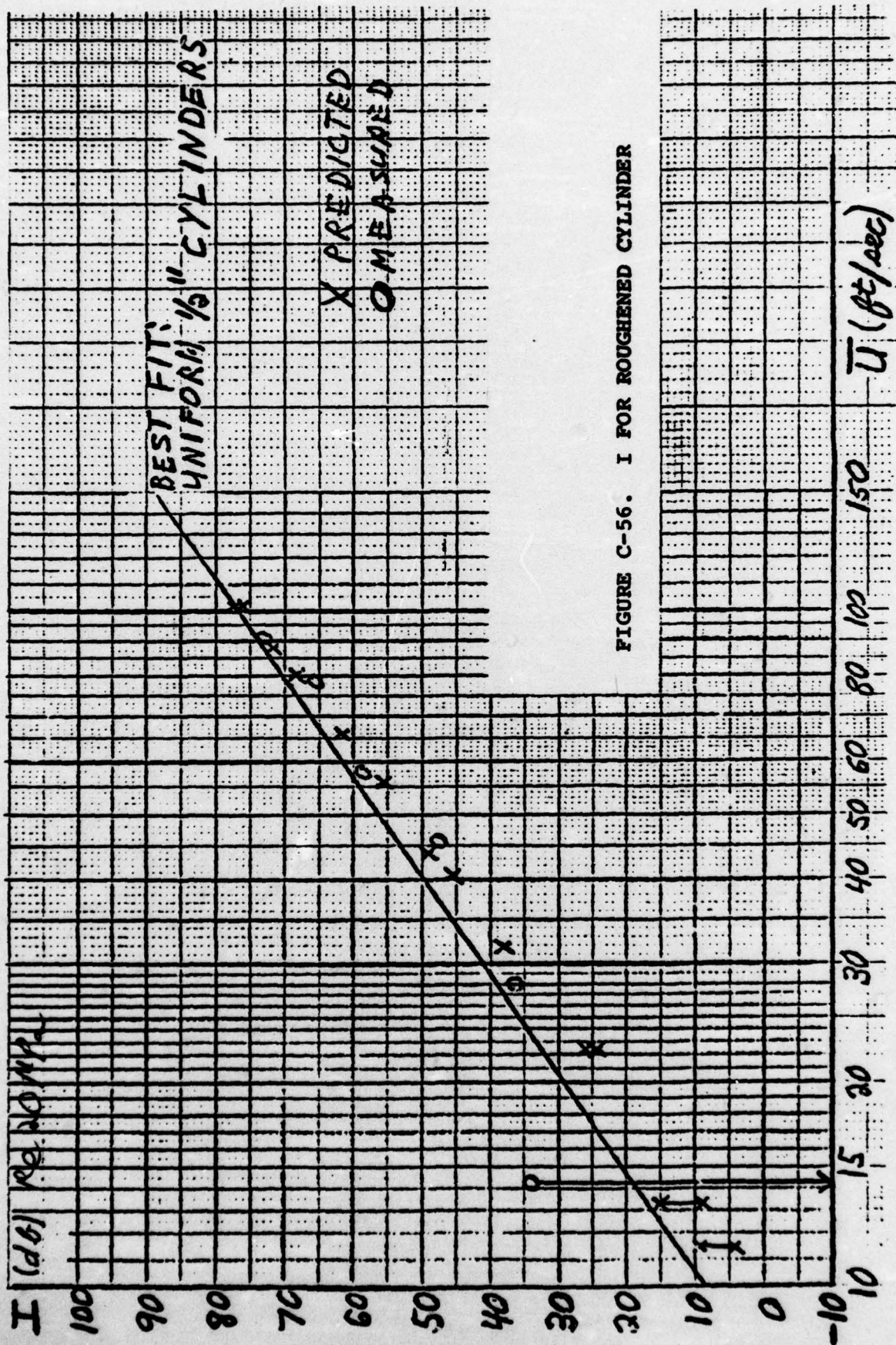
FIGURE C-56. I FOR ROUGHENED CYLINDER
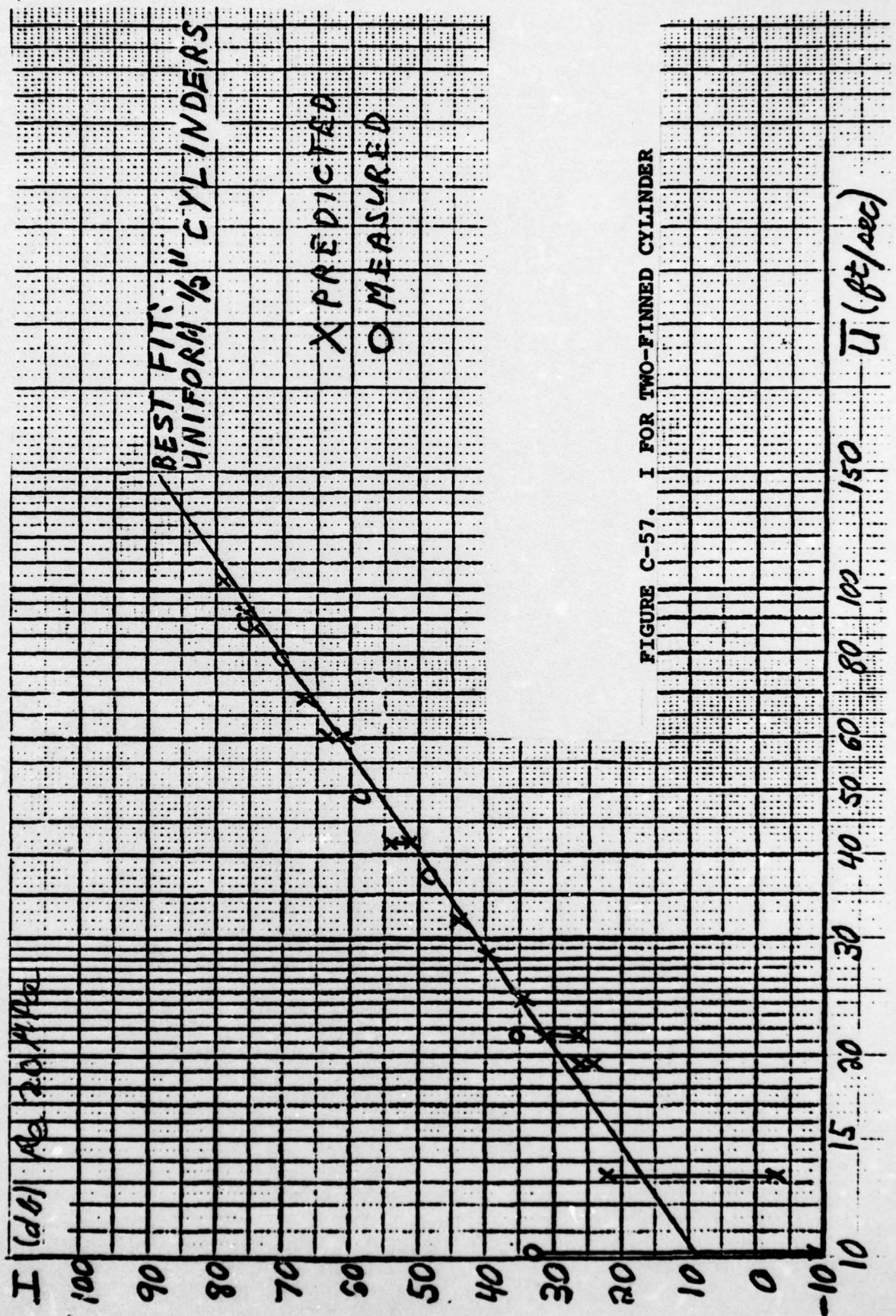
FIGURE C-57. I FOR TWO-FINNED CYLINDER

231
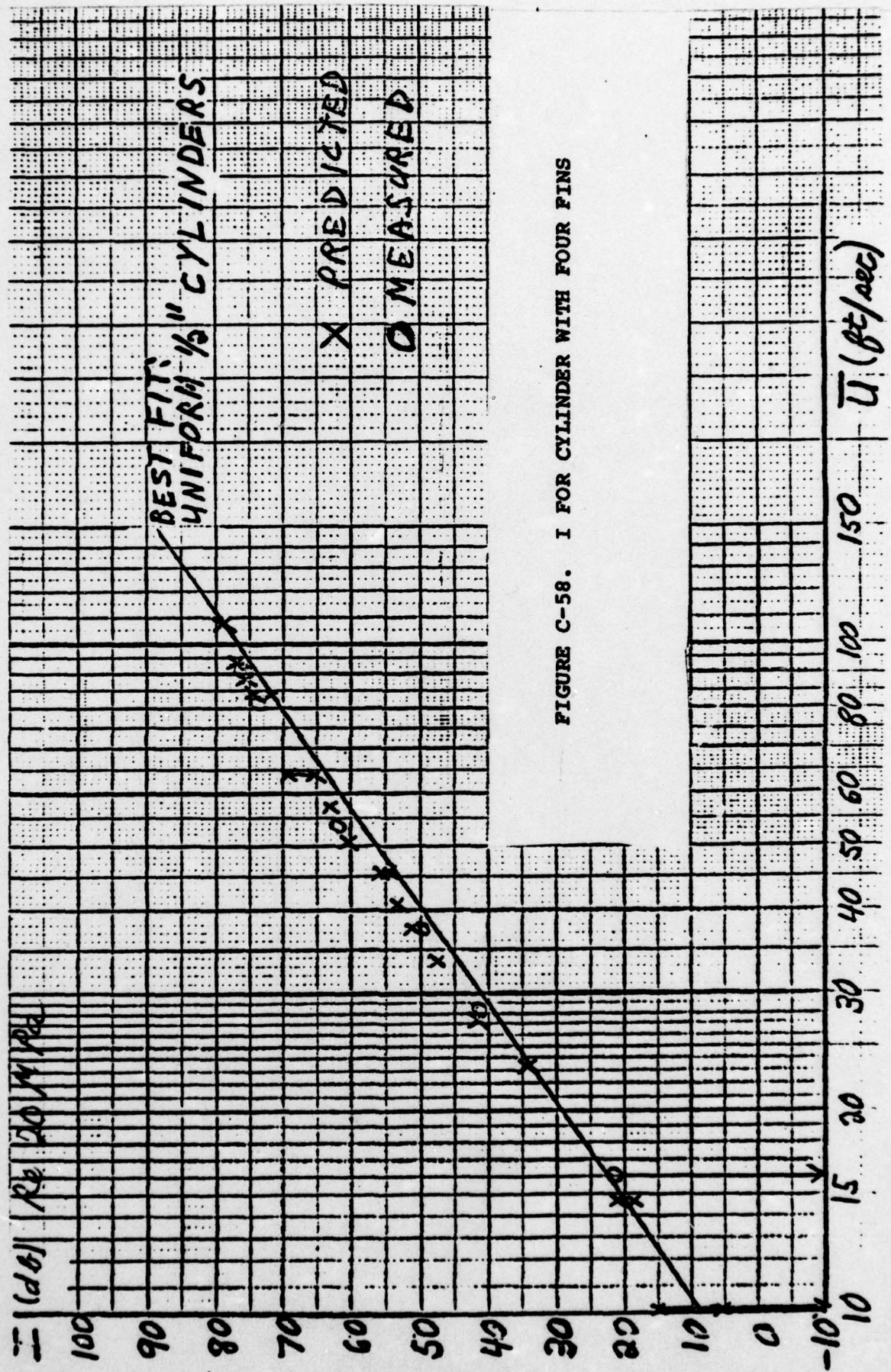
FIGURE C-58. I FOR CYLINDER WITH FOUR FINS
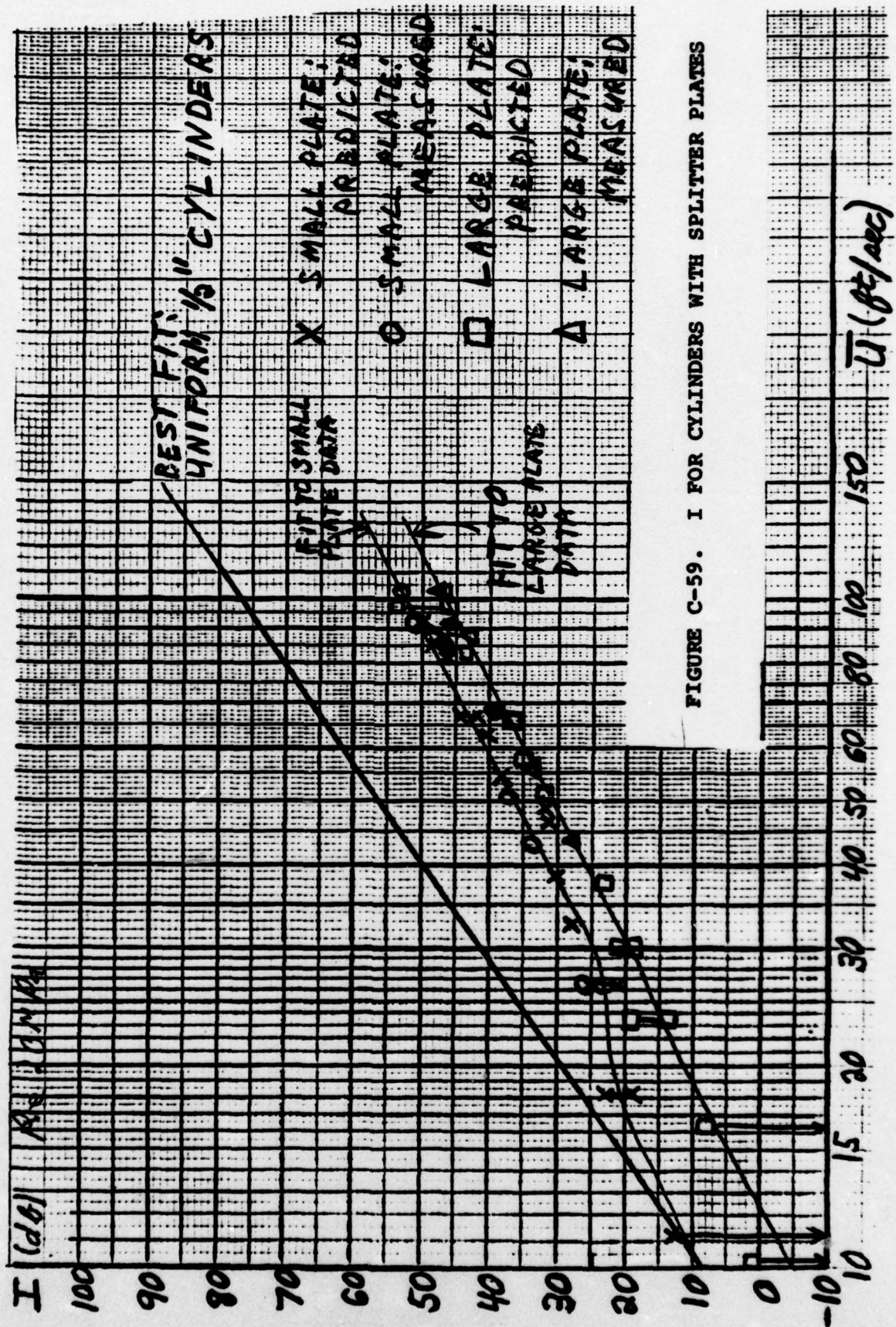
FIGURE C-59. I FOR CYLINDERS WITH SPLITTER PLATES
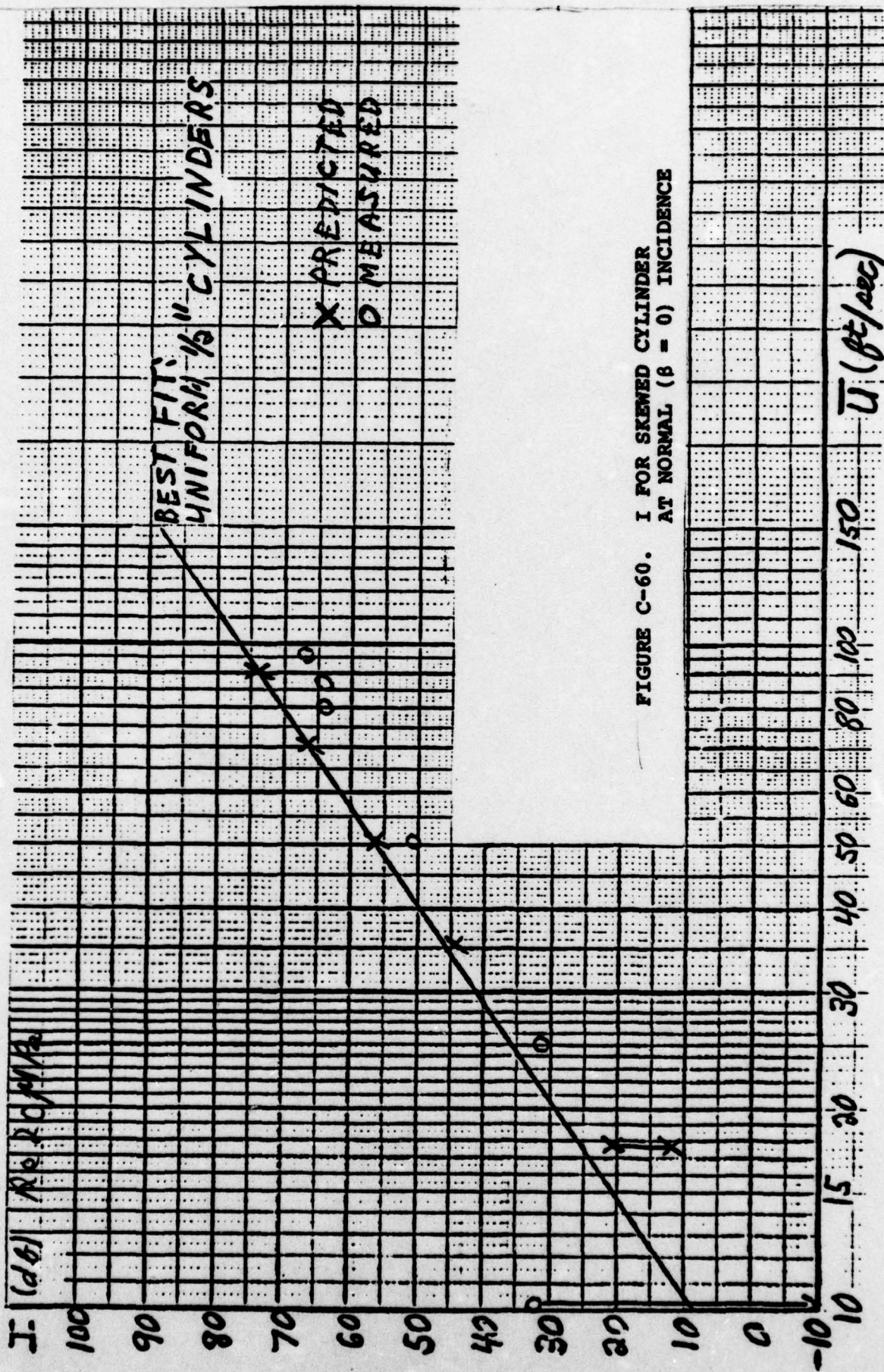
FIGURE C-60. I FOR SKEWED CYLINDER AT NORMAL (β = 0) INCIDENCE

234
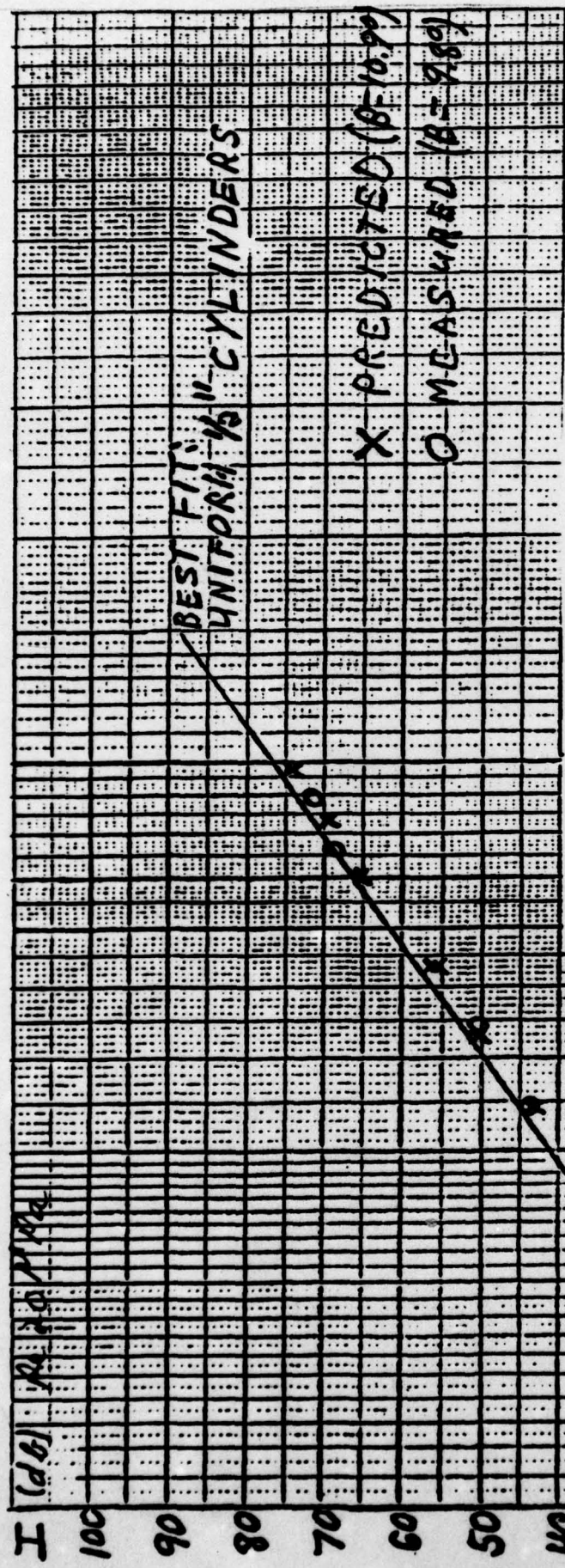
FIGURE C-61.   I FOR SKEWED CYLINDER: β = 10°
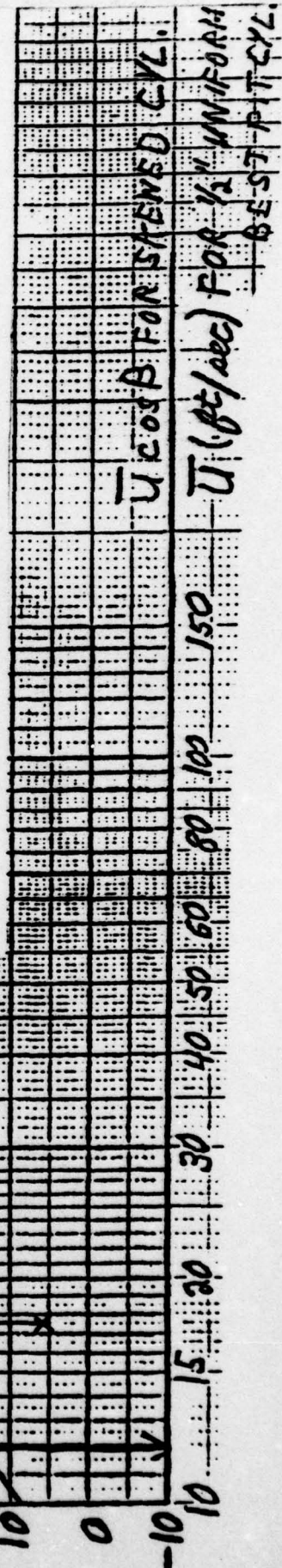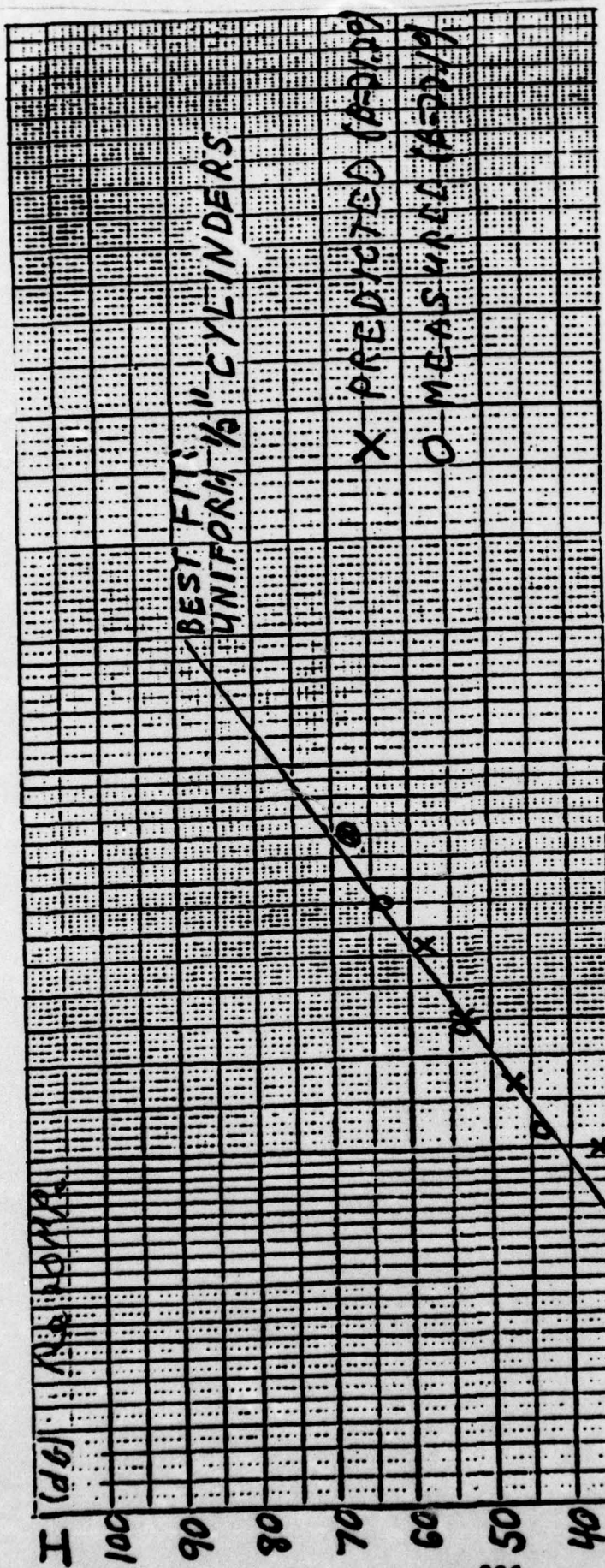
FIGURE C-62. I FOR SKEWED CYLINDER: β = 21°
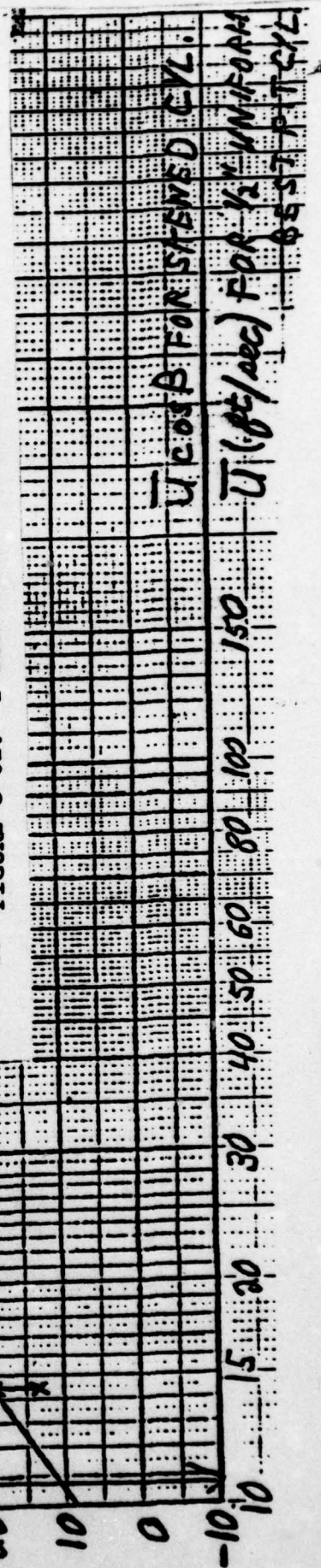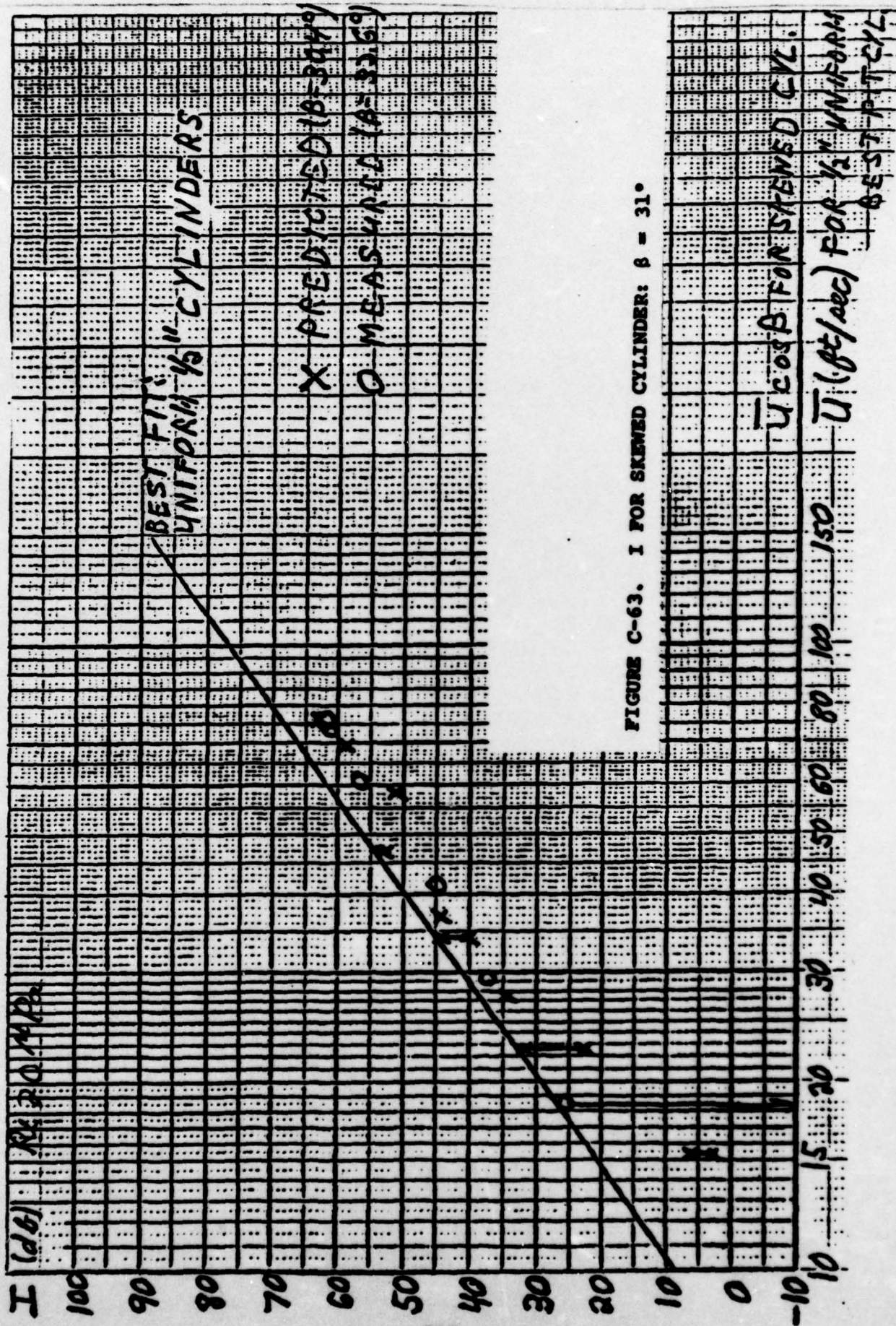
FIGURE C-63. I FOR SKEWED CYLINDER: β = 31°

237

FIGURE C-64.   I FOR SKEWED CYLINDER: β = 39°
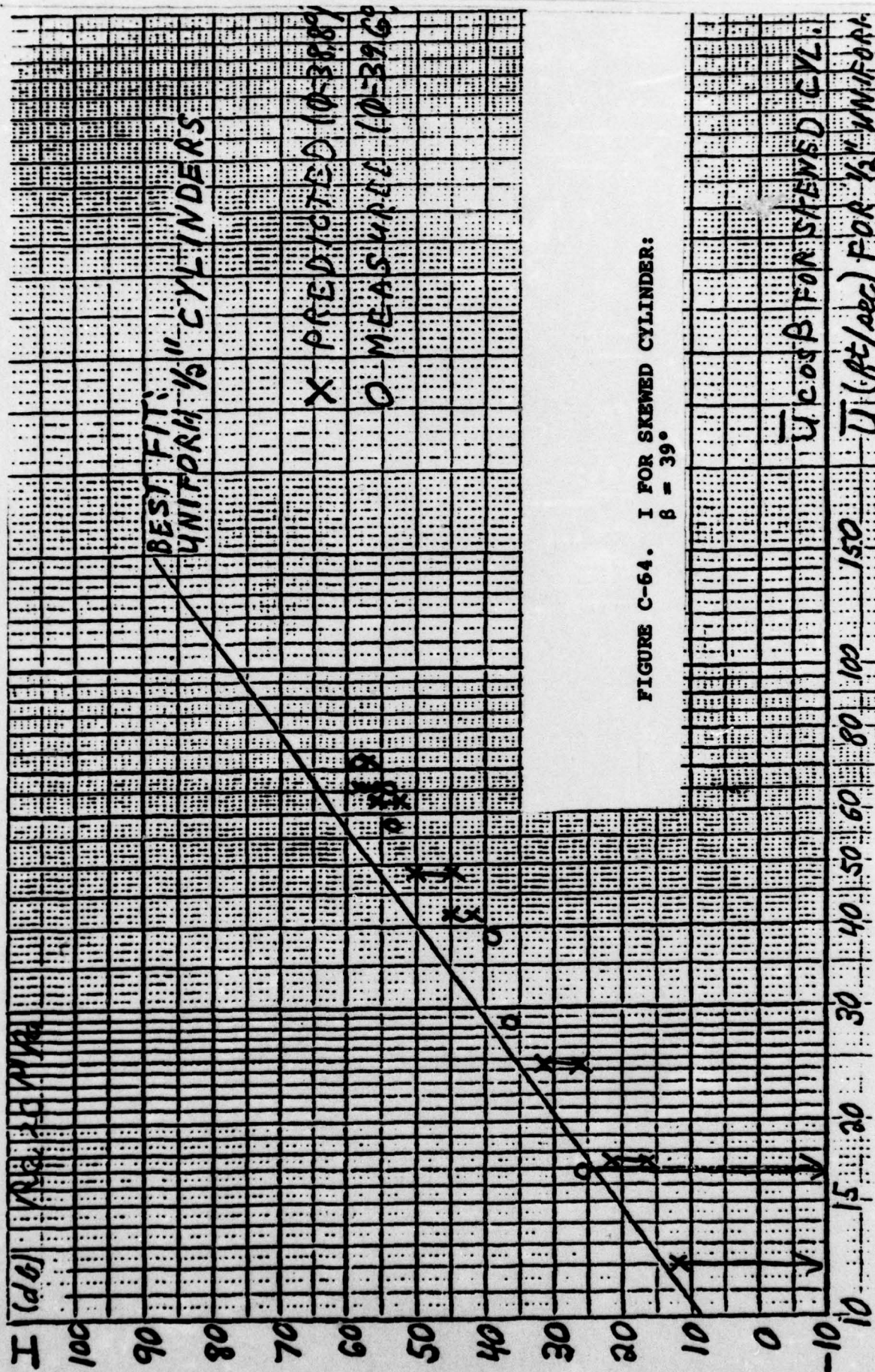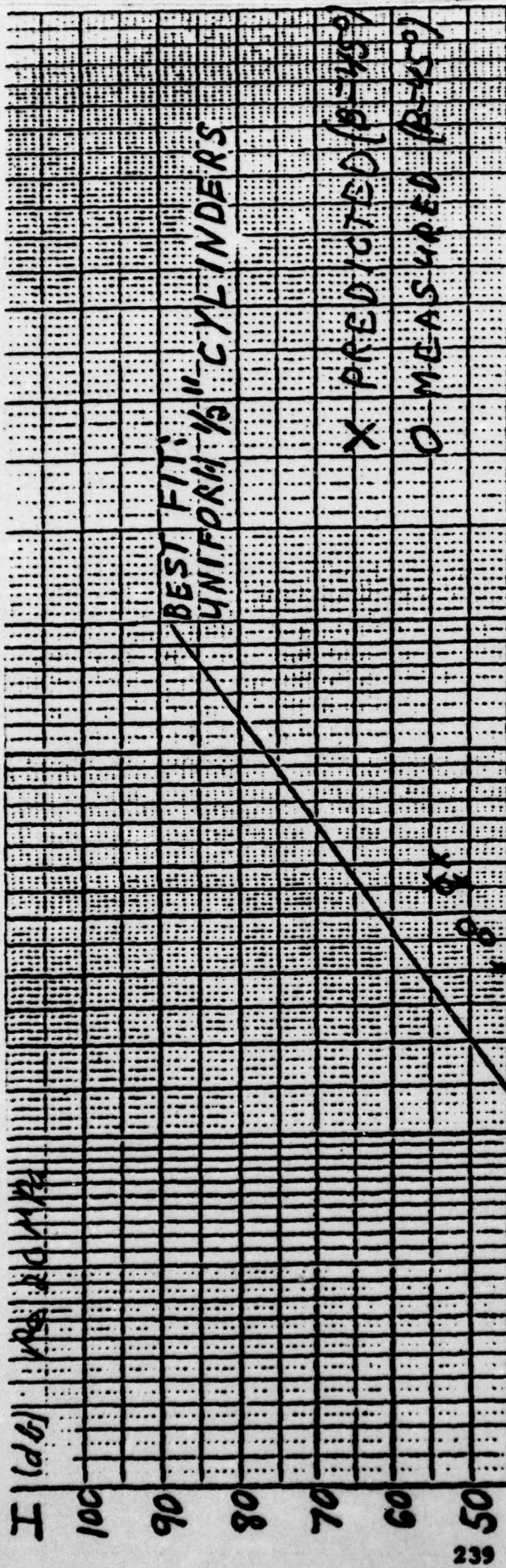
FIGURE C-65. I FOR SKEWED CYLINDER
$\beta = 45°$
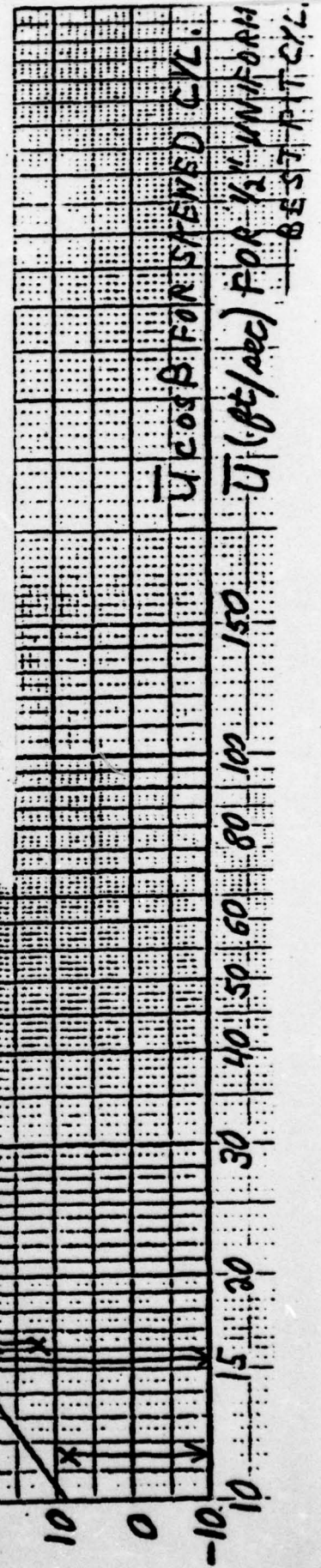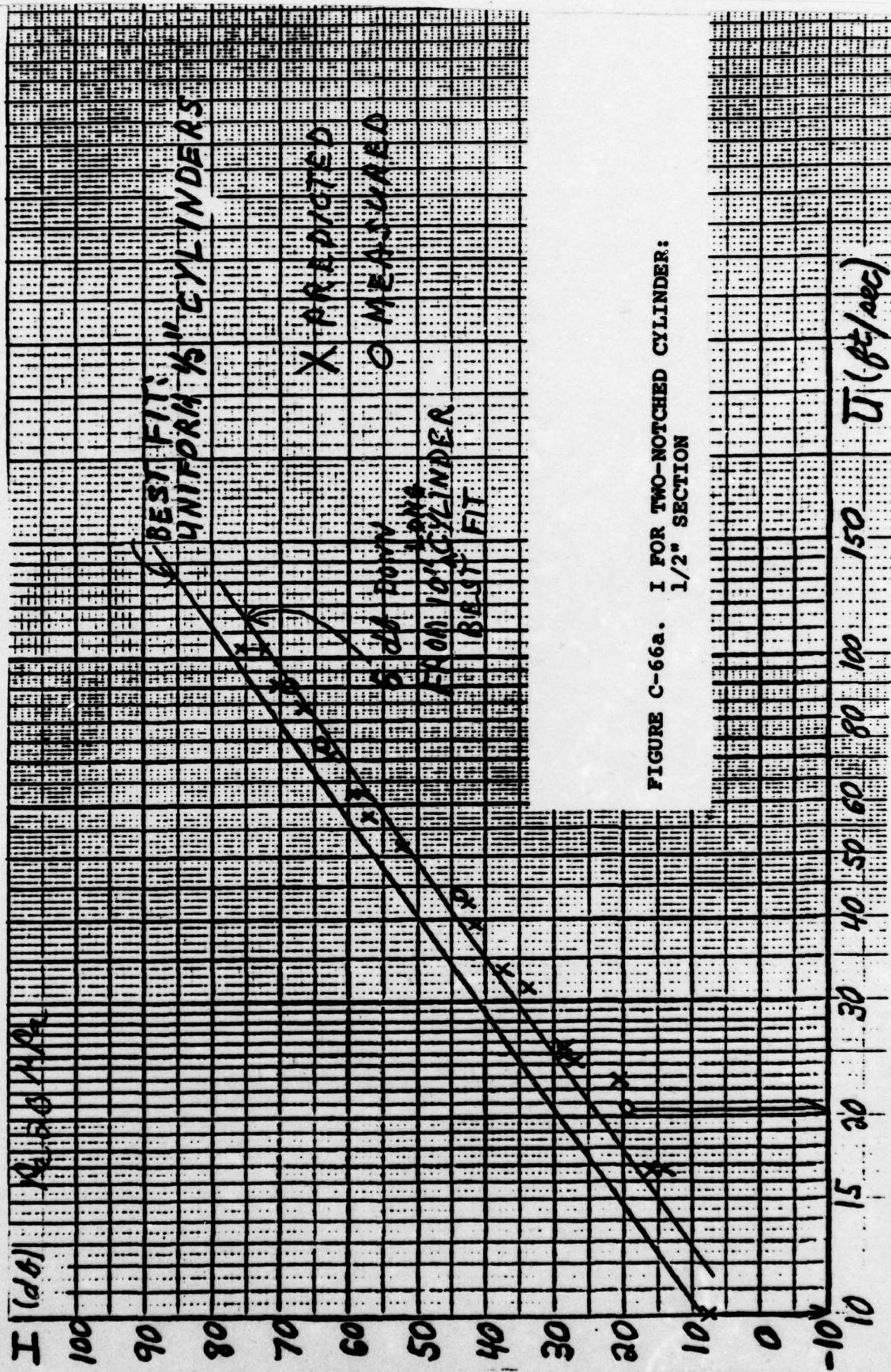
FIGURE C-66a. I FOR TWO-NOTCHED CYLINDER:
1/2" SECTION
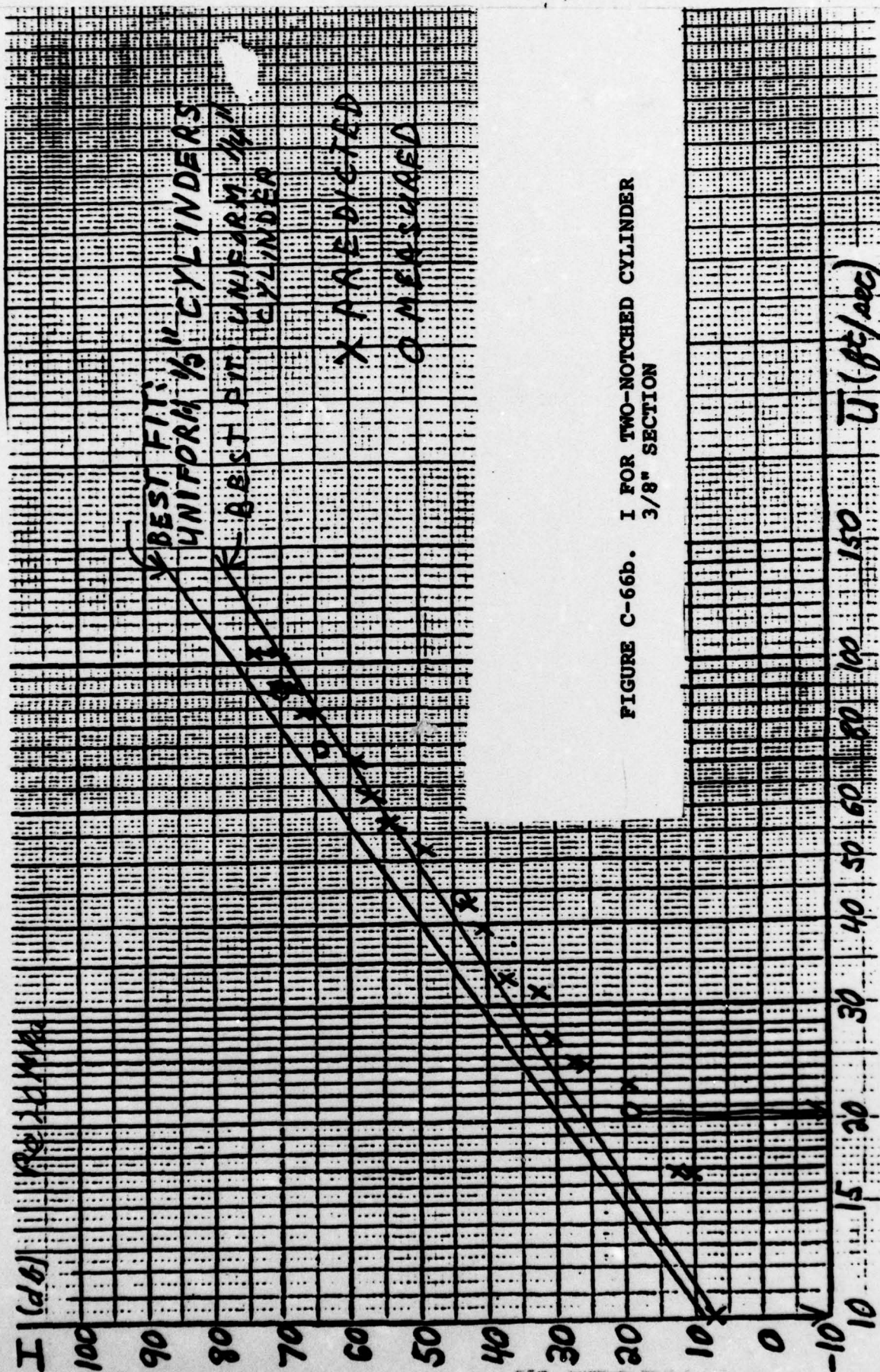
FIGURE C-66b. I FOR TWO-NOTCHED CYLINDER
3/8" SECTION

BEST FIT, UNIFORM 1/3" CYLINDERS

ABS. PTT. UNIFORM 1/4" CYLINDER

X AVERAGED
O MEASURED

$\sqrt{U} (-ft/sec)$

$I (db)$

241
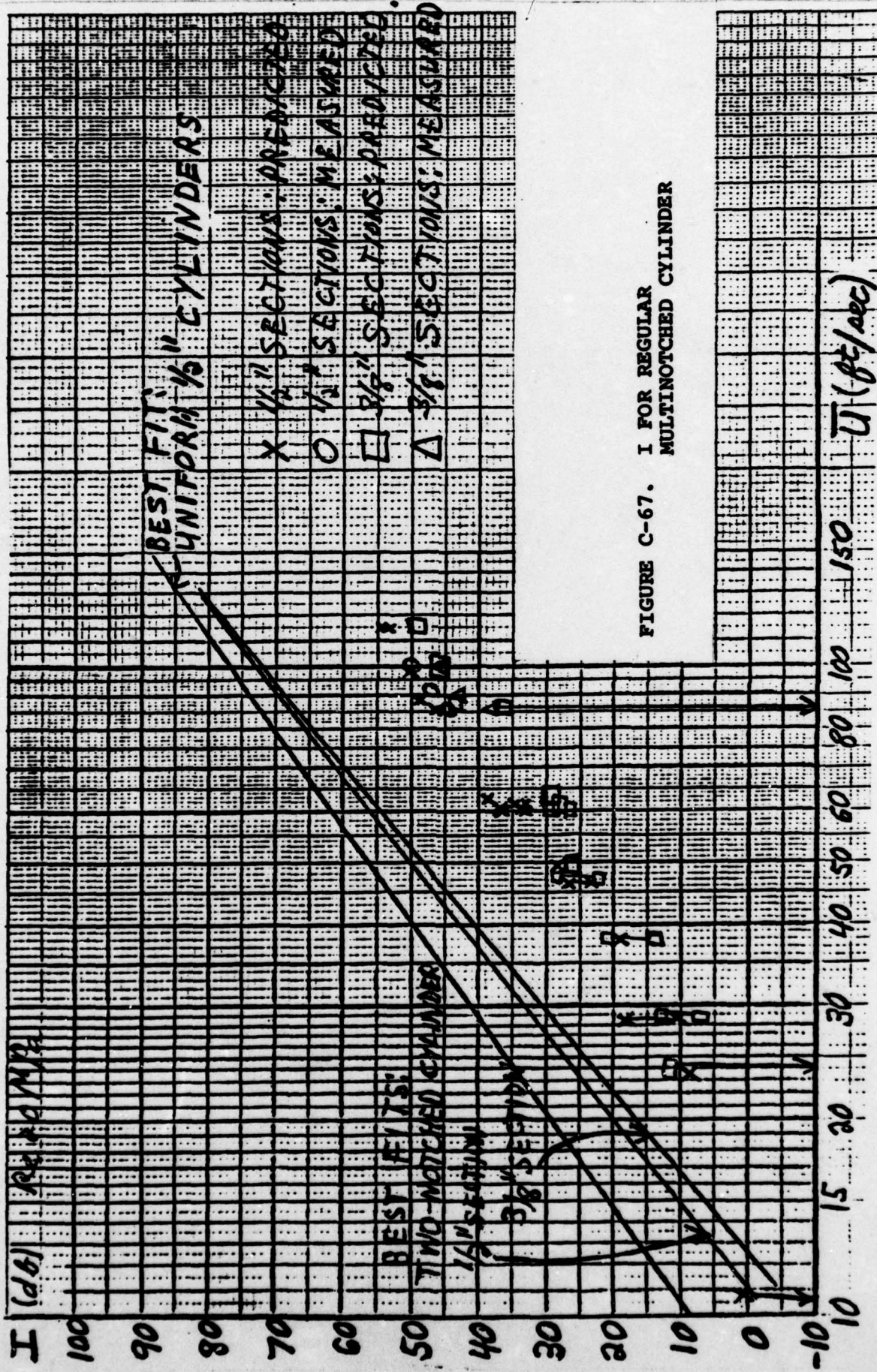
FIGURE C-67. I FOR REGULAR
MULTINOTCHED CYLINDER

242

FIGURE C-68.   ROUGHENED CYLINDER C_L

243

FIGURE C-69. ℓ_c AND $\bar{\gamma}$ FOR THE ROUGHENED CYLINDER

x ℓ_c
o $\bar{\gamma}$

244
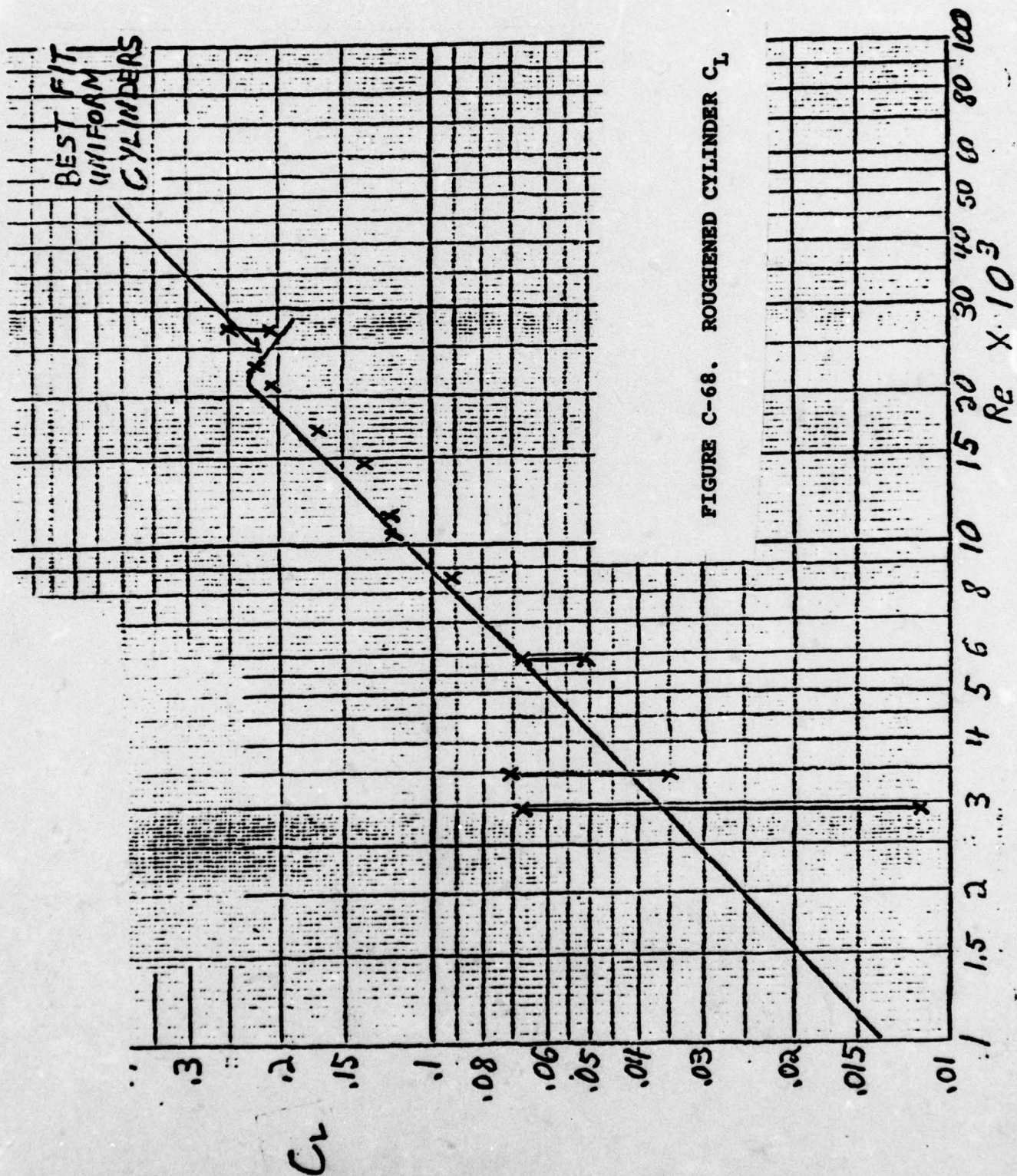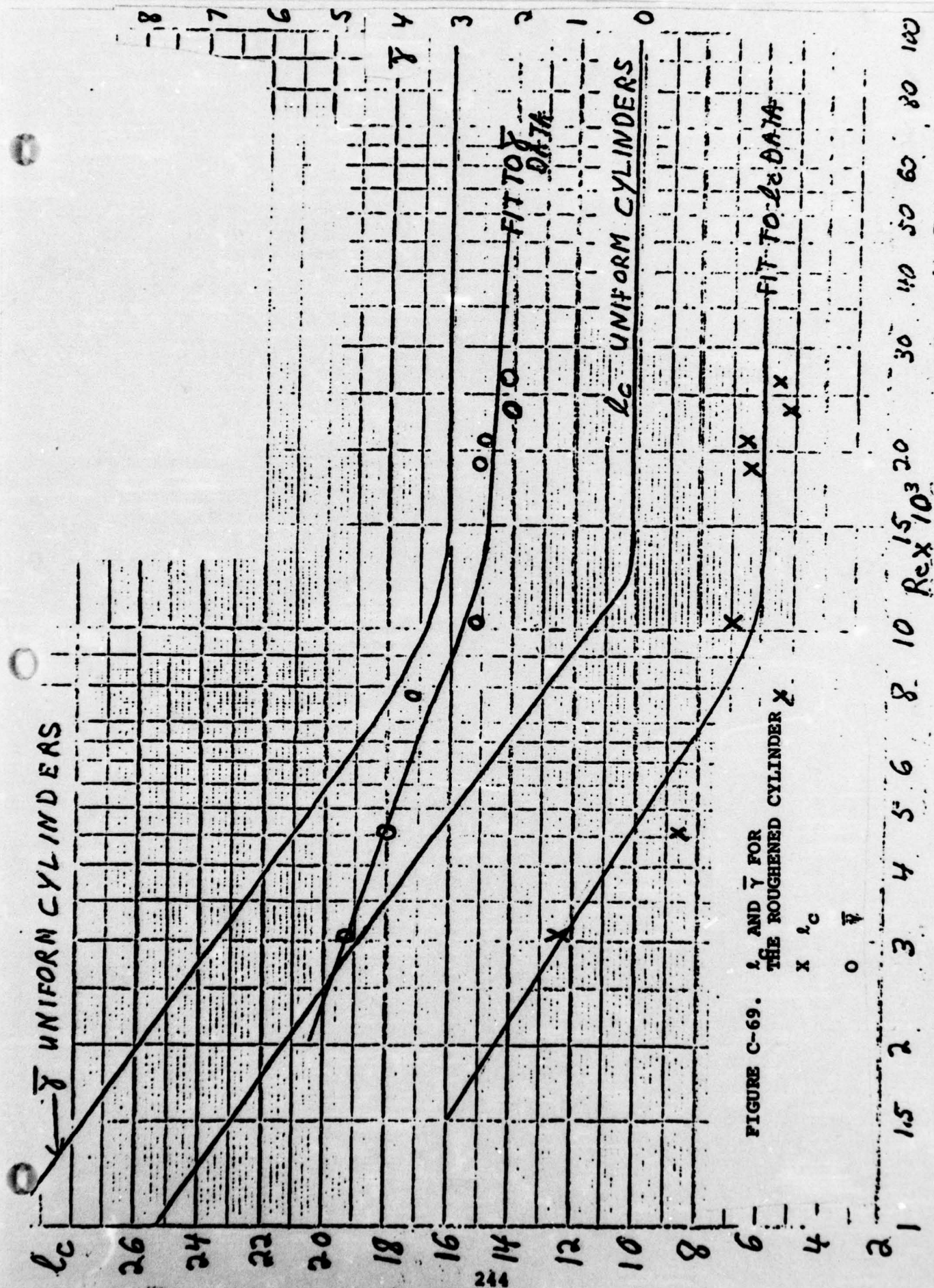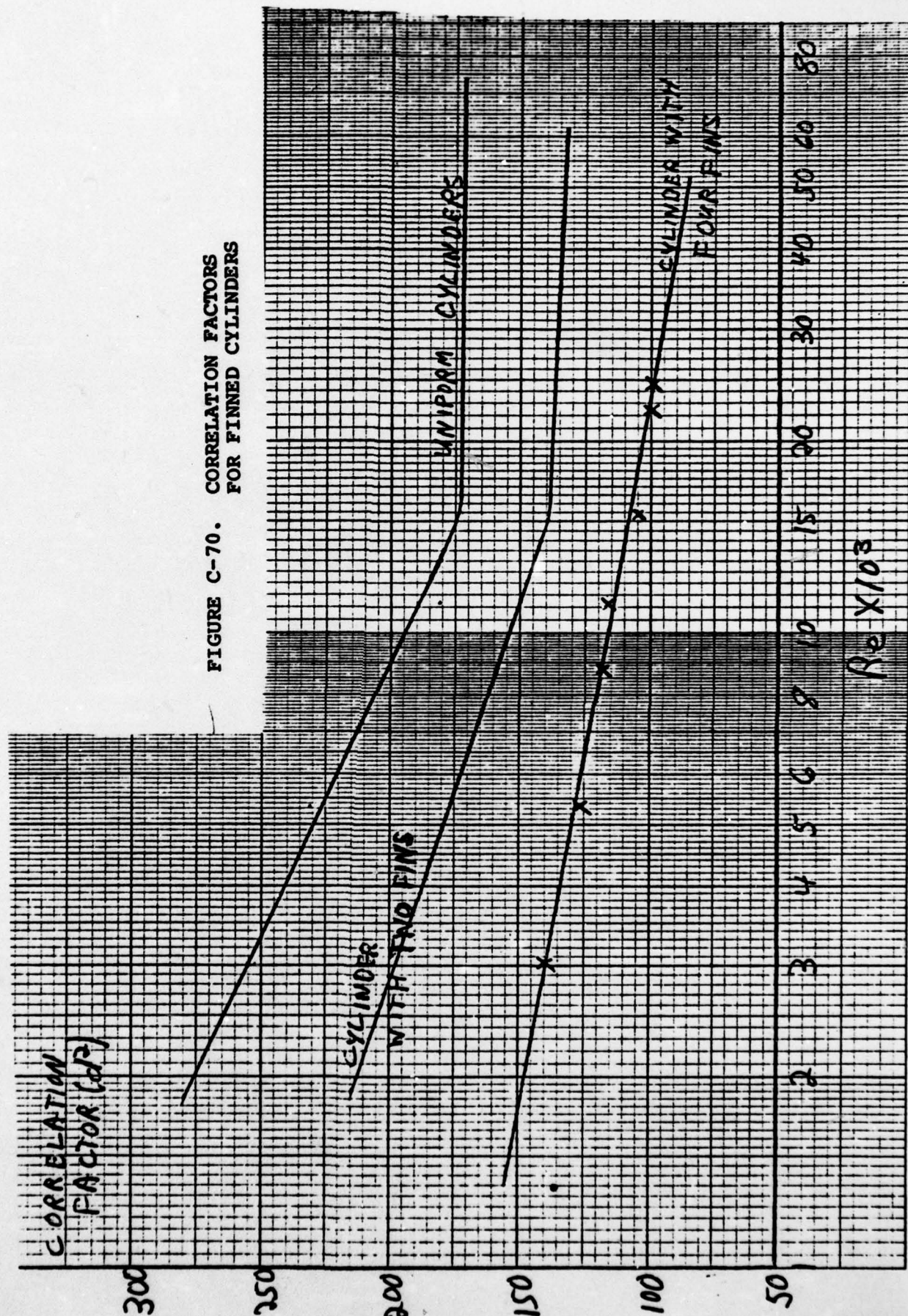
FIGURE C-70. CORRELATION FACTORS FOR FINNED CYLINDERS
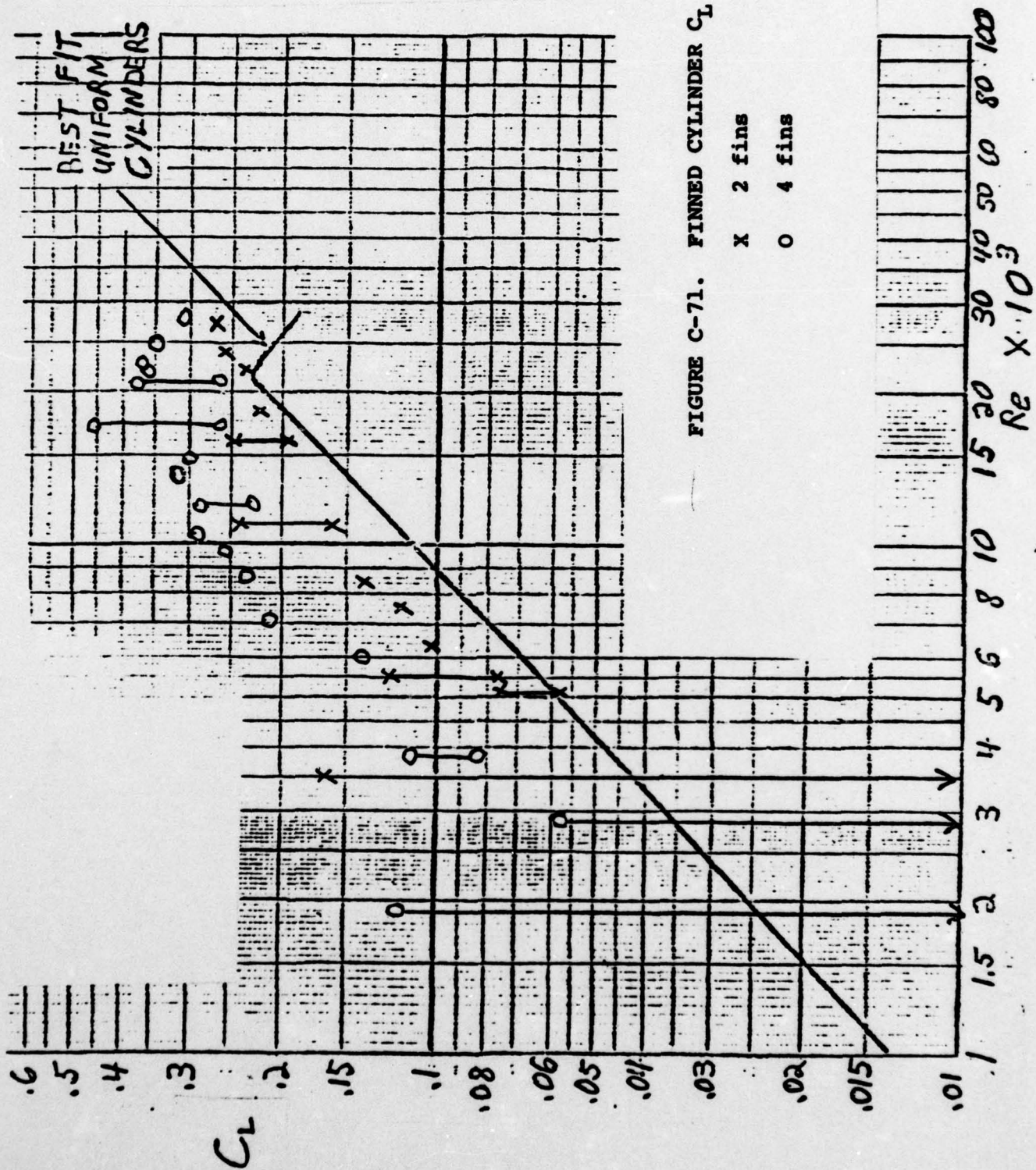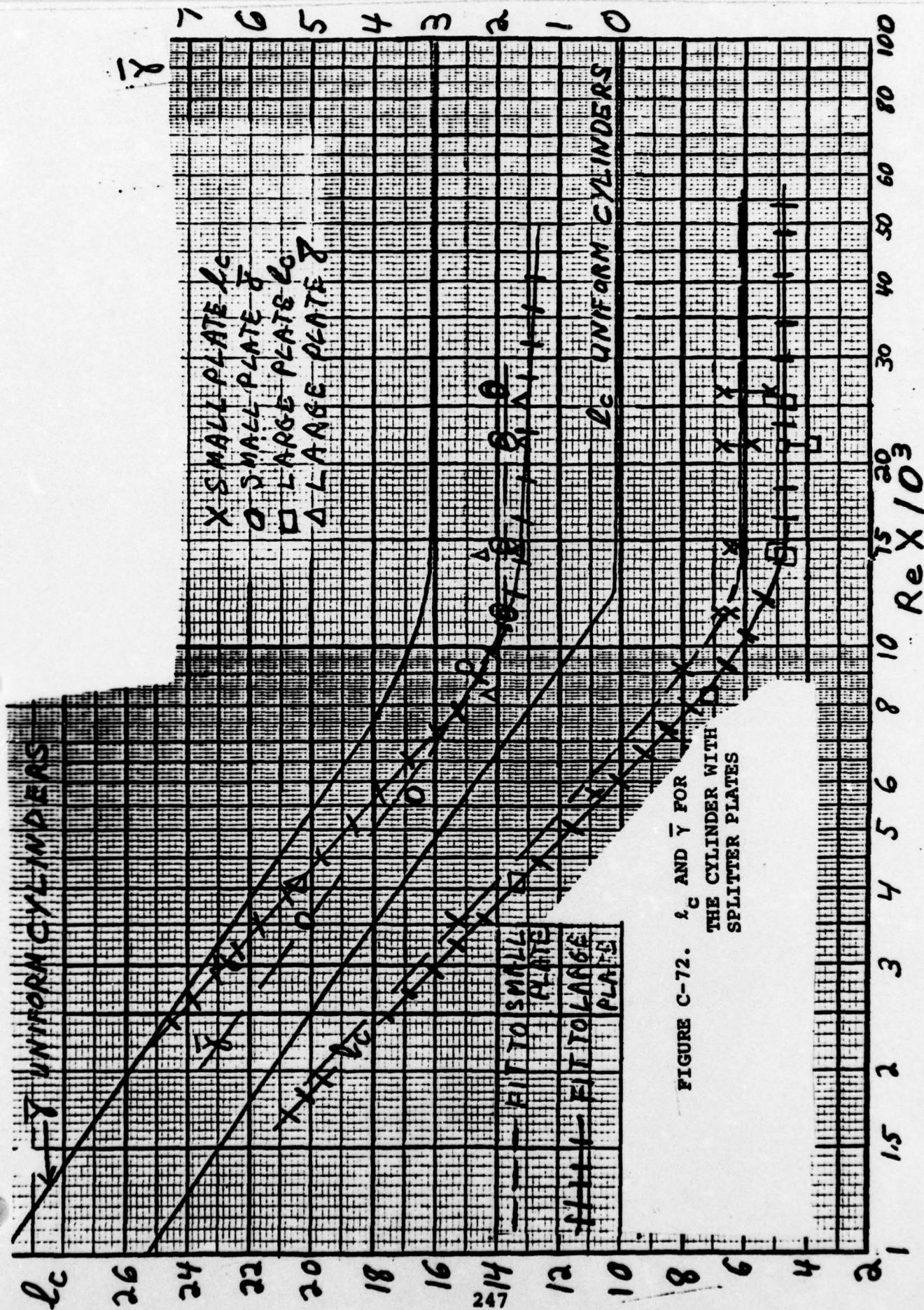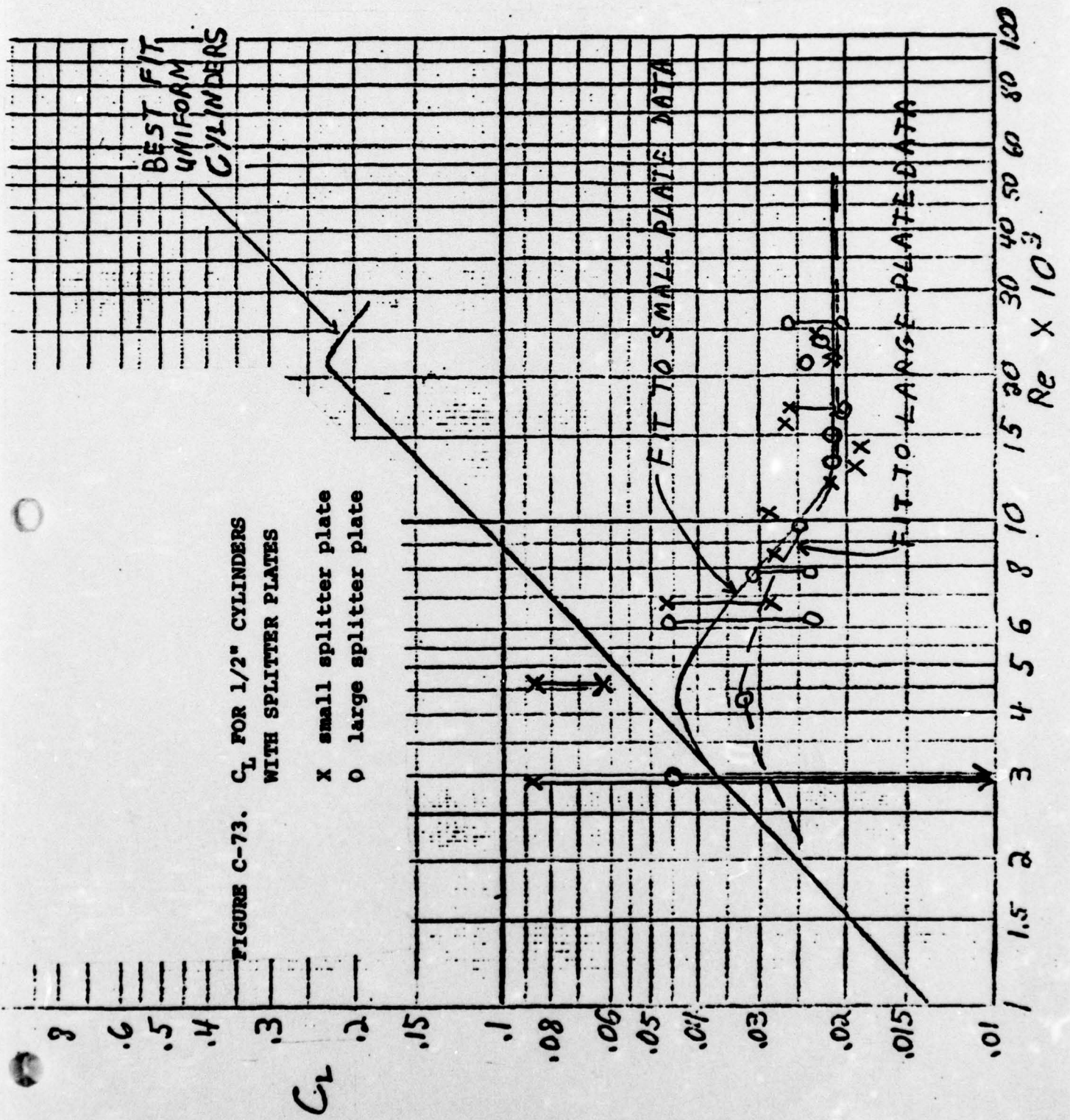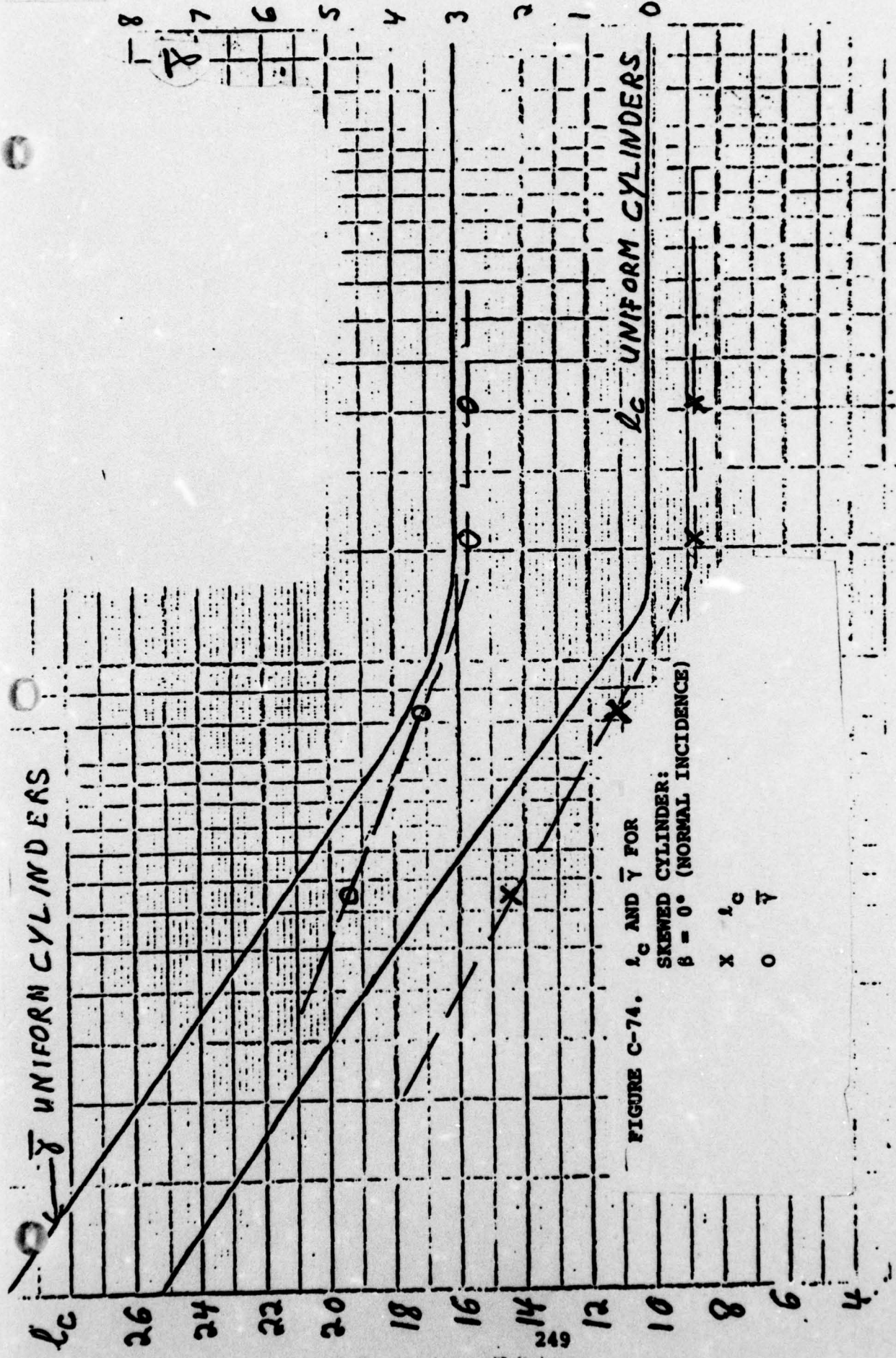
FIGURE C-71. FINNED CYLINDER C_L

x 2 fins

o 4 fins

FIGURE C-72. ℓ_c AND $\bar{\gamma}$ FOR
THE CYLINDER WITH
SPLITTER PLATES

247

FIGURE C-73. C_L FOR 1/2" CYLINDERS WITH SPLITTER PLATES

x small splitter plate
o large splitter plate

FIGURE C-74. ℓ_c AND $\bar{\gamma}$ FOR

SKEWED CYLINDER:
$\beta = 0°$ (NORMAL INCIDENCE)

X ℓ_c
O $\bar{\gamma}$

249

FIGURE C-75. ℓ_c AND $\bar{\gamma}$ FOR SKEWED CYLINDER: $\beta = 10.9°$

X ℓ_c
O $\bar{\gamma}$
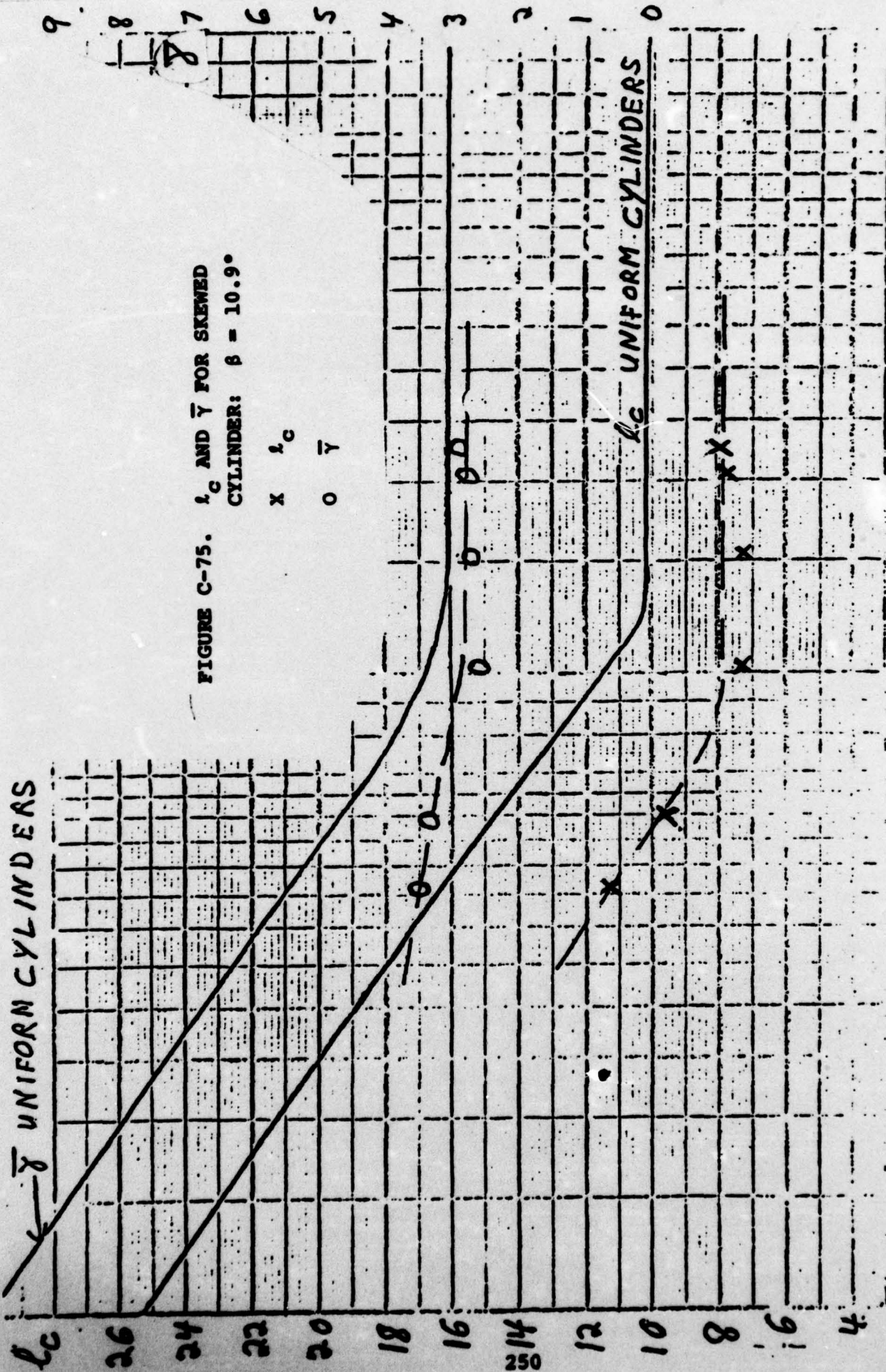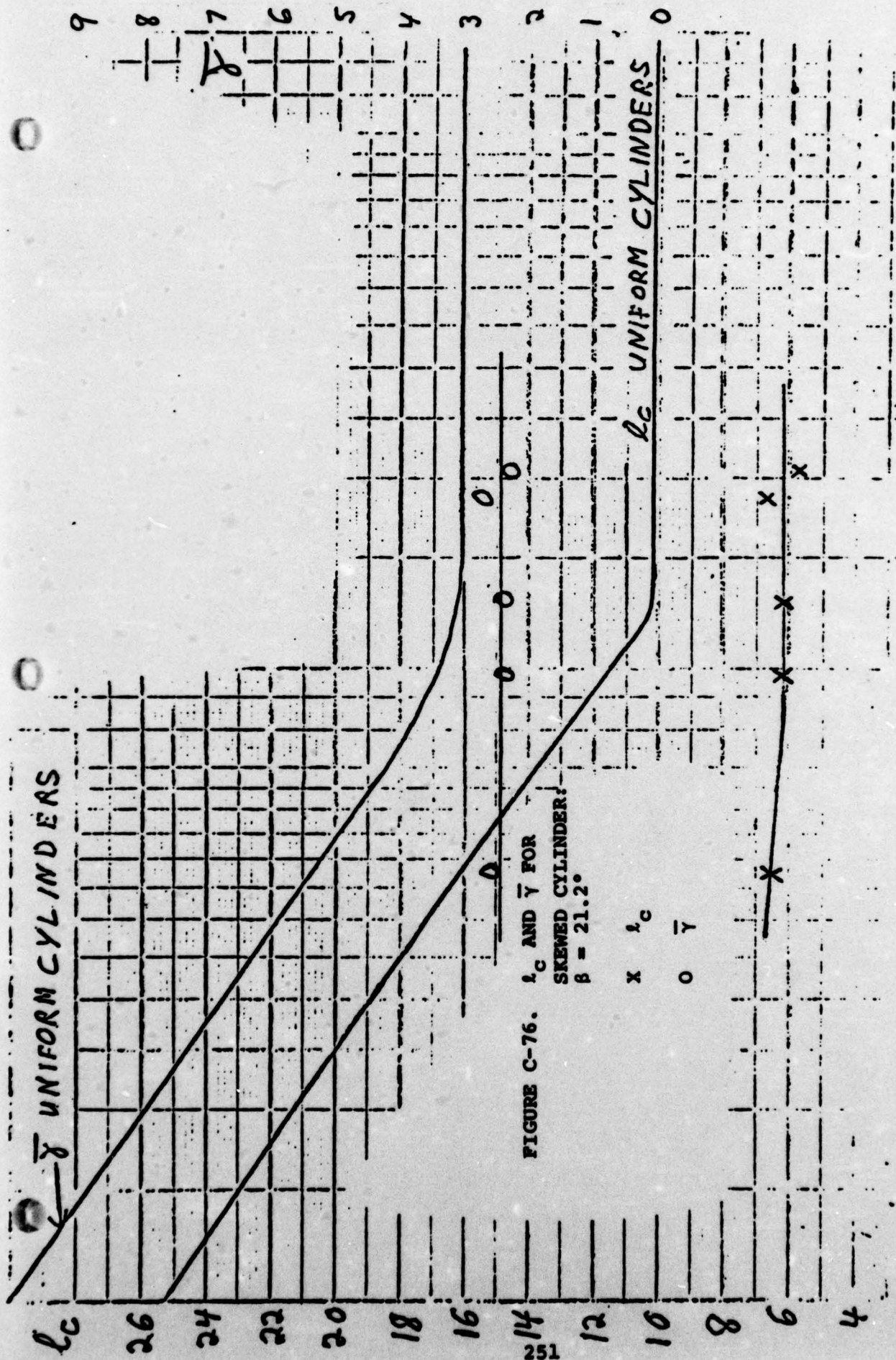
FIGURE C-76. ℓ_c AND $\bar{\gamma}$ FOR SKEWED CYLINDER;
$\beta = 21.2°$

x ℓ_c

o $\bar{\gamma}$

251

FIGURE C-77. ℓ_c AND $\bar{\gamma}$

252

FIGURE C-78. ℓ_c AND $\bar{\gamma}$
FOR SKEWED CYLINDER:
$\beta = 38.8°$

x ℓ_c
o $\bar{\gamma}$

FIGURE C-79. ℓ_c AND $\bar{\gamma}$ FOR

SKEWED CYLINDER:

$\beta = 45°$

x ℓ_c

o $\bar{\gamma}$

254

$Re \approx NU$ 3 FOR UNIFORM CYLINDER. $\cdot$, $(Re \times 10^3)$ $Cos \beta$ FOR SKEWED CYLINDER

FIGURE C-80. C_L FOR SKEWED CYLINDER
AT NORMAL (β = 0) INCIDENCE

255

FIGURE C-81. C_L FOR SKEWED CYLINDER
$\beta = 10.9°$

x based on measured ℓ_c, $\bar{\gamma}$

o based on normal stress/ ℓ_c, $\bar{\delta}$

$(R_E \times 10^3) \cos \beta$ FOR SKEWED CYL.; $R_E \times 10^3$ FOR UNIFORM CYL.; BEST FIT

FIGURE C-82. C_L FOR SKEWED CYLINDER

$\beta = 21.2°$

x   based on measured ℓ_c, $\overline{\gamma}$

o   based on normal skewed ℓ_c, $\overline{\gamma}$

$(R_E \times 10^3)/\cos\beta$ FOR SKEWED CYL.; $R_E \times 10^3$ FOR UNIFORM CYL.
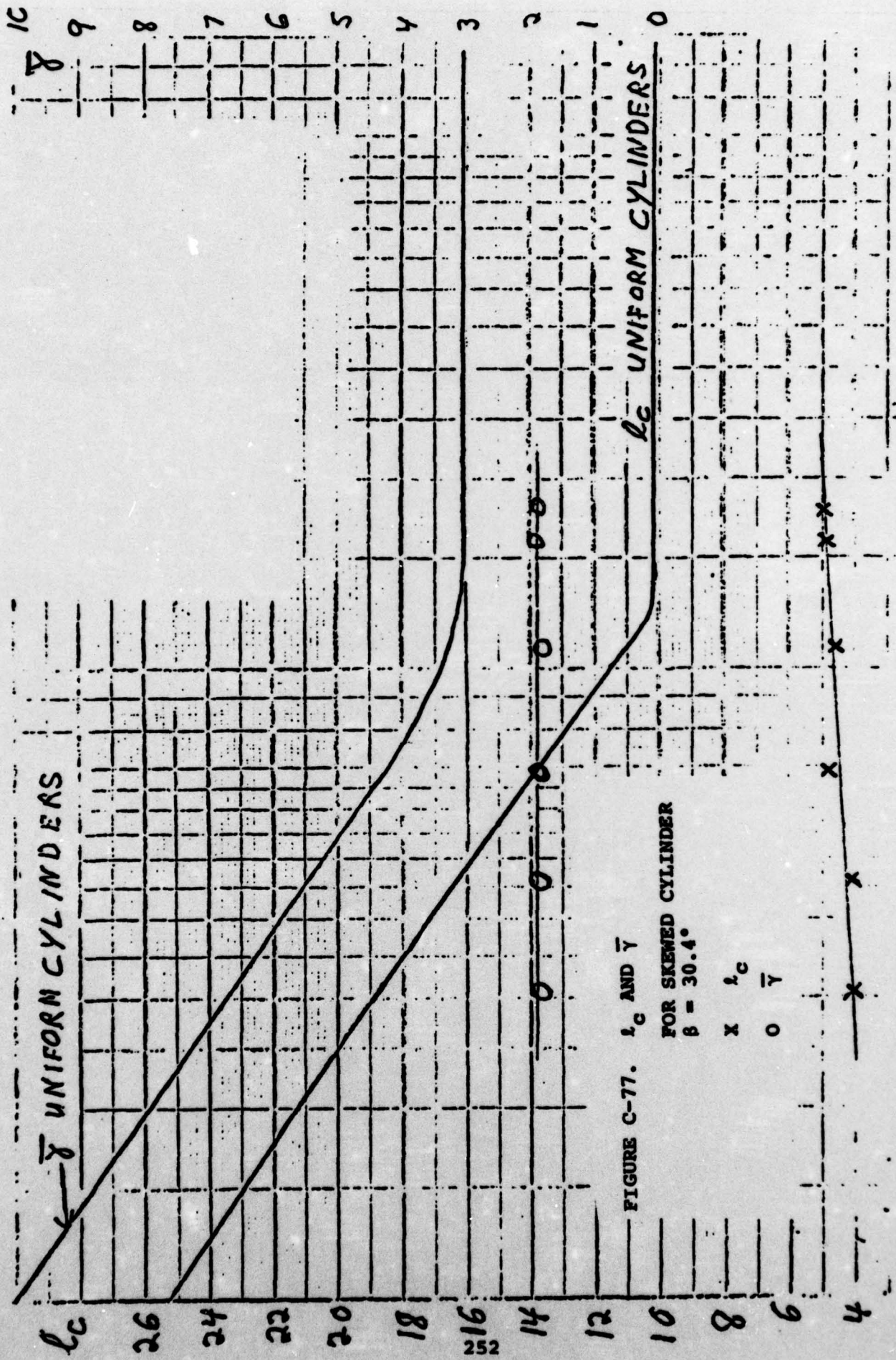
FIGURE C-83. C_L FOR SKEWED CYLINDER:
$\beta = 30.4°$.

x based on measured ℓ_c, $\bar{\gamma}$

o based on normal skewed ℓ_c, $\bar{\gamma}$

FIGURE C-84. C_L FOR SKEWED CYLINDER
$\beta = 38.8°$

x   based on measured ℓ_c, $\bar{\gamma}$

o   based on normal skewed
$\dfrac{\ell_c'}{\bar{\gamma}}$

259

FIGURE C-85
C_L FOR SKEWED CYLINDER
$\beta = 45°$

x based on measured ℓ_c, $\bar{\gamma}$

o based on normal skewed cylinder, $\frac{1}{\ell_c}$, $\bar{\gamma}$

BEST FIT UNIFORM CYLINDERS

$Re \times 10^3$ FOR UNIFORM CYL BEST FIT

$(Re \times 10^3) \cos \beta$ FOR SKEWED CYL.

C_L
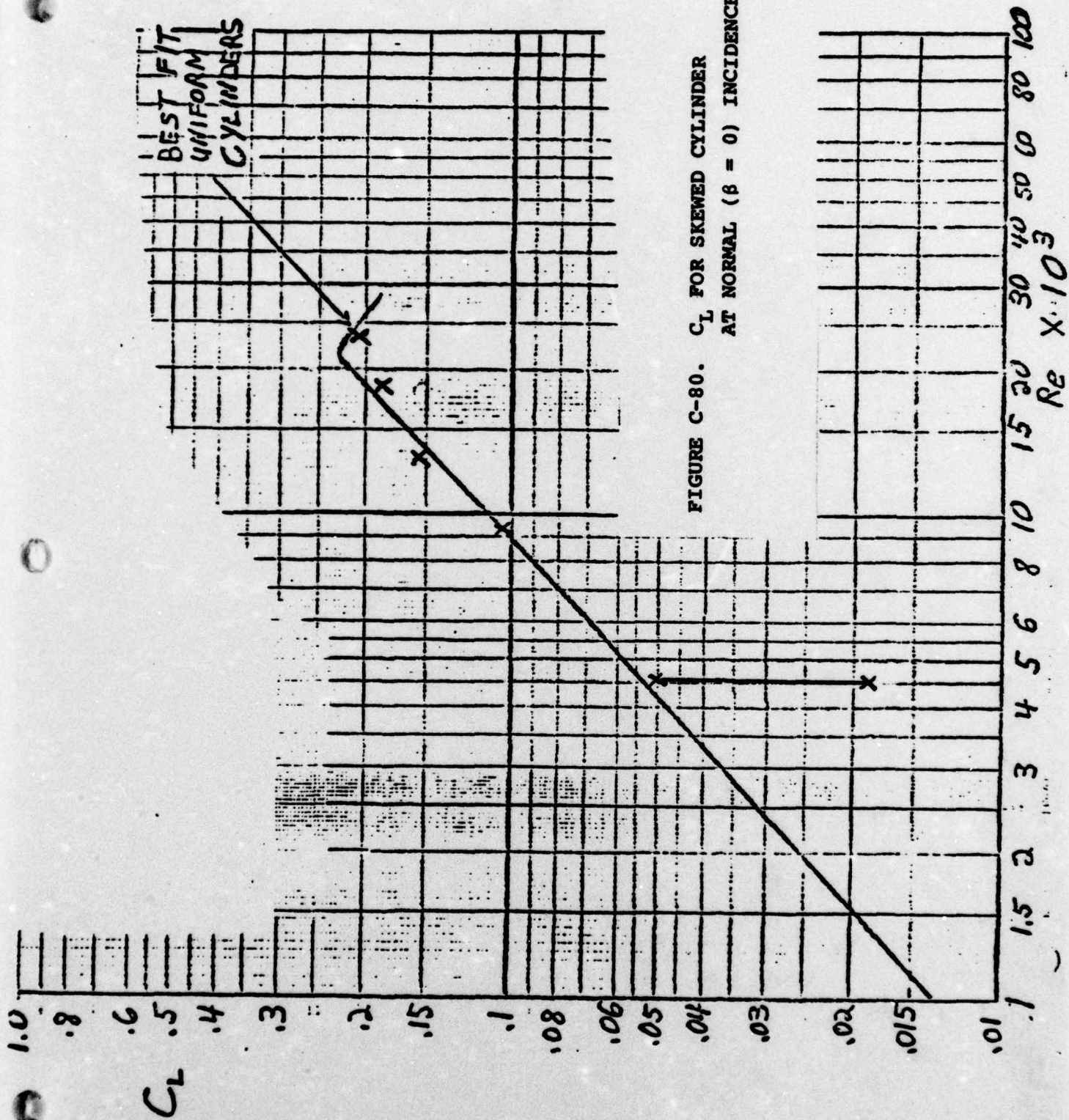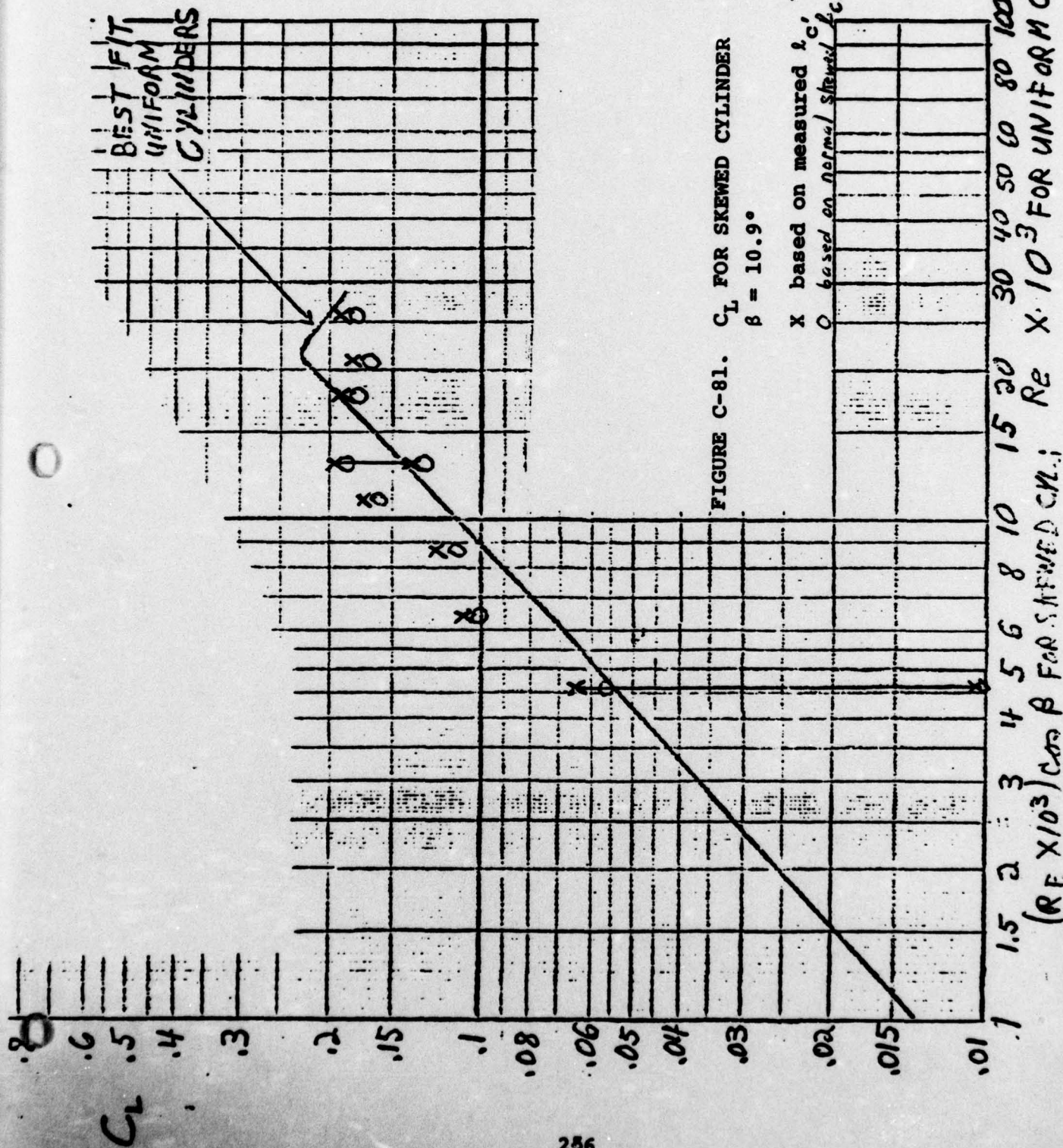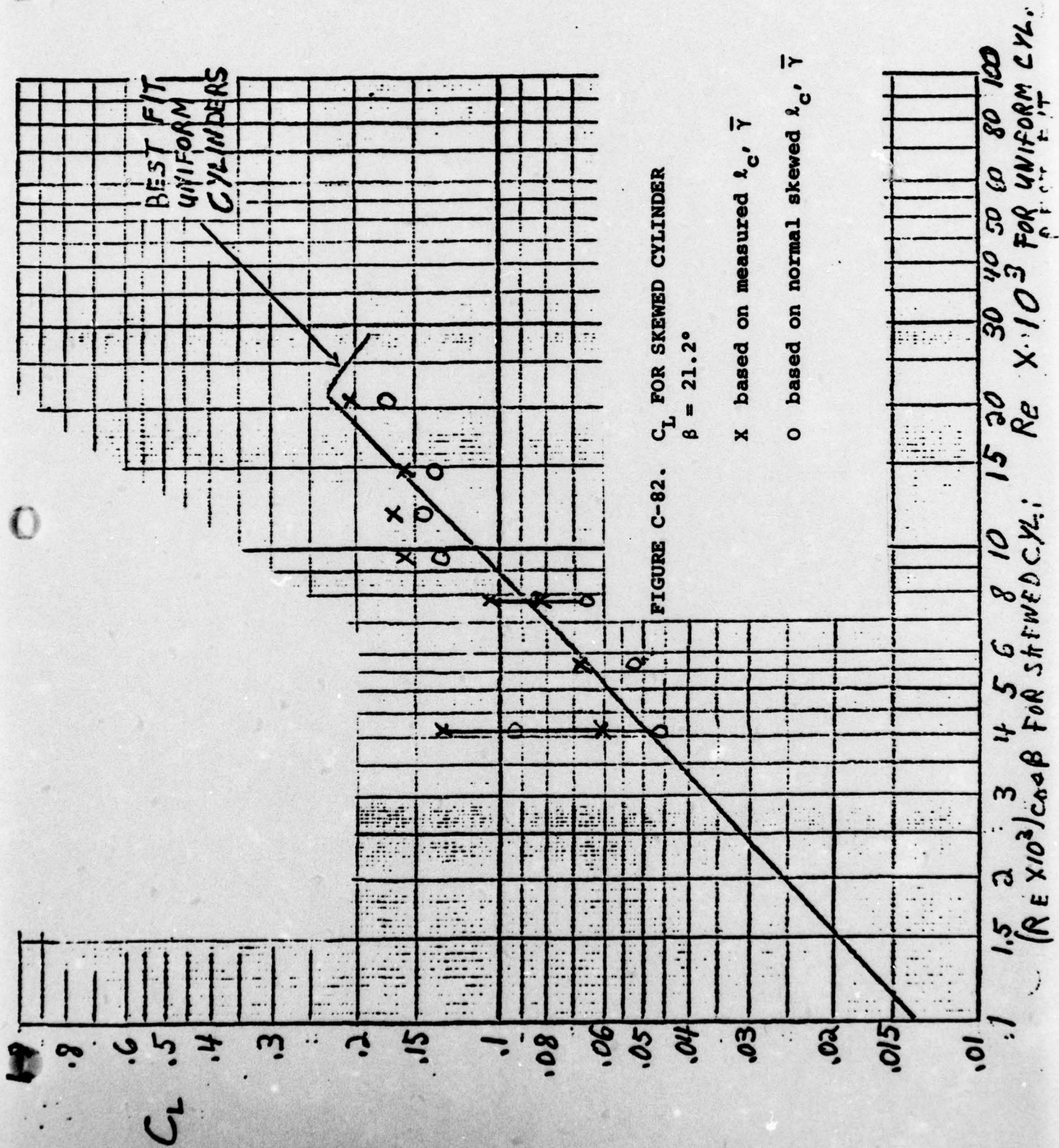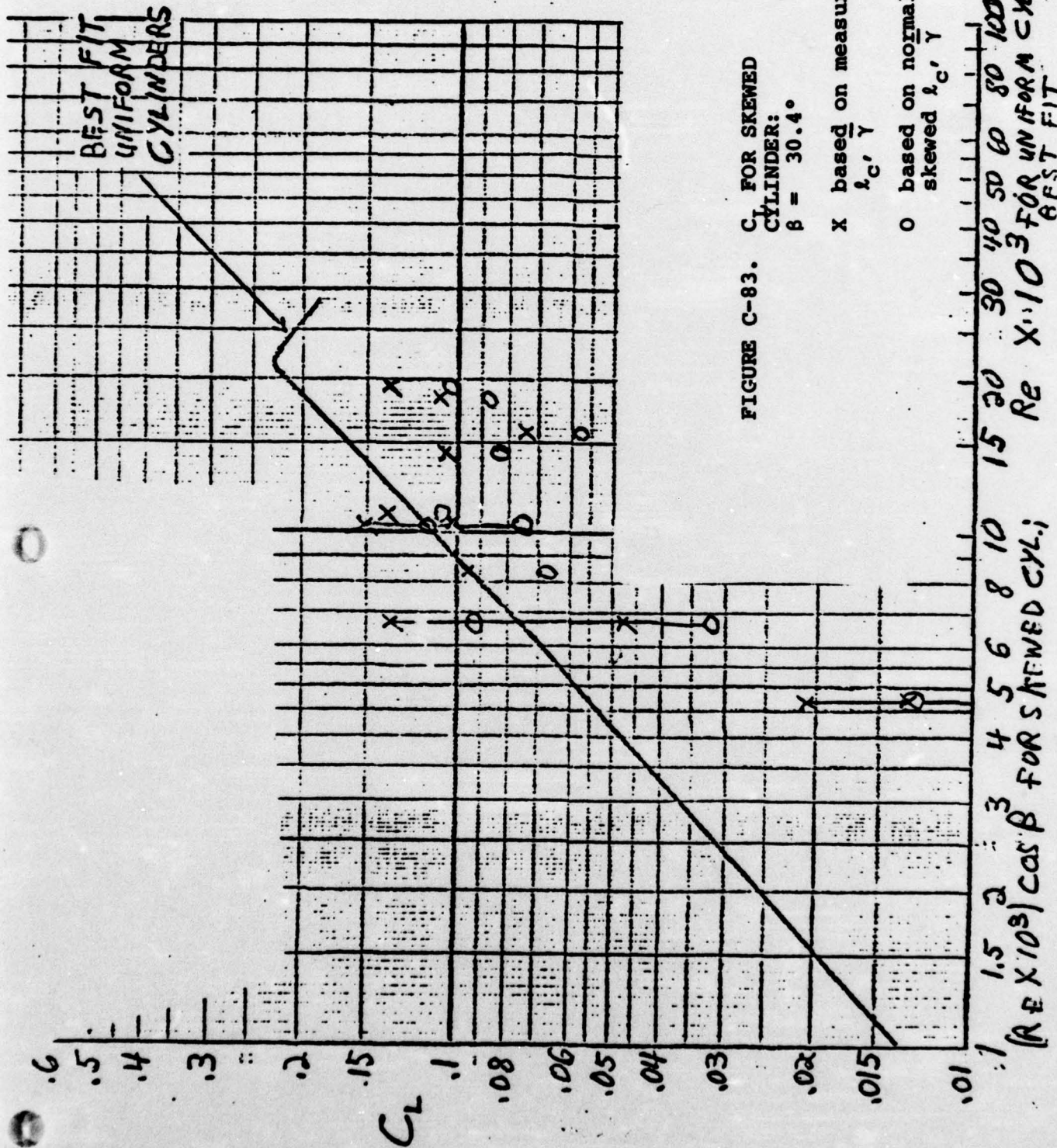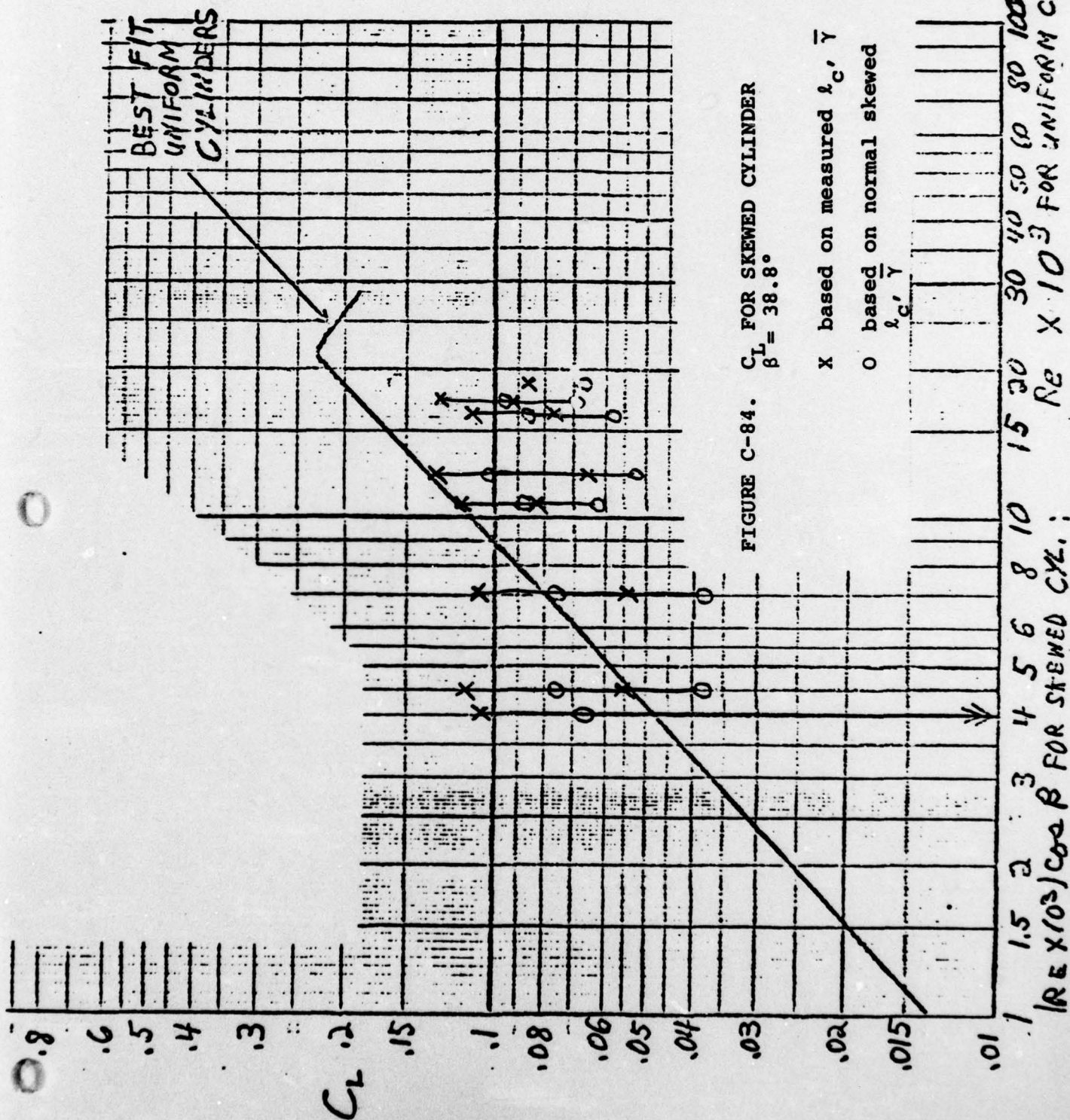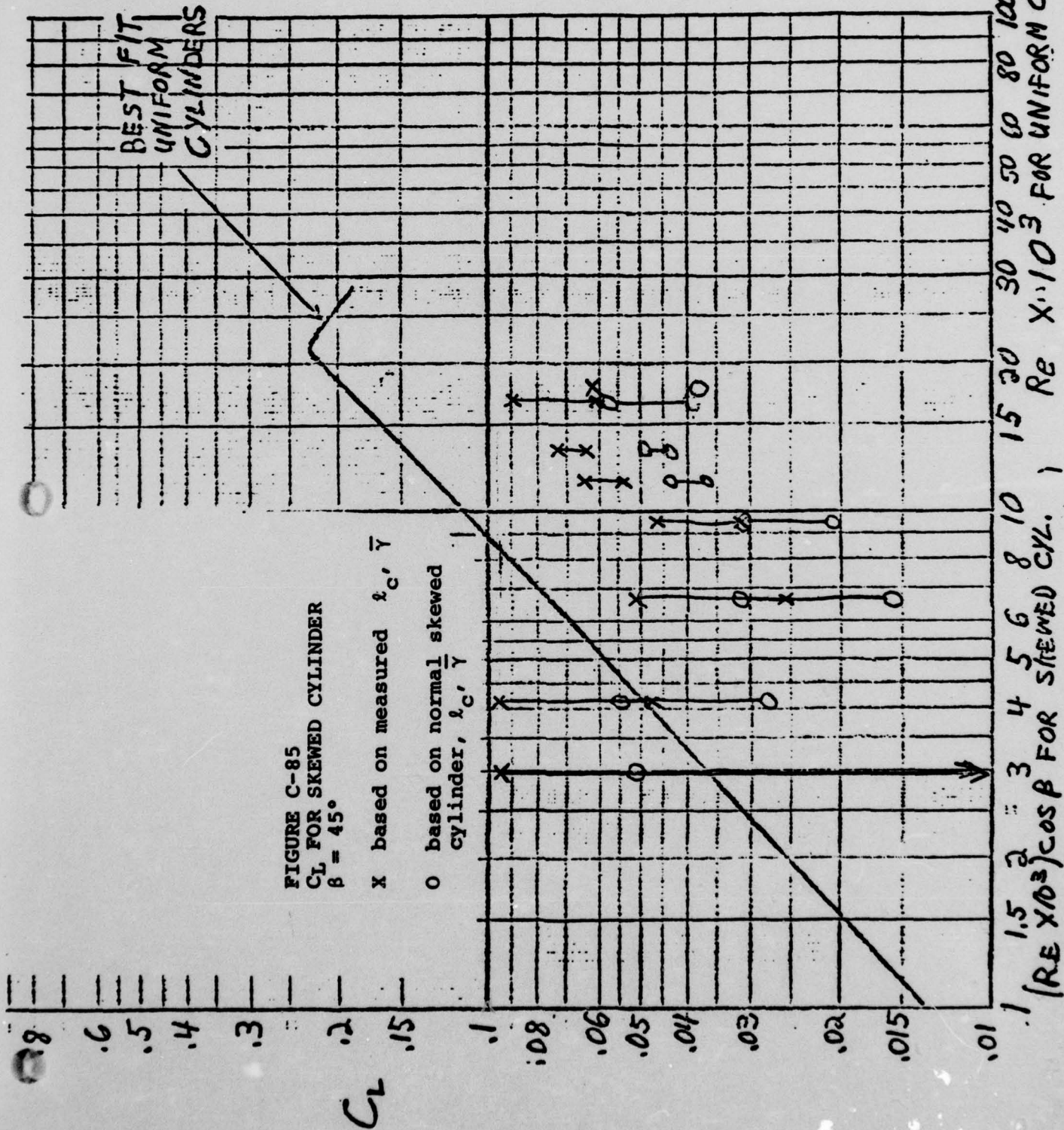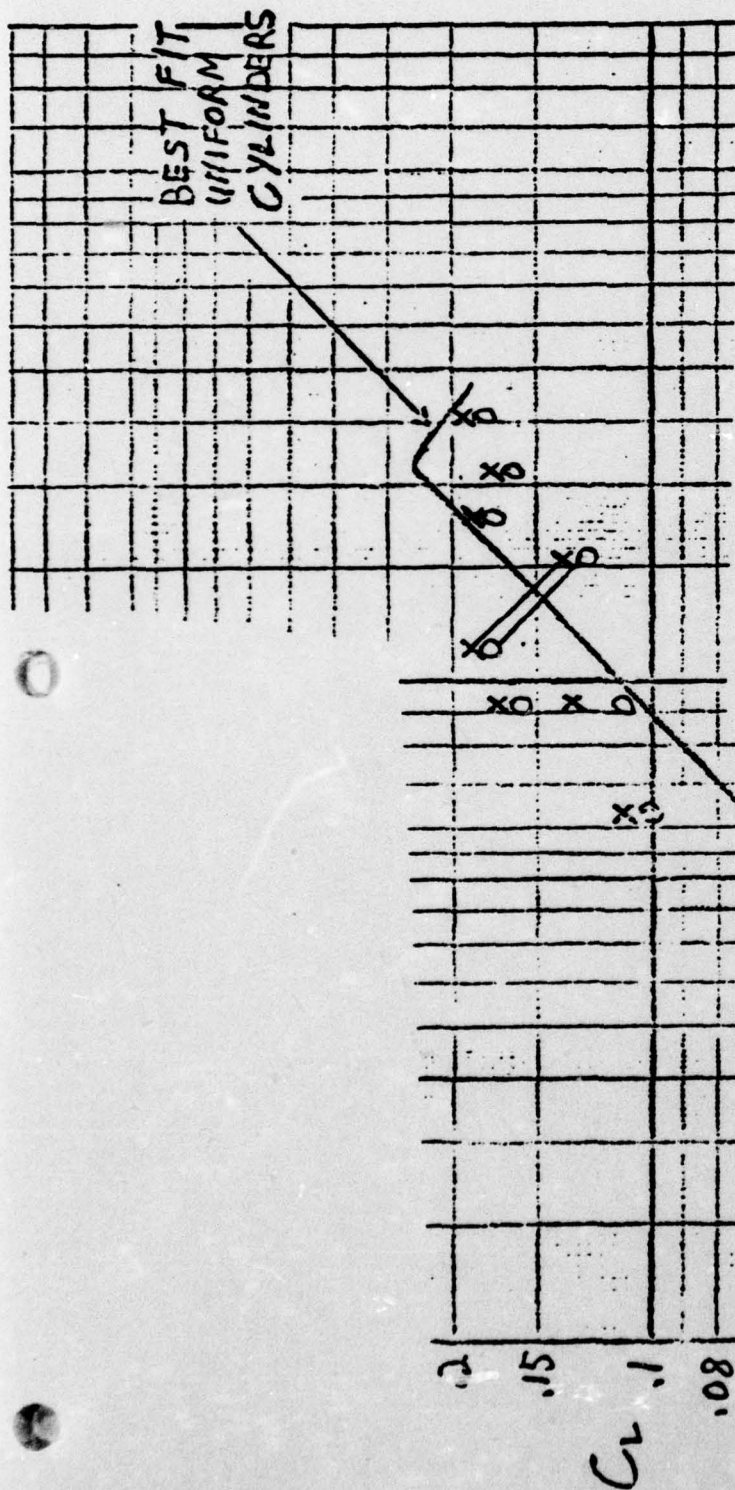
FIGURE C-86. ALTERNATIVE C_T FOR
SKEWED CYLINDER
$\beta = 10.9°$

x based on measured ℓ_c, $\bar{\gamma}$

o based on normal skewed
cylinder ℓ_c, $\bar{\gamma}$
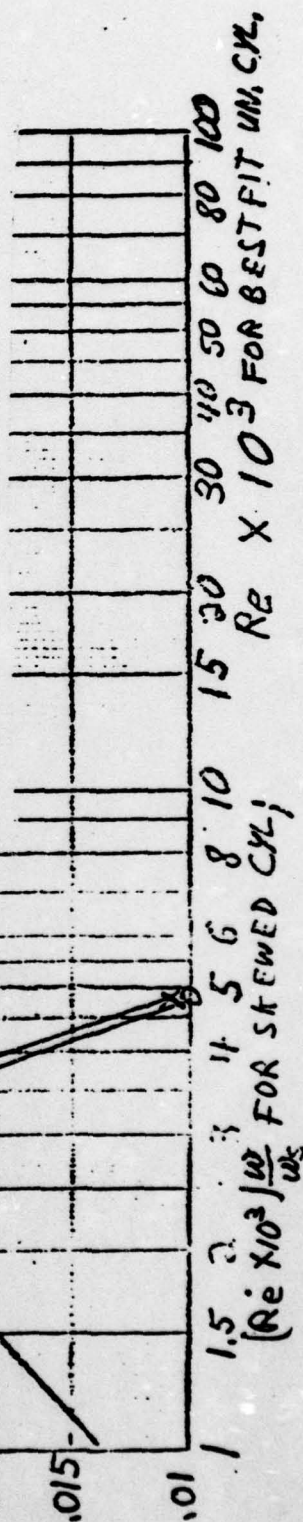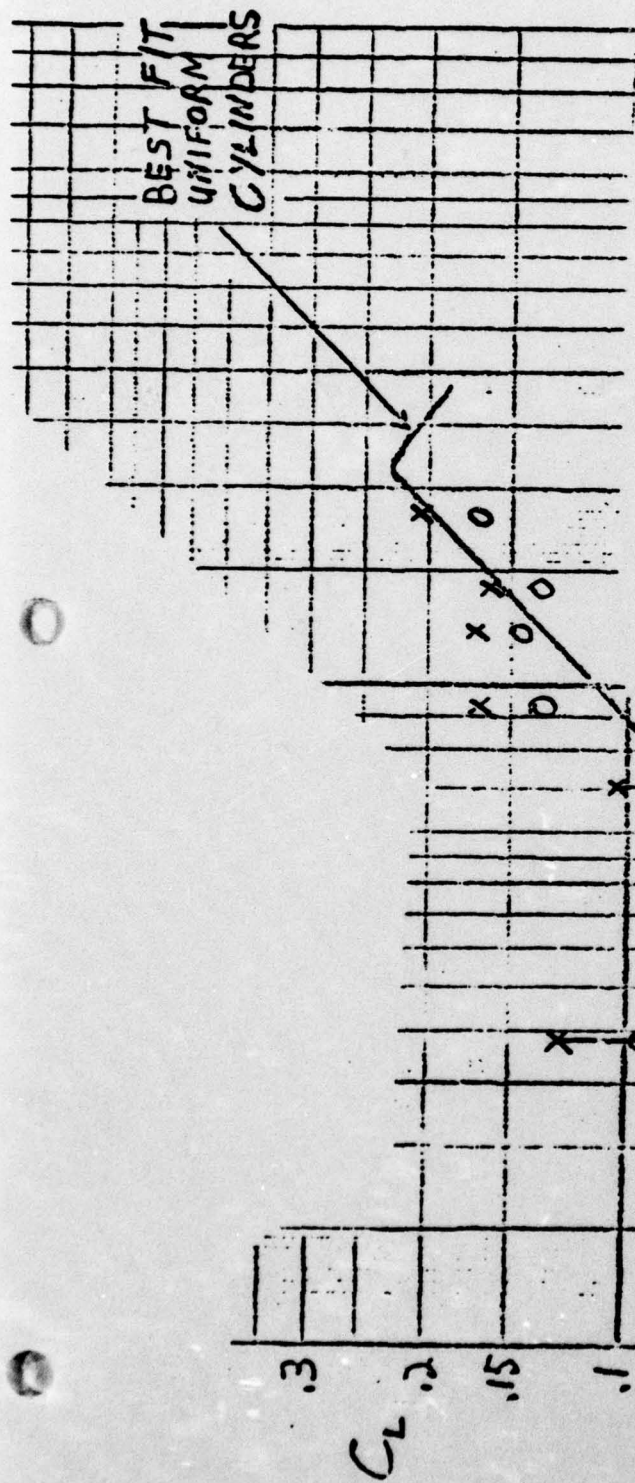
FIGURE C-87. ALTERNATIVE C_L FOR SKEWED CYLINDER: $\beta = 21.2°$

x based on measured ℓ_c, $\bar{\gamma}$

o based on normal skewed cylinder ℓ_c, $\bar{\gamma}$

FIGURE C-88. ALTERNATIVE C_L FOR SKEWED CYLINDER: $\beta^L = 30.4°$

x based on measured ℓ_c, $\bar{\gamma}$

o based on normal skewed cylinder, ℓ_c, $\bar{\gamma}$

FIGURE C-89. ALTERNATIVE C_I FOR SKEWED CYLINDER: $\beta = 38.8°$

O based on normal skewed cylinder ℓ_c, $\bar{\gamma}$

X based on measured ℓ_c, $\bar{\gamma}$

FIGURE C-90.
ALTERNATIVE C_L FOR
SKEWED CYLINDER $\beta = 45°$

x based on measured ℓ_c, $\overline{\gamma}$

o based on normal skewed
cylinder ℓ_c, $\overline{\gamma}$

265
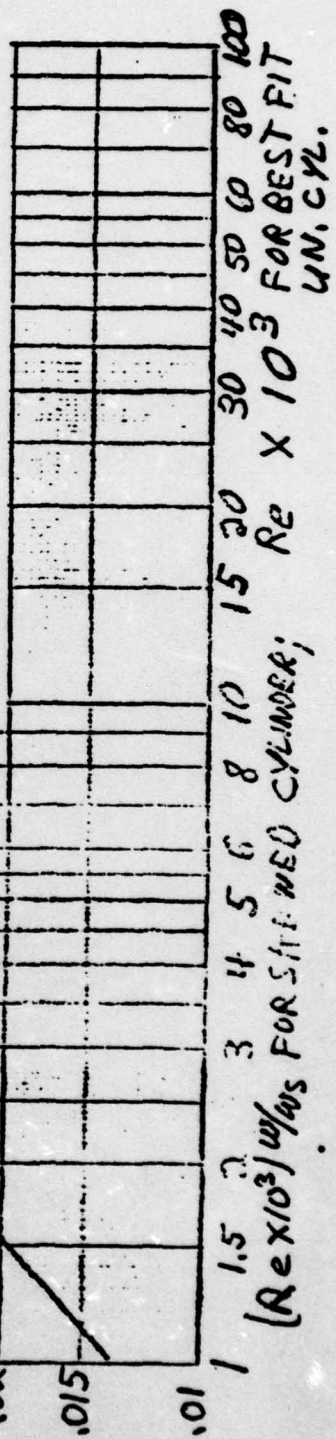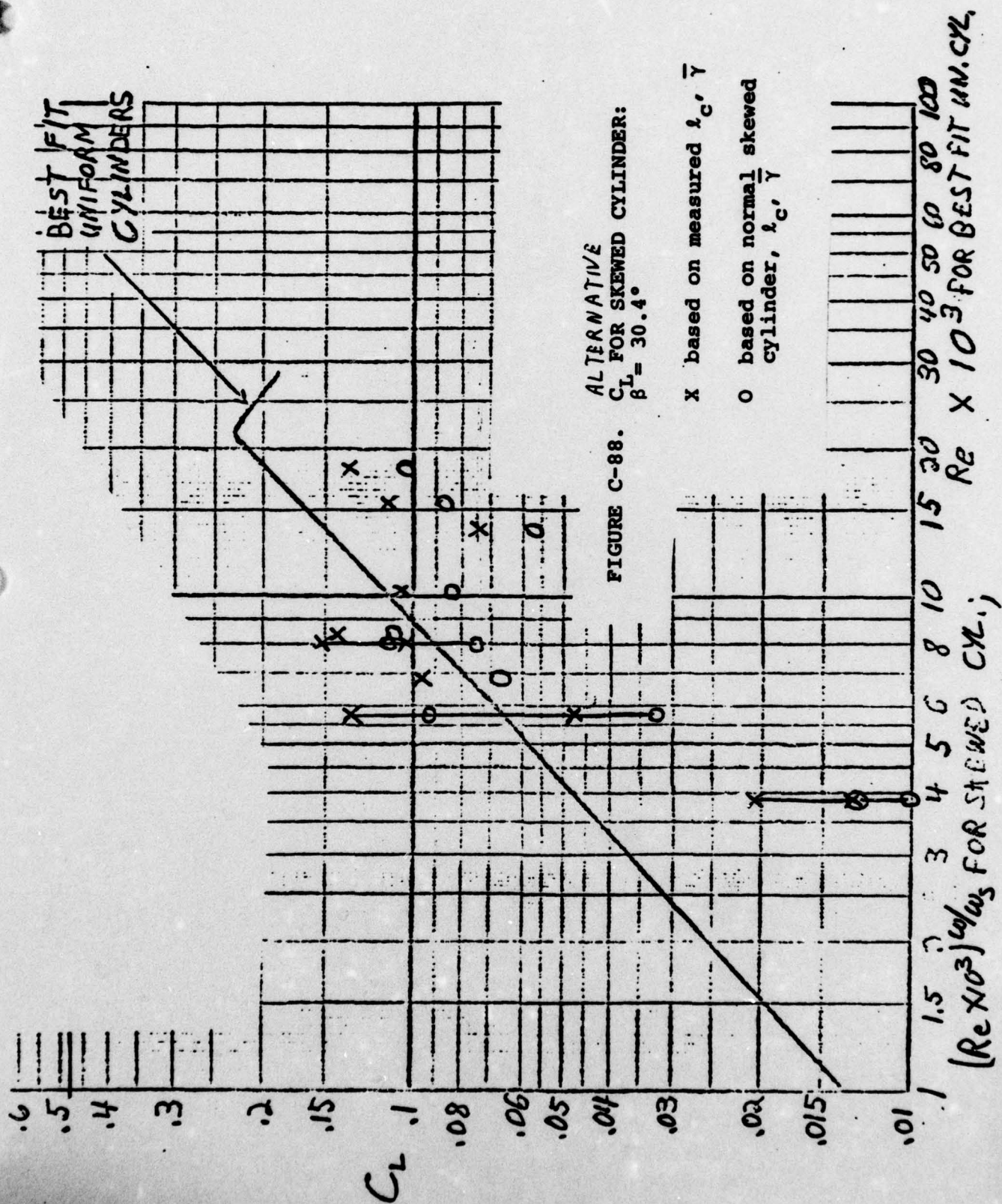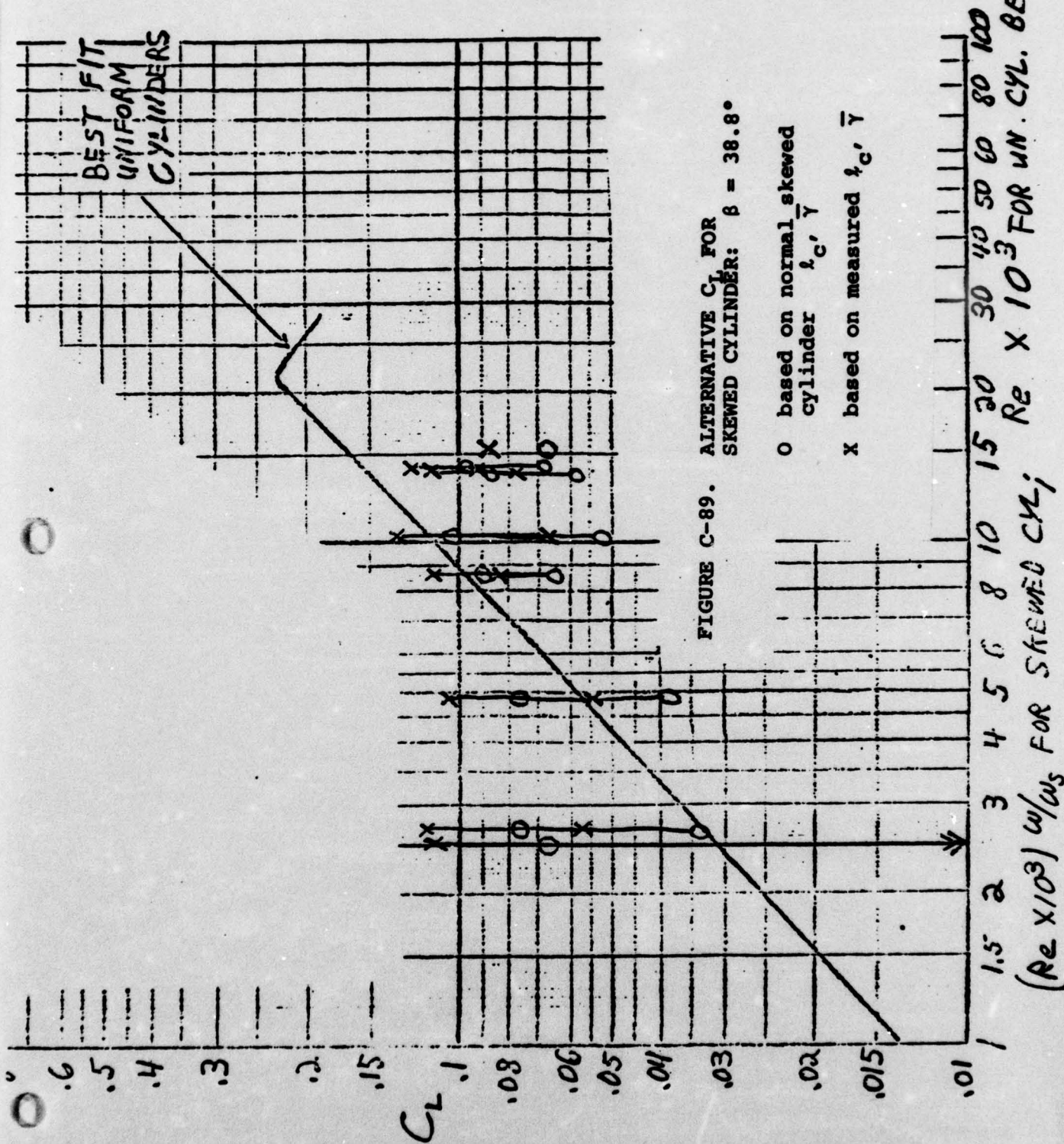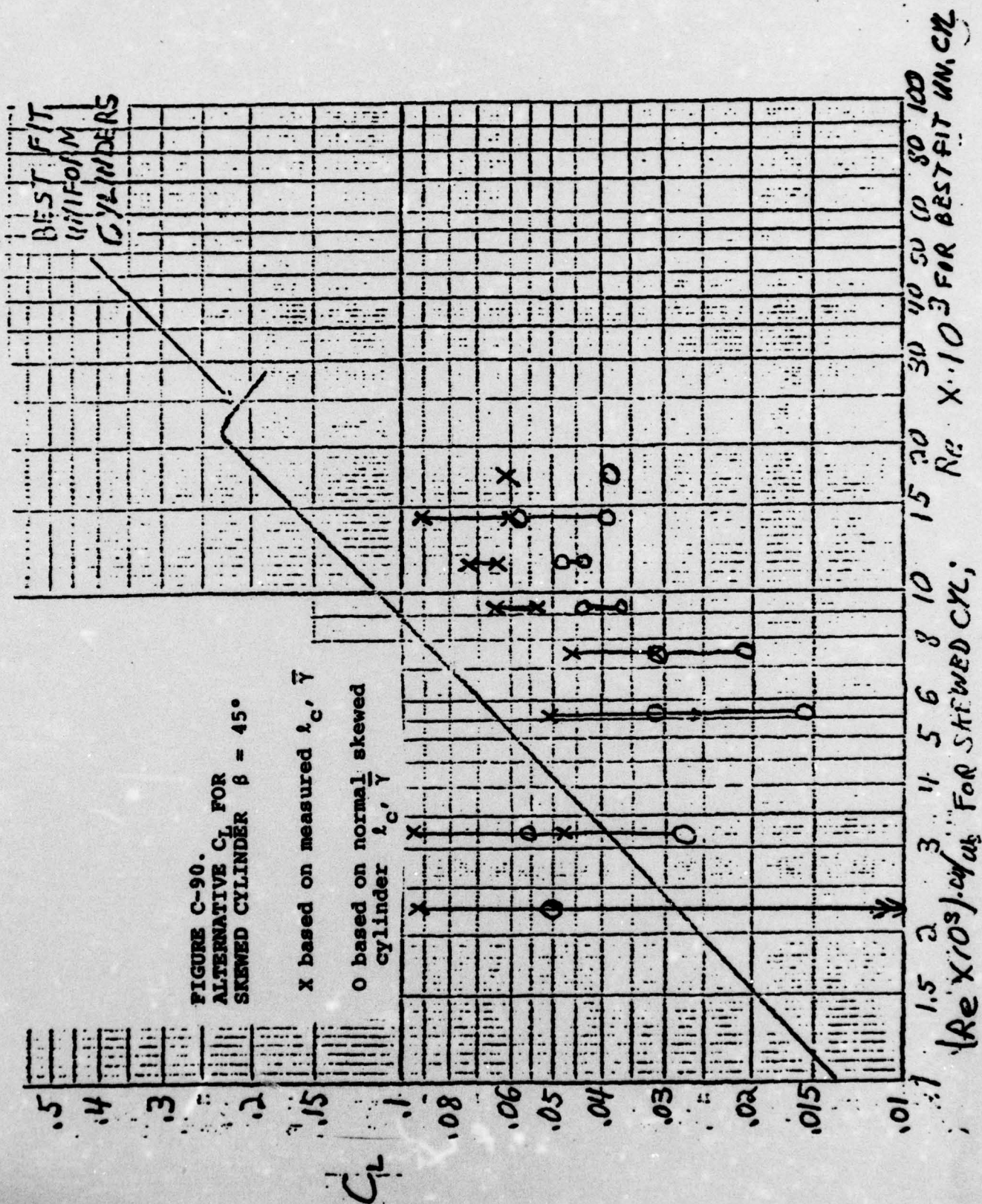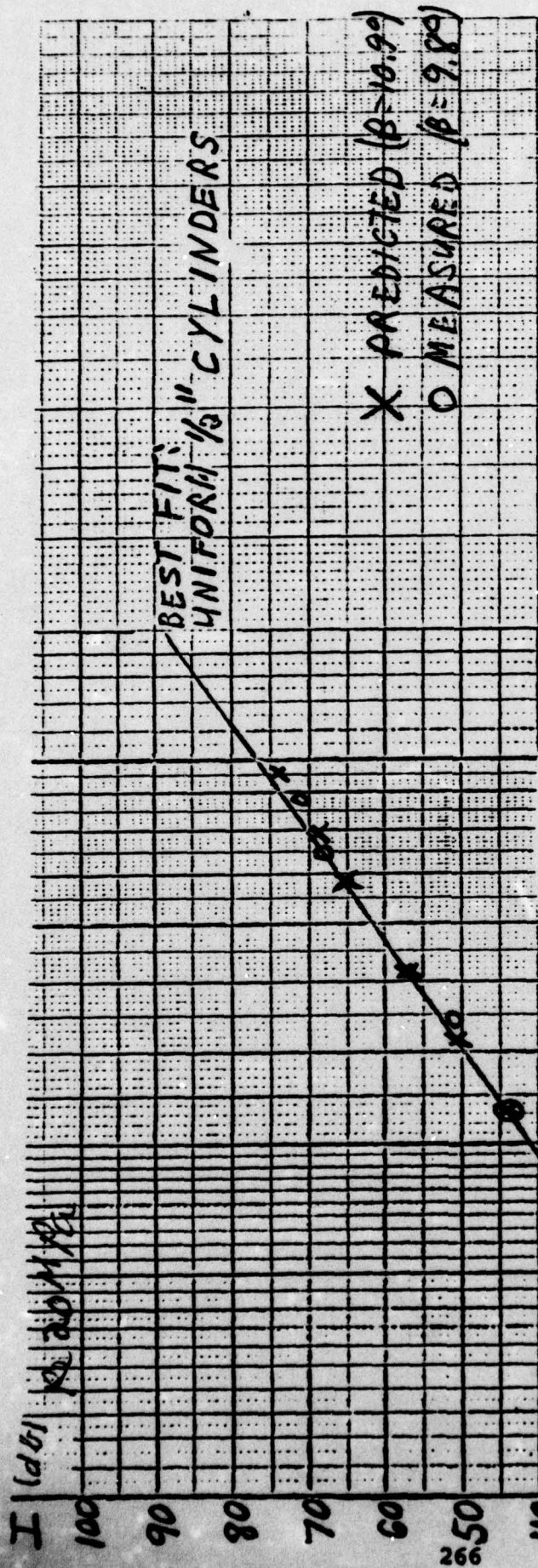
FIGURE C-91. ALTERNATIVE PLOT:
I FOR SKEWED CYLINDER
β = 10°

FIGURE C-92. ALTERNATIVE PLOT:
I FOR SKEWED CYLINDER
β = 21°

FIGURE C-93. ALTERNATIVE PLOT:
I FOR SKEWED CYLINDER
β = 31°

FIGURE C-94. ALTERNATIVE PLOT:
I FOR SKEWED CYLINDER
$\beta = 39°$
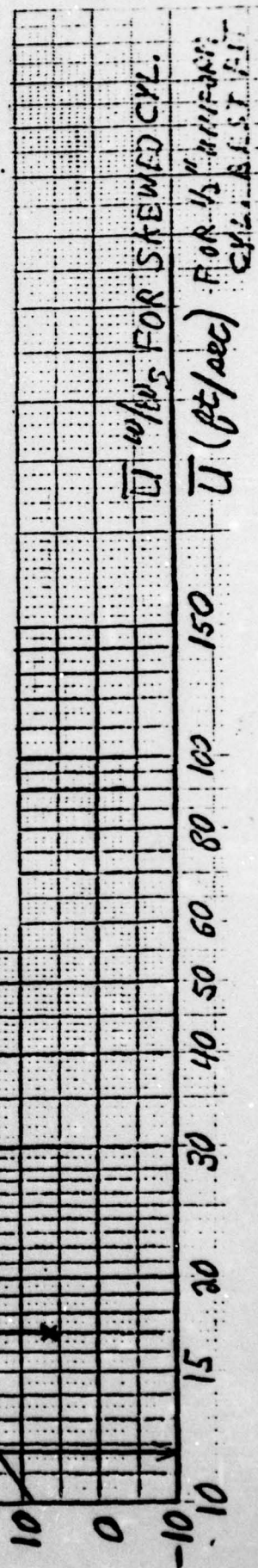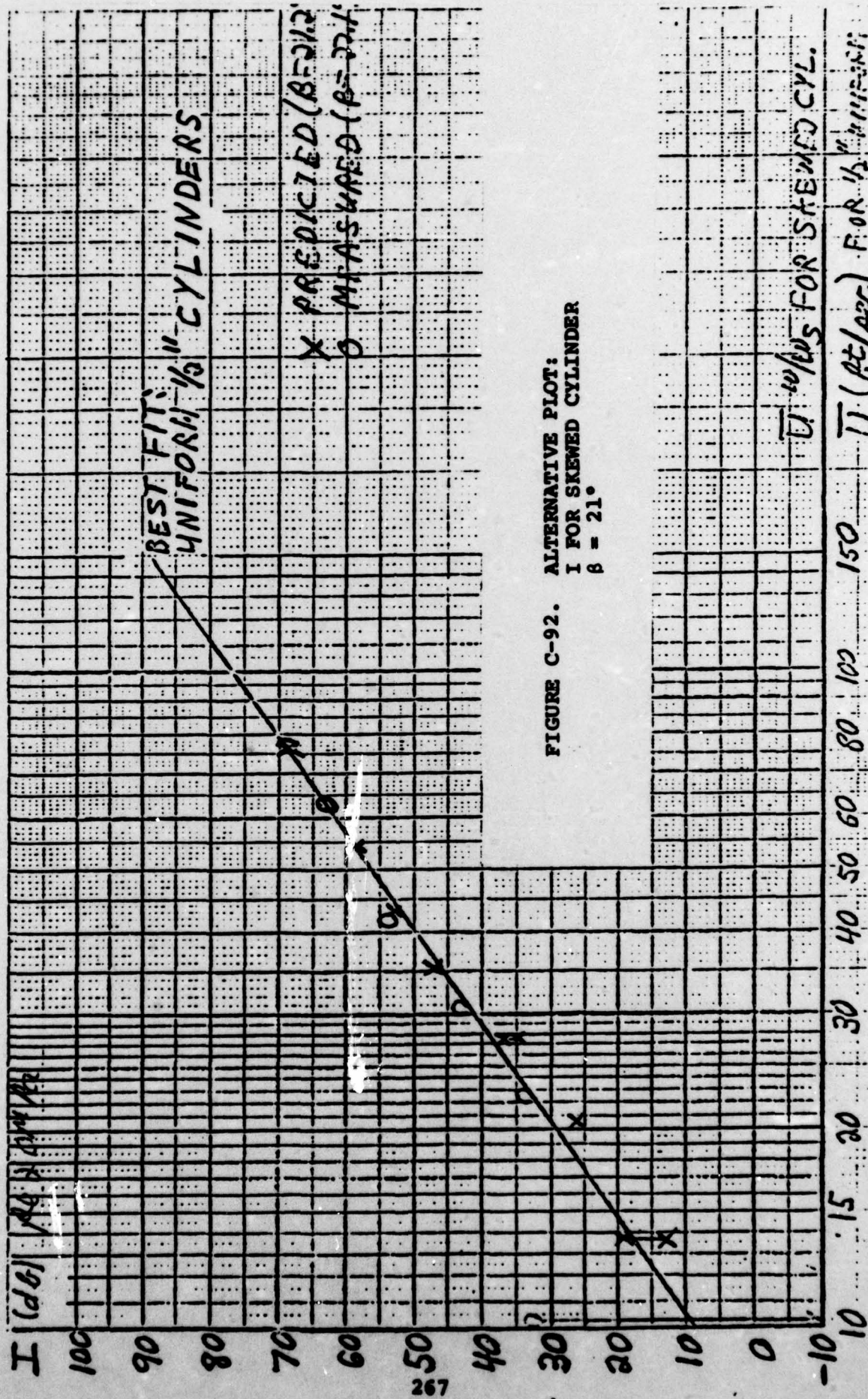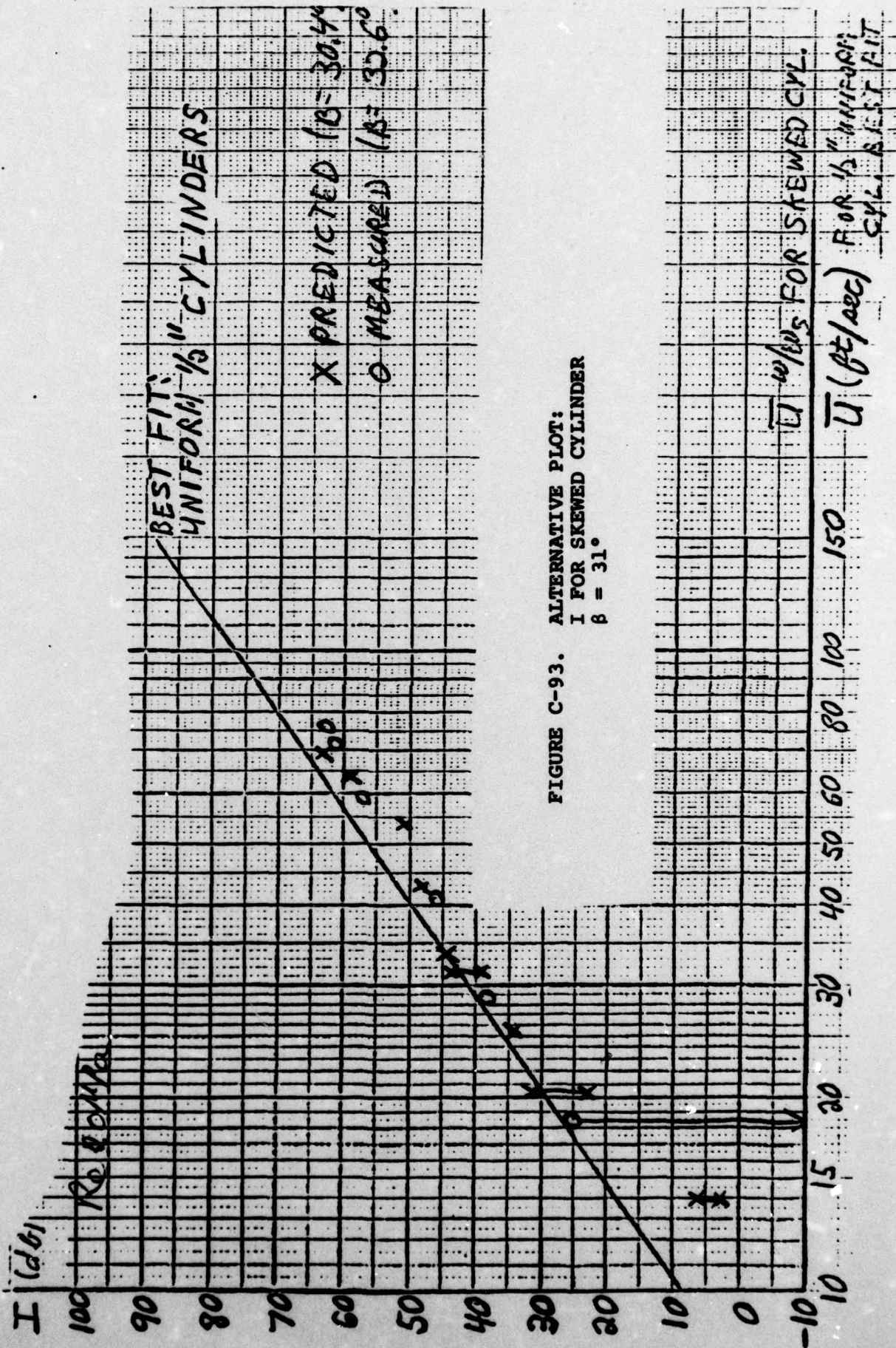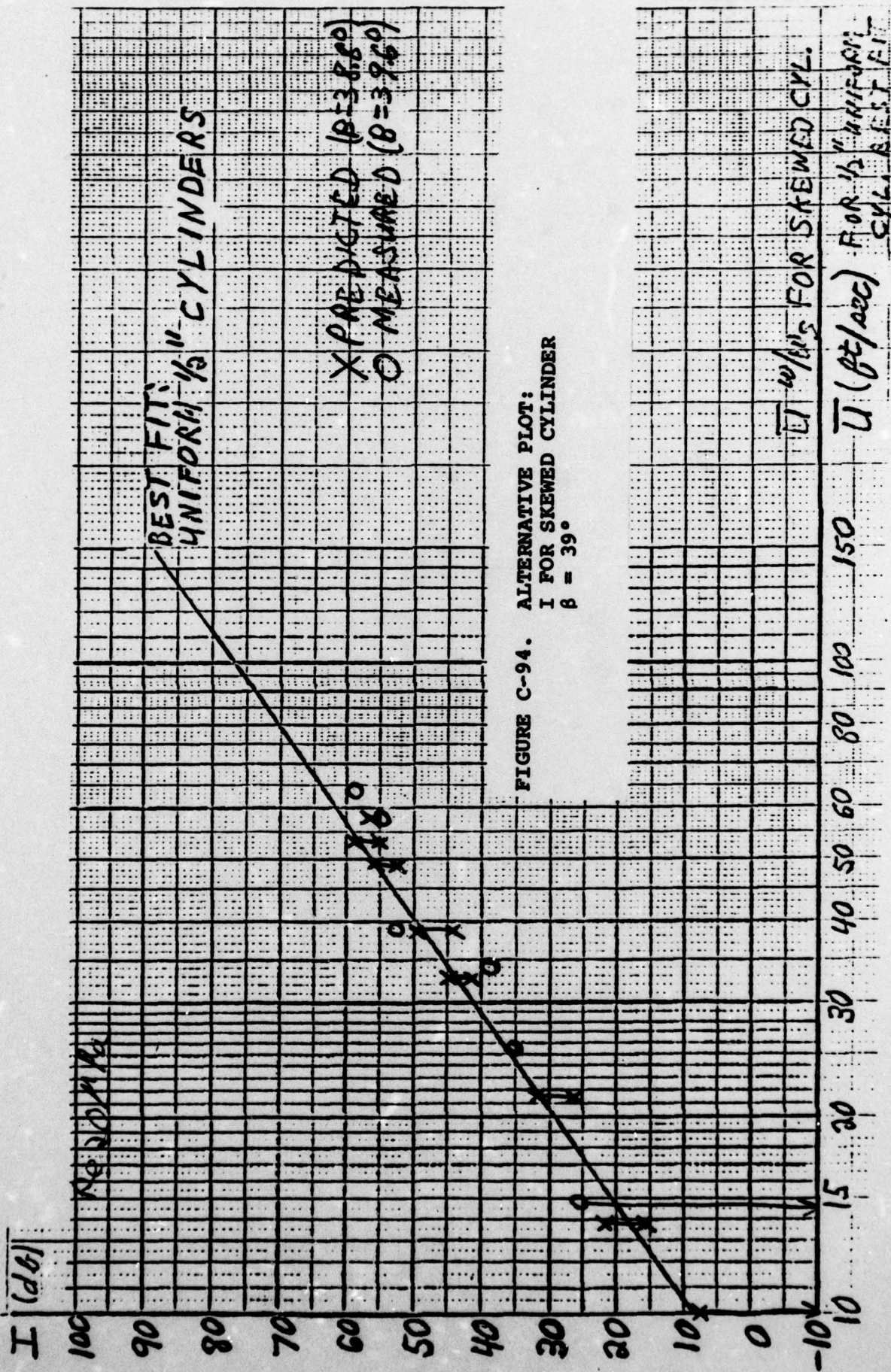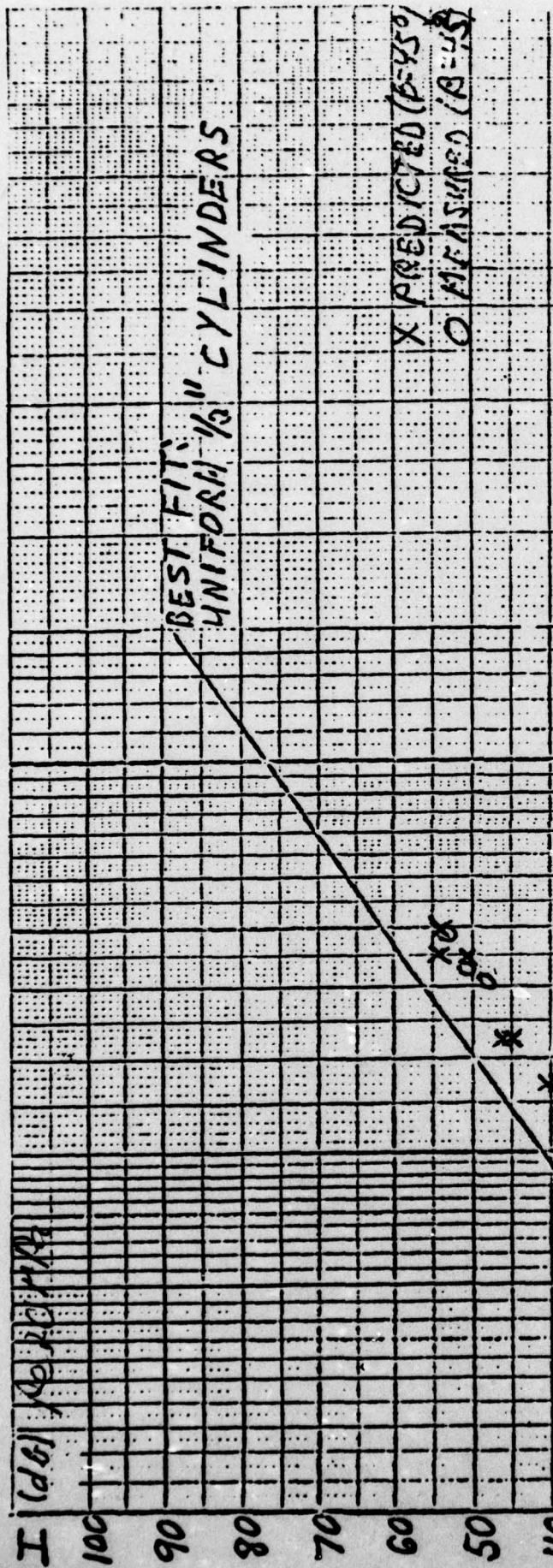
FIGURE C-95. ALTERNATIVE PLOT:
I FOR SKEWED CYLINDER
β = 45°
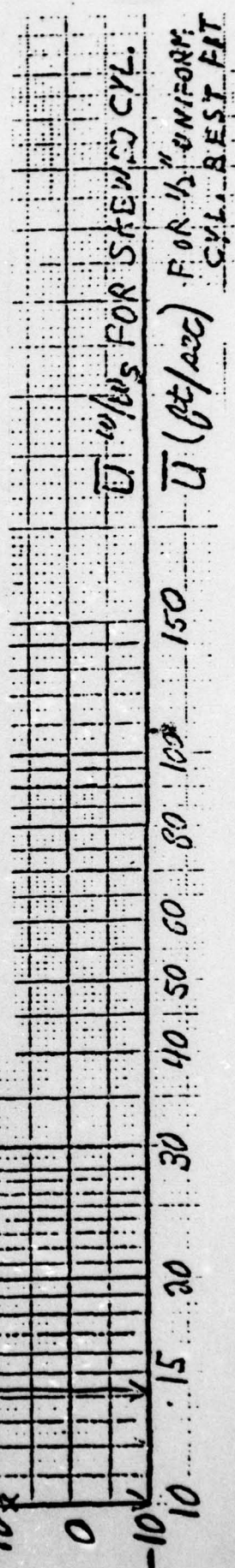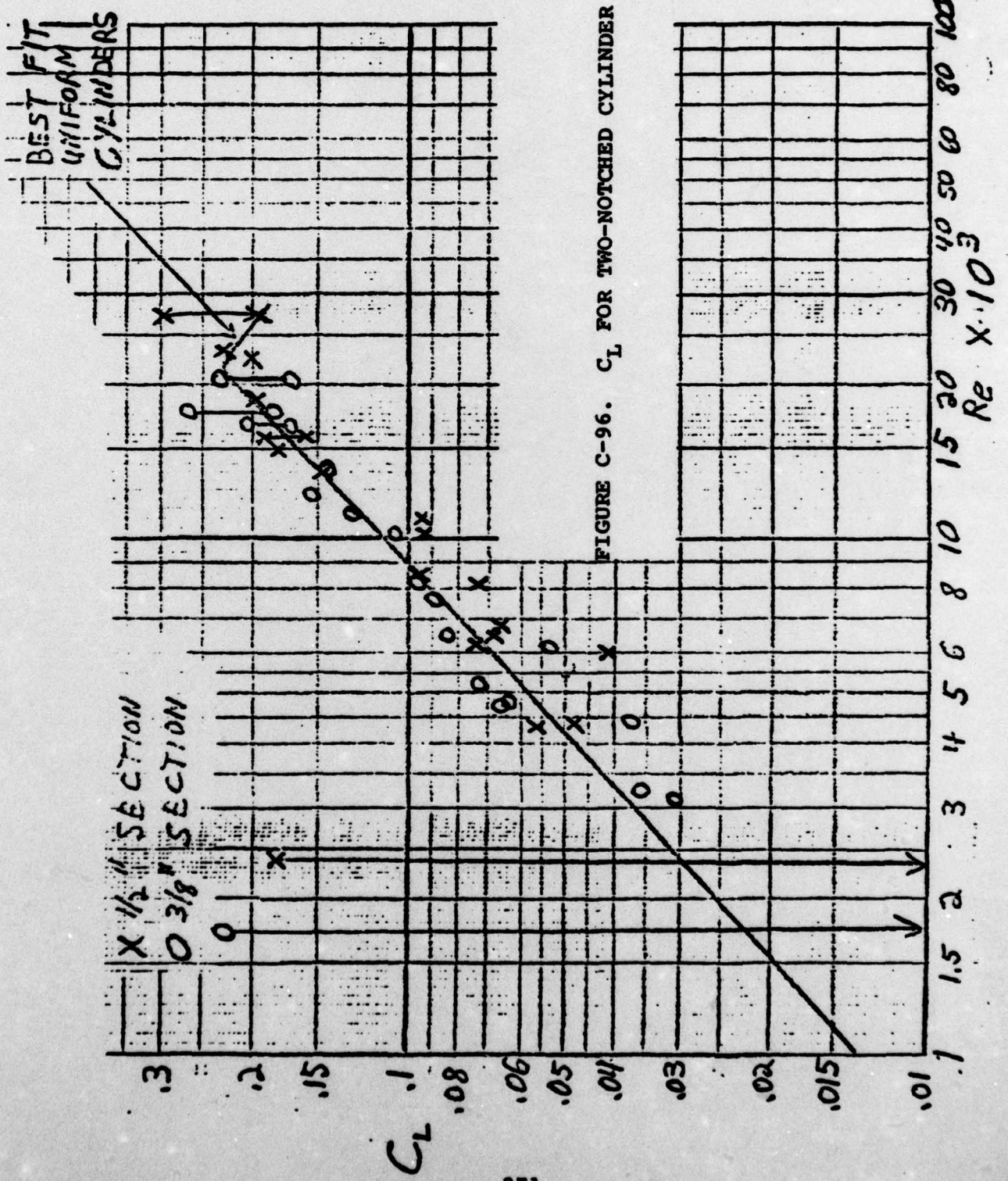
FIGURE C-96. C_L FOR TWO-NOTCHED CYLINDER

271

FIGURE C-97. C_L FOR REGULAR MULTINOTCHED CYLINDER: 1/2" SECTION

272
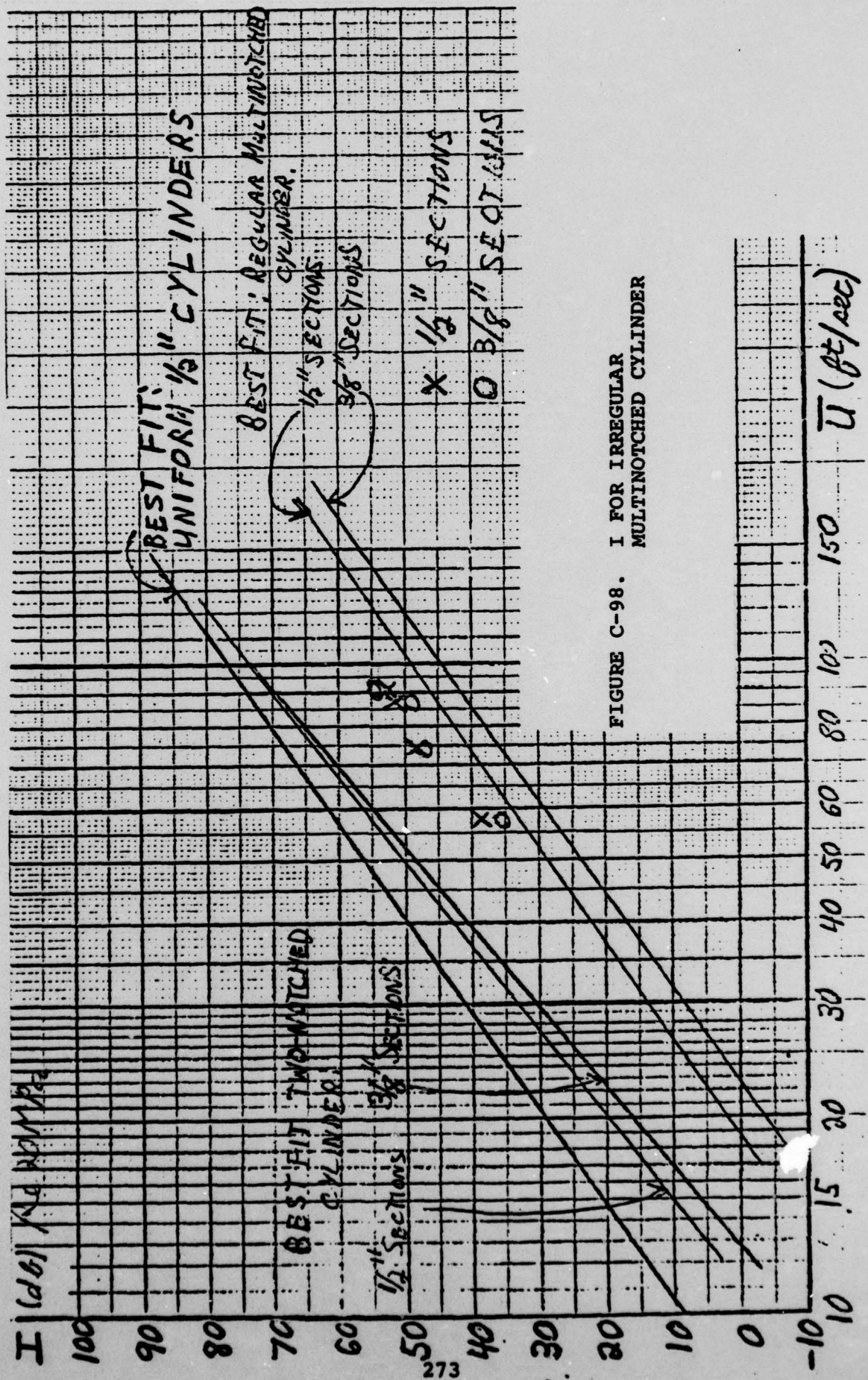
FIGURE C-98. I FOR IRREGULAR
MULTINOTCHED CYLINDER

FIGURE C-99. C_L FOR IRREGULAR
MULTINOTCHED CYLINER

274
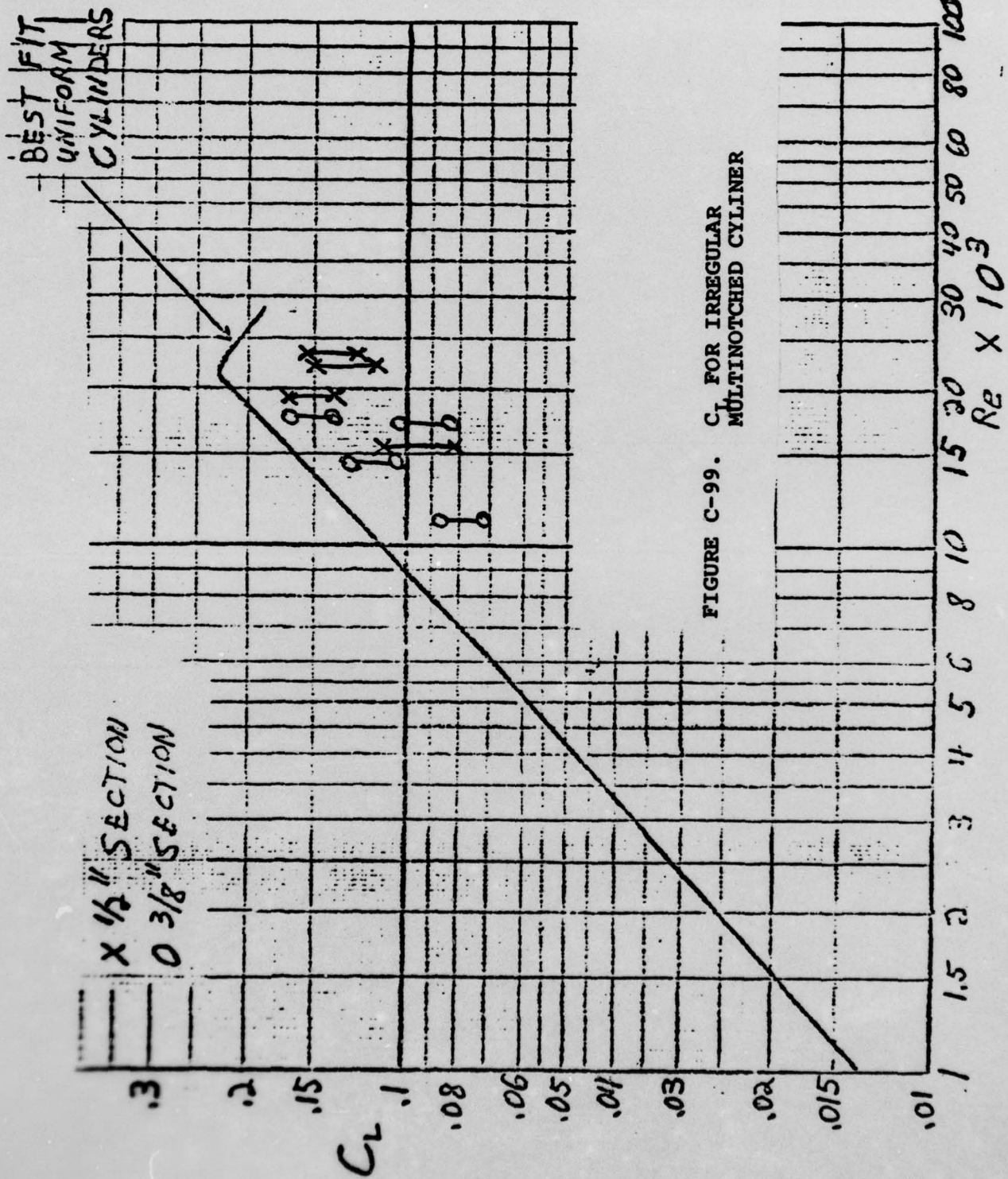
APPENDIX D: PLATES
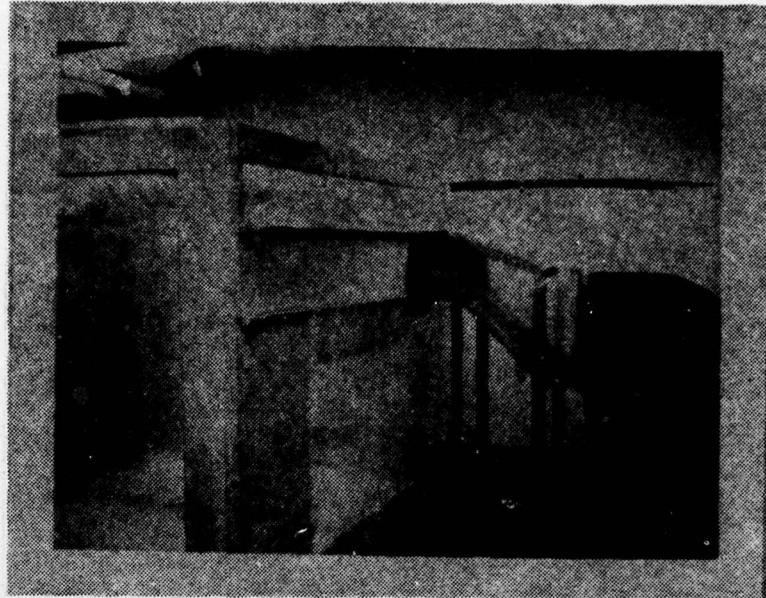
PLATE D-1. WIND TUNNEL: PLENUM CHAMBER AND BLOWER
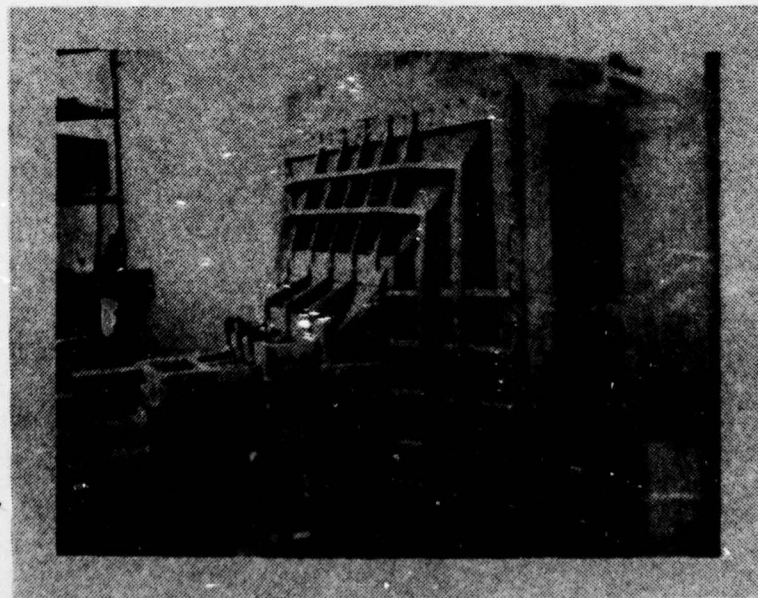
PLATE D-2. WIND TUNNEL: PLENUM CHAMBER AND
CONTRACTION (SIDE VIEW)

275
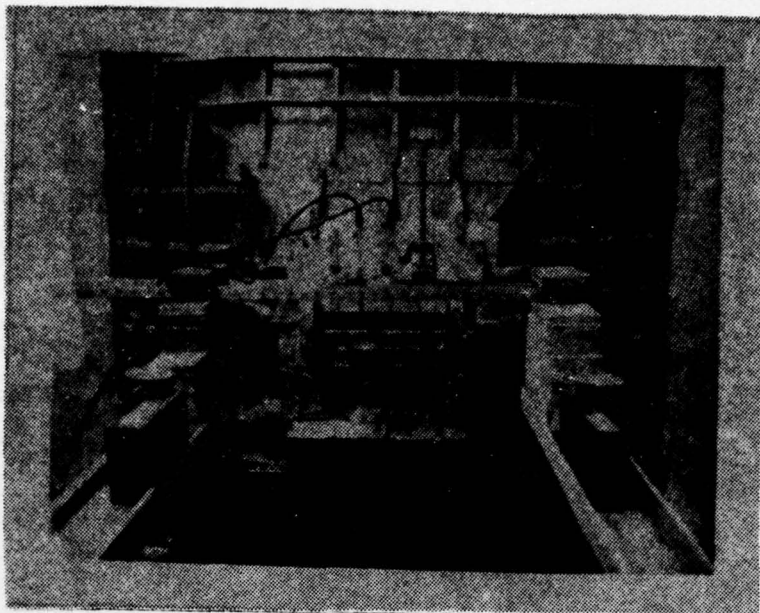
PLATE D-3. WIND TUNNEL CONTRACTION AND CYLINDER SUPPORT STAND (END VIEW)

PLATE D-4. F_L: HIGH $\bar{U}$
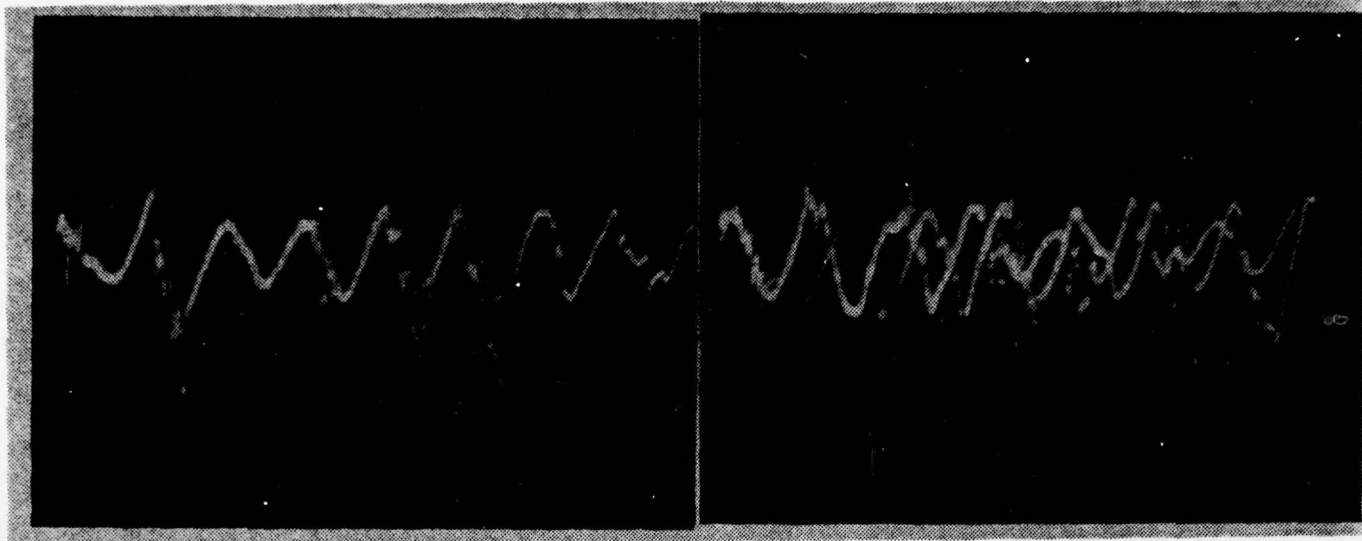
276
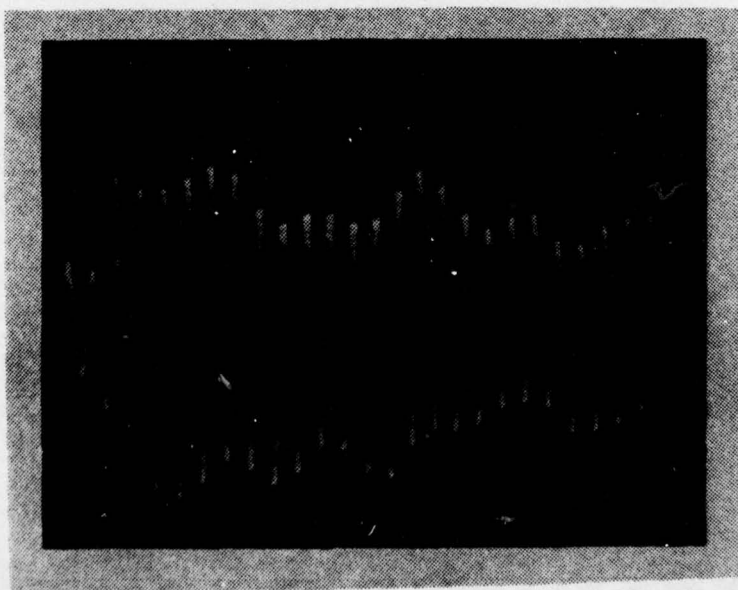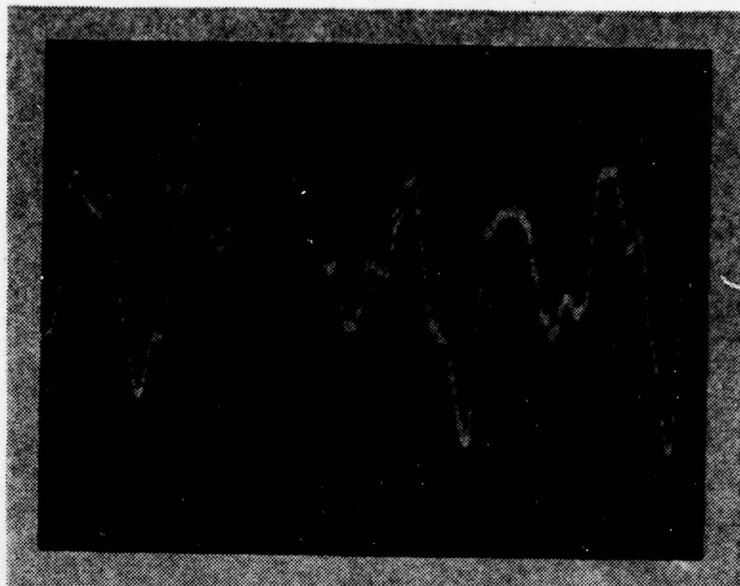
PLATE D-5. F_L: LOW $\bar{U}$
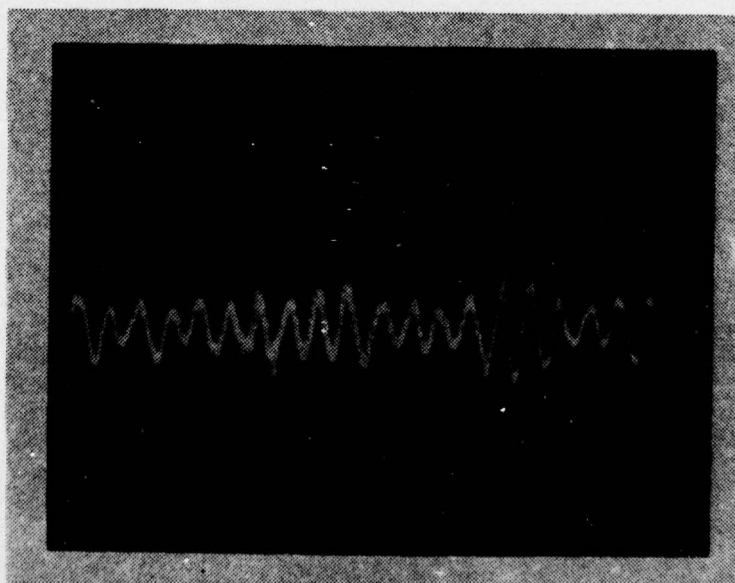
PLATE D-6. ANEMOMETER SIGNAL: GOOD LOCATION
FOR $R(\gamma)$ MEASUREMENT

277

(a)   (b)

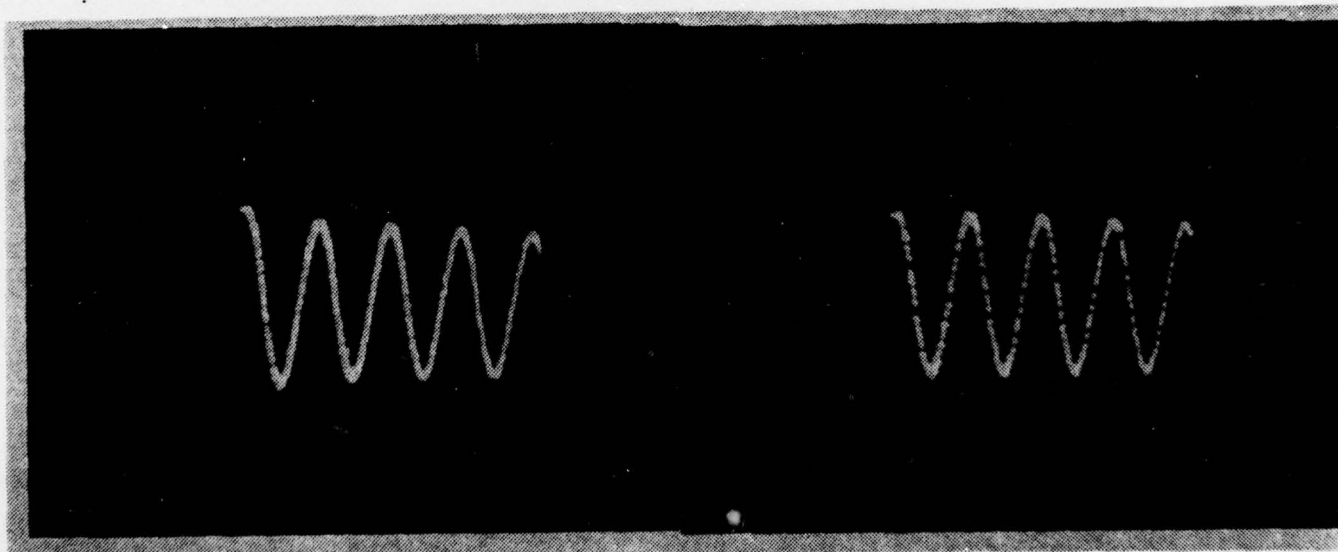PLATE D-7. ANEMOMETER SIGNAL: POOR LOCATION FOR
R(γ) MEASUREMENT

PLATE D-8. AUTOCORRELATION   PLATE D-9. AUTOCORRELATION
OF POOR S/N SIGNAL   OF GOOD S/N SIGNAL
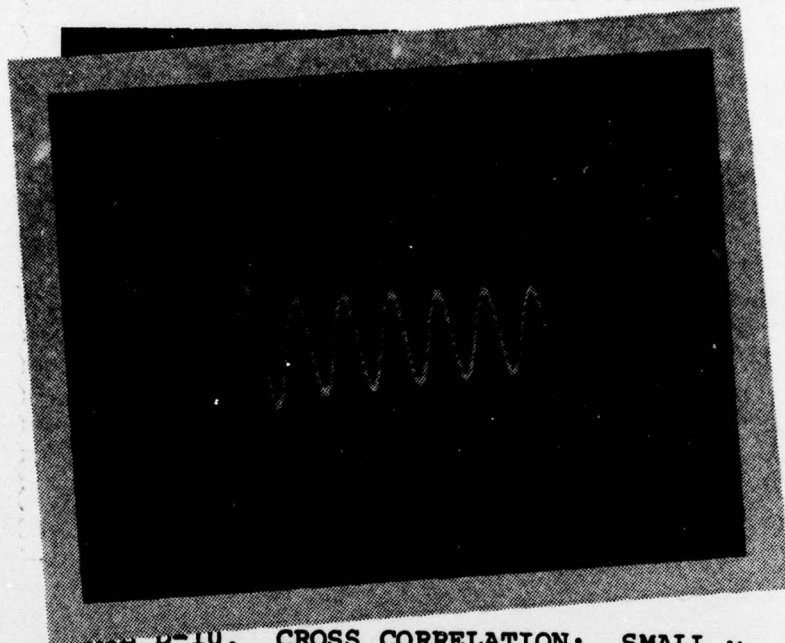
PLATE D-10. CROSS CORRELATION: SMALL γ
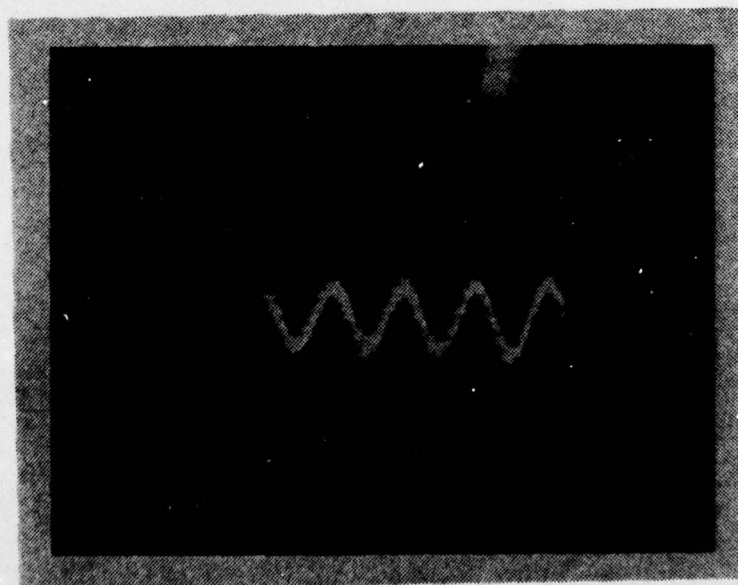

PLATE D-11. CROSS CORRELATION: LARGE γ

279

INITIAL DISTRIBUTION LIST

No. Copies

1. Defense Documentation Center   2
   Cameron Station
   Alexandria, Virginia 22314

2. Library, Code 0212   2
   Naval Postgraduate School
   Monterey, California 93940

3. Prof. J. V. Sanders   1
   Department of Physics and Chemistry
   Naval Postgraduate School
   Monterey, California 93940

4. Prof. O.B. Wilson, Jr.   1
   Department of Physics and Chemistry
   Naval Postgraduate School
   Monterey, California 93940

5. Prof. G. S. Sackman   1
   Department of Electrical Engineering
   Naval Postgraduate School
   Monterey, California 93940

6. Prof. T. M. Houlihan   1
   Department of Mechanical Engineering
   Naval Postgraduate School
   Monterey, California 93940

7. Prof. K.E. Woehler   2
   Department of Physics and Chemistry
   Naval Postgraduate School
   Monterey, California 93940

8. Dr. Jack Hoyt   1
   Naval Undersea Center
   San Diego, California 92132

9. LCDR Steven R. Cohen   2
   344 Pine Wood Lane
   Los Gatos, California 95030